Interaction Between Fast Ions and Microturbulence in Thermonuclear Devices: Theory and Modelling

THÈSE N^{O} 5164 (2011)

PRÉSENTÉE LE 14 OCTOBRE 2011

À LA FACULTÉ SCIENCES DE BASE

CRPP - THÉORIE

PROGRAMME DOCTORAL EN PHYSIQUE

ÉCOLE POLYTECHNIQUE FÉDÉRALE DE LAUSANNE

POUR L'OBTENTION DU GRADE DE DOCTEUR ÈS SCIENCES

PAR

Mattia ALBERGANTE

acceptée sur proposition du jury:

Prof. O. Schneider, président du jury
Prof. A. Fasoli, Dr J. Graves, directeurs de thèse
Prof. W. Heidbrink, rapporteur
Dr D. Testa, rapporteur
Dr F. Zonca, rapporteur

ÉCOLE POLYTECHNIQUE
FÉDÉRALE DE LAUSANNE

Suisse
2011

Our work is never over.
[Daft Punk]

Abstract

The work carried out in this thesis focuses on the interaction between fast ions and turbulence. The aim of the project is to explore this phenomenon and develop the numerical framework required for investigations on present day machines and predictions for burning plasmas. The analysis of the background plasma turbulence and the resulting fast ion diffusivities is carried out with the gyrokinetic code GENE. A set of *kinetic* transport quantities are defined in order to discriminate the transport of ions with different energies. *Gyroaveraging* effects are studied. It is observed that only at large values of the E/T_e ratio is the particle transport efficiently suppressed (E is the energy of a fast particle and T_e the electron temperature). For smaller values, $E/T_e < 15$, larger fast ion transport is observed due to resonant interactions between the particle motion and the phase velocity of the underlying turbulent waves. The transport of fusion generated alpha particles induced by electrostatic fluctuations is lower than collisional expectations, due to their large energies. Magnetic turbulence has an even smaller effect.

To verify whether similar conclusions can be drawn for neutral beam ions, substantial upgrades to the VENUS code have been implemented. The results of numerical simulations of the beam ion transport in ITER, DEMO and TCV, with the inclusion of collisional and turbulent effects, are discussed. It is demonstrated that the transport of the 1 MeV ions generated by the neutral beam injector of ITER is only marginally affected by microturbulence and it is concluded that fast ion confinement is not compromised. Given the large plasma temperatures foreseen for DEMO, anomalous transport of beam ions is significant, and in particular collisional models fail to estimate the correct heat deposited on the ions and the electrons. Given the low energy of the planned TCV NBI injector, even stronger anomalies are expected. The effect, however, can be regulated with auxiliary ECRH heating, which would allow for new studies of the fast ion turbulent transport.

keywords: plasma physics, gyrokinetics, microturbulence, fast ions, anomalous transport, ITER, DEMO, TEXTOR, TCV, neutral beam injection, alpha particles

Version abrégée

Le travail effectué dans le cadre de cette thèse est dédié à l'analyse de l'interaction entre les ions rapides et la turbulence agissant à petite échelle. L'objectif de ce projet est d'explorer ce phénomène et de construire les outils numériques nécessaires à l'analyse de cette interaction dans les tokamaks actuels et futurs. L' étude de la turbulence du fond et de la diffusion des ions rapides sont effectuées avec le code gyrocinétique GENE. Une théorie définissant un ensemble de variables *cinétiques* est développée afin d'analyser le transport des ions en fonction de leur énergie, constante sur leur orbites: les effets de moyennage sur ces dernières y sont ainsi étudiés. Seulement pour des valeurs élevées du rapport E/T_e, il est montré que le transport des particules est efficacement réduit (E est l'énergie de la particule et T_e la température électronique). Pour des valeurs plus faibles ($E/T_e < 15$), un transport accru des ions est observé, dû à l'interaction résonnante entre le mouvement des particules et la vitesse de phase des ondes turbulentes. Le transport des particules alphas générées par les réactions de fusion et sujettes aux oscillations électrostatiques du fond est très faible: il est en fait moins élevé que celui généré par les collisions coulombiennes. Les effets électromagnétiques de la turbulence sont encore plus faibles.
Pour vérifier le transport des ions produits par l'injection de faisceaux neutres, le code VENUS a été améiloré. Les résultats pour ITER, DEMO et TCV, en considérant l'effet collectif des collisions et de la turbulence, sont présentés. Il est montré que le transport des ions à 1 MeV est faiblement perturbé par la micro-turbulence, ce qui nous amène à la conclusion que le confinement des particules rapides dans ITER ne devrait pas être compromis. Par contre, les températures prévues pour DEMO sont telles que le transport des ions rapides devrait être fortement influencé par la turbulence. Par consquent, les modèles coulombiens ne sont pas en mesure de prévoir correctement la chaleur déposée sur le fond ionique et électronique. Même un transport plus élevé est prevu pour les ions rapides dans TCV. Ces derniers sont générés par un système d'injection de faisceaux neutres à des énergies comparables à la température électronique. Cependant, cet effet peut être contrôlé par le chauffage ECRH. Ce système pourrait donc permettre de nouvelles études sur le transport des ions rapides.

mots clefs: physique des plasmas, gyrocinétique, micro-turbulence, particules rapides, transport anormal, ITER, DEMO, TEXTOR, TCV, injection de faisceaux neutres, particules alpha

Contents

Chapter 1
Introduction

During the course of this thesis project two events took place that radically changed the way we look at energy production. In April 2010, following the unexpected pressure rise in the conduit used for underwater oil extraction, a massive explosion severely damaged the Deepwater Horizon, an offshore drilling rig in the Gulf of Mexico. The resulting leak, given the great depth where the damage was caused, was extremely difficult to stop, and consequently 4.9 million barrels (780,000 m^3) of oil were spilt in four months of failed attempts to seal the pipeline. The damage to the health of the population, to the environment and to the local economy are vast and still difficult to assess.

In March 2011 a magnitude 9.0 earthquake hit Tōhoku, in Japan. It was one of the strongest seismic activities ever recorded, and triggered a devastating tsunami that reached Japan's coast within an hour, causing massive destruction and more than 12'000 deaths. The Fukushima Dai-ichi nuclear power plant was also struck by the tsunami and, although it was protected by a seawall, it could not withstand the 14 meter wave. The facility was isolated from the power grid, the emergency generators were destroyed and the cooling system, which was needed to absorb the heat produced by the natural decay of fission products, was lost. The resulting overheat caused a meltdown in at least three reactors, numerous explosions and fires. The leak of radioactive materials, as of today the second most serious after Chernobyl's nuclear accident in 1986, is still impossible to accurately quantify and new concerns about the safety of nuclear energy were raised. Some countries, such as Switzerland and Germany, decided to gradually withdraw from their nuclear energy program.

These two examples indicate the risk associated with fossil fuels and nuclear fission, which, as of today, produce more than 80% of world's electricity. Both methods are also a great health and political concern even in the absence of accidents. For example, more than 3 million annual deaths are related to carbon dioxide emission and other air pollutants, according to the World Health Organization (WHO). The combustion of fossil fuels also contributes to the increasing concentration of greenhouse gases in the atmosphere and the resulting global warming. Furthermore, about 80% of world crude oil reserves are held by the twelve countries of the Organization of Petroleum Exporting Countries (OPEC). Ten of these are listed as "authoritarian regimes" in *The Economist*'s democracy index while the remaining two, Iraq and Ecuador, belong to the group of "hybrid regimes." In these countries, the general population hardly benefits from the vast profits of the extraction of state-owned oil and the recent upheaval in Libya demonstrates

Figure 1.1: Satellite image of the damaged Fukushima nuclear facility (Left, Photograph: Digital Globe). The image on the right shows the sinking of the Deepwater Horizon after the devastating explosions of April 2010 (Photograph: U.S. Coast Guard).

the strong separation between the oil-funded authorities and the common people. Nuclear power plants, on the other hand, produce large amounts of radioactive waste. In the US alone, more than 2000 tons of long-lived radioactive waste is produced every year. Finding the appropriate storage for these dangerous materials still represents a considerable challenge [1]. Nevertheless, nuclear fission still is, as of today, one of the cleanest and safest forms of energy production.

Renewable energy from natural resources potentially offers a clean, carbon-free alternative to conventional energy production. Solar and wind power, for example, can be efficiently exploited in some areas and their share of global energy output is rapidly growing. The ambitious example of Munich, the capital of Bavaria, is particularly encouraging. This german city is planning to cover with renewable sources the electricity consumption of its households (in 2015) and enterprises (in 2025). The goal will be reached with the installation of solar panels, solar-thermal heat collectors and wind turbines, among others. Given the limited resources in the region surrounding Munich, part of the installations will be built in Spain and in the North Sea. Electricity production with natural resources, however, strictly depends on weather conditions and requires considerable investments. Better efficiency also contributes to reducing, or at least stabilizing, the ever growing energy demand. This is the goal of Germany, for example, which plans to cut 50% of the domestic electrical consumption by 2050, an ambitious goal requiring technological advances and great costs for the tax-payer. On a global scale, the energy demand is nevertheless expected to increase in the forthcoming decades and new forms of efficient and reliable energy production should be sought to meet the energy gap.

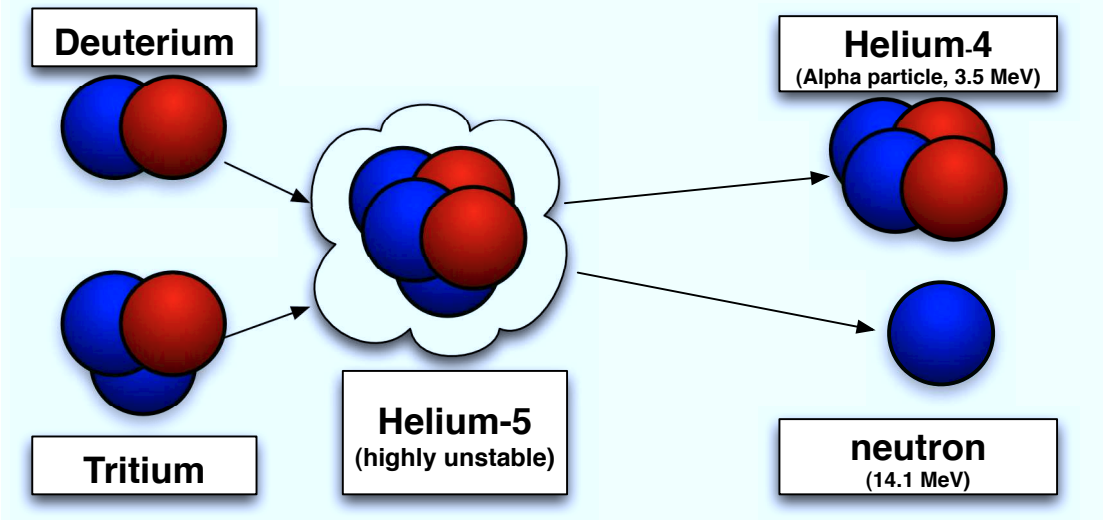

Figure 1.2: Nuclear fusion principle. The energy indicated under the alpha particle and the neutron is only the component liberated by the fusion reaction. The ^{5}He particle is highly unstable (half-life: $\simeq 10^{-22}$ seconds).

1.1 Nuclear fusion

An alternative source of energy production is nuclear fusion. While nuclear fission occurs when heavy nuclei are split into smaller elements, the opposite happens for fusion, which occurs when light nuclei, usually isotopes of hydrogen, are *fused* together. The resulting elements have a larger binding energy than the initial nuclei, so that the reaction is exothermal and energy is produced. An example is the fusion of deuterium (D) and tritium (T) nuclei, shown in figure 1.2. The D-T reaction produces an alpha particle (α), a neutron (n) and releases 17.6 MeV of energy which are shared among the products. The neutron, in particular, carries 14.1 MeV and can be used to produce electrical power in a way similar to conventional fission power plants. For the reaction between a 100 keV deuteron and a stationary target, the D-T cross section is at least two orders of magnitude larger than for D-D and D-He^3 reactions. Therefore, this reaction is the most accessible in a laboratory.

Nuclear fusion represents a "clean" solution to the energy problem. The reactants are widely available in nature and only a small amount of radioactivity is produced. In the D-T example, for instance, some materials can become radioactive by neutron activation. Tritium, with a half-life of 13 years, also contributes to the radioactivity of a nuclear fusion power plant, which would nevertheless be short-lived compared to nuclear fission reactors. Another advantage with respect to fission is the limited risk associated with nuclear proliferation [2].

Naturally, more energy must be produced by the fusion reactions than that required to initiate them. Large energies are needed to overcome the Coulomb repulsion between the positively charged nuclei. The reactants must in fact reach

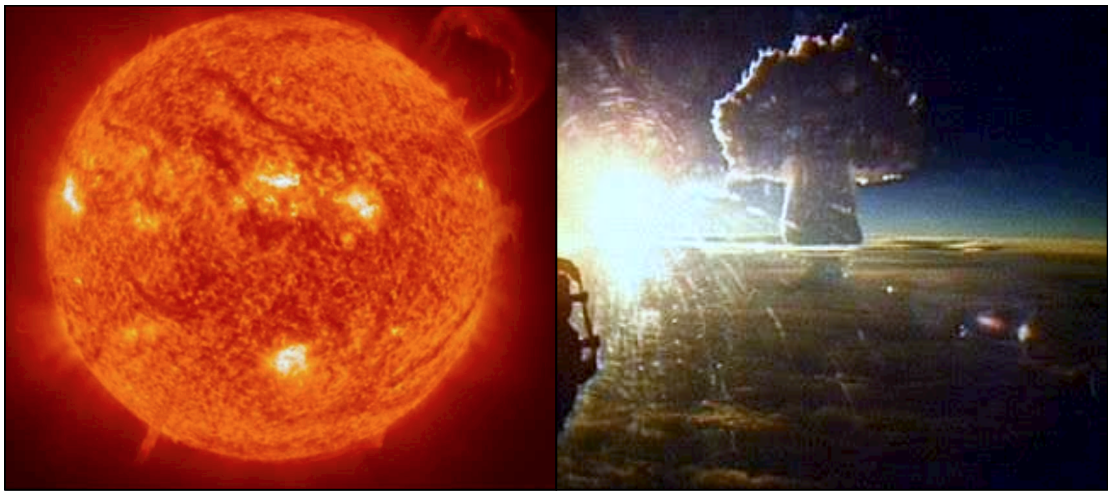

Figure 1.3: The sun, the star at the center of the solar system, sustains nuclear fusion with gravitational confinement (left). The Tsar bomb, detonated by the USSR in 1961, is the most powerful man-made nuclear fusion device ever created (right).

energies well above their ionization point and a mixture of unbound electrons and ions, called a *plasma*, is created.

The confinement of high temperature plasmas is crucial for sustaining nuclear fusion reactions. Since the beginning of nuclear fusion research it was envisaged that, in a DT reaction, the neutrons would have been used to produce electrical energy and the alpha particles would have heated the plasma. The self-sustainment of plasma burn with fusion products, called "ignition", and the more manageably, yet energy efficient, sub-ignited regime with large fusion power gain, are only possible if their energy is confined within the plasma for a sufficiently long time. Let us consider a plasma with density n, and in which the energy is confined for a time τ_{E}. Lawson [3] identified a minimal value of the product $n\tau_{\mathrm{E}}$, which is a function of the plasma temperature, to obtain ignition. This product has a minimum at the plasma temperature $T \simeq 10 - 20$ keV, for which [4]

$$n\tau_{\mathrm{E}} > 1.5 \times 10^{20}\mathrm{m}^{-3}\mathrm{s}. \tag{1.1}$$

The confinement of energy (which sustains τ_{E}) and particles (sustains n) is therefore crucial to satisfy Lawson's criterion.

In nature, gravitational attraction is used by the stars to confine the burning reactants. On earth, different techniques are explored. The most promising methods as of today are inertial and magnetic confinements. Inertial confinement fusion (ICF) is obtained by compressing a fuel pellet containing a DT mixture. The employment of magnetic fields represents the other viable solution for plasma confinement, and the most promising configuration for this is the *tokamak*.

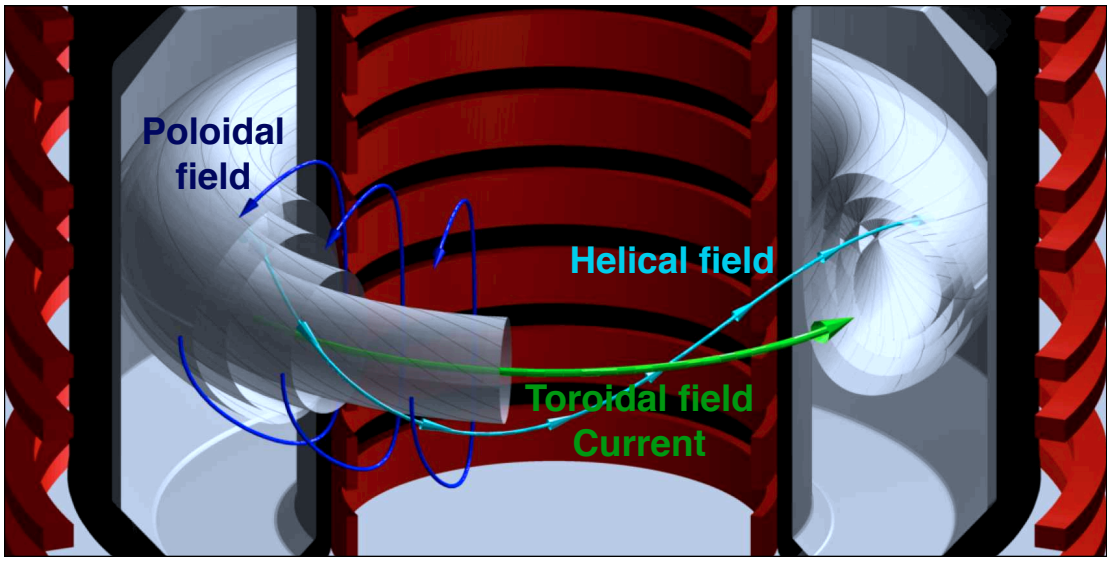

Figure 1.4: The tokamak configuration: a donut-shaped plasma is confined by helical magnetic field lines (light blue) created with the superposition of a toroidal (green) and a poloidal (blue) component. The poloidal field is generated by a current (green) circulating in the same direction as the toroidal current. Helical magnetic field lines are situated over surfaces at constant plasma pressure ("flux surfaces", light grey). The geometry is inspired by the Tokamak à Configuration Variable , described in Chapter 5.

1.1.1 The tokamak configuration

The tokamak is a toroidal device in which a donut-shaped plasma is confined with helical magnetic fields, obtained with the superposition of a toroidal and a poloidal component (figure 1.4). The toroidal magnetic field is created with electromagnetic coils encompassing the plasma. The poloidal component is created by a plasma current flowing in the toroidal direction. The resulting helical field lines enable good confinement of the charged species (figure 1.5). Furthermore, the magnetic field lines lie in nested "flux" surfaces characterized by constant plasma pressure. The closed configuration of the tokamak ensures that there are no losses along the field lines (parallel losses), which is the major advantage compared to linear devices, e.g., magnetic mirrors. Cross-field transport is nevertheless present and results in the loss of particles and heat. Coulomb collisions, for example, stochastically move the charged particles in the device. The interaction with electromagnetic waves and background plasma relaxations is even more important in thermonuclear conditions.

Plasma waves can appear in rather different forms. Some of these, such as Alfvén waves [5] and fishbones [6, 7, 8], are characterized by large spatial scales, often comparable to the size of the plasma. Similar large-scale events, such as "sawteeth" [9, 10] and neoclassical tearing modes [11], can also induce important

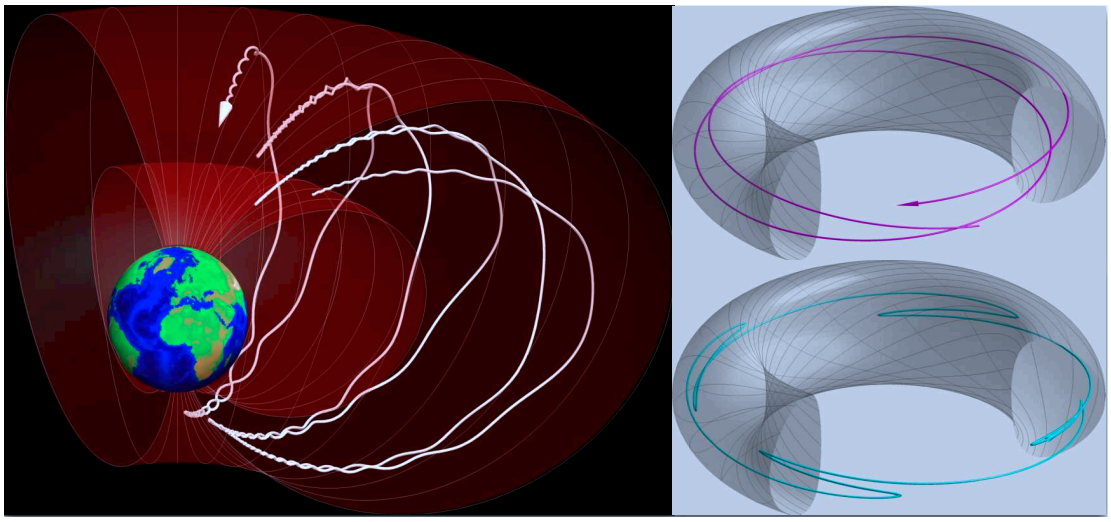

Figure 1.5: Particle orbits in the helical magnetic field of a tokamak (right): the motion of the two particles, called passing (magenta) and trapped (blue), is determined by the alignment with the magnetic field line. Trapped particles are also found in the Earth's magnetosphere (left).

transport events as they lead to local modifications of the confining magnetic field topology. A combination of particle motion and the plasma pressure generates small-scale *turbulent* fields [12]. These exhibit length scales of the order of the ion Larmor radius and strongly interact with the background plasma. This is the major cause of particle and heat transport, leading to an important deterioration of plasma performance. To compensate for the energy lost with the microturbulent induced transport, additional plasma heating is required to keep the plasma hot, the reaction cross section large, and the fusion rate satisfactory.

1.2 Plasma heating and steady state operation

The Lawson criterion is more easily satisfied with plasma temperatures of approximately 15-20 keV. To reach this goal, substantial plasma heating is required.

Ohmic heating. The toroidal current not only acts as a requirement to create the helicity of the field lines but also as a source of heating. Due to the Joule effect, the power given to a plasma with resistivity η by a current with density j is

$$P = \eta j^2. \tag{1.2}$$

Ohmic heating is very efficient at low temperatures but becomes negligible at high temperatures because $\eta \propto T_e^{-3/2}$. This reduction in the Ohmic heating efficiency can not be compensated by driving larger currents, as these might lead to unstable plasmas and, ultimately, to disruptive events.

External additional heating. If the Ohmic power given to the plasma is not sufficient, larger temperatures can be obtained with auxiliary heating. This initially creates a population of particles with energies much larger than the bulk species. The energy of these particles is then transferred to the background through Coulomb collisions. The two most commonly used methods are described here below.

With electron and ion cyclotron resonance heating (ECRH/ICRH), a fraction of the plasma is directly heated with the injection of electromagnetic waves. The resonant absorption of these waves depends on the magnetic field and the mass of the heated particles. One can then change the frequency of the incident radiation to optimize the position of the absorption layer. Many experiments also demonstrated that ECRH and ICRH techniques can both be used to control plasma stability (e.g., see [13, 14]).

The other common form of external heating is the injection of neutral beams (NBI). These particles are ionized in the plasma column, follow the helical magnetic field lines of the tokamak and transfer their energy to the bulk species via Coulomb collisions. The characteristics of the NBI injectors must be chosen to maximize the penetration of the beam, avoiding at the same time any structural damage, which might result if large fractions of the neutrals exit the plasma without being ionized. The neutral beam system in ITER is designed for the injection of 50 MW of 1 MeV deuterons. With the correct alignment of the injection angle, NBI can also be a source of non inductive current.

Alpha particle heating and burning plasma operation. In the D-T reaction envisaged for future devices, fusion reactions generate alpha particles with 3.5 MeV of energy. Part of this energy is transferred to the background plasma, whose temperatures are of the order of 10-20 keV, through Coulomb collisions. The goal of next step devices such as ITER [15] and DEMO [16] is to create "burning plasmas" in which heating is provided mostly by alpha particles. Therefore, a good confinement of alpha particles is crucial for the success of these experiments.

Non-inductive current drive and steady state operation. Plasma current in present day tokamaks is mostly obtained from the toroidal electric field generated by a transformer, an intrinsically transient method. Long pulse operation is therefore limited by this choice and alternative current drive techniques are envisaged. For example, "bootstrap" currents are driven in plasmas with a pressure gradients. The bootstrap current fraction can become important, as it was demonstrated in the Tokamak à Configuration Variable , where the entire plasma current was sustained with this approach [17]. However, current profile control in burning plasma operations is needed to stabilize the plasma. The bootstrap fraction, being challenging to regulate, is not suitable for this purpose. Alternative techniques are lower hybrid current drive (LHCD [18, 19]) and electron cyclotron current drive (ECCD [20, 21]). Non inductive currents can also be driven with

energetic ions. In particular, the neutral beam current drive technique (NBCD) is obtained with tangential NBI injection. With this method, advanced scenarios have been attained in present day tokamaks (see, e.g., refs. [22, 23, 24, 25]) and future experiments, such as ITER, rely on the NBI driven current for steady state operation [26].

In summary, the physics of energetic ions is of fundamental importance for burning plasma operation. The confinement of fusion born products is essential to heat the plasma, which would then produce more fusion reactions. Furthermore, to avoid damage to plasma facing components, alpha losses must be kept below very low levels (~ 5 % in ITER, for example). Fast ions generated by auxiliary heating methods are important, too. They are required to increase plasma temperatures to the point where fusion reactions are sufficiently numerous, and can be used to drive non inductive currents and stabilize the plasma. Therefore, a broad knowledge of the fast ion physics is crucial to predict and control the performance of future devices.

1.3 Fast ion physics

Fast ions are particles characterized by energies well above the plasma temperature [27]. As a consequence, these particles have orbits that are different from the bulk species (figure 1.6). For example, the motion of a thermal ion in a plasma can be considered to be bound to the flux surface where the particle is created. Energetic ions, on the other hand, can undergo significant displacement, which becomes larger with increasing energy. Several fast ion orbits can be defined, depending on the magnetic configuration and on the alignment of the particle velocity with respect to the magnetic field in the background. A survey of this orbits can be found in [28]. In this work, we mainly focus on "passing" and "trapped" particles, namely those illustrated in figure 1.5.

1.3.1 Fast ion "prompt" and "ripple" losses

Let us consider the large orbit width of the alpha particles shown in figure 1.6. The curves in black represent the orbit of (slow) thermal ions, which are bound to the flux surfaces. The curves in red represent alpha particles, whose displacement from the flux surfaces is considerable. Despite the large excursion on the plasma cross section, these particles appear to be well confined. Different conclusions are drawn for the curves in magenta, still representative of alpha particle orbits. The velocity of the ion in the left figure, in particular, is unfavorably aligned with the magnetic field and the ion escapes the plasma (a "prompt" loss). The one on the right is only barely confined and almost touches the outer limit of the plasma (the "last closed flux surface"). It is easy to imagine that, in the presence of even a minimal interaction with the background plasma, this particle would be lost

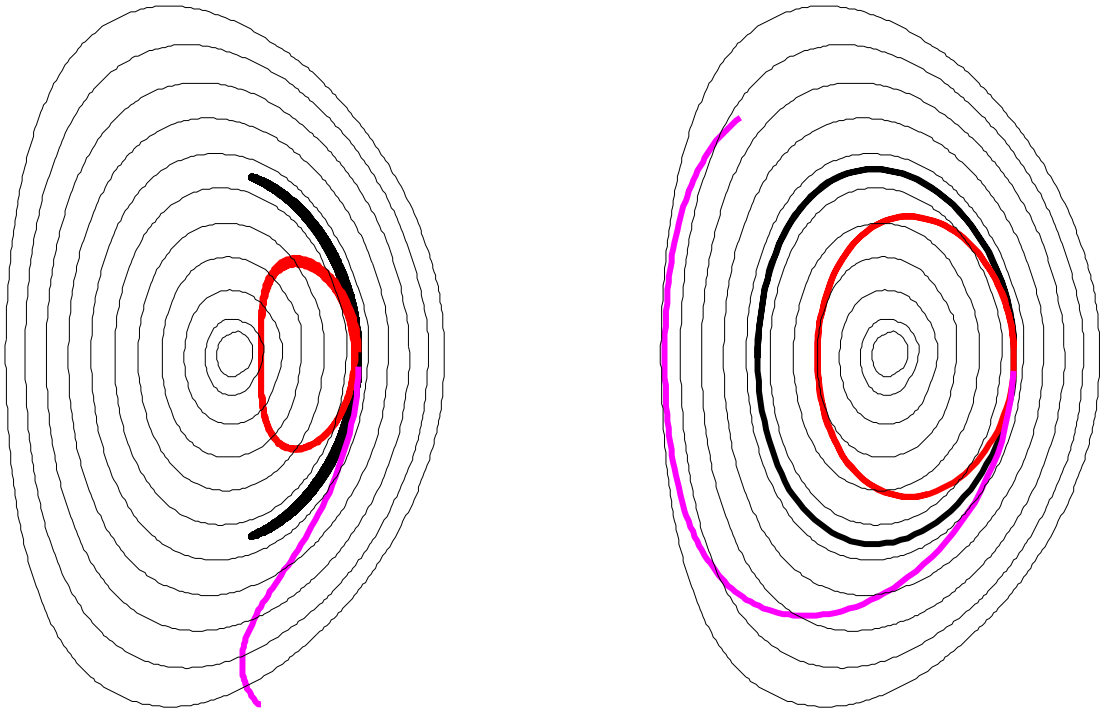

Figure 1.6: Particle orbits in a tokamak: in the left figure the motion of trapped alpha particles is shown in red and in magenta. The trajectory of a thermal ion is shown in black. The same color code is employed in the figure on the right which shows passing particles. Red and black particles have the same alignment ("pitch") with respect to the magnetic field lines.

as well. The large energy carried by fusion products would be deposited on the plasma facing materials and represent a threat for the integrity of the device.

Energetic ion confinement can also be affected by the presence of a finite number of field coils for the generation of the toroidal magnetic field, which results is a "ripple" in the field lines close to the plasma edge. This breaks the axi-symmetry of the ideal infinite-coil approximation and influences the motion of particles that can be trapped in the local magnetic "well". The vertical grad-B drift then pushes these particles outside the plasma, the effect being more important for trapped ions with bounce tip close to the plasma edge. Although large fast ion losses can be induced, they can relatively easily be calculated as the underlying physics is rather well understood [29]. Plasma scenarios where the effect is negligible, especially for alpha particles, are therefore planned for burning plasma experiments. In addition, it was shown that the insertion of ferritic steel between the field coils significantly reduces the magnetic field imperfection and therefore the particle losses [30].

1.3.2 Interaction with large scale modes

It is not only the "static" losses described in the previous paragraph that can compromise plasma operation and performance. Some "dynamic" losses also appear when particles interact with plasma waves. A large number of fast particles are generally concerned by this phenomenon and the resulting losses and redistribution can affect fusion performance and the properties of the background plasma.

Alvén waves [5] are an example of such plasma perturbations. In ITER, the phase velocity of these waves, which could bend and compress the magnetic field lines, will be around the same as the characteristic velocities of fusion alpha particles. Strong redistribution and losses are possible with this interaction, which has motivated extensive research for decades [31, 32, 33]. A large number of experimental efforts are still being carried out to unveil the fundamental properties of this interaction [34, 35, 36, 37, 38, 39]. Development of sophisticated interpretative and predictive tools is also undertaken [40, 41, 42, 43]. Reviews on the physics of Alfvén waves and their interaction with energetic ions can be found in refs. [29, 44, 45].

Other examples of the interaction between energetic ions and large scale modes can be found. The interaction with "fishbones", for instance, has been extensively studied in the literature (see, e.g., the first experimental observation of the mode [46] and a more recent investigation [47]). Recent studies demonstrated that the frequency of some important plasma relaxations, called "sawteeth", can be modified by energetic ions [48]. It was also proved that this interaction is strongly nonlinear, as energetic ions can also be redistributed by this mode [49, 50]. The interesting observation of fast ion losses driven by neoclassical tearing modes, particularly dangerous for ITER, were observed in 2007 in ASDEX [51]. Despite the great effort deployed to study energetic ions, the interaction with turbulence, presented in the next section, has not been the subject of extensive research until recently.

1.4 The interaction between fast ions and small scale turbulence

It was anticipated that the transport of the background plasma is mostly driven by small scale turbulent fields while energetic ions interact more importantly with fast waves at much longer wavelength. The interaction between fast ions and turbulence, which is the subject of this thesis, has only recently been discovered.

Studies on the finite Larmor radius effects on the fast ion transport were first performed in 1979 [52]. A series of studies was undertaken since then and it was concluded that the fast motion of energetic particles would average the (slowly evolving) small scale turbulent fields [53, 54, 55]. This effect is illustrated in figure 1.7. The "gyromotion" of an alpha particle at 3.5 MeV is characterized by length scales larger that those of the underlying microturbulence. Furthermore,

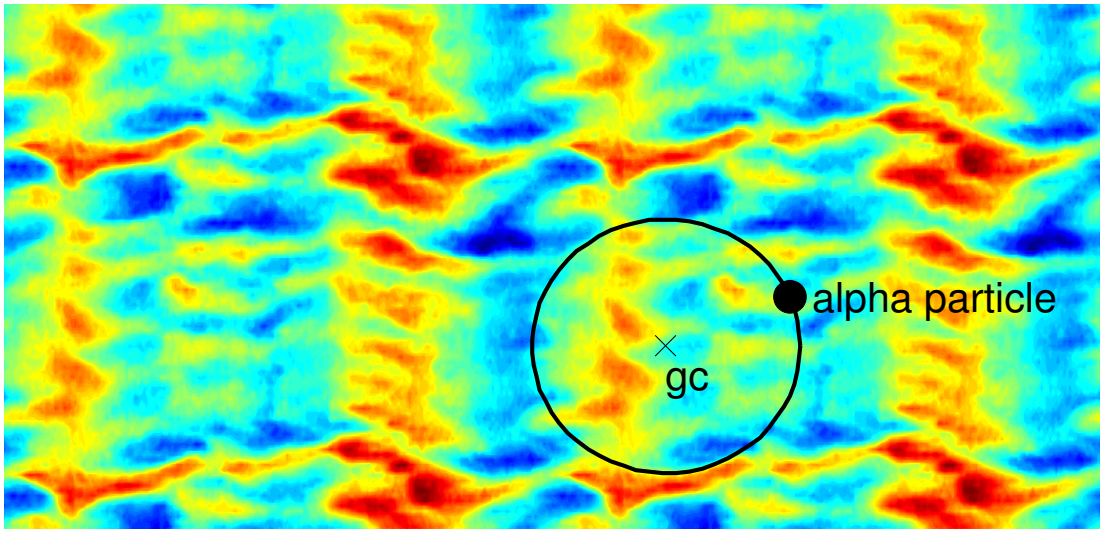

Figure 1.7: Alpha particle gyromotion and small scale turbulent fields, as simulated by the GENE code. The particle center of gyration ("gc") is indicated with a cross.

the gyromotion is much faster than the evolution of the background fields

$$\frac{t_{\text{turbulence}}}{t_{\text{gyromotion}}} \geq 500. \tag{1.3}$$

The large scale separation between the two phenomena would therefore introduce the important "gyroaveraging" phenomena. A similar "orbit-averaging" effect is expected from the drift orbit motion shown in figure 1.6, which still takes place on longer (and faster) scales than the background turbulence.

An apparent confirmation of these theoretical conclusions was found in early experiments at the Tokamak Fusion Test Reactor (TFTR) [56, 57, 58, 59], where an upper limit for fast ion diffusivities was set to 0.1 $\text{m}^2 \cdot \text{s}^{-1}$, an order of magnitude smaller than that of thermal ions. Since 2006, however, renewed interest has been triggered by both theoretical [60] and experimental [61] observations of enhanced fast ion transport. Estrada-Mila and co-authors discussed in [60] the possibility that early theories might have overestimated the beneficial gyro- and orbit-averaging effects previously discussed. In particular, they demonstrated that Maxwellian distributions at temperatures much larger than the background plasma can be subject to significant radial transport. During the same period, the first evidence of the anomalous transport of NBI ions at the Axial Symmetric Divertor EXperiment Upgrade (ASDEX Upgrade [62]) was discussed by Günther and colleagues in [61]. Since the fast ion redistribution was correlated with the background plasma heat transport, the tentative conclusion that the anomaly was caused by microturbulence was drawn.

On the theoretical side, earlier results on the transport of particles characterized by large energies have recently been extended. First-principles calculations

of the transport of trace ions in a slab geometry indicated that the complex interplay of gyroaveraging, field anisotropies and poloidal drift effects can lead to non negligible diffusivities for energetic particles [63, 64]. Not all evidence, however, pointed to the conclusion of a large anomalous transport. In [65, 66], for example, the authors claimed that the conclusions drawn by Estrada-Mila [60] were affected by the particular normalization chosen for the quantities studied. Furthermore, linear and nonlinear simulations proved that the transport of a slowing down distribution is negligible in ITER. The analysis of refs. [60, 65, 66], although rigorous from a numerical point of view, drew conclusions based on ensemble transport properties from the entire distribution, rather than considering the contribution to the overall transport given by particular regions in phase space. The extension to a velocity space resolved analysis by means of the GENE code [67, 68] was undertaken in ref. [69], where a large particle diffusivity was observed in the presence of small scale turbulence. The conclusion that turbulent transport could be responsible for the anomalous redistribution of NBI driven current observed on ASDEX Upgrade [61] was reinforced. Velocity space analyses were performed by means of the GTC code [70, 71] and the GENE code [72, 73], where the high energy decay of the particle diffusivity was discussed. A set of gyrokinetic velocity space dependent quantities was proposed in the context of this thesis and discussed in [74, 75]. It was concluded that suprathermal ions can be transported strongly, especially in the intermediate energy range ($1 < E/T_e < 15$). The analysis presented in [70, 71, 72, 73], and with this thesis work in ref. [74, 75], explained the absence of anomalous transport phenomena in early experiments: the energies of the fast ions studied in [56, 57, 58, 59] were much larger than the background plasma temperature. The work in [73] and part of the analysis presented in this manuscript and discussed in [75] concern the importance of magnetic turbulence. It was concluded that large transport levels are expected for neutral beam ions for strong perturbations of the background magnetic equilibrium. However, further analyses were carried out with the work of this thesis and it was shown that the effects for fusion alphas and beam ions are foreseen to be negligible for ITER [76].

Experimental evidence of energetic ion transport was also found in recent years. On the DIII-D tokamak [77], a series of experiments for the development of advanced scenarios were characterized by the unexpected behaviour of energetic ions [78]. This anomaly was particularly interesting due to the absence of coherent, high frequency modes known to drive fast ion transport. The introduction of an anomalous diffusion coefficient was needed to improve the agreement between TRANSP calculations and the motional Stark Effect (MSE) polarimetry observations. Further investigations have then been carried out and a series of experiments with varying plasma temperatures, while keeping the injected fast ion characteristics unaltered, were undertaken by Heidbrink and co-workers [79]. It was shown in this work how a discrepancy between experimental data, such as the one collected with from the MSE and the fast-ion D_α (FIDA [80]) diagnostics, and theoretical predictions. The disagreement, particularly evident at

large temperatures, could be reduced by introducing an anomalous diffusion coefficient from gyrokinetic predictions. It was concluded that microturbulence was responsible for the observed anomaly. Energetic ion anomalies in fusion devices have been found at the Joint European Torus (JET [81, 82]) and at the Mega-Ampere Spherical Tokamak (MAST [83, 84]). The investigation of such anomalies is still ongoing and the hypothesis of microturbulent transport still needs to be confirmed.

The need to understand the interaction between fast ions and turbulence at a fundamental level motivated studies in a linear machine and in a simple magnetized plasma. Recent investigations at the Large Plasma Device demonstrated that fast ions experience non-diffusive phenomena in the presence of drift-wave turbulence [85]. Similar studies are being performed in TORPEX using a movable fast ion source to investigate the energetic ion transport in presence of blobs and interchange modes [86]. The advantage offered by these investigations is the easier access to diagnostics and control parameters. Even more importantly, the observations made in non-tokamak devices prove the universality of these phenomena.

1.5 Contribution of this thesis

The main goal of this thesis, devised in 2007 when the only relevant publication on the theoretical side of the subject were found in [60], was to clarify whether the motion of energetic ions could be affected by turbulence in future burning plasma experiments. The analysis was performed with the GENE code using transport quantities that, for the first time, depicted the fast ion transport as a function of the velocity of the particle. With these tools, the analysis of ITER plasmas reveals that alpha particle transport would be negligible. Furthermore, the velocity space investigations demonstrate the great similarity of the apparently different results of [60] and [65] and corroborate the single particle analyses of Hauff [73] and Zhang [70]. The results shown in this manuscript also show that the most threatening transport arises at intermediate energies, $1 < E/T_e < 15$. These energies are much lower than those envisaged for the establishment of the phase space-averaging theories much debated in [70, 73]. A theoretical explanation of the enhanced transport in this energy regime is also provided in this thesis. The intermediate energy behaviour might be relevant for beam ions, which motivated the development of a numerical platform based on the VENUS code for NBI transport studies. The numerical code was employed to interpret the experimental data of the TEXTOR device and to predict the behaviour of energetic ions in TCV, ITER and DEMO. It is shown for the first time that beam ion transport would not be a concern in ITER. On the other hand, microturbulence could cause significant redistribution in DEMO. Further experiments, such as those planned in TCV with an NBI upgrade (studied in this thesis), are required to verify these predictions and to refine our knowledge of this phenomenon.

1.6 Outline

In Chapter 2 the introductory analysis of circular plasmas is presented. The study is carried out with the GENE code focusing on the transport of large temperature Maxwellian populations. Similar analyses with the single particle code HMGC are presented. The velocity space dependent transport is presented in Chapter 3. The variables are defined starting from the standard definition of gyrokinetic transport quantities. Benchmarks with the GENE code and preliminary investigations of burning plasmas are discussed. In Chapter 4 we present the upgrades to the single particle code VENUS. The new collision operator and the anomalous diffusion module, which is coupled with the GENE code, are shown. Benchmarks against the ASCOT code and the analysis of experimental data in TEXTOR are presented. The application to another experimental device, the Tokamak à Configuration Variable , is presented in Chapter 5, where the fast ion physics associated with the planned NBI upgrade is studied. The analysis of shine-through and prompt losses is carried out with the VENUS code for several plasma discharges. Anomalous NBI transport is then simulated with the GENE-VENUS interface. In Chapter 6 we present the analysis of the beam ion physics in two devices that are planned to demonstrate the feasibility of fusion and its possible development as a commercial energy source: ITER and DEMO. GENE simulations of the ITER steady state scenario are discussed and the results are implemented in the VENUS code to simulate the neutral beam driven current redistribution. A similar analysis is carried out for DEMO. Conclusions are drawn in 7. The work is completed with two appendices at the end of the manuscript. The mapping of turbulent fields from the flux tube geometry of the GENE code to the real space tokamak geometry is discussed in Appendix A. In Appendix B we present the analytical derivation of the large temperature Maxwellian transport.

Chapter 2

Anomalous transport of Maxwellian distributed energetic particles

In this chapter the introductory analysis of microturbulent fast ion transport is presented. The transport of large temperature populations in the presence of small scale fields is investigated, following the Maxwellian approximations employed by E. Mila and co-workers [60]. The GENE code, whose main features are described in the following section, is the numerical tool used for the investigation. A survey of the different transport quantities of interest is also given to shed light on the advantages and drawbacks of certain normalizations. We then perform a first set of simulations to clarify the main features of the fast ion transport. The conclusion of the initial investigations is that the transport of high temperature Maxwellian distributions is rather strong, despite the presence of gyroaveraging effects. Inward transport is also found for passive species with large temperature gradients. To assess whether the fast ion transport is inward (beneficial) or outward (detrimental), we model the alpha particle density and temperature profiles in a burning plasma scenario. The results, obtained with parameters from the ITER internal transport barrier (ITB) scenario, demonstrate that no inward transport is expected for high energy populations. Indeed, fast ions are expected to experience a significant radial displacement towards the plasma boundary, in line with the findings of ref. [60]. Even with the particle flux reduction at large temperatures, collisional levels are exceeded. Further analyses with the single particle HMGC code, which calculates the single particle motion in the presence of fields calculated by GENE, confirm these results. The investigations point to the conclusion of an enhanced collective transport of energetic ions. However, details on the precise behaviour of different classes of particles (i.e., passing or trapped) are still absent.

2.1 The GENE code

The numerical simulations of the fast ion turbulent transport are performed with the gyrokinetic turbulence code GENE [67, 68]. The Vlasov equation, given by

$$\frac{\partial f}{\partial t} + \mathbf{v} \cdot \boldsymbol{\nabla} f + \mathbf{F} \cdot \boldsymbol{\nabla}_v f = 0, \tag{2.1}$$

is solved in the gyrokinetic limit. Here, f is the particle distribution function, $\mathbf{v}$ is the particle velocity, $\mathbf{F}$ the Lorentz force and $\boldsymbol{\nabla}_v$ is the gradient in velocity space. In the gyrokinetic approximation, the evolution of the perturbed fields is assumed to be much slower than the charged particle gyrofrequency. Further assumptions are made on the scale length of the underlying turbulence. With this "gyro-ordering", summarized in (2.2) of [87], one obtains the gyrokinetic equation for the distribution function f

$$\begin{aligned} &\frac{\partial f}{\partial t} + \left[\mathbf{v}_{gc} + \frac{B_0}{B^\star_{0\parallel}} \delta \mathbf{u} \right] \cdot \\ &\qquad \cdot \left[\boldsymbol{\nabla} f - \frac{q}{m v_\parallel} \left(\boldsymbol{\nabla} \delta \bar{\Phi} + \mathbf{b}_0 \delta \dot{\bar{A}}_\parallel + \frac{\mu}{q} \boldsymbol{\nabla} B_0 \right) \frac{\partial f}{\partial v_\parallel} \right] = 0. \end{aligned} \tag{2.2}$$

Here,

- $\mathbf{v}_{gc}$ is the particle drift in the presence of the equilibrium magnetic field,
- $\delta \mathbf{u}$ is the particle drift generated by electromagnetic perturbations,
- $\delta\Phi$ and $\delta A_\parallel$ are perturbations in the electrostatic and magnetic potentials,
- a "dot" indicates a time derivative,
- an overbar is used for gyroaveraged quantities,
- $\mathbf{b}_0$ is the equilibrium magnetic field unit vector,
- $B^\star_{0\parallel} = \mathbf{b}_0 \cdot \left[\boldsymbol{\nabla} \times \left(\mathbf{A}_0 + (m/q) v_{\parallel,g} \mathbf{b}_0 \right) \right]$ and $v_{\parallel,g}$ is the parallel component of the particle drift.

The solution of the gyrokinetic equation is obtained with a δf scheme. In brief, the existence of an equilibrium distribution function f_0 is assumed which satisfies equation (2.2) in the absence of perturbed potentials. The equation for δf finally

reads

$$\begin{aligned}
&\frac{\partial \delta f}{\partial t} + \left(\mathbf{v}_{gc} + \frac{B_0}{B_{0\|}^\star} \delta \mathbf{u} \right) \boldsymbol{\nabla} \delta f + \\
&\quad - \left(v_\| \mathbf{b} + \frac{B_0}{B_{0\|}^\star} \mathbf{v}_c \right) \cdot \frac{\mu}{m v_\|} \boldsymbol{\nabla} B \frac{\partial \delta f}{\partial v_\|} = \\
&= - \frac{B_0}{B_{0\|}^\star} \delta \mathbf{u} \boldsymbol{\nabla} f_0 + \frac{B_0}{B_{0\|}^\star} \delta \mathbf{u} \frac{\mu}{m v_\|} \boldsymbol{\nabla} B \frac{\partial f_0}{\partial v_\|} + \\
&\quad + \left(\mathbf{v}_{gc} + \frac{B_0}{B_{0\|}^\star} \delta \mathbf{u} \right) \frac{q}{m v_\|} \left(\boldsymbol{\nabla} \delta \bar{\Phi} \right) \frac{\partial f_0}{\partial v_\|},
\end{aligned} \tag{2.3}$$

where $\mathbf{v}_c$ is the curvature drift. The parallel nonlinearity $\delta \bar{A}_\| \partial_{v_\|} f_0$ is neglected in the GENE code. Equation (2.3) is solved in the 5-dimensional space $(x, y, z, v_\|, \mu)$ together with Poisson's equation and Ampère's law. The real space domain is described by the set of field-aligned coordinates (figure 2.1)

$$x = \mathcal{A} \sqrt{\psi_t / \psi_{t,\text{edge}}}, \tag{2.4}$$

$$y = \mathcal{B} \left(q\theta - \phi \right), \tag{2.5}$$

$$z = \mathcal{C} \theta, \tag{2.6}$$

where $\mathcal{A}$, $\mathcal{B}$ and $\mathcal{C}$ are normalizing factors, ψ_t the toroidal flux and q the safety factor. The parallel velocity $v_\| = \mathbf{v} \cdot \mathbf{B}/B$ and the magnetic moment $\mu = m v_\perp^2 / (2B)$ complete the set of variables describing the velocity space domain. The equilibrium magnetic geometry is either chosen from a circular equilibrium or provided by the CHEASE code [88]. In the flux-tube limit, the code solves the Vlasov-Maxwell system in the surrounding of a flux surface ψ_0 with finite difference methods and a fixed phase space grid. The time evolution is obtained with a 4^{th} order Runge-Kutta scheme for the time evolution. A comprehensive description of the GENE code can be found in [87].

GENE is designed to handle an arbitrary number of particle species. For each species, the perturbed distribution function δf is calculated given the structure of the background turbulent fields. The gyrokinetic Maxwell equations are then solved and the electromagnetic perturbations calculated for the next iteration. Background species can actively influence the evolution of the microturbulent fields or can be passively transported by the background fluctuations. The latter choice is a good approximation if the population carries negligible modifications to the structure of the turbulent fields in a real plasma, as is the case for highly diluted energetic ions [65]. We will demonstrate in the next chapter that the transport features of passive populations are easier to unveil.

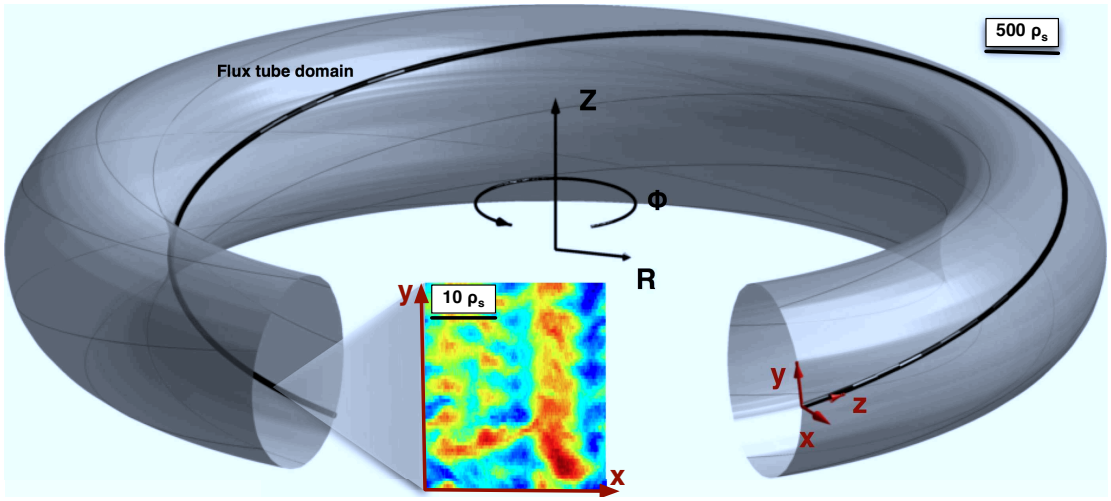

Figure 2.1: Schematic representation of the (x, y, z) coordinates employed in the GENE code. Also represented are the real space variables (R, Z, ϕ). An example of the electrostatic turbulent field simulated by the GENE code is also shown to clarify the scale length of the turbulent problem. Magnetic field lines are shown in grey.

The nonlinear particle transport in the gyrokinetic framework can be characterized by the flux

$$\mathbf{\Gamma} = \int d\mathbf{v} \delta f \delta \mathbf{u}. \tag{2.7}$$

The perturbed drift $\delta \mathbf{u} = \left(\delta \mathbf{u}_{E\times B} + \delta \mathbf{u}_{A_\parallel}\right)$ contains the following electrostatic and electromagnetic contributions

$$\delta \mathbf{u}_{E\times B} = -\frac{\boldsymbol{\nabla} \delta \bar{\Phi} \times \mathbf{B}}{B^2}, \tag{2.8}$$

$$\delta \mathbf{u}_{A_\parallel} = -v_\parallel \frac{\boldsymbol{\nabla} \delta \bar{A}_\parallel \times \mathbf{B}}{B^2}, \tag{2.9}$$

where an overbar denotes a gyroaveraged quantity. Consequently, two different components of the particle flux can be defined

$$\mathbf{\Gamma} = \mathbf{\Gamma}^{es} + \mathbf{\Gamma}^{m} = \int d\mathbf{v}\, \delta f \delta \mathbf{u}_{E\times B} + \int d\mathbf{v}\, \delta f \delta \mathbf{u}_{A_\parallel}, \tag{2.10}$$

usually referred to as the "electrostatic" and the "magnetic" components, respectively. This separation must be interpreted with caution, as magnetic contributions in δf become important, at finite β, also for the "electrostatic" component. We now briefly introduce the transport quantities usually employed in the literature and discuss their advantages and limitations.

2.1.1 Definition of transport related quantities and normalizations

Starting from the basic definition of the nonlinear particle flux of eq. (2.7), the particle transport of a generic species f can be described in terms of several different quantities.

- *Flux per particle (α) scaled to background ion (i) flux per particle* - This normalization, mainly applied in ref. [60], is based on the definition of a flux per particle as Γ_j/n_j, with Γ given by eq. (2.7). The ratio of this variable to the background ion flux per particle is therefore

$$\hat{\Gamma}_f = (\Gamma_f/n_f)/(|\Gamma_i|/n_i). \tag{2.11}$$

  The interpretation of the results in terms of this quantity can be misleading, however, when the studied species and background thermal ions are characterized by different temperature and density profiles. The electrostatic particle flux Γ is proportional to both ∇n and ∇T of the population [89]. When normalizing the flux of two populations characterized by different gradients, the results should then be considered with caution, especially when the background ion flux is small [65].

- *Effective particle diffusivity normalized to background-core ion diffusivity* - In this case, the analysis relies on the definition of an effective diffusivity for the j-th species as $D_j^{\text{eff}} = -\Gamma_j/\nabla n_j$. The particle diffusivity can be quantified in relation to the background ion diffusivity

$$\hat{D}_f^{\text{eff}}(T_f) = D_f^{\text{eff}}(T_f)/\left|D_i^{\text{eff}}\right|. \tag{2.12}$$

  The density gradient dependence of the particle flux is then partially removed. When Γ_i is negligible, however, the same limitations described for eq. (2.11) still hold.

- *Diffusivity scaled to thermal values* - The effective diffusivity of a suprathermal population is normalized to the D^{eff} of the same population as if it were in thermal equilibrium with the bulk plasma

$$\hat{D}_\alpha^{\text{eff}}(T_f) = D_f^{\text{eff}}(T_f)/\left|D_\alpha^{\text{eff}}(T_f = T_e)\right|. \tag{2.13}$$

  This choice, mainly adopted in ref. [65], is particularly useful when analyzing gyro- and orbit- averaging effects on the transport of passive species.

From now on, we will drop the "eff" superscript from the diffusivity variable, to simplify the notation.

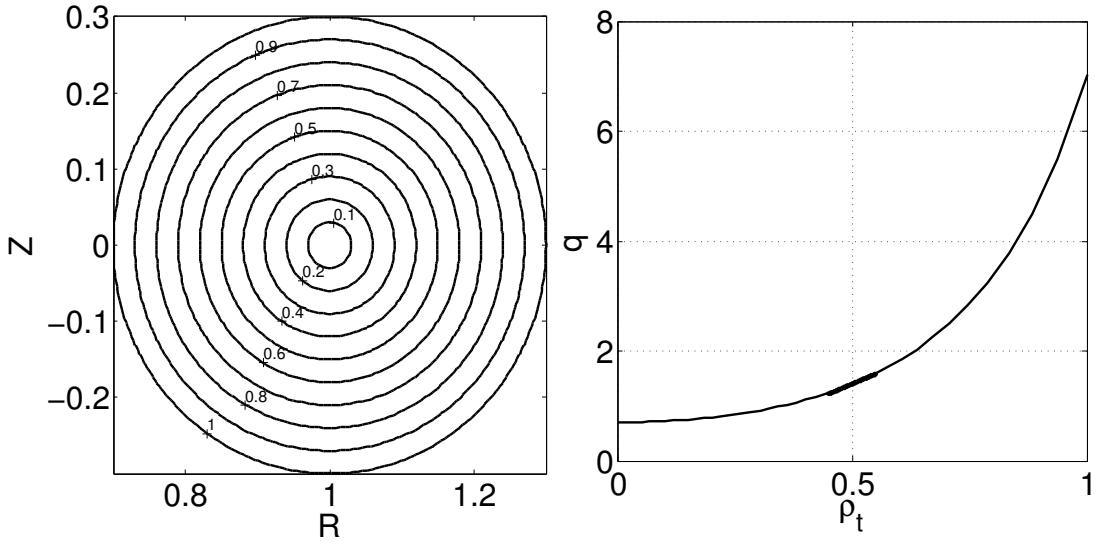

Figure 2.2: Main features of the circular plasma simulated with the GENE code. The left panel illustrates the position of the normalized toroidal flux surfaces. The safety factor profile is shown in the right panel curve, the thicker line corresponding to the linear q profile expansion in the GENE code.

2.1.2 Comparison between different normalizations

Numerical simulations are run to better understand the similarities, and differences, between these normalizations. The first numerical simulations are performed on a scenario specifically designed for this introductory analysis. A simple circular plasma characterized by a monotonic q profile is studied (figure 2.2). We choose a safety factor of $q_0 = 1.4$ with a positive magnetic shear $\hat{s} = (\rho_t/q_0)\,(\mathrm{d}q/\mathrm{d}\rho_t) = 0.8$. A radial box size of 50 ρ_s with a real space resolution $N_{(x,y,z)} = (128, 32, 16)$ is employed. This choice guarantees sufficient detail to resolve microturbulent fields. The velocity space domain of the j-th species stretches up to $(L_{v_\parallel}, L_\mu) = (3v_{th_j}, 9T_j)$ on a grid size of $(N_{v_\parallel}, N_\mu) = (32, 8)$ points. The background electrons are characterized by a reduced mass ratio $m_i/m_e = 400$. This choice optimizes computational performance without compromising the relevant physics, as discussed in ref. [69]. The density and temperature gradients are defined as

$$\Omega_\chi = \frac{R_0}{L_\chi} = \frac{R_0}{a}\frac{\mathrm{d}\ln\chi}{\mathrm{d}\rho_t}, \tag{2.14}$$

where ρ_t is a radial variable and R_0 the major radius. We employ the following values of Ω for the simulation: $\Omega_{n_{e,i}} = 3$ and $\Omega_{T_{e,i}} = 9$. Finally, we choose a passive population characterized by $m_\alpha = 2\,m_i$, $\Omega_{n_\alpha} = 3$ and $\Omega_{T_\alpha} = 0$.

The result of this numerical simulation can be observed in figure 2.3. We can see how two different normalizations rescale an otherwise identical curve, and consequently different conclusions might be drawn if the two curves are viewed

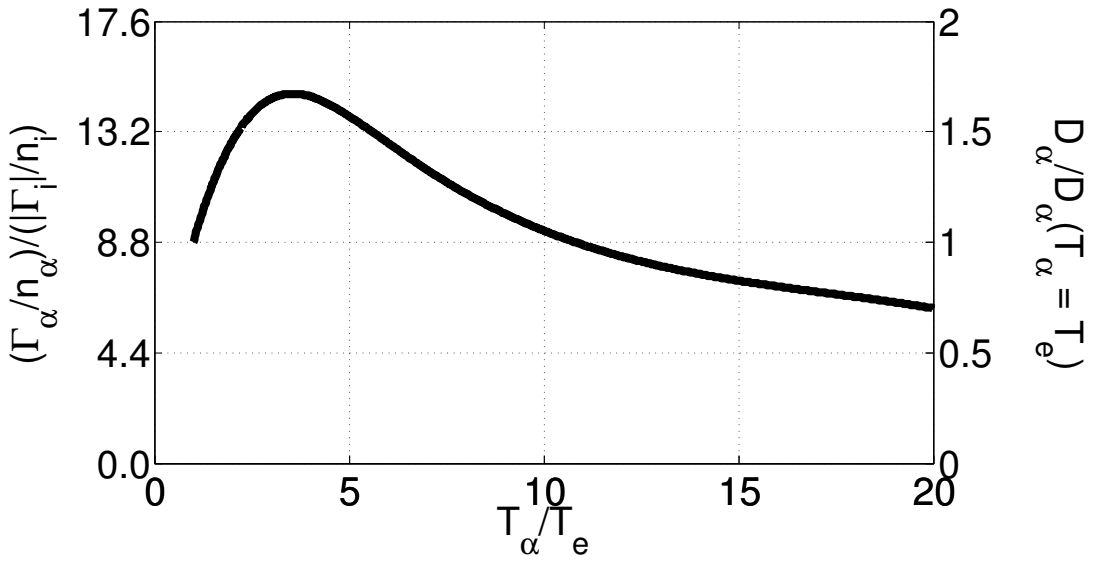

Figure 2.3: Flux per particle normalization (left axis) compared to an effective diffusivity normalization (right axis), as a function of the temperature of the population considered.

independently. The analysis of the curve in figure 2.3 with the $\hat{\Gamma}_\alpha$ normalization (left y-axis) might suggest that a strong fast ion transport is present, as suprathermal populations with $T_\alpha = 20\,T_e$ are transported across the flux surfaces as much as two to three times faster than the background species. As a consequence, we might conclude that gyroaveraging effects does not reduce the transport, and particle transport is not suppressed. The alpha and background ion species, however, are characterized by different temperature gradients. As already remarked in ref. [65] the observation of a higher flux is then related to the choice of the profile gradients and similar misleading conclusions would be drawn if one chooses $D_\alpha/\left|D_i\right|$ from eq. (2.12). Gyroaveraging effects can be investigated with the more appropriate choice of an *internal* normalization. When dealing with $\hat{D}_\alpha$ defined in eq. (2.13), the interpretation differs significantly. The right y-axis in the figure clearly suggests that fast ion transport is reduced up to a factor of two with respect to a thermal case, due to gyroaveraging effects. We can now see how the interpretation of fast ion transport strongly depends on the chosen normalization. From now on, we analyze the transport as a function of the effective diffusivity defined in eq. (2.13), since we are mostly interested in the gyro- and orbit-averaging effects on the transport. Absolute values are considered only when the analysis is focused on the particle diffusivity of ITER fast ions in a specific reference scenario.

2.1.3 Collective fast ion transport in a burning plasma scenario

We now compare the transport properties of Maxwellian populations characterized by different density and temperature gradients. Different combinations of Ω_n and Ω_T can give rise to very different fluxes, including even opposite directions of the particle flux. The importance of gyroaveraging effects is also assessed by changing the temperature of the passive population. We begin by creating a scenario where the bulk plasma parameters are the same as the ones described in the previous section. Two passive populations, characterized by the same density gradient $\Omega_n = 3$, are specified in the code. A difference between the two temperature gradients is introduced to reflect the differences between the high temperature alphas and the low energy ^{4}He (*ash*) populations,

$$\Omega_T^{\alpha} = 0,$$
$$\Omega_T^{\mathrm{ash}} = 9.$$

The flat temperature profile ($\Omega_T = 0$) is more representative of alpha particles, whose high energies ($\mathrm{E}_\alpha \simeq 3.5$ MeV) are not significantly modified by the properties of the thermal plasma. Helium impurities, on the other hand, inherit the characteristics of the bulk plasma profiles. We emphasize the similarity between the parameters and the results shown in figure 2.4 and those of ref. [60]. The results presented in figure 2.4 suggest that an inward particle flux, due to thermodiffusive effects, will arise for the $\Omega_T^{\mathrm{ash}} = 9$ ash distribution when its temperature exceeds roughly two times the background ion temperature. This undesirable situation would lead to an accumulation of impurities in the core, thus decreasing the fusion production rate and enhancing Bremsstrahlung losses. The flat temperature distribution, $\Omega_T^{\alpha} = 0$, shows an outward particle flux for all temperatures considered. The intensity of the flux will not vanish by increasing the temperature, and a decrease of 50% in D_α is observed when $T_\alpha = 20\,T_e$. In the next section we present similar results obtained in a single particle framework.

2.1.4 The HMGC code

In this section we verify whether the results obtained in the previous section could be reproduced with a different numerical approach. Instead of Eulerian, i.e. fixed grid techniques, we now choose the drift-kinetic HMGC code [40] to track the influence of microturbulent fields on the particle motion. The HMGC code simulates the particle motion in the presence of the background magnetic field and a time-varying electrostatic potential Φ. The code works with the assumption of nested circular magnetic surfaces, similar to the s-α approach in the GENE code represented in figure 2.2.

The structure of the electrostatic potential Φ is obtained from GENE simulations. As the HMGC code is *global* with respect to the real space domain, a

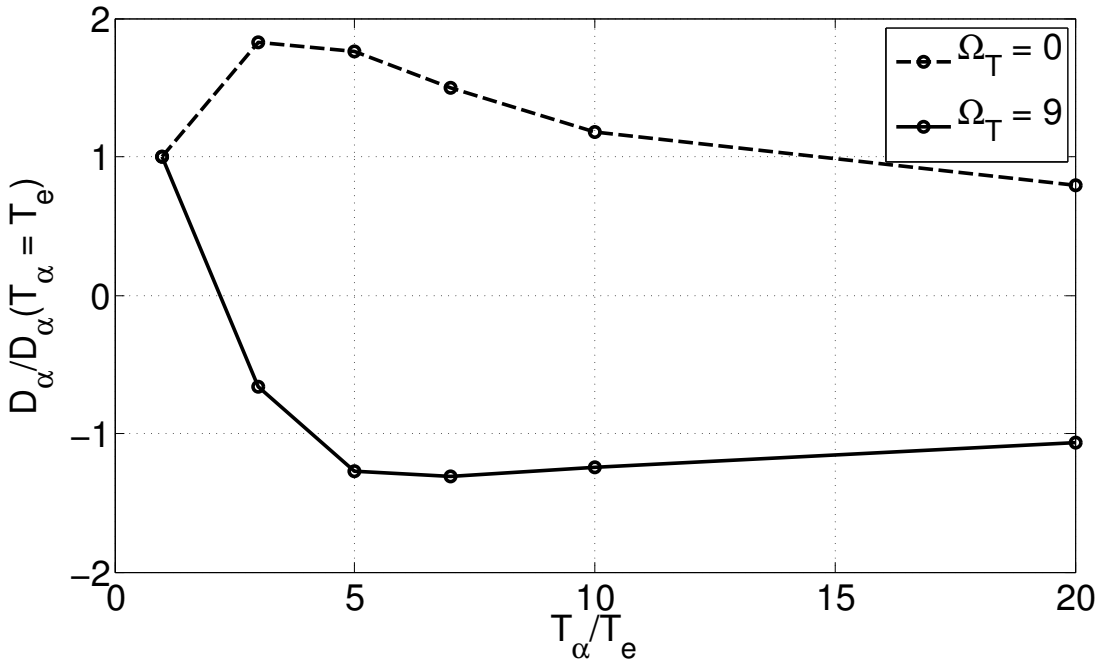

Figure 2.4: Effective diffusivity of a Maxwellian distribution as a function of temperature for two different populations: ash ($\Omega_T = 9$) and alphas ($\Omega_T = 0$). High temperature populations exhibit either thermodiffusive characteristics, for peaked temperature gradients (ash), or large diffusivities, for flat temperature distributions (alphas).

mapping is needed to reconstruct the fluctuating potential in the full torus from the flux-tube form of the GENE code. This mapping, obtained by a technique developed in the framework of this thesis, is obtained by replicating the flux tube domain in the toroidal direction (figure 2.5). More technical details on the flux tube field mapping can be found in Appendix A. To study the fast ion transport in the HMGC code we load a population of 10^5 Maxwellian distributed markers. The only conceptual difference between the HMGC code and the GENE code is the absence of gyroaveraging effects in the former. We would therefore expect the energetic ion transport as calculated with the single particle approach to be stronger especially at higher temperature T_α. The results illustrated in figure 2.6 confirm this expectation. The diffusivity in the HMGC simulations decays approximately as $D_\alpha(T) \sim T^{-\gamma}$, with $\gamma < 1/2$, while a faster decay is observed for the GENE code, meaning that transport is stronger in HMGC than in GENE.

A common conclusion from the two different numerical techniques can be reached. The transport of thermal populations with a high energy content decreases with increasing temperature, although rather slowly. The GENE code also showed the importance of density and temperature gradients for determining the particle flux strength. Furthermore, it is also demonstrated the existence of a high energy pinch. A beneficial consequence of such a phenomenon would be

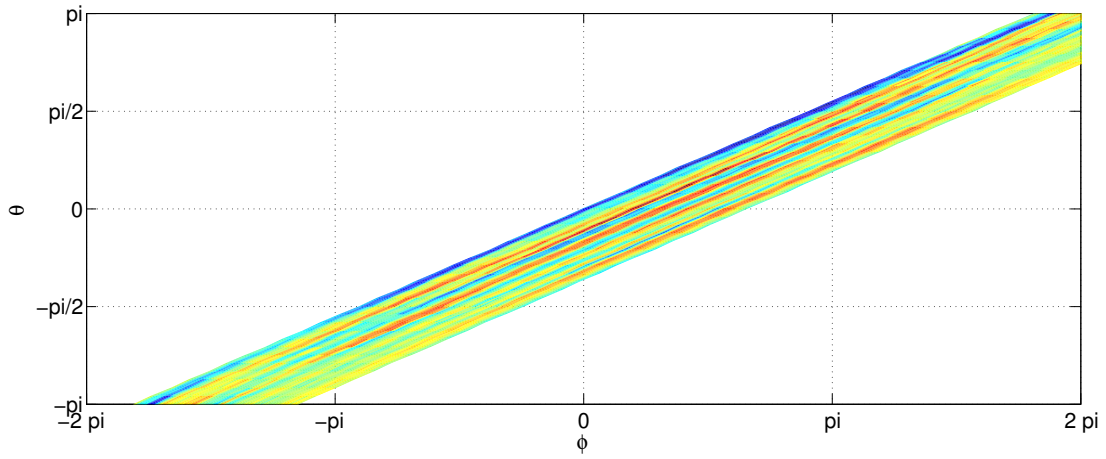

Figure 2.5: Illustration of the real space domain simulated by the GENE, for a particular flux surface. GENE variables span a $2\pi/N$ domain in the toroidal direction, as described in appendix A. The full real space reconstruction is obtained with N replicas in the toroidal direction (here N is kept artificially low for illustration purposes).

the inward transport of alpha particles. Furthermore, gyroaveraging effects must be retained when dealing with energetic ion populations as drift orbit approximations, such as those of the HMGC code, overestimate transport.

Two questions arise at this point. First, is it possible that suprathermal ash will be pinched towards the core of an actual fusion device? Second, is the high temperature particle diffusivity a reliable estimate for fusion born particles in future tokamaks? To answer these two questions, thermal density and temperature profiles need to be carefully modeled.

2.2 ITER modeling

This section focuses on simulations of the ITER tokamak. We choose, in particular, the ITB steady-state scenario discharge described in ref. [26]. This scenario is designed for obtaining long pulses with $Q > 5$, where Q is the ratio of fusion power and power input to the plasma. The profiles in figure 2.7 [90] are employed to define the background plasma parameters at mid-radius, $\Omega_{n_{i,e}} = 0.5$, $\Omega_{T_i} = 7$, $\Omega_{T_e} = 0$. The choice of a flat electron temperature profile permits a better analysis of ion temperature gradient (ITG) modes. The magnetic configuration is characterized by the safety factor value $q_0 = 1.5$ and the shear $\hat{s} = 0.4$. An artificially low ion to electron mass ratio ($m_i/m_e = 400$) is once again employed to save computational time while retaining the most important properties of the instability considered. The radial extension for these simulations is $L_x = 200\rho_s$. The real space grid is defined as $N_x = 128$, $N_{k_y} = 32$, $k_y^{\min}\rho_s = 0.05$, $N_z = 32$, $N_{v_\parallel} = 32$, and $N_\mu = 8$. We choose $\beta_{\text{mid-radius}} = 0.6\%$, a value safely below the

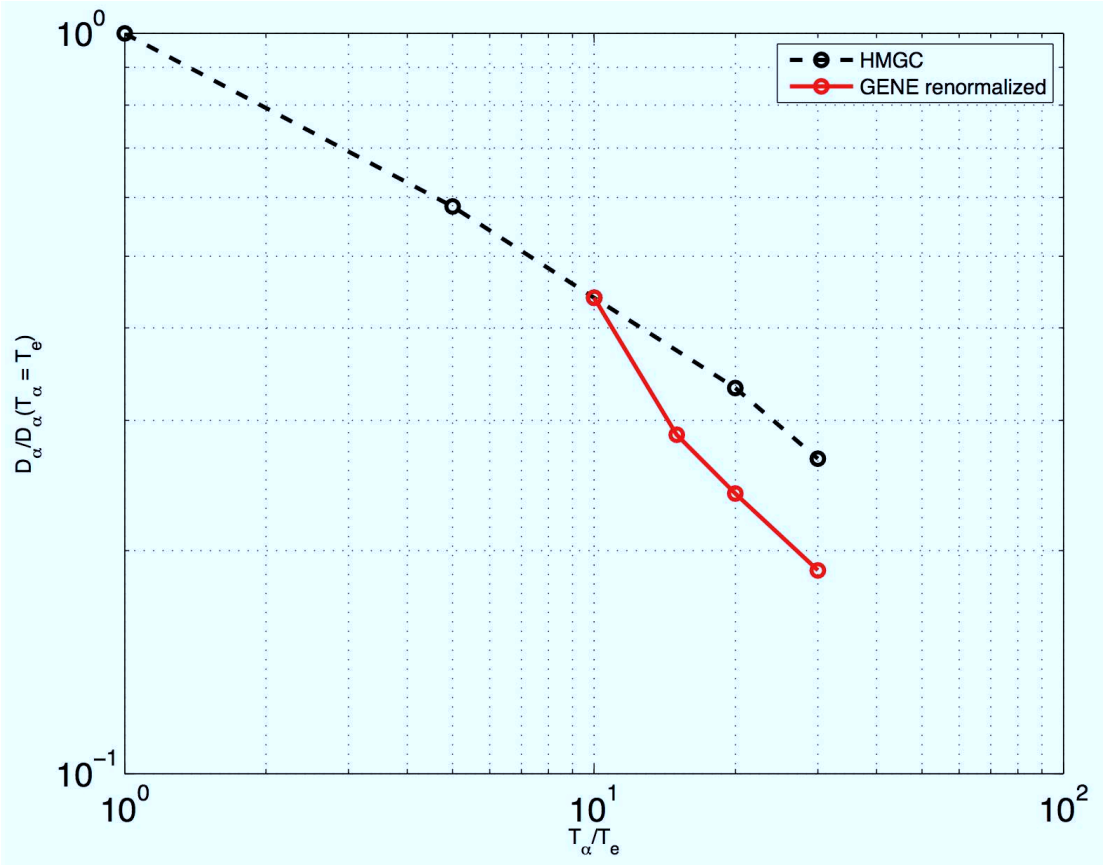

Figure 2.6: Diffusivity as a function of temperature for both a Eulerian (red) and Lagrangian (black) approach. The red curve has been normalized in order to match the diffusivity obtained at $T_\alpha = 10T_e$ with the HMGC code.

threshold for the onset of kinetic ballooning modes (KBM, ref. [91]), expected in this case at $\beta_c = 1.2\%$. We employ the circular magnetic geometry in the s-α equilibrium, with the parameter α kept equal to zero. Linear simulations with different values of α show no differences with respect to the $\alpha = 0$ case for the simple s-α model. An ITG instability is dominant with the most unstable mode peaking at $k_y\rho_s = 0.3$.

We now need to model the temperature and density gradient of the high energy population. To do so, we recall that an isotropic slowing down function

$$f_s(r,v) = \frac{S_0(r)\tau_s(r)}{4\pi}\frac{\Theta(v_\alpha - v)}{v^3 + v_c^3(r)} \tag{2.15}$$

describes the fusion alpha particle distribution undergoing collisional thermalizations. In eq. (2.15) S_0 is the fusion production rate,

$$\tau_s \propto T_e^{3/2}(r)/n_e(r), \tag{2.16}$$

$$v_c = \left[3/4\sqrt{\pi}m_e/m_\alpha Z_1(r)\right]^{1/3} v_{the}(r), \tag{2.17}$$

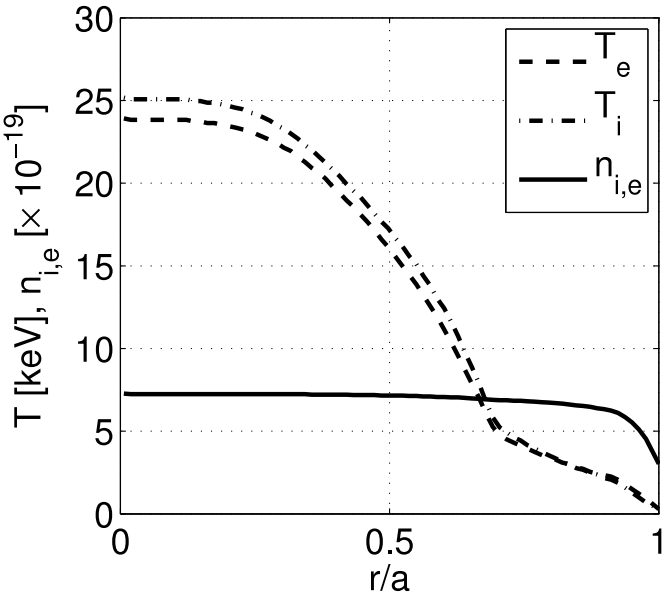

Figure 2.7: Density and temperature profiles of the bulk plasma for an ITER steady-state scenario discharge. These profiles have been used for determining the characteristics of the alpha particle ITER populations.

and Z_l is 5/3 for a D-T plasma. To find a link between this distribution and the Maxwellian f_0 employed by the GENE code we follow an approach similar to refs. [60, 65]. We model the alpha particle distribution as a Maxwellian characterized by "equivalent" density and temperature profiles. The equivalent density is given by the zeroth moment in velocity space of the slowing down distribution function while the temperature $T_\alpha(r)$ of the equivalent Maxwellian is equal to the second moment (divided by the density). The integrals defining the moments of f are calculated while separating between low and high energy ranges in velocity space. Specifically, the equivalent density profile of thermal ("ash") particles is obtained by integrating the distribution function f up to two times v_{th_i}, the background ion thermal velocity. The density profile of energetic ("hot") particles, on the other hand, is provided by integrating above this value. The same treatment is applied to the calculation of the equivalent temperature of the Maxwellian:

$$n_\alpha^{\mathrm{hot}}(r) = \int_{2v_{\mathrm{th_i}}}^{v_\alpha} f_s(r,v)d\mathbf{v}, \tag{2.18}$$

$$n_\alpha^{\mathrm{ash}}(r) = \int_{0}^{2v_{\mathrm{th_i}}} f_s(r,v)d\mathbf{v}, \tag{2.19}$$

$$T_\alpha^{\mathrm{hot}}(r) = \frac{m_\alpha}{n_\alpha^{\mathrm{hot}}(r)} \int_{2v_{\mathrm{th_i}}}^{v_\alpha} v^2 f_s(r,v)d\mathbf{v}, \tag{2.20}$$

$$T_\alpha^{\mathrm{ash}}(r) = \frac{m_\alpha}{n_\alpha^{\mathrm{ash}}(r)} \int_{0}^{2v_{\mathrm{th_i}}} v^2 f_s(r,v)d\mathbf{v}. \tag{2.21}$$

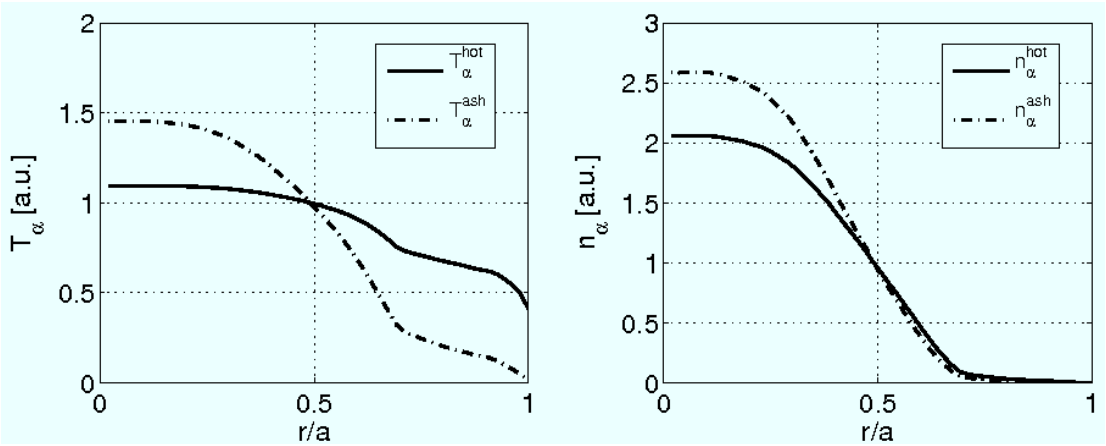

Figure 2.8: ITER alpha particle profiles, normalized at mid-radius, as obtained from integration of the slowing down distribution function of alpha particles. A separation between thermal (*ash*) and suprathermal (*hot*) particles has been introduced in the integration.

Here v_α is the birth velocity of the alpha particle. The resulting profiles are shown in figure 2.8. By taking the radial derivative of these profiles we obtain the parameters for the GENE simulation ($\Omega_{n_\alpha}^{\mathrm{hot/ash}} = 15/18$, $\Omega_{T_\alpha}^{\mathrm{hot/ash}} = 1.5/7$ at $r/a = 0.5$ for species with $m_\alpha = 2\,m_i$). For each species, again, we perform a temperature scan, as shown in figure 2.9, to see whether the low temperature pinch appears for the ash. In addition, we want to investigate to what extent the transport of the high energy population is suppressed by averaging effects. From figure 2.9, where the diffusion coefficient is expressed in absolute units, it is clear that the inward flux for the ash is absent, mainly due to the presence of strong density gradients overcoming the thermodiffusive pinch. Due to the possible drawback of impurity retention, this result represents a positive result for ITER operation. Considering the high energy particles, diffusivities above 0.4 $\mathrm{m}^2 \cdot \mathrm{s}^{-1}$ are observed over the temperature range $T_{\mathrm{hot}} = 20 - 50\ T_e$. Significant energetic transport levels such as those observed within this framework can have a detrimental impact for ITER heat and particle confinement. Nevertheless, some clarifications should be made at this point. First, evaluating the transport of an entire distribution clearly gives only an average picture and does not exclude that the enhanced diffusivity is due to the lower energy particles only, i.e. high energy (3.5 MeV) particles might be hardly affected. Second, detailed transport studies require more elaborate numerical frameworks, merging collisional (in velocity space) and turbulent (in real space) phenomena. The slowing down approximation, for instance, is valid only in a limited number of cases and for particular energetic ion sources [92]. Finally, the equivalent Maxwellian approximation of an energetic ion distribution is well-founded only in a narrow range of plasma temperatures, as shown in ref. [66]. To overcome these difficulties and draw conclusions on the microturbulence driven transport of fast ions, a velocity space resolved analysis is required. In the next

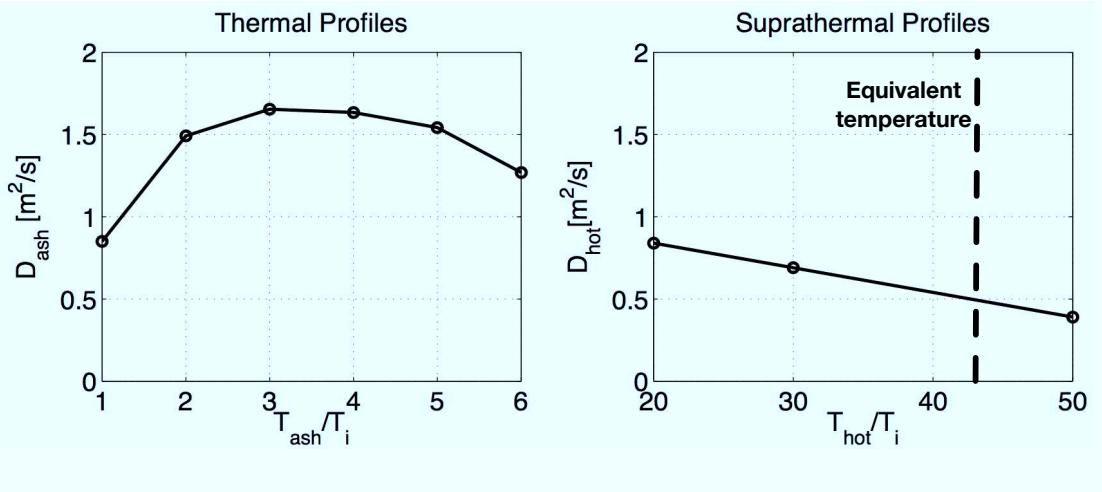

Figure 2.9: Particle diffusivity of Maxwellian populations in ITER, modeled according to the profiles of figure 2.8. For low temperature distributions the pinch present in figure 2.4 is not observable. A residual diffusivity at high temperatures is still present, thus indicating the possibility of an enhanced transport of alpha particles in ITER, whose equivalent temperature is also shown (black dashed line).

chapter, relevant quantities for velocity space investigations will be introduced. A departure from the standard approach seen elsewhere in the literature [60, 65, 66] will be presented.

2.3 Conclusions

The analyses performed in this chapter focused on the collective turbulent transport of large temperature Maxwellian populations, representative of alpha particles. Employing the GENE code, first simulations were performed to clarify the most important turbulent transport phenomena in fusion devices. It was shown that populations characterized by large density gradients are strongly driven *outward*, as one would expect from Fick's law of diffusion. Given the rather peaked density profile foreseen for fusion products during burning plasma operation, alpha particle are therefore expected to be displaced far from the plasma core. Gyroaveraging effects, expected to be important for this temperature range, does not guarantee a sufficient suppression of the turbulent fields. Large temperature gradients, more characteristic of helium impurities (i.e. thermalized fusion products), generally drive an important *inward* flux. An immediate drawback would be core impurity retention. The results were also compared with the findings of Estrada-Mila [60] and a very good agreement was found.

To assess how strongly alpha particles will be driven outward in a fusion device and to verify the direction of the turbulent flux for helium impurities, further

simulations were performed. Starting from ITER background plasma profiles, an analytical approach was used to generate the radial density profiles of alpha particles and helium ash. The idea was to examine diffusion in a more consistent way than that undertaken by Estrada-Mila. We observed that helium impurity retention is not present for the case studied, due to the favorable combination of temperature and density gradients. Less optimistic results were obtained for alpha particles, where previous observations of a limited efficiency of the fast ion averaging were confirmed also by the single particle code HMGC. Most importantly, alpha particle diffusivities were observed to be larger than collisional estimates, so far expected to be the dominant transport channel for these ions.

Overall, results suggest a strong anomalous fast ion transport in fusion devices. As the thermalization and confinement of fusion products represent the cornerstone of future experiments, turbulent phenomena could significantly affect the efficiency of fusion devices. However, the analyses presented so far only give a rough indication of the collective response of thermal populations to microturbulent fields. The behavior of individual alpha particles could be rather different. To shed light on the different responses of individual particles to the turbulent fields, a novel analytical framework is needed. This is the aim of the next chapter, where new transport related variables are obtained as a function of the particle energy.

Chapter 3

Modelling the fast ion turbulent transport

First principle estimates of the fast ion turbulent transport, based on a Maxwellian description of the energetic particle distribution, were presented in the previous chapter. Here, we introduce the theoretical and numerical foundation employed in the remainder of this thesis for anomalous transport studies. In particular, the definition of velocity space dependent diffusion and convection is presented. The new variables, obtained from gyrokinetic transport equations, are applied to the output of the GENE code. It is shown that only the non-perturbed part of the gyrokinetic operator influences the fast ion motion. Furthermore, convection is negligible for experimentally relevant fast ion distributions.

A first set of numerical simulations is performed to investigate the fast ion transport in a circular tokamak plasma. Large transport levels, partially explained by the theories developed in refs. [64, 70], are observed. A comparison with the latter work is also provided and good agreement is found. An important observation in the analysis concerns the large transport at intermediate energies ($1 < E/T_e < 10$), not described by previous investigations. A theoretical description of this energy region, based on the numerical results, is therefore provided. This theory provides an analytical particle diffusivity which is then used to compare the velocity space analyses with previous Maxwellian investigations (refs. [60, 66]). Once again, an encouraging agreement is found and we therefore conclude that the novel transport quantities introduced here are suitable for fast ion studies.

3.1 Velocity space resolved anomalous transport quantities

The main objective of this section is to propose a new definition of transport variables in a velocity space dependent, i.e. *kinetic*, framework. The quantities introduced here will be used throughout the thesis to assess the impact of turbulent transport on different classes of particles. First, we investigate the δf term which enters the definition of the nonlinear particle flux, such as the one employed in the GENE code,

$$\mathbf{\Gamma} = \int d\mathbf{v} \delta f \delta \mathbf{u}. \tag{3.1}$$

We recall that the perturbed particle drift $\delta\mathbf{u}$, already presented in the previous chapter, is given by

$$\delta \mathbf{u}_{E\times B} = -\frac{\boldsymbol{\nabla}\delta\bar{\Phi}\times\mathbf{B}}{B^2}, \tag{3.2}$$

$$\delta \mathbf{u}_{A_\parallel} = -v_\parallel \frac{\boldsymbol{\nabla}\delta\bar{A}_\parallel\times\mathbf{B}}{B^2}, \tag{3.3}$$

where gyroaveraged quantities are marked with an overbar. In this section we focus on particles that do not modify the evolution of the background turbulence, nor δu. We call these particles *passive tracers*.

3.1.1 The perturbed distribution function δf

The δf quantity represents the perturbation of the stationary distribution function f_0. To find an expression for δf, we can write the gyrokinetic equation

$$\begin{aligned}\frac{\partial \delta f}{\partial t} + (\mathbf{v}_{gc} + \delta\mathbf{u}')\cdot\boldsymbol{\nabla}\delta f + \delta\mathbf{u}'\mu\boldsymbol{\nabla}B\frac{\partial\delta f}{\partial E} = \\ = -\delta\mathbf{u}'\boldsymbol{\nabla}f_0 + (\mathbf{v}_{gc}+\delta\mathbf{u}')\,q\left(\boldsymbol{\nabla}\delta\bar{\Phi} + \mathbf{b}_0\delta\bar{A}_\parallel\right)\frac{\partial f_0}{\partial E}.\end{aligned} \tag{3.4}$$

This is a more convenient form than the one solved by the GENE code. Here, $\mathbf{v}_{gc}$ is the drift motion of a particle in the presence of the equilibrium magnetic field and

$$\delta\mathbf{u}' = \frac{B_0}{B^\star_{0\parallel}}\delta\mathbf{u}. \tag{3.5}$$

To ease the notation we define

$$-(\mathbf{v}_{gc}+\delta\mathbf{u}')\,q\left(\boldsymbol{\nabla}\delta\bar{\Phi} + \delta\bar{A}_\parallel\right) \equiv F. \tag{3.6}$$

Similarly to [89], we introduce a non-perturbed and a perturbed component of the gyrokinetic operator

$$\hat{\mathbf{G}} = \hat{\mathbf{L}} + \delta\hat{\mathbf{L}}, \tag{3.7}$$

where

$$\hat{\mathbf{L}} = \frac{\partial}{\partial t} + \mathbf{v}_{gc} \cdot \boldsymbol{\nabla}, \tag{3.8}$$

$$\delta\hat{\mathbf{L}} = \delta\mathbf{u}' \cdot \boldsymbol{\nabla} + \delta\mathbf{u}' \cdot \mu\boldsymbol{\nabla}B\frac{\partial}{\partial E}. \tag{3.9}$$

The following relationships are valid,

$$\hat{\mathbf{L}} f_0 = 0, \tag{3.10}$$

$$\hat{\mathbf{G}}\delta f = \left(\hat{\mathbf{L}} + \delta\hat{\mathbf{L}}\right)\delta f = -\left(\delta\mathbf{u}' \cdot \boldsymbol{\nabla} f_0 + F\,\partial_E f_0\right). \tag{3.11}$$

The solution for δf is

$$\delta f = -\hat{\mathbf{G}}^{-1}\left\{\boldsymbol{\nabla} f_0 \cdot \delta\mathbf{u}'\right\} - \hat{\mathbf{G}}^{-1}\left\{F\,\partial_E f_0\right\} = \delta f_1 + \delta f_2, \tag{3.12}$$

where

$$\delta f_1 = -\hat{\mathbf{G}}^{-1}\left\{\boldsymbol{\nabla} f_0 \cdot \delta\mathbf{u}'\right\}, \tag{3.13}$$

$$\delta f_2 = -\hat{\mathbf{G}}^{-1}\left\{F\,\partial_E f_0\right\}. \tag{3.14}$$

The operator $\hat{\mathbf{G}}^{-1}$ represents an integration along the *perturbed* particle motion (i.e. including microturbulent fields). Two terms therefore define the turbulent particle flux (3.1)

$$\boldsymbol{\Gamma} = \int d\mathbf{v}\,\delta f \delta\mathbf{u} = \underbrace{\int d\mathbf{v}\,\delta f_1 \delta\mathbf{u}}_{\Gamma_1,\,\text{(thermo)diffusive}} + \underbrace{\int d\mathbf{v}\,\delta f_2 \delta\mathbf{u}}_{\Gamma_2,\,\text{convective}}. \tag{3.15}$$

The well known (thermo)diffusive component of the particle transport, generated by gradients in the distribution, is described by Γ_1. The term Γ_2 represents the convective component.

If we neglect the perturbed part of the gyrokinetic operator $\delta\hat{\mathbf{L}}$, the perturbed distribution function in the local limit reads

$$\begin{aligned}\delta f &= -\hat{\mathbf{L}}^{-1}\left(\delta\mathbf{u}' \cdot \boldsymbol{\nabla} f_0 + F\,\partial_E f_0\right) = \\ &= -\boldsymbol{\nabla} f_0 \cdot \hat{\mathbf{L}}^{-1}\delta\mathbf{u}' - \partial_E f_0 \cdot \hat{\mathbf{L}}^{-1}F = \delta f_1^L + \delta f_2^L,\end{aligned} \tag{3.16}$$

where

$$\delta f_1^L = -\boldsymbol{\nabla} f_0 \cdot \hat{\mathbf{L}}^{-1}\delta\mathbf{u}', \tag{3.17}$$

$$\delta f_2^L = -\partial_E f_0 \hat{\mathbf{L}}^{-1}F. \tag{3.18}$$

Here, $\hat{\mathbf{L}}^{-1}$ corresponds to an integration along *unperturbed* orbits (i.e. those generated by the background magnetic field). Therefore, the gradient of the distribution function f_0 can be taken out of the integral only if it is constant along the particle motion. This condition is true for particles drifting under the influence of $\mathbf{v}_{gc}$, i.e. in the non-perturbed limit. We will show in the next paragraphs that the approximation $\hat{\mathbf{G}} \simeq \hat{\mathbf{L}}$ is indeed applicable to the case of passive tracers.

3.1.2 Velocity space dependent (thermo)diffusion

The (thermo)diffusive flux of eq. (3.15) is quantified by local gradients in the equilibrium distribution function

$$\mathbf{\Gamma}_1 \equiv \int d\mathbf{v} \delta f_1 \delta \mathbf{u} = -\int d\mathbf{v} \left(\boldsymbol{\nabla} f_0 \cdot \hat{\mathbf{L}}^{-1} \delta \mathbf{u}' \right) \delta \mathbf{u}. \tag{3.19}$$

To find the kinetic analog of the fluid particle diffusivity we focus on the radial particle transport

$$\Gamma_1 = \left[\int d\mathbf{v} \delta f_1 \delta \mathbf{u} \right] \cdot \mathbf{e}_r = \int d\mathbf{v} \delta f_1 \delta u. \tag{3.20}$$

From this relation we can define a microscopic particle flux per unit velocity space volume $\Gamma_{1,v}$ such that $\Gamma_1 = \int d\mathbf{v}\, \Gamma_{1,v}$

$$\Gamma_{1,v} = \delta f_1 \delta u. \tag{3.21}$$

The velocity space dependent particle diffusivity D_v is defined in terms of Γ_v and $\nabla_r f_0$ as

$$D_v = -\frac{\Gamma_{1,v}}{\nabla_r f_0} = -\frac{\delta f_1 \delta u}{\nabla_r f_0}, \tag{3.22}$$

where a subscript "r" indicates a radial projection (to simplify the notation, the subscript is from now on dropped from radial gradients). Equation (3.22) can be considered as a generalized Fick's law in the local limit. Here, D_v has units of $\mathrm{m}^2 \cdot \mathrm{s}^{-1}$, like its fluid counterpart. Let us consider eq. (3.22) and eq. (3.16). If it is valid to ignore the effect of the perturbed operator, D_v does not depend on the equilibrium distribution function, nor on its gradients:

$$D_v \simeq D_v^L = \frac{\left[\boldsymbol{\nabla} f_0 \cdot \hat{\mathbf{L}}^{-1} \left(\delta \mathbf{u}' \right) \right]}{\nabla f_0} \delta u = \left[\hat{\mathbf{L}}^{-1} \left(\delta \mathbf{u}' \right) \right]_r \delta u. \tag{3.23}$$

Here, we assume that the equilibrium distribution function f_0 is characterized by gradients only in the radial direction, a reasonable assumption in tokamak devices.

If it is necessary to keep the perturbed operator, the definition in (3.22) would still depend on $\boldsymbol{\nabla} f_0$

$$D_v = \frac{\left[\hat{\mathbf{G}}^{-1}\left(\boldsymbol{\nabla} f_0 \cdot \delta \mathbf{u}'\right)\right]}{\nabla f_0} \delta u = D_v^L + \delta D_v, \tag{3.24}$$

where δD_v is the term retaining $\boldsymbol{\nabla} f_0$ dependencies. For the particular case of a Maxwellian distribution in the local limit, the only dependency in f_0 and $\boldsymbol{\nabla} f_0$ is in the energy. The reason why the $\hat{\mathbf{L}}$ operator does not influence $\boldsymbol{\nabla} f_0$ is the energy conservation along the unperturbed particle motion. On the other hand, the perturbed operator $\delta\hat{\mathbf{L}}$ *does* modify the particle energy, which is not a constant of the perturbed particle motion. We will verify in the upcoming section that the importance of the δD_v term is limited.

In the GENE code, where f_0 is a Maxwellian, we calculate the kinetic diffusivity as follows

$$D_v = -\frac{\delta f_1 \delta u}{f_0 \left[(E/T - 3/2) \ln \nabla T + \nabla \ln n\right]}. \tag{3.25}$$

This definition appeared for the first time in ref. [74], although an attempt to investigate similar quantities can be found in earlier work [69, 73]. We can immediately observe that the ordinary Fick's law is satisfied by the velocity space average of D_v over the equilibrium distribution function,

$$D = \frac{\int d\mathbf{v} f_0 D_v(\mathbf{v})}{\int d\mathbf{v} f_0}. \tag{3.26}$$

3.1.3 Velocity space dependent convection

An analogous reasoning can be outlined for the convective particle transport. The particle flux generated by the δf_2 component is

$$\Gamma_2 \equiv \int d\mathbf{v} \delta f_2 \delta u = -\int d\mathbf{v} \left(\partial_E f_0 \hat{\mathbf{L}}^{-1} F\right) \delta u. \tag{3.27}$$

A velocity space dependent convection can be obtained similarly to the particle diffusivity D_v as

$$C_v = n \frac{\delta f_2 \delta u}{f_0}. \tag{3.28}$$

In this case, the convective component of the particle flux does not depend on density or temperature gradients. The macroscopic convective transport is obtained by averaging C_v over the stationary distribution f_0

$$C = \frac{\int d\mathbf{v} f_0 C_v}{\int d\mathbf{v} f_0} = \int d\mathbf{v} \delta f_2 \delta u. \tag{3.29}$$

In numerical simulations where the particle flux is calculated from eq. (3.1), without an explicit separation between Γ_1 and Γ_2, the convective component is identified by setting $\nabla f_0 = 0$. This choice enables the suppression of (thermo)diffusive effects.

3.1.4 Validation of the velocity space dependent transport quantities

Given the importance of the quantities described in sections 3.1.2 and 3.1.3, a set of tests to confirm their plausibility is needed. The benchmarks are run with the GENE code, which provides a set of diagnostics for extracting the quantity $\delta f \delta u$. The code does not separate δf_1 and δf_2, so the convective and diffusive components must be indentified with an appropriate choice of density and temperature gradients. The parameters for this simulation are chosen from a circular case in the s-α approximation for a deuterium plasma. Strong density and temperature gradients are chosen to generate a mixture of ITG and trapped electron modes (TEM), $\Omega_{n,e} = 3.5, \Omega_{T,e} = 12, \Omega_{n,i} = 4, \Omega_{T,i} = 4$. The size of the real space domain is $(L_x, L_y) = (125, 125)\,\rho_s$ and one poloidal turn along the z coordinate. Several passive species are added to the simulation to identify diffusive, thermodiffusive and convective components. These are used to demonstrate the validity of the presented theoretical framework.

- *Diffusion invariance for ∇n driven transport* - In the definition of a kinetic diffusivity we stressed that some perturbed terms, via the $\delta\hat{\mathbf{L}}$ operator, might be present. This would result in an ill-posed definition of D_v which would depend on ∇f_0. To verify whether this effect is important, i.e. whether δD_v in (3.24) is not negligible, we perform a series of tests. We introduce in the GENE code several passive distributions characterized by different values of $\nabla \ln n$ (i.e. ∇f_0). If the perturbed part of the operator has small effects, the quantity D_v should be the same for each distribution considered (i.e. independent of ∇f_0). The curves in fig. 3.1, describing the results of the numerical simulations, provide a clear proof of the validity of the theoretical framework. Very small differences can be observed at large energies where the particle transport becomes negligible (fig. 3.2). The $\delta\hat{\mathbf{L}}$ term is probably responsible for this discrepancy, although residual convection might also be present. This conclusion is further motivated by the observation that the dissimilarities between the different curves appear to vanish as $\Omega_n \to \infty$. In conclusion, we observe that the transport of passive tracers is mostly influenced by the non-perturbed component $\hat{\mathbf{L}}$ of the gyrokinetic operator. The effects from the perturbed operator $\delta\hat{\mathbf{L}}$ are negligible for the parameters used here.

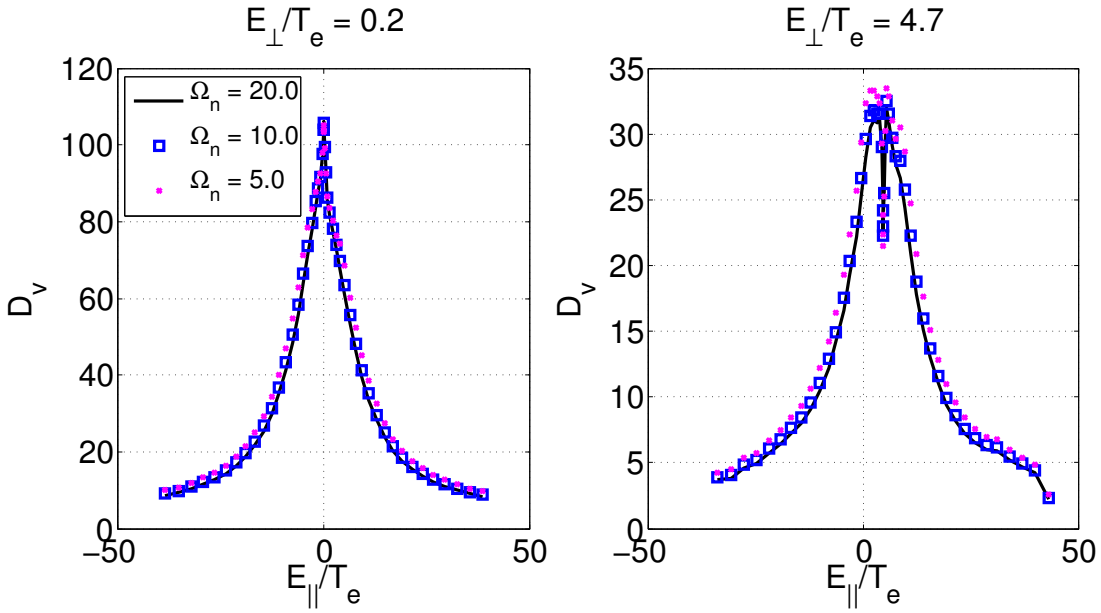

Figure 3.1: Comparison between the velocity space dependent diffusivity of three populations characterized by different density gradients. Left to right, the perpendicular energy of the passive tracer is increased, showing a good agreement over a wide range of energies.

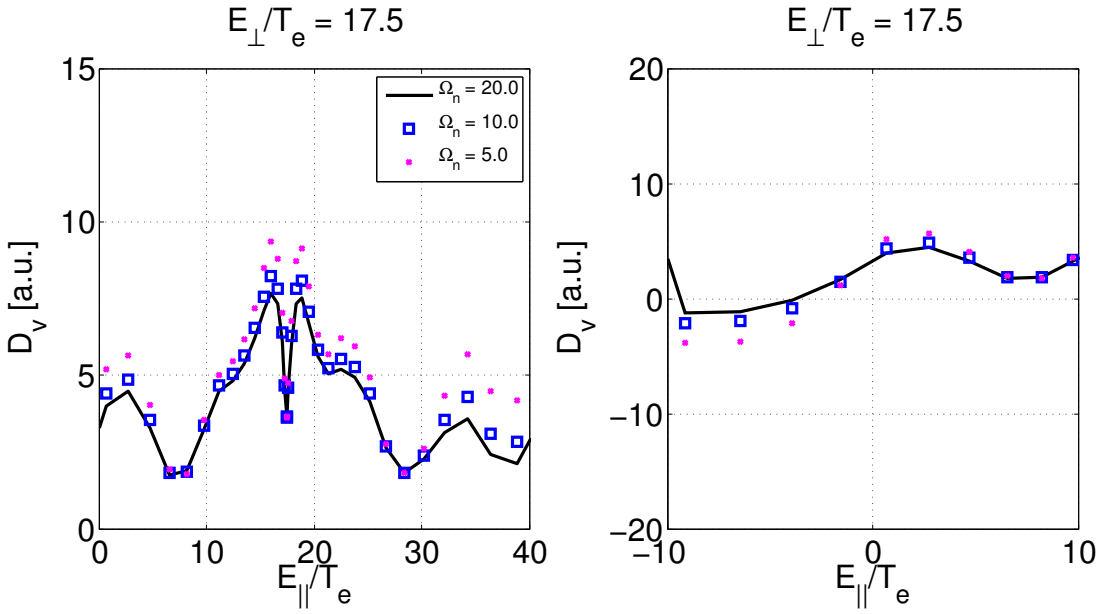

Figure 3.2: Comparison between the velocity space dependent diffusivity of three populations characterized by different density gradients. A magnification is shown in the right panel to clarify the small discrepancies observed.

- *(Thermo)diffusion invariance* - We now want to verify whether the kinetic diffusivity D_v is invariant for ∇T- or ∇n-driven transport for $\nabla f_0/f_0 \gg 1$. We perform a simulation with two passive populations, one characterized by $\nabla \ln T \gg 1, \nabla n = 0$ and the other by $\nabla T = 0, \nabla \ln n \gg 1$. For large density and temperature gradients convective contributions are negligible, as required for this demonstration. We therefore have:

$$\underbrace{\Gamma_v}_{\text{from GENE}} = \delta u \delta f = \delta u \delta f_1 \left[1 + \underbrace{\frac{\delta f_2}{\delta f_1}}_{\propto f_0/\nabla f_0 \ll 1} \right] \simeq \delta u \delta f_1 = \Gamma_{1,v}. \tag{3.30}$$

For the first species we calculate the quantity D_v as

$$\begin{aligned} D_{\nabla T,v} &= -\frac{\delta f \delta u}{f_0 \nabla \ln T \left(E/T_e - 3/2 T_{\text{passive}}/T_e\right)} = \\ &= -\frac{\delta f \delta u}{f_0 \nabla \ln T \left(E/T_e - 6.5\right)}, \end{aligned} \tag{3.31}$$

while for the second population we define

$$D_{\nabla n,v} = -\frac{\delta f \delta u}{f_0 \nabla \ln n}. \tag{3.32}$$

To verify that $D_{\nabla T,v} = D_{\nabla n,v}$, we analyze the curves of figure 3.3. We only observe minor differences, located only in the low energy where the condition $(E/T_e = 3/2 T_{\text{passive}}/T_e = 6.5)$ at the denominator of (3.31) is met. The two diffusivities are thus equal and differences arise from the normalization against a vanishing quantity. The fast ion diffusivity with the GENE code can be obtained with nonlinear simulations including a distribution of passive tracers characterized by a large $\nabla \ln n$.

- *Superposition principle* - As a last test, we want to verify the superposition principle. Once the kinetic transport quantities are known, the particle flux of a passive population can be calculated as

$$\begin{aligned} \Gamma_j &= \int d\mathbf{v} f_{0,j}\left(\mathbf{v}, T_j\right) W_v(\mathbf{v}), \\ W_v\left(\mathbf{v}\right) &= -D_v(\mathbf{v}) \left[\nabla \ln n + \nabla \ln T \left(E/T_j - 3/2\right)\right] + C_v(\mathbf{v}) \end{aligned} \tag{3.33}$$

One could therefore obtain C_v and D_v from two species characterized by large and null ∇f_0, respectively. The particle flux of a third species with arbitrary $\nabla \ln n$ and $\nabla \ln T$ can then be reconstructed from equation (3.33). The validation can also be made in velocity space since W_v can be extracted from the GENE code. The validity of the approach is once again confirmed by the results of fig. 3.4 where particle flux is obtained with eq. (3.33) (green

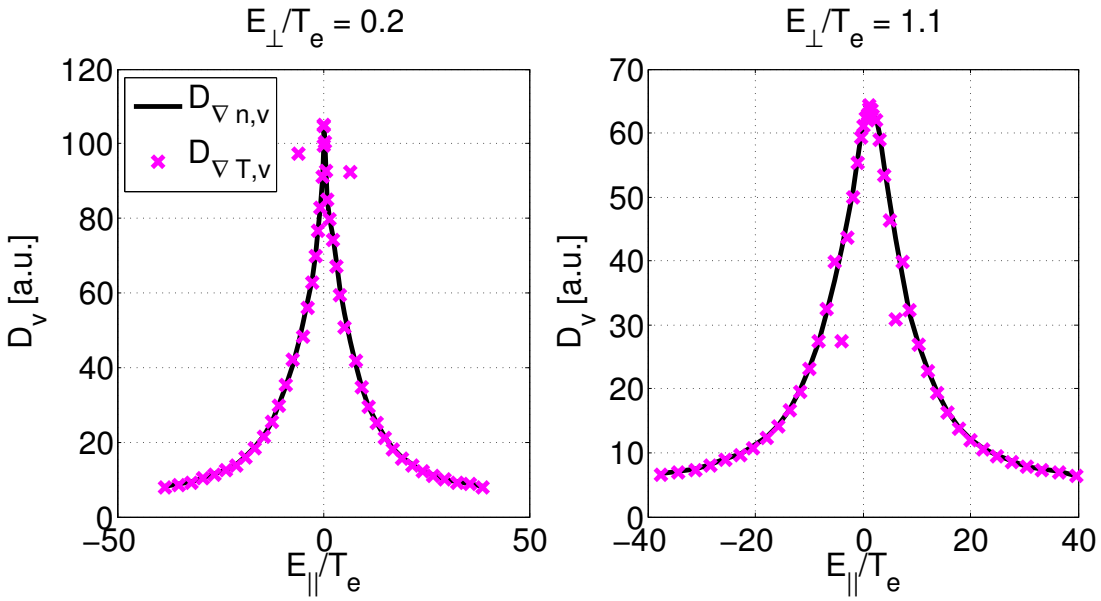

Figure 3.3: Comparison between the kinetic diffusivity obtained by analyzing the particle transport of two different populations with $\nabla \ln T \gg 1, \nabla n = 0$ and $\nabla T = 0, \nabla \ln n \gg 1$, respectively. The normalization against a vanishing quantity (see eq. (3.31)) is the cause for the small discrepancy visible in the figures at $E/T_e = 1.5\,(T_{\text{passive}}/T_e) = 6.5$.

curve) and the GENE code (blue curve). No discrepancies in velocity space can be observed. Only minor differences are observed in the reconstructed time trace of the particle flux. Such discrepancies are most likely caused by the perturbed component of the gyrokinetic operator.

In summary, the velocity space dependent model presented in this section can overcome the well known limitations of the Maxwellian approach. The variables introduced here can be employed to validate, or disprove, recent theoretical predictions for the fast ion diffusivity at large energies. A first example is given in the next section, where the results discussed by Zhang and co-workers [70] are analyzed. It was shown in this work that fast ion turbulent transport is predominantly diffusive, an observation which can be explained with the set of variables presented in this section.

3.1.5 Prevalence of diffusion phenomena in fast ion physics

The relative importance between diffusion, thermodiffusion and convection is given by the radial gradients of the particle distribution function. The ratio between diffusive and thermodiffusive fluxes, as an example, is roughly proportional

to the ratio between the density and temperature gradients of the distribution

$$\frac{\text{diffusive flux}}{\text{thermodiffusive flux}} = \frac{\nabla \ln n}{\nabla \ln T}. \tag{3.34}$$

As observed in section 2.2, this quantity is much larger than one for energetic ions. The reason for this is due to the creation of mono-energetic distribution of particles by fusion reactions or NBI heating. Their mean energy is radially invariant and are usually generated in the core, with strongly peaked distributions. Following the same reasoning of section 2.2, we can conclude that diffusive transport is dominant over thermodiffusion for beam ions and fusion products. Energetic ions heated with ICRH techniques might not fulfill these requirements. However, the more general conclusion that both thermodiffusive and diffusive phenomena are important can be drawn in this case.

We can now demonstrate that, in general, kinetic convection is smaller than velocity space dependent (thermo)diffusion and is negligible for peaked fast ion distributions. In figure 3.5 we compare the two fundamental particle transport components C_v and D_v. The relative strength of diffusion to convection is given by the ratio illustrated in the figure. A clear observation is that diffusion dominates

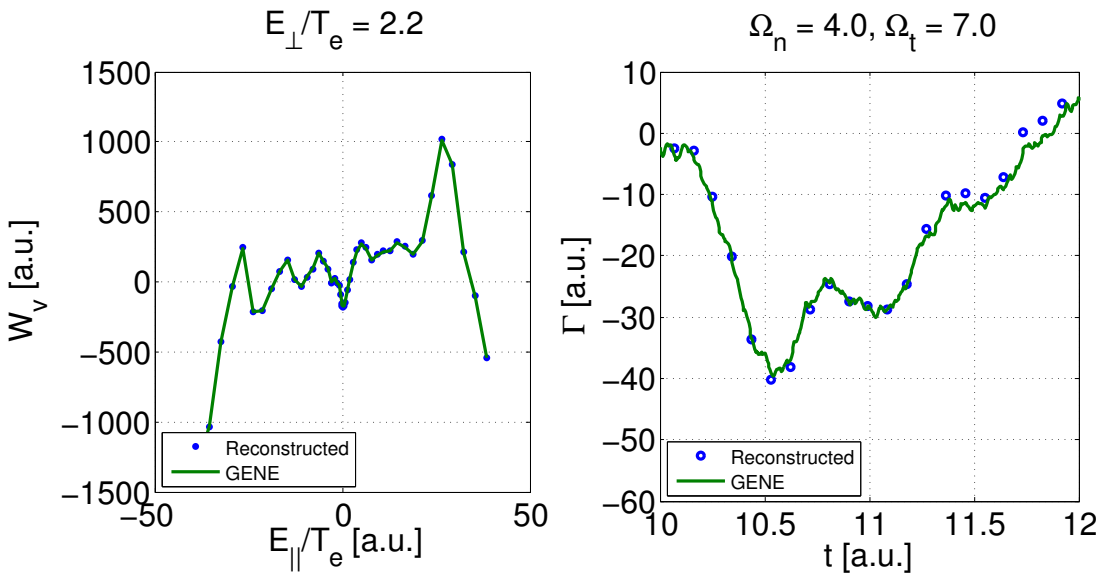

Figure 3.4: (Left) Kinetic weight function W_v, as a function of $E_\parallel/T_e$, obtained by GENE calculation and by the linear superposition depicted in equation (3.33) (blue and green, respectively). Very good agreement is observed between the two different methods. (Right) Time trace of the turbulent particle flux of a passive species calculated with the superposition principle and by nonlinear GENE simulations.

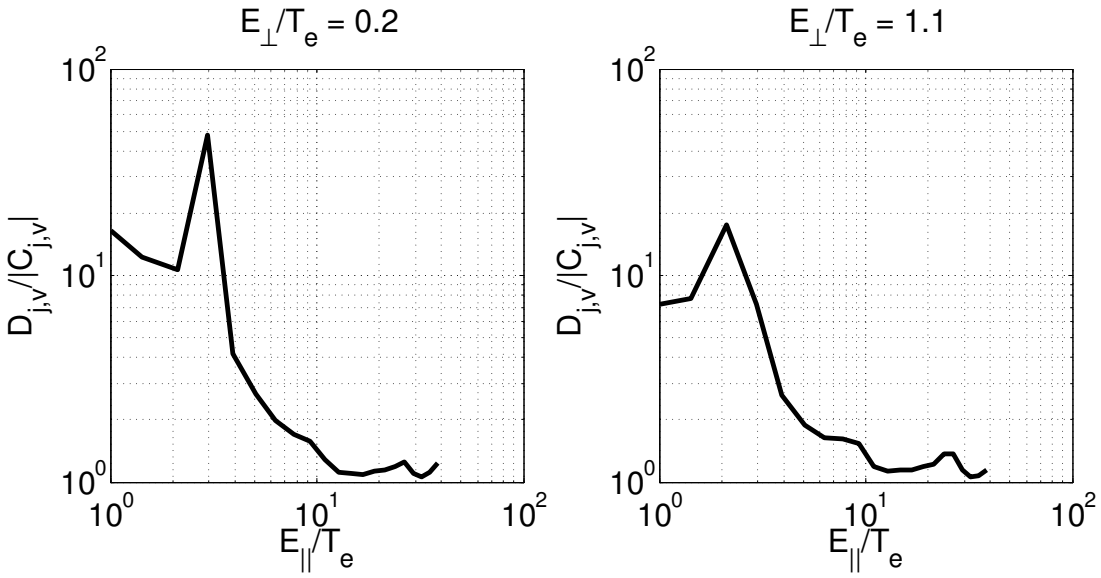

Figure 3.5: Particle diffusion to convection ratio as a function of the passive ion parallel energy. Convection, whose absolute value is considered here, is a minor phenomenon over a wide range of energies.

over all energies. For the relevant case where ions have a peaked density profile,

$$\Gamma = -D\boldsymbol{\nabla}\ln n + C = \\ = -D\boldsymbol{\nabla}\ln n\left[1 - \underbrace{\frac{R_0 C}{D}}_{<1}\underbrace{\frac{1}{R_0\boldsymbol{\nabla}\ln n}}_{\ll 1}\right] \simeq D\boldsymbol{\nabla}\ln n. \tag{3.35}$$

We can conclude that fast ion transport is expected to be predominantly diffusive. This conclusion is in agreement with the important observation of ref. [70], where fast ions in ITG turbulence suffered from Gaussian radial kicks, a property typical of diffusive phenomena. In the latter work and in ref. [72], theoretical predictions for the fast ion diffusivity were given. It is the aim of the next section to provide a further benchmark of the kinetic quantities studied in this section with observations made in early work.

3.2 Velocity space analysis of a circular plasma

This section is dedicated to the first application of the theoretical framework just presented, to give a first assessment of the fast ion transport and to compare the observations with previous theoretical investigations. To do so, we generate the nonlinear background microturbulence with the GENE code. The parameters described in section 2.2 are again employed in the s-α equilbrium where α is once

again set to zero. At mid-radius, $\Omega_{n_{i,e}} = 0.5$, $\Omega_{T_i} = 7$ and $\Omega_{T_e} = 0$ are chosen, focusing on ITG modes. The safety factor value $q_0 = 1.5$ and the shear $\hat{s} = 0.4$ characterize the magnetic configuration. A finite β of 0.6% was chosen. As we shall see, a low beta (pure electrostatic) case would be characterized by different transport levels. The particle diffusivity of a third species characterized by a large density gradient is studied. As previously observed, an arbitrary choice for $\Omega_{n,\text{fast}}$ can be made without affecting the value of D_v. We focus on the following quantity

$$D_v(\mathbf{v}) = \langle \langle D_v(\mathbf{v}, t) \rangle_{\mathbf{R}} \rangle_t \,, \tag{3.36}$$

where

$$\langle X \rangle_{\mathbf{R}} = \frac{\int d\mathbf{R} J(\mathbf{R}) X}{\int d\mathbf{R} J(\mathbf{R})}, \quad \text{and} \quad \langle X \rangle_t = \frac{1}{\Delta t} \int_{t_{\min}}^{t_{\max}} dt X, \tag{3.37}$$

J is the Jacobian and $\mathbf{R}$ is the real space variable. For this introductory analysis we focus on the electrostatic component of the fast ion diffusivity, obtained combining eq. (3.22) and eq. (2.8)

$$D_v = -\frac{\delta f \delta u}{\nabla f_0} \rightarrow \delta u = \delta \mathbf{u}_{E\times B} \cdot \hat{\mathbf{e}}_r = -\left[\frac{\boldsymbol{\nabla} \delta \bar{\Phi} \times \mathbf{B}}{B^2}\right] \cdot \hat{\mathbf{e}}_r. \tag{3.38}$$

3.2.1 Turbulent transport of a passive fast ion species

Figure 3.6 illustrates the turbulent transport of a passive fast ion species in the presence of ITG turbulence. Particle diffusion is shown in gyro-Bohm units

$$D_{gb} = \frac{c_s \rho_s^2}{R_0} = \frac{T_e^{3/2}}{eBR_0\sqrt{m_i}}. \tag{3.39}$$

This quantity represents the order of magnitude of the bulk plasma transport in fusion devices. In this particular scenario, background particle diffusivities $D_i/D_{gb} \simeq 2$ are found. Similar values are found for the energetic ion diffusivities. It is observed that transport is of the order of 0.1 D_{gb} for energies up to $E \simeq 30\, T_e$. This value is larger than collisional estimates for burning plasma scenarios, suggesting that phase space averaging effects are present although limited. This unexpected observation is partially explained in the theoretical models of refs. [70, 72]. These investigations showed that fast ion diffusivity decays as fast as $(E/T_e)^{-1}$ for passing ions, thus indicating only a rather slow turbulent field suppression. The results for trapped particles were different. The decorrelation argument brought in by Hauff predicted $D \simeq (E/T_e)^{-3/2}$, while Zhang, founding his research on quasilinear models, obtained a slightly faster $D \simeq (E/T_e)^{-2}$ scaling.

Particle diffusivities at increasing energy can be obtained by slicing the results of fig. 3.6 for a fixed value of $\mu B_0/E$. Both trapped and passing particles are

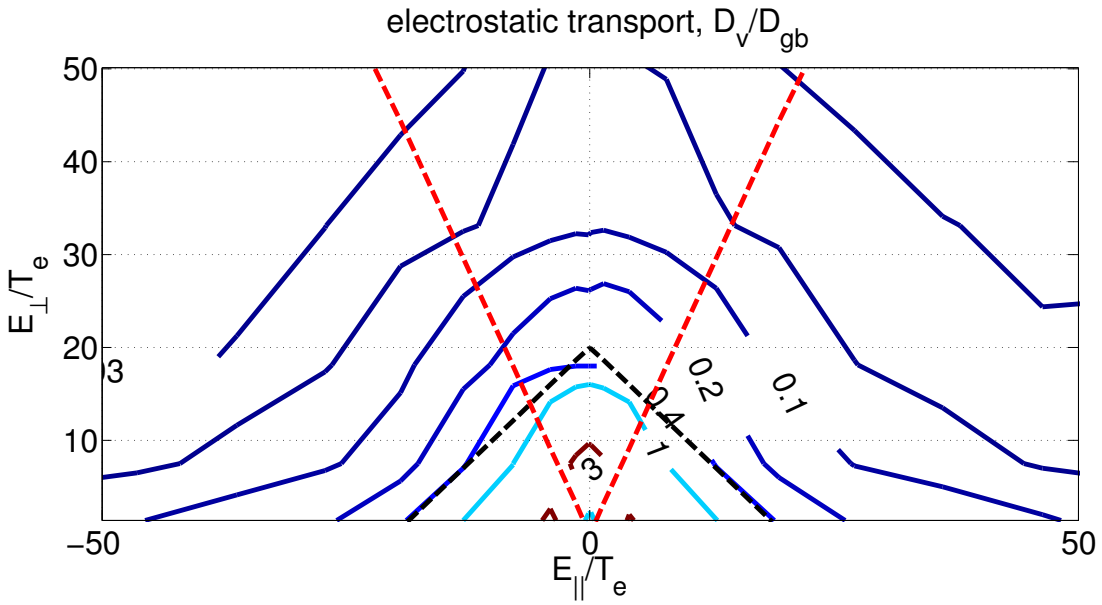

Figure 3.6: (Color online) Anomalous transport of a passive species in a circular turbulent plasma, as a function of the velocity characteristics of the particle. The red line indicates the boundary between passing and trapped particles (at $\epsilon = r/R_0 = 0.18$). The dashed black line corresponds to the critical energy for hydrogen beams over hydrogen background ($E_c \simeq 19T_e$).

investigated, the boundary between them being located at $\mu B_0/E \simeq 0.7$. One slice is performed at $\mu B_0/E = 0.05$ (small Larmor radius, passing particles) while the other at $\mu B_0/E = 0.9$ (trapped particles). The results for these pitch angles, characteristic of tangentially injected NBI distributions and ICRH distributions respectively, are shown in figure 3.7. For passing ions, the high energy scaling is similar to the $D_v \simeq (E/T_e)^{-1}$ behavior expected at large energies. Some discrepancies can be justified by the large number of modes included in GENE simulations and the monochromatic approach of phase space averaging theories. The results for deeply trapped particles can be found in agreement both with the $(E/T_e)^{-3/2}$ predictions in ref. [72] and with the $(E/T_e)^{-2}$ of ref. [70]. Altogether, particles at energies comparable to $E \simeq 20\ T_e$ can have transport levels comparable to background transport levels. The assumption of large phase space averaging effects is certainly not valid for the intermediate ($1 < E/T_e < 20$) energy regime.

3.2.2 Finite beta effects on the transport of suprathermal ions

The particle diffusivity calculated in this section,

$$D_v = -\frac{\delta f \delta u}{\nabla f_0}, \tag{3.40}$$

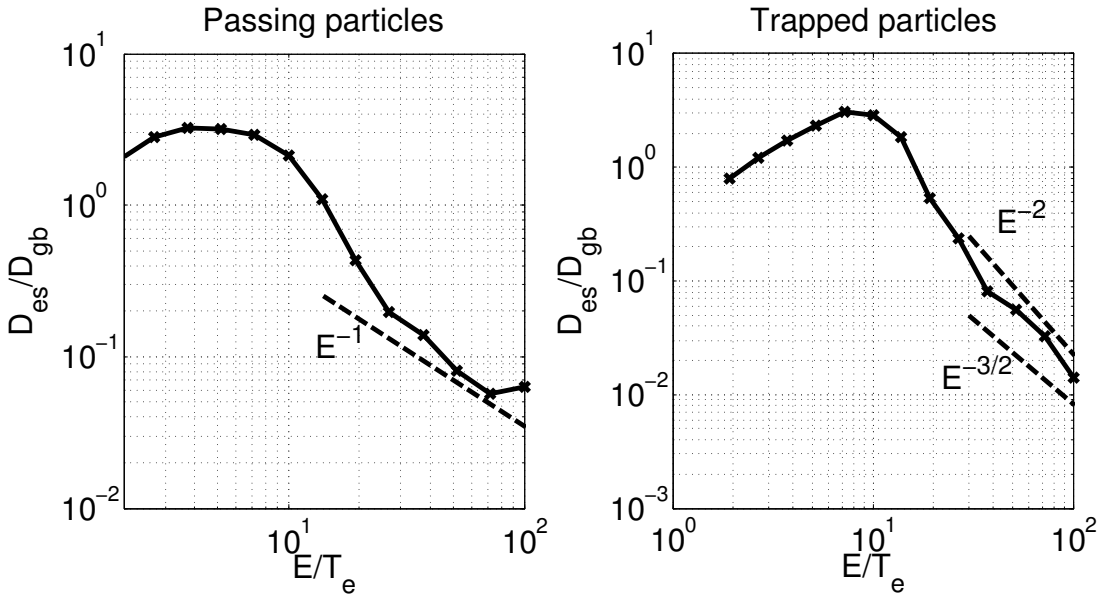

Figure 3.7: Anomalous transport of passing ($\mu B_0/E = 0.05$) and trapped ($\mu B_0/E = 0.9$) particles, as a function of energy. The dashed lines represent the high energy decay proposed in refs. [70, 72], namely $(E/T_e)^{-1}$ for passing particles and $(E/T_e)^{-(1.5,2)}$ for trapped particles.

only included the $E \times B$ drift in the δu term. We called the resulting diffusivity "electrostatic" although magnetic perturbations are included in δf. Let us investigate the difference between the results obtained with $\beta = 10^{-4} \equiv \beta^{\text{low}}$ (purely electrostatic perturbations) and the simulations presented in the previous section where $\beta = 0.6\% \equiv \beta^{\text{high}}$. In the linear phase, the growth rate of the most unstable ITG mode is $\gamma = 0.12\,\mathrm{c_s/R_0}$ for β^{high} and $\gamma = 0.35\,\mathrm{c_s/R_0}$ for β^{low}. The observed stabilizing effect of the magnetic perturbations on ITG modes is in agreement with the findings of refs. [91, 93, 94, 95]. The nonlinear evolution of the simulation reflects the linear behavior, as we observe $D(T = 30\,T_e)/D_{gb} = 2.6$ compared to $D(T = 30\,T_e)/D_{gb} = 0.3$ obtained in the finite beta case. Here, D_{gb} is the gyro-Bohm diffusivity. A similar enhancement is observed in the alpha particle heat diffusivity, increasing by an order of magnitude when decreasing β by the amount described above. When exploring the velocity space dependence of the particle diffusivity, as in the previous section, a large increase in the transport is again observable when choosing a negligible β (fig. 3.8). It is thus clear that finite β effects must be retained in the simulation of a burning plasma.

3.2.3 Kinetic transport in the intermediate energy region

Despite the importance of the high energy tail of the particle diffusivity, the results of figure 3.7 demonstrate that particle transport at intermediate energies

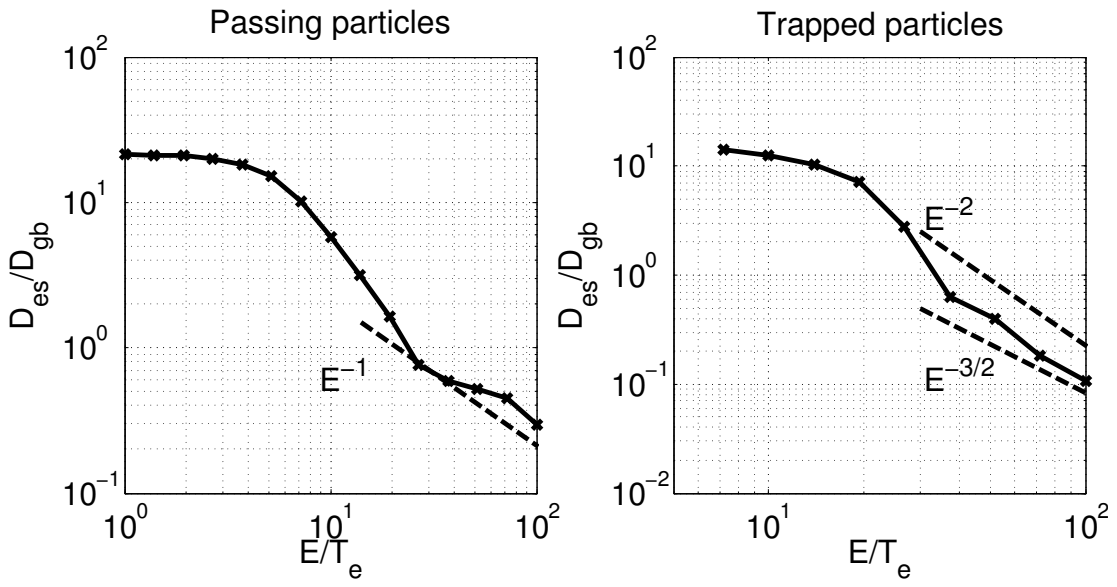

Figure 3.8: Anomalous transport of deeply passing ($\mu B_0/E = 0.05$) and deeply trapped ($\mu B_0/E = 0.9$) particles, as a function of energy, in presence of electrostatic turbulent fields assuming negligible β. The dashed lines represent the high energy decay proposed in ref. [72], i.e. E^{-1} for passing and $E^{-3/2}$ for trapped particles. The alternative E^{-2} scaling proposed in ref. [70] is also shown.

determines the overall fast ion behaviour. Quasilinear models and phase space averaging theories, however, do not describe this energy region. Consequently, the common assumption that fast ion transport is negligible is a result of the incorrect interpretation of these theories. Averaging effects, as mentioned earlier, suppress turbulent transport and the $D_v \simeq (E/T_e)^{-3/2}$ particle diffusivity is expected. It might appear reasonable to conclude that, for example, particles at $E = 10\,T_e$ are transported as much as $D_v/D_{\text{background}} \simeq 10^{-3/2}$, or 96% less than the bulk plasma. The diffusivity decay, however, does not appear except at large energies, and previous numerical results based on this erroneous approximation should be questioned.

Let us try to estimate the energy range characterized by small turbulent field suppression. The intermediate energy interaction is generated by resonances between the characteristic frequencies of the drift orbit motion and the turbulent field frequency. As an example, let us calculate the resonant condition between the toroidal precession drift of trapped particles [72]

$$v_y \sim (1-\eta)^2 \left(\frac{E}{T_e}\right) \frac{\rho_s c_s}{R_0}, \tag{3.41}$$

where $\eta = v_\parallel / v$, and the drift wave velocity along the y direction

$$v_{dr} = \frac{\omega}{k_y} \simeq 1.5 \frac{\rho_s c_s}{R_0}, \tag{3.42}$$

where ω is the frequency of the turbulent mode. For the parameters employed here, the resonant interaction is expected at $6 < E/T_e < 20$, which is confirmed by the numerical results. At larger energies the transport is smaller and its magnitude is both influenced by the position of the resonant peak, and the class of particles considered (whether trapped or passing).

This discussion, as well as the theories presented in refs. [70, 72], are based on a single-mode approach. In reality, the transport generated by each wavelength needs to be taken into consideration. Each mode generates a different resonant interaction and a different point where averaging effects step in. Particle diffusivity scalings are therefore difficult to assess in a full nonlinear scenario and more general numerical models, such as the GENE code, must be taken into account to evaluate transport levels.

3.2.4 Comparison with previous work

So far, we have developed the theoretical framework required for velocity space investigations. The validity of the model was demonstrated with a first set of consistency tests with the GENE code. First comparisons with previous work were also studied and a very good agreement was found. The aim of this section is to further validate the numerical results in this chapter by creating a link between the velocity space treatment and previous Maxwellian analyses. As the latter can result in cumulative velocity space behaviour, we expect similar results (analog to what is usually observed between kinetic and fluid models). We are interested in particular in the findings of Estrada-Mila [60] and Angioni [66]. We recall that in the analysis of ref. [60], the transport of Maxwellian distributions of Helium impurities at varying temperature was studied. The particle diffusivity of populations characterized by a large temperature was then associated with the transport of alpha particles. Let us recall the definition of the averaged diffusivity of eq. (3.26)

$$\langle D \rangle (T_\alpha) = \frac{\int d\mathbf{v} f_0 (\mathbf{v}, T_\alpha) \; D_v (\mathbf{v})}{\int d\mathbf{v} f_0 (T_\alpha)}. \tag{3.43}$$

To compare the results in this chapter with those presented in ref. [60], we can solve equation (3.43) for an unperturbed Maxwellian $f_0 (\mathbf{v}, T_\alpha)$, at increasing temperature. An appropriate choice of $D(\mathbf{v})$ is needed.

The choice of an analytical form of the particle diffusivity $D(E)$ of eq. (3.26) can ease the comparison with previous work. During the discussion of the velocity space results we observed a rather flat diffusivity for intermediate energy regions $E/T_e < L$, where $5 < L < 10$ (see figure 3.8). The diffusivity $D(E)$ of eq. (3.26)

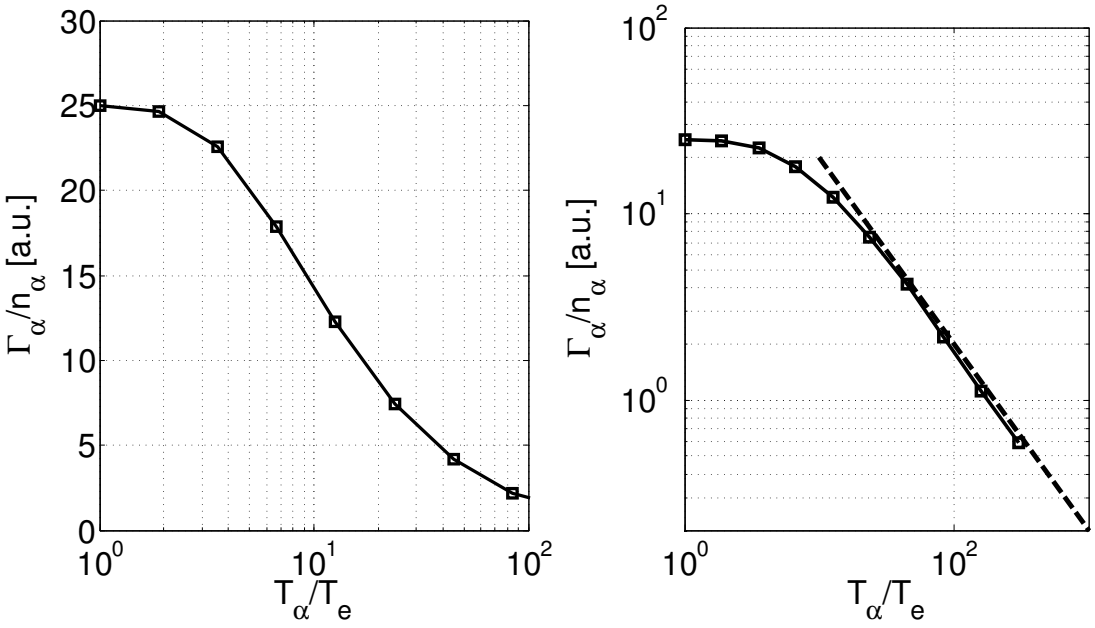

Figure 3.9: Particle diffusivity for a Maxwellian population of alpha particles, as a function of the temperature of the distribution (left and right panel). An arbitrary normalization has been included in the curve to simplify the comparison with the results presented in ref. [60]. The right panel shows the same data, but plotted in log-log scale, in order to demonstrate the $\Gamma \simeq (T_e/T_\alpha)$ dependence and eventual power-law (dashed line).

is then assumed to be constant for particles with energies smaller than $E = LT_e$. At larger value, we observed that phase space averaging becomes important and the energy decay follows a power law $D \simeq (T_e/E)^n$. We have

$$D/D_{\text{background}} = \begin{cases} 1 & \text{if } E \leq LT_e \\ [T_e/(LE)]^n & \text{elsewhere.} \end{cases} \tag{3.44}$$

We choose parameters consistent with the results presented in the previous section, $L = 7$ and $n = 1.2$ (predominantly passing particles) and we numerically integrate equation (3.43). The results obtained with this procedure, presented in fig. 3.9, are in very good agreement with the findings of ref. [60]. In fig. 3.9 we can also observe the diffusivity decay at high temperatures, which follows the power law $D \simeq (T_e/T_\alpha) \equiv \lambda_\alpha^{-1}$. A similar scaling is also obtained analytically in appendix B.

The scaling law $D \simeq \lambda_\alpha^{-1}$ has also been found by Angioni and co-workers. For example, it can be inferred from Figure 6 of ref. [66]. Further similarities can be found by solving eq. (3.26) for both particle and heat diffusivities of Maxwellian distributions. By applying the normalization employed in ref. [66], we obtain the results of fig. 3.10, whose resemblance with Figure 6 of Angioni's work is noticeable. Also investigated in ref. [66] was the electrostatic transport of alpha particles modeled as a slowing-down population and implemented in the GS2 code [96]. The

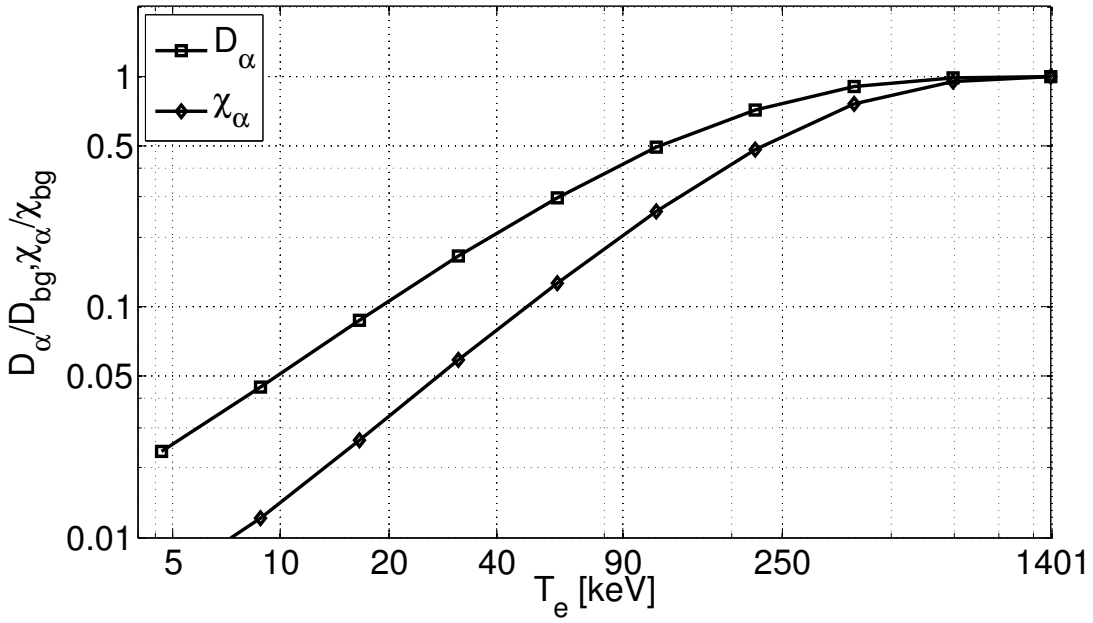

Figure 3.10: Particle and heat diffusivity for a Maxwellian population of alpha particles, as a function of the plasma temperature. This figure is in good agreement with the results of figure 7 in Angioni, ref. [66].

anomalous particle transport obtained by means of nonlinear gyrokinetic simulations was then implemented in the ASTRA code for evaluating the impact of microturbulence on the alpha particle density profile. The conclusion that electrostatic turbulence has a negligible effect on the transport of alpha particles was eventually drawn. We can show that the contradiction between these conclusions and the results shown in this chapter is only apparent by replacing the Maxwellian distribution of eq. (3.26), with a slowing down function $f_{sd,0}$

$$f_{sd,0}(E) \simeq \frac{1}{E^{3/2} + E_c^{3/2}}. \tag{3.45}$$

For alpha particles, we obtain $D_\alpha / D_{\text{background}} = 0.07$ or $D_\alpha \simeq 0.15\ \text{m}^2 \cdot \text{s}^{-1}$ for ITER values. This is larger than neoclassical predictions, but nevertheless small. The reason for this relatively small estimate comes from the weighting function $f_{sd,0}$, which has long energy tails and selects the low diffusivity of very energetic particles. As a consequence, the transport of a slowing down distribution of alpha particle is negligible, as concluded in ref. [66]. Nevertheless, those populations characterized by a lower birth energy and a larger passing fraction, such as for an NBI distribution, could still be significantly transported. For the NBI population, the expected diffusivity would be $D_{nbi} / D_{\text{background}} = 0.24$, or $D \simeq 0.5\ \text{m}^2 \cdot \text{s}^{-1}$, and hence very significant. Though, as we will see, this value still represents an averaged estimate. In the following chapters we will show that the particle energy (relative to T_e) is one of the two parameters determining fast ion anomalous

transport. The other is the energetic particle slowing down time, which depends on the temperature and density of background populations.

3.2.5 Comment on the passive fast ion approach

The choice of a passive population for fast ion transport investigations introduces a few advantages. The numerical benefit is the possibility to choose arbitrary density and temperature gradients in order to extract the transport component (diffusive/convective) of interest. Indeed, it was shown that transport coefficients are only determined by the background turbulence, which in turn is not influenced by the passive species parameters. But how reasonable is the choice of a passive population? Diluted charge particles can have an impact on the linear and nonlinear evolution of microturbulent fields. In particular, the presence of an external species, characterized by different mass and charge with respect to the bulk plasma, reduces plasma instabilities. Furthermore, large population energies have a stabilizing effect on the background microturbulence and promising studies are being carried out in the context of this thesis [97].

For the cases studied in this thesis, however, the assumption of a passive distribution is always valid. In the Tokamak à Configuration Variable (TCV), described in the chapter 5, the injection energy of the planned neutral beam system is too close to plasma temperature to have a stabilizing effect. On the other hand, energetic particles in future plasma experiments such as ITER and DEMO are present in a sufficiently low concentration to justify the passive tracer approach. For example, the concentration of alpha particles in ITER is of the order of 1 % for which stabilizing effects are negligible (figure 3.11).

3.3 Predicting the fast ion transport in tokamaks

Fast ion diffusivity is no the only parameter influencing the fast ion motion. The longer the time spent by a fast particle over the turbulent background, the larger the number of stochastic radial kicks it will experience. For this reason, collisions fundamentally influence the anomalous fast ion redistribution as a stronger collisionality can reduce the interaction with microturbulent fields. One can therefore define a simple estimate for predicting the importance of anomalous effects [98]

$$\Delta = \frac{\text{radial spread}}{\text{minor radius}} \simeq \sqrt{\langle D \rangle \, \tau_{sd}}/a, \tag{3.46}$$

where $\langle D \rangle$ is the averaged diffusivity experienced by the fast ion population over a slowing down time τ_{sd}. A value close to one indicates the possibility of anomalous redistribution while $\Delta = 0$ is an appropriate value for scenarios where turbulence is strong (or collisions quickly thermalize the fast ions). The intrinsic limitation

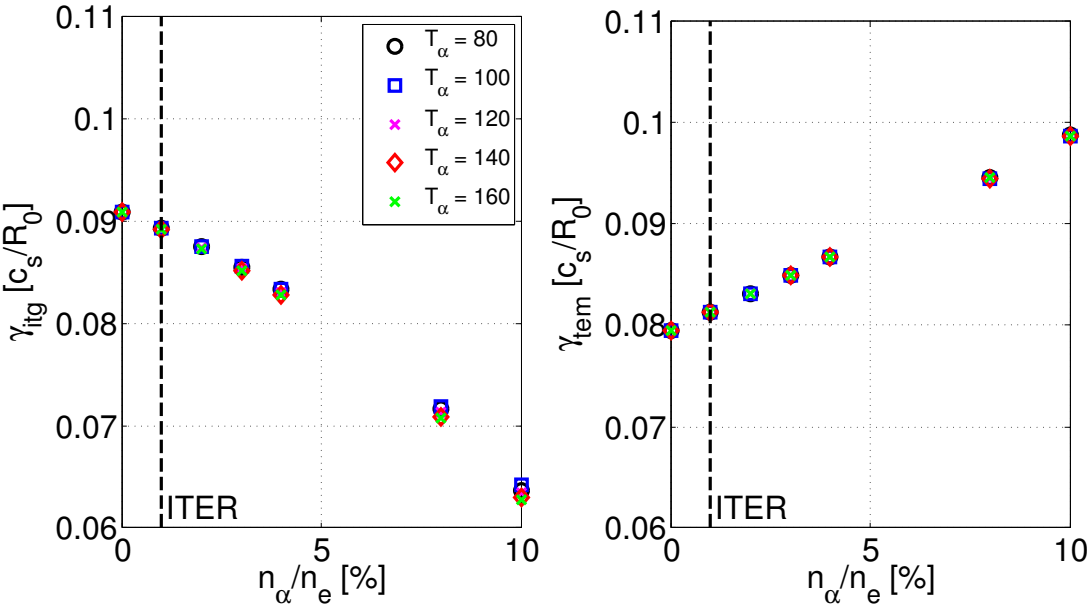

Figure 3.11: Growth rate of ITG (left) and TEM (right) modes as a function of alpha particle concentration. Simulations are run with the GENE code assuming a Maxwellian distribution of alpha particles. Different temperatures are considered with only limited effect on the stabilization of ITG modes.

of this approach is in the choice of $D(E)$ and of the distribution function $f(E)$ to be used in the velocity space average

$$\langle D \rangle = \frac{\int dE \sqrt{E} f(E) D(E)}{\int dE \sqrt{E} f(E)}. \tag{3.47}$$

An isotropic slowing down function (3.45) is used for f. Finding a reasonable expression for D is more complicated, as this strongly depends on the background turbulence. Given that the shape of D is determined by the phase velocities of the underlying turbulence, different scenarios will result in different shapes of D. In figure 3.12, for instance, we can observe the outcome of two GENE simulations of the ITER steady state scenario characterized by different values of the instability drive (more details on the parameters will be given in the final chapter of the thesis). We can observe that the shape of D is changing according to the change of the phase velocity of the background ITG modes. Namely, as v_{ph} becomes smaller, the resonant interaction described in this chapter moves towards smaller energies. A simple expression of D, such as the one in (3.44), can be used for first principle estimates. To determine Δ in the remainder of this work, we will use $n = 1.5$ and $L = 4$. The fast ion slowing down time τ_{sd} strongly depends on the background plasma features and the energy of the particle [4]. In the forthcoming chapters, when Δ is evaluated, the slowing down time will be estimated from simulations of the single particle code VENUS.

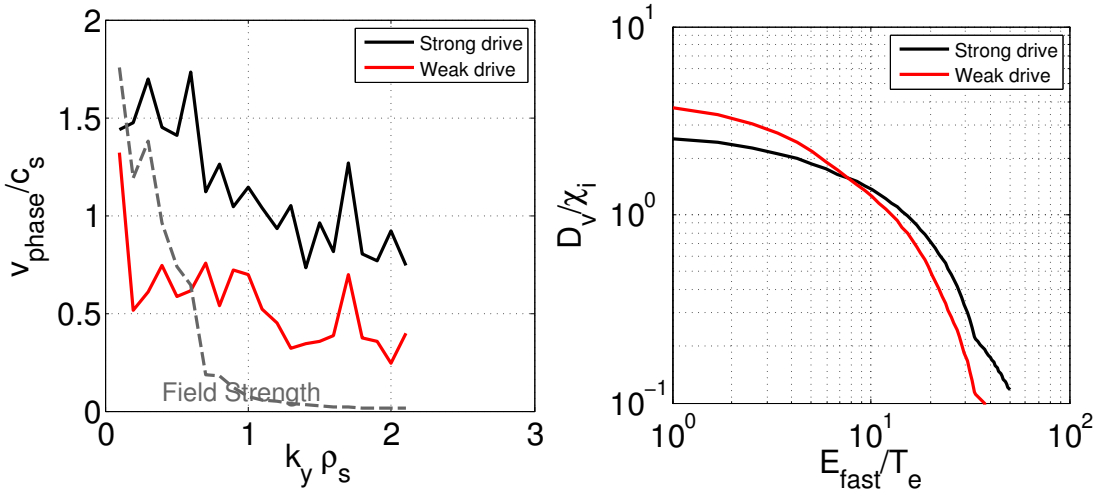

Figure 3.12: Phase velocity of drift-wave turbulence in two simulations performed with the GENE code (left panel). The resulting diffusivity as a function of the particle energy, normalized over the background heat conductivity, is represented on the right panel.

3.4 Conclusions

The work described in this chapter was dedicated to the creation of a theoretical framework capable of describing the fast ion behaviour in nuclear fusion devices. This was achieved by first creating a velocity space description of the anomalous fast ion transport, for which new transport quantities are defined. The integral form of the gyrokinetic transport equations was removed and their velocity space dependent, i.e. *kinetic*, equivalent was introduced. A set of diagnostics to extract this information from the gyrokinetic GENE code were presented and kinetic diffusion and convection were therefore studied. It was shown, for example, that (thermo)diffusion dominates the fast ion particle transport as convection only represents a marginal component of the energetic ion particle flux.

A second important part of the study consisted of the analysis of the fast ion transport in a circular plasma. The background turbulence in this simple scenario was generated by deuterium ions, and mostly consisted of ITG modes. It was observed that the energetic ion response, modeled with a strongly peaked passive distribution of helium, was important. One observation is that the figure of merit for energetic ion transport is the quantity E/T_e, representing the decoupling between the fast ion motion and microturbulence evolution. At first, energetic ions are transported as much as the background plasma for quite a large energy region $1 < E/T_e < 20$. Above this energy, particle diffusivities decay quite strongly for trapped particles ($D \simeq (E/T_e)^{-2}$) or more weakly for passing ions ($D \simeq (E/T_e)^{-1}$). These results were found to be in agreement with early velocity space theoretical investigations [70, 72] as well as with the Maxwellian analysis of refs. [60, 66]. The conclusion that anomalous transport could generate important fast ion redistribution in thermonuclear plasmas was drawn, the effect being more important for passing beam ions at intermediate energies.

Chapter 4

The Neutral Beam Module in the VENUS code

This chapter is dedicated to the development of a numerical platform for fast ion studies. The single particle code VENUS [99] represents the core of this interpretative tool. After the update of the collision term in the single particle motion equations, the Monte Carlo operator describing the stochastic behavior of fast ions diffusing in turbulent fields is implemented. The structure of the operator is adapted to the form of kinetic transport quantities defined in the previous chapter and relies on numerical data provided by the GENE code. The framework is completed with a numerical module simulating the neutral beam source present in a large number of tokamak experiments.

A series of benchmarks of the numerical platform are then presented. The beam deposition modules of the VENUS code and the ASCOT code [100] are compared, with excellent results. In section 4.5 the data from the Collective Thomson Scattering (CTS) diagnostic in TEXTOR [101] are compared with the numerical results of our platform. Further benchmarks with the ASCOT code are also presented. Good agreement both with the latter code and with experiments are found. The capabilities and limitations of the numerical platform, employed in the remainder of this work to simulate current day machines and future tokamaks, are addressed at the end of the chapter.

4.1 The guiding center drift motion

The VENUS code was originally developed for the study of the unperturbed guiding center drift motion, calculated with the equations described in ref. [102]. The code works with magnetic equilibrium quantities reconstructed with the VMEC code [103]. No modifications were made to the 4^{th} order Runge-Kutta scheme used for calculating the time evolution of the particle position. Three examples of the typical drift orbits simulated by the VENUS code are shown in figure 4.1, where the motion of two passing ions and a trapped particle in the JET tokamak [24] are illustrated. Passing particles stream along the magnetic field lines and their confinement depends on their velocity with respect to the plasma current. Ions streaming in the same direction as the current are called *co-passing* and represented in yellow in the figure. Counter passing particles (*cr-passing*, blue), on the other hand, are characterized by a toroidal velocity opposite to the plasma current. If created in the low field side of the tokamak, the confinement

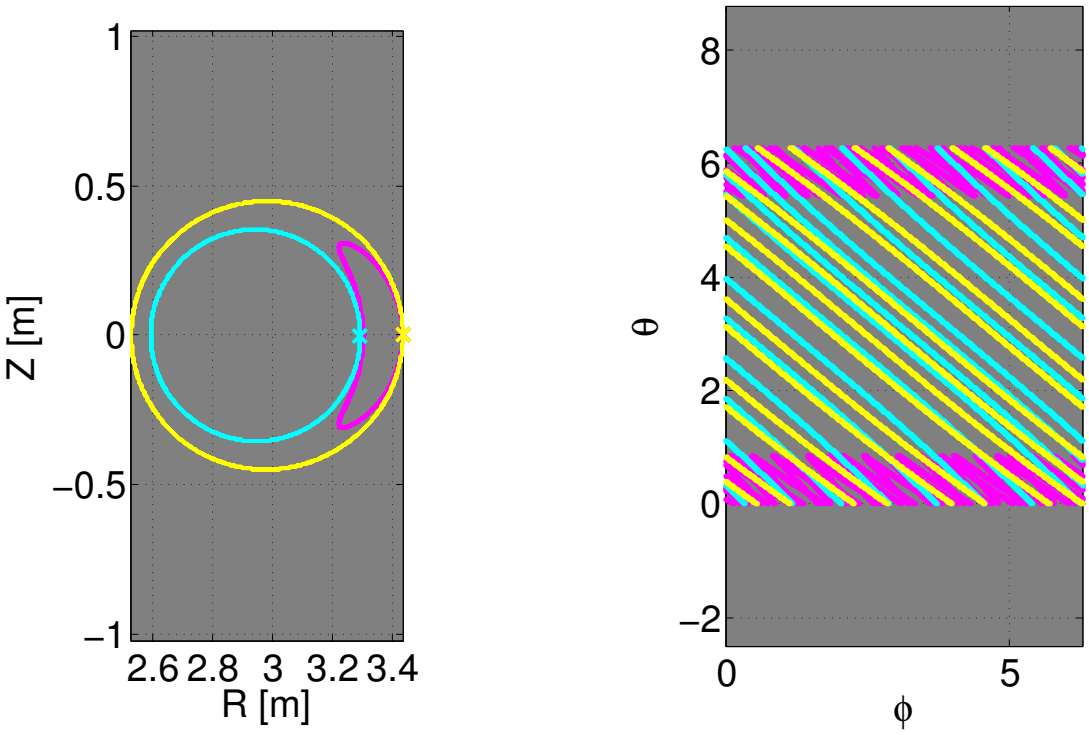

Figure 4.1: Unperturbed particle orbits of co-passing (yellow), cr-passing (blue) and trapped (magenta) ions as simulated by the VENUS code (left panel). The particle birth point is indicated by a cross. Small radial excursions drifts characterize passing particles in this scenario, based on the equilibrium reconstruction of plasma discharge #76189 of the JET tokamak. The right panel illustrates, with the same color code, the particle streaming on a flux surface.

of the latter particles is not guaranteed. Their orbits might cross the last closed flux surface before completing the first poloidal turn, an effect known as first-orbit losses. Neutral beam ions are typically injected in the same direction as the plasma current to guarantee a good particle confinement of the dominant passing particles. Trapped ions, represented in magenta in the figure, experience the same confinement issues as passing ions. However, their orbits are much wider than those of passing ions and even poorer confinement is expected for trapped particles streaming in the counter-current direction. Nevertheless first orbit losses of trapped ions are removed by co-injection.

The orbits of figure 4.1 can also be shown in real space after a convenient coordinate mapping (figure 4.2). The same orbits are represented in a three dimensional fashion where the VENUS coordinates (s, θ, ϕ) are also represented. From this figure the dominant motion of particles streaming along the magnetic field lines (represented in light grey) is much clearer. The same figure illustrates one of the plasma configurations employed in present day tokamaks, where mag-

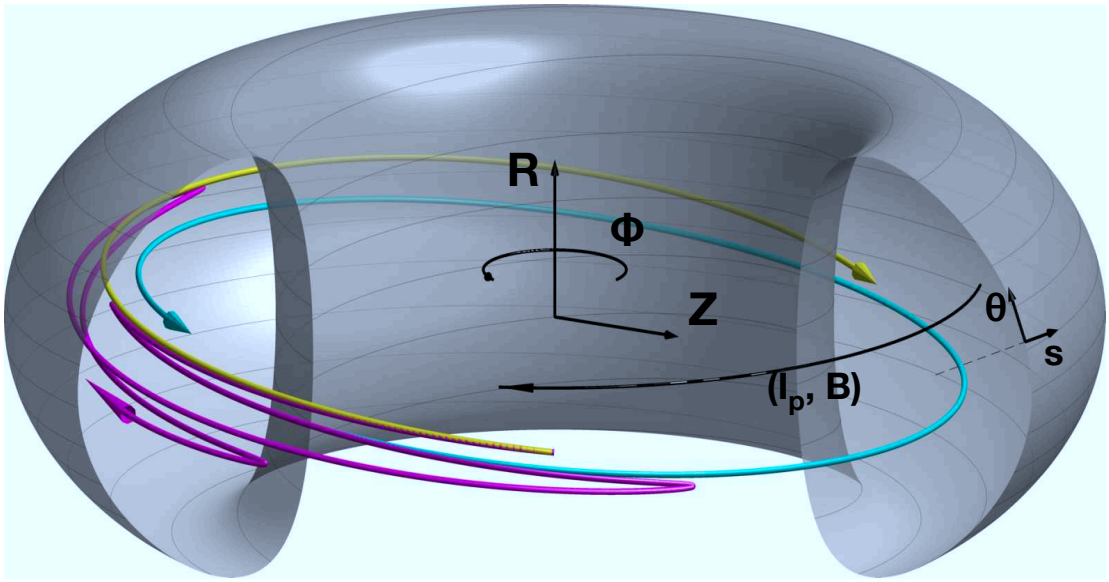

Figure 4.2: Particle orbits for trapped (magenta), co-passing (yellow) and cr-passing (blue) particles. Also represented is the last closed flux surface of the JET tokamak, together with the magnetic field lines at $\rho_t \simeq 1$ (light grey and grey, respectively). The (s, θ, ϕ) coordinate system employed in the VENUS code is also shown, together with the plasma current and toroidal magnetic field direction (here shown as aligned).

netic field and plasma current follow the same direction. Various alignments are nevertheless possible. For example, the TEXTOR tokamak, described in section 4.5, employs a plasma current flowing in the opposite direction with respect to figure 4.2.

4.2 Neutral beam deposition module

The neutral beam module in the VENUS code provides the particle source term for numerical simulations of NBI heated plasmas. The MATLAB routines constituting this module also allow for an estimate of the neutral beam shine through. The latter phenomena describe the amount of neutral particles not ionized along the plasma and thus striking against the tokamak vessel. The number of neutrals injected with an NBI system and traveling through the plasma region is regulated by the following differential equation

$$\frac{dI(\ell)}{d\ell} = -n_e(\ell)\sigma_{\text{eff}}(\ell)I(\ell). \tag{4.1}$$

Here, $I(\ell) = N_b(\ell)v_b$, where ℓ is the beam path, which is a function of the real space coordinates and the beam geometry. The number of neutral particles is given by $N_b(\ell)$, while their velocity is v_b. The interaction cross section σ_{eff} embeds

several processes that generate ionized particles, such as charge exchange and ionization by background ions and impurities. Equation (4.1) can also be cast in an integral form

$$\frac{I(\ell)}{I_0} = \frac{N_b(\ell)}{N_{b,0}} = e^{-\int_0^\ell n_e(\ell')\sigma_{\text{eff}}(\ell')d\ell'}. \tag{4.2}$$

This equation provides the beam attenuation $N_b(\ell)$ along the injection line. The beam fraction $N_b(L)/N_{b,0}$, where L is the last position where plasma is present, can be non-negligible and represents shine-through losses. In particular, L and n_e can be smaller than optimal, or the interaction cross section σ_{eff}, a monotonically decaying function of the beam energy, not large enough. One must therefore inject neutral beams spanning the largest plasma volume, therefore avoiding the so called normal injection (perpendicular to the field lines) for small plasma cross sections. The initial condition $N_{b,0}$ is given by the number of particles injected every second by a neutral beam system

$$N_{b,0} = P_{\text{nbi}}/E_{\text{nbi}}. \tag{4.3}$$

NBIs are also characterized by the presence of beam particles at fractional energies, the results of unwanted molecular ions (D^{2+} and D^{3+}, e.g., for deuterium beams). Each *fractional* component generates a different number of neutral particles per second

$$N_{b,0}^j = \left[P_{\text{nbi}}^j / \left(E_{\text{nbi}}/j\right)\right], \tag{4.4}$$

with the condition $\sum_j P_{\text{nbi}}^j = P_{\text{nbi}}^{\text{tot}}$.

To simulate the beam attenuation we first choose a number N of numerical particles (markers). We then divide the beam path in N equidistant points in real space, each point corresponding to a numerical particle. The differential equation (4.2) is then solved over this grid employing the background plasma densities and temperatures. The number of neutral particles per real space grid point $N_b(\ell_j)$, with ℓ_j the discretization of the beam line, is then known. To reproduce the physical beam particles, the marker at the position ℓ_j carries a weight proportional to the number of ionizations occurring in that particular position. As each ionization corresponds to the loss of a neutral particle, the numerical weight is given by

$$w_j = N_b\left(\ell_j\right) - N_b\left(\ell_{j-1}\right). \tag{4.5}$$

This numerical technique provides a method for the creation of an ensemble of markers, and their respective weight, describing the neutral beam source.

In real experiments neutral beams are influenced geometrical effects such as the finite size of the neutral source and beam spreading. To mirror the imperfect focusing of NB injectors we introduce particle displacements from the ideal beam

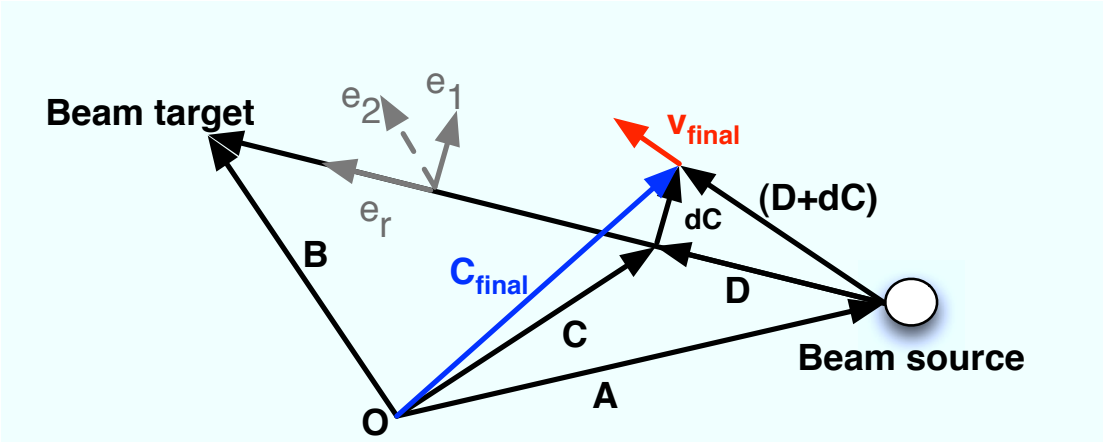

Figure 4.3: Schematics of the beam deposition modelling. The beam line with perfect focusing, indicated by the unit vector $\mathbf{e}_r$, is displaced to model a realistic beam spread.

line position (figure 4.3). We first parametrize the particle position given the beam source, $\mathbf{A}$, and the beam target, $\mathbf{B}$ (both lying outside the plasma volume), as

$$\mathbf{x}(t) = \mathbf{A} + (\mathbf{B} - \mathbf{A}) \cdot t, \tag{4.6}$$

where $t \in \Re$. We then define an orthonormal system (e_1, e_2, e_r) where

$$\mathbf{e}_r = \frac{\mathbf{B} - \mathbf{A}}{|\mathbf{B} - \mathbf{A}|}, \tag{4.7}$$

$$\mathbf{e}_1 = x(t_\perp), \tag{4.8}$$

$$\mathbf{e}_2 = \mathbf{e}_1 \times \mathbf{e}_r. \tag{4.9}$$

The quantity $t_\perp$ satisfies the condition $\mathbf{e}_r \cdot \mathbf{e}_1 = 0$ and can be expressed as

$$t_\perp = -\frac{\mathbf{B} \cdot \mathbf{A}}{|\mathbf{A}|^2 + |\mathbf{B}|^2 - 2\mathbf{A} \cdot \mathbf{B}}. \tag{4.10}$$

We give a first displacement to the position vector $\mathbf{C}$ to reproduce the beam source geometry. If we choose a square beam source, we define the new position of the beam particle as

$$\mathbf{C} = \mathbf{C}^{\text{point-source}} + L\left(\mathcal{R}_1 \mathbf{e}_1 + \mathcal{R}_2 \mathbf{e}_2\right), \tag{4.11}$$

where $\mathcal{R}_{1,2}$ are two variables uniformly distributed between -1/2 and 1/2 and L is the length of the beam source side.

The second step is to reproduce the beam spread. By choosing a spread angle θ, we calculate the new position of the particle as

$$\mathbf{C}^{\text{final}} = \mathbf{C} + \mathrm{d}\mathbf{C} \tag{4.12}$$

$$\mathrm{d}\mathbf{C} = \mathcal{R}_3 \|\mathbf{D}\| \tan\theta. \tag{4.13}$$

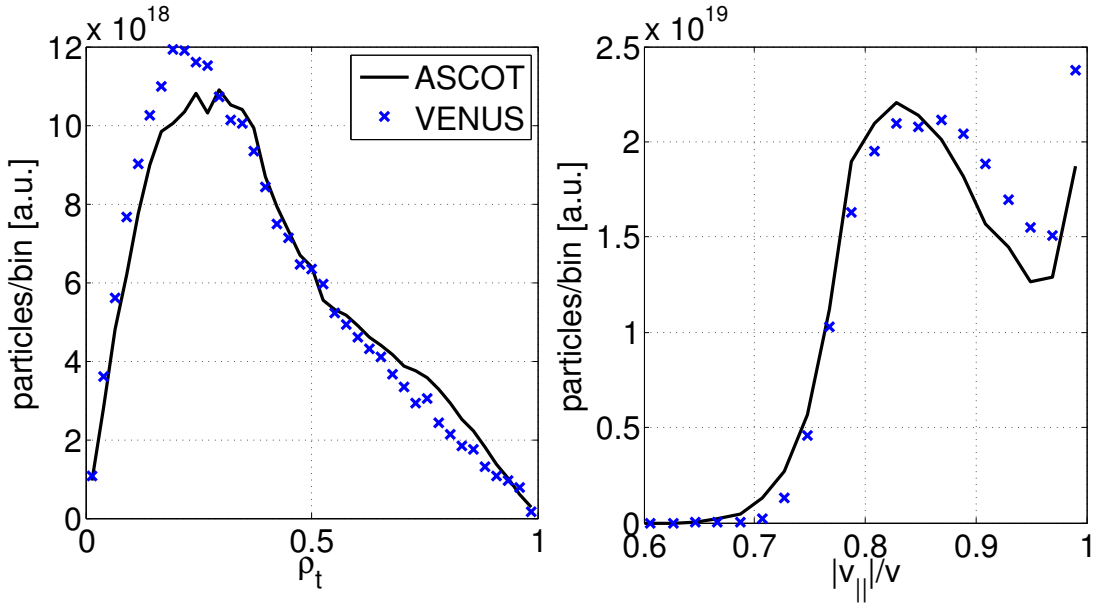

Figure 4.4: Comparison between the beam deposition distribution modules of the ASCOT and the VENUS code (black line and blue cross, respectively). The curves in the left panel represent the binning of the particle radial position. The pitch angle distribution, largely dominated by passing particles, is also shown (right panel).

Here, $\mathcal{R}_3 \in N(0,1)$ and the quantity $\|\mathbf{D}\| \tan\theta$ is a spread proportional to the distance from the beam source. The particle velocity vector is given by

$$\mathbf{v} = \frac{\mathbf{D} + \mathrm{d}\mathbf{C}}{\|\mathbf{D} + \mathrm{d}\mathbf{C}\|}. \tag{4.14}$$

The last quantity required by VENUS to fully define a particle position in phase space is $\lambda = v_\parallel / v$. Once the background equilibrium is known, it is straightforward to calculate $\lambda = v_\parallel / v = (\mathbf{v} \cdot \mathbf{B}) / |B|$. A test is then performed to verify whether the new position lies within the plasma boundary. If not, the particle weight is set to zero.

The procedure so far described is then repeated for each energy fraction and, if specified, for each injector (PINI) to be simulated. The comparison between the markers generated with the beam deposition modules of the ASCOT [100] and the VENUS codes is illustrated in figure 4.4. Very good agreement is found between the two modules. The minor discrepancies observed in the figure are due to slightly different equilibrium reconstructions. The illustration of figure 4.4 corresponds to TEXTOR plasma discharge #111508. Further numerical analyses of this fusion device will be presented in section 4.5.

The numerical particles generated with the model so far described are then used in the VENUS code. A numerical simulation of the NBI deposition and

evolution starts by generating a population of $\mathcal{N}$ markers with the beam deposition module. A number of injections $\mathcal{M}$ and a total simulation time t_{fin} are then chosen in the VENUS code. During the VENUS simulation, every $\Delta T = t_{\text{fin}}/\mathcal{M}$ time interval, a subsample of $\mathcal{N}/\mathcal{M}$ particles is added to the simulation. Given a ΔT sufficiently small compared to the beam slowing down time, the NBI source is reliably simulated.

4.3 The collision operator

VENUS now employs a collision operator slightly modified with respect to the one originally present in the code. The previous collision operator described the pitch angle scattering and slowing down of ICRH heated ions. These interactions, mostly involving collisions with electrons, appear at the very large energies characterizing these particles. The updated version of the collision operator in VENUS now allows for the precise description of the interactions at energies smaller than $E_c \simeq 19\,T_e$, where particles interact with background ions through pitch angle scattering.

The influence of Coulomb collisions in tokamak plasmas can be rather important for energetic particles as the energy transferred from alpha particles and neutral beam ions to the background plasma is vital to sustain fusion reactivity. The full non-linear Fokker-Planck equation describing the time evolution of the i-th species reads [104, 105, 106]

$$\frac{\partial f_i}{\partial t} = \sum_j C_{ij}\left[f_i, f_j\right], \tag{4.15}$$

where C_{ij} is the Landau operator describing collisions between species i and j

$$C_{ij}[f_i, f_j] = \gamma_{ij} m_j \int \mathrm{d}\mathbf{v}'\ \mathbf{U}(\mathbf{u}) \left(\frac{1}{m_j}\frac{\partial}{\partial \mathbf{v}'} - \frac{1}{m_i}\frac{\partial}{\partial \mathbf{v}}\right) f_i\left(\mathbf{v}\right) f_j\left(\mathbf{v}'\right). \tag{4.16}$$

The quantity $\mathbf{u}$ represents the relative velocity between two particles $\mathbf{v} - \mathbf{v}'$ and the tensor $\mathbf{U}$ is defined

$$\mathbf{U}\left(\mathbf{x}\right) = \frac{1}{x}\left(\frac{\mathbf{x} : \mathbf{x}}{x^2}\right). \tag{4.17}$$

The matrix $\mathbf{s} = \mathbf{x} : \mathbf{y}$ has components $s_{ij} = x_i y_j$, which makes the operator $\mathbf{U}$ symmetric. The quantity γ_{ij} is defined as follows

$$\gamma_{ij} = 2\pi \frac{\ln \Lambda_{ij}}{m_i m_j} \frac{Q_i^2}{4\pi\varepsilon_0} \frac{Q_j^2}{4\pi\varepsilon_0}. \tag{4.18}$$

The variables Q_k and m_k define the charge and mass, respectively, of the particle. It is convenient to write the Landau operator in velocity variables $(v, \lambda = v_\parallel/v)$,

$$\begin{aligned} C_{ij}[f_i, f_j] =& \frac{\nu_{\lambda,ij}(x)}{2}\left[\frac{\partial}{\partial\lambda}\left(1-\lambda^2\right)\frac{\partial}{\partial\lambda}\right]f_i + \\ & -\frac{1}{v^2}\frac{\partial}{\partial v}\left[v^2\nu_{E_j}\left(\frac{T_j}{m_i}\frac{\partial}{\partial v}f_i + v_i f_i\right)\right], \end{aligned} \tag{4.19}$$

where we have assumed collisions over a thermal (Maxwellian) background plasma. The velocity variables now represent species i. The collision frequencies are given by the following expressions

$$\nu_{\lambda_{ij}} = \left[\frac{Q_i^2 Q_j^2 \ln\Lambda_j n_j}{4m_i^2\pi\varepsilon_0^2}\right]\frac{\phi(x) - \Psi(x)}{v^3} \tag{4.20}$$

$$\nu_{E_{ij}} = \left[\frac{Q_i^2 Q_j^2 \ln\Lambda_j n_j}{4m_i^2\pi\varepsilon_0^2}\right]\frac{m_i}{m_j}\frac{\Psi(x)}{v_{thj}^2 v_i} \tag{4.21}$$

where

$$v_{th,j} = \sqrt{\frac{2T_j}{m_j}} \tag{4.22}$$

$$x = \frac{v}{v_{th,j}} \tag{4.23}$$

$$\phi(x) = \mathrm{erf}(x) = \frac{2}{\sqrt{\pi}}\int_0^x e^{-y^2}\mathrm{d}x, \tag{4.24}$$

$$\Psi(x) = \frac{\phi(x) - x\phi'(x)}{2x^2}. \tag{4.25}$$

We can now transform the energy term in the right hand side of Eq. (4.19) by applying a change of variables

$$\frac{\partial}{\partial v} = \frac{\partial}{\partial E}\frac{\partial E}{\partial v} = \sqrt{2Em_i}\frac{\partial}{\partial E}. \tag{4.26}$$

The energy part of the collision operator, corresponding to particle slowing down, becomes

$$\begin{aligned} C_{ij}^E &= -\frac{m_i}{2E}\sqrt{2m_iE}\frac{\partial}{\partial E}\left[\frac{2E}{m_i}\nu_{E_{ij}}\left(\frac{T_j}{m_i}\sqrt{2m_iE}\frac{\partial f_i}{\partial E} + \sqrt{\frac{2E}{m_i}}f_i\right)\right] \\ &= -\frac{1}{\sqrt{E}}\frac{\partial}{\partial E}\left[2E\nu_{E_{ij}}\left(\sqrt{E}T_j\frac{\partial f_i}{\partial E} + \sqrt{E}f_i\right)\right] \\ &= -\frac{1}{\sqrt{E}}\frac{\partial}{\partial E}\left[2E^{3/2}\nu_{E_{ij}}\left(T_j\frac{\partial f_i}{\partial E} + f_i\right)\right]. \end{aligned} \tag{4.27}$$

We now want to write the slowing down operator in the form of an advection-diffusion equation in velocity space

$$\begin{aligned}
\sqrt{E}C_{ij}^{E} =& -\frac{\partial}{\partial E}\left[2E\nu_{E_{ij}}\left(f_i\sqrt{E}\right)\right] \\
& -2\frac{\partial}{\partial E}\left[\frac{\partial}{\partial E}\left(f_i T_j E^{3/2}\nu_{E_{ij}}\right) - \frac{\partial}{\partial E}\left(T_j E^{3/2}\nu_{E_{ij}}\right) f_i\right] \\
=& -\frac{\partial}{\partial E}\left[2E\nu_{E_{ij}}\left(f_i\sqrt{E}\right)\right] - 2\frac{\partial^2}{\partial E^2}\left[T_j E\nu_{E_{ij}}\left(\sqrt{E}f_i\right)\right] \\
& +2\frac{\partial}{\partial E}\left[\frac{3}{2}f_i\sqrt{E}T_j\nu_{E_{ij}} + E^{3/2}T_j\frac{\mathrm{d}\nu_{E_{ij}}}{\mathrm{d}E}f_i\right], \qquad (4.28) \\
\sqrt{E}C_{ij}^{E} =& -2\frac{\partial}{\partial E}\left\{\left(f_i\sqrt{E}\right)\left[E\nu_{E_{ij}} - \frac{3}{2}T_j\nu_{E_{ij}} - ET_j\frac{\mathrm{d}\nu_{E_{ij}}}{\mathrm{d}E}\right]\right\} \\
& -\frac{\partial^2}{\partial E^2}\left[2T_j E\nu_{E_{ij}}\left(\sqrt{E}f_i\right)\right]. \qquad (4.29)
\end{aligned}$$

For a generic number of species, then, we can reformulate the energy term in the Fokker-Planck equation as follows

$$\begin{aligned}
&\frac{\partial\sqrt{E}f_i}{\partial t} + \sum_j \sqrt{E}C_{ij}^{E} = 0, \\
&\frac{\partial\sqrt{E}f_i}{\partial t} + \frac{\partial}{\partial E}\left\{\left(\sqrt{E}f_i\right)\sum_j \underbrace{\left[2\nu_{E_{ij}}\left(-E + T_j\left(\frac{3}{2} + \frac{E}{\nu_{E_{ij}}}\frac{\mathrm{d}\nu_{E_{ij}}}{\mathrm{d}E}\right)\right)\right]}_{\text{Advection}}\right\} + \\
&\quad -\frac{\partial^2}{\partial E^2}\underbrace{\left[\sum_j\left(2T_j E\nu_{E_{ij}}\right)\left(\sqrt{E}f_i\right)\right]}_{\text{Diffusion}} = 0. \qquad (4.30)
\end{aligned}$$

This equation can be solved by evolving the velocity space characteristic of a population of markers whose energy is changed according to the following stochastic scheme

$$\begin{aligned}
\Delta E =& -\sum_j 2\left(\nu_{E_{ij}}\Delta t\right)\left[E - \left(\frac{3}{2} + \frac{E}{\nu_{sj}}\frac{\mathrm{d}\nu_{sj}}{\mathrm{d}E}\right)T_j\right] \\
& +2\mathcal{R}\sqrt{\sum\left(T_j\nu_{E_{ij}}\right)E\Delta t}, \qquad (4.31)
\end{aligned}$$

where $\mathcal{R} \in N(0,1)$: normal PDF with null mean and unit variance. Δt is the numerical time step. We can similarly find a solution for the pitch angle scattering

term in the collision operator

$$\frac{\partial f_i}{\partial t} + C^{\lambda}_{ij} = \frac{\partial f_i}{\partial t} + \sum_j \frac{\nu_{\lambda,ij}(x)}{2}\left[\frac{\partial}{\partial \lambda}\left(1-\lambda^2\right)\frac{\partial}{\partial \lambda}\right] f_i =$$

$$= \frac{\partial f_i}{\partial t} + \left\{ \frac{\partial^2}{\partial \lambda^2} \underbrace{\left[\sum_j \frac{\nu_{\lambda_{ij}}}{2}\left(1-\lambda^2\right) f_i\right]}_{\text{Diffusion}} - \frac{\partial}{\partial \lambda} \underbrace{\left[\sum_j \nu_{\lambda_{ij}} \lambda f_i\right]}_{\text{Advection}} \right\} = 0. \tag{4.32}$$

The numerical scheme is given by

$$\Delta\lambda = -\sum_j \lambda \nu_{\lambda_{ij}} \Delta t + \mathcal{R}\sqrt{\left(1-\lambda^2\right)\sum \nu_{\lambda_{ij}} \Delta t}. \tag{4.33}$$

The new definitions of the collision frequencies $\nu_{\lambda_{ij}}$ and $\nu_{E_{ij}}$ represent the major difference with respect to the previous collision operator [108, 109]. Earlier versions of the code employed a reduced model assuming the interaction between energetic ions and light particles j where $m_{\text{fast}}/m_j \gg 1$. This represented a solid approximation for ICRH heated particles which interact predominantly with electrons. The new operator hereby presented, on the other hand, is a choice more suitable in a larger number of cases and energy ranges.

In figure 4.5 we can observe particle slowing down a 25 keV deuteron in the TCV tokamak. Both slowing down and pitch angle scattering effects are observed in the figure. The slight acceleration caused by the electron drag at large velocities is observed in the left panel illustration at $t \simeq 0$. This effect creates a small number of particles with energy larger than the injection energy of neutral beam ions [92]. Pitch angle scattering is more clear in the right panel curve where the particle position stretches from the high energy birth position to thermal velocities.

The influence of collisional processes over large particle populations is shown in figure 4.6 for the TEXTOR tokamak. The cumulative effect of slowing down and pitch angle scattering can be observed in the figures. Slowing down effects make particles follow the black line towards the lower energy region of velocity space (i.e. decreasing energy). Then, pitch angle scattering effects tend to make the distribution isotropic thus moving particles along the magenta arrows (i.e. constant energy). The latter interaction is mostly important in the low energy region where collisions with background ions dominate. Slowing down, on the other hand, is most effective when energetic ions collide with electrons. Plasma current and magnetic field in the TEXTOR tokamak point in different directions.

The collisional events presented in this section closely interact with anomalous transport. We observed in section 3.2 that anomalous transport depends on particle energy and pitch angle, two quantities influenced by collisions. Typically, collisions lower the energy of the fast particle which in turn experiences larger turbulent diffusivities. The consequent radial displacement is modeled with the numerical scheme presented in the next section.

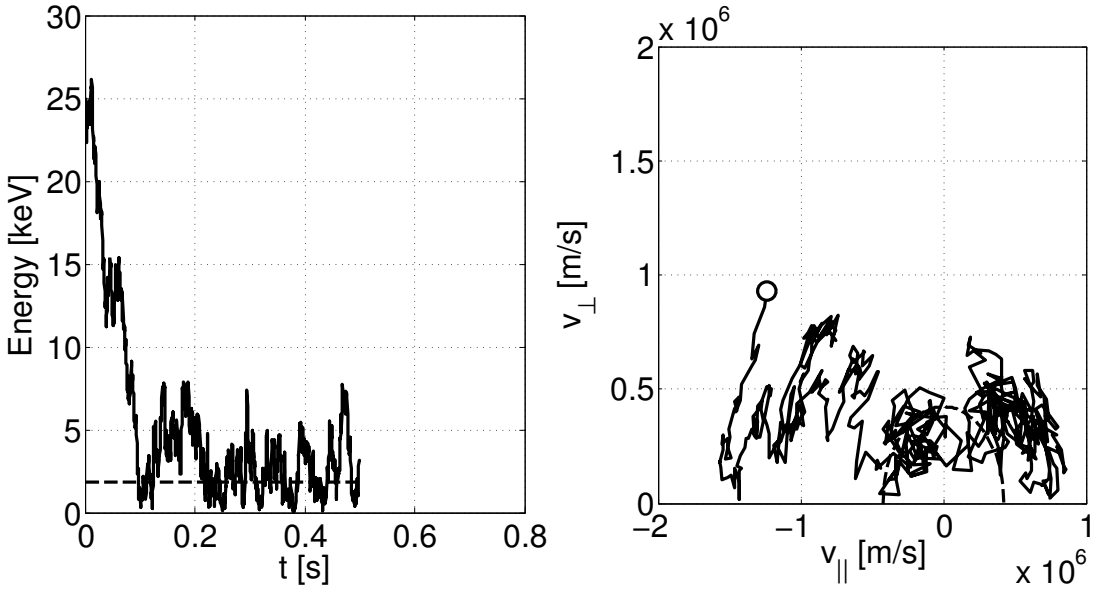

Figure 4.5: Time evolution of the energy of a 25 keV deuterium particle in the TCV tokamak (left panel). The dashed line corresponds to the background plasma temperature. The right panel represents the particle motion in velocity space. The dashed line once again represents background thermal velocities while the circle indicates the particle birth point.

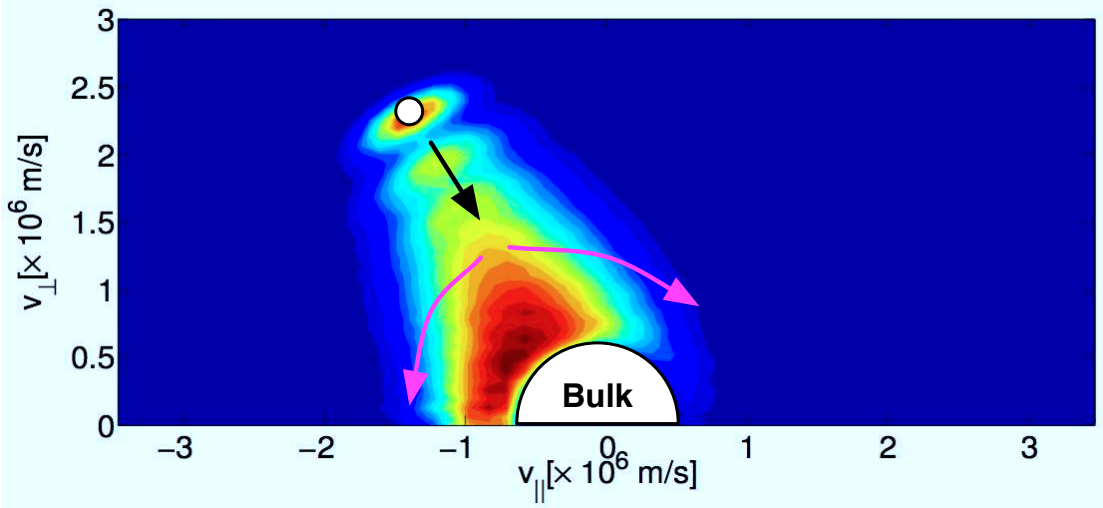

Figure 4.6: Slowing down distribution function of a high energy population of ions in the TEXTOR tokamak. Particles are injected at 100 keV (white circle) and are subject to slowing down (along the black arrow) and pitch angle scattering (magenta). Particles are removed from the simulation when their velocity is comparable to the thermal bulk, also indicated in the figure.

4.4 Monte Carlo anomalous diffusion: implementation in VENUS

In this section we provide the Monte Carlo anomalous diffusion scheme consistent with the theoretical framework of section 3.1 and the quantities extracted from the GENE code. Numerical simulations of the anomalous fast ion transport are then first performed first with the GENE code, which simulates the numerical kinetic diffusivity presented earlier. Then, the particle diffusivity D_v is introduced in the Monte Carlo scheme presented here which, together with the collision operator, will determine the fast ion motion.

Let us start by writing the continuity equation

$$\frac{\partial n}{\partial t} + \nabla \cdot \mathbf{\Gamma} = 0. \tag{4.34}$$

To create the link with the diffusivity obtained with GENE simulations, a series of approximations are required. We assume radial fluxes to be dominant in a large aspect ratio tokamak, therefore

$$\frac{\partial n}{\partial t} + \frac{1}{r}\frac{\partial}{\partial r}\left(r\Gamma\right) = 0, \tag{4.35}$$

where

$$n = \int d\mathbf{v} f_0(\mathbf{v}), \tag{4.36}$$

$$\Gamma = \int d\mathbf{v} \delta f \delta \mathbf{u}. \tag{4.37}$$

Equation (4.34) can be cast in the integral form

$$\int d\mathbf{v} \left[\frac{\partial f_0}{\partial t} + \frac{1}{r}\frac{\partial}{\partial r}\left(r\delta f \delta u\right)\right] = 0. \tag{4.38}$$

The aim at this point is to create a Monte Carlo operator in real space, similar to the velocity space operator for the collisions previously studied. To recreate a diffusion-advection equation, we remove the integral from the previous equation and we obtain

$$\frac{\partial f_0}{\partial t} + \frac{1}{r}\frac{\partial}{\partial r}\left(r\delta f \delta u\right) = 0. \tag{4.39}$$

Equation (4.39) represents the velocity space dependent continuity equation and can be interpreted as a reduced Vlasov equation. By also comparing with equation (3.22) we obtain an even more recognizable form

$$\frac{\partial f_0}{\partial t} - \frac{1}{r}\frac{\partial}{\partial r}\left[rD_v\frac{\partial f_0}{\partial r}\right] = 0. \tag{4.40}$$

We can reformulate the latter relation in VENUS quantities, thus making it simpler to implement a diffusion algorithm. If we define

$$y = r^2 \rightarrow dy = 2rdr \rightarrow \frac{\partial}{\partial r} = \frac{\partial}{\partial y} 2\sqrt{y}, \tag{4.41}$$

equation (4.40) becomes

$$\frac{\partial f_0}{\partial t} - \frac{\partial}{\partial y}\left[4yD_v \frac{\partial f_0}{\partial y}\right] = 0, \tag{4.42}$$

$$\frac{\partial f_0}{\partial t} - \frac{\partial^2}{\partial y^2}\left[4yD_v f_0\right] + \frac{\partial}{\partial y}\left[4\frac{\partial}{\partial y} f_0 \left(yD_v\right)\right] = 0. \tag{4.43}$$

If we assume a slow radial variation for the anomalous diffusion coefficient one obtains

$$\frac{\partial f_0}{\partial t} - \frac{\partial^2}{\partial y^2}\left[4yD_v f_0\right] + \frac{\partial}{\partial y}\left[4D_v f_0\right] = 0. \tag{4.44}$$

The radial variable in the VENUS code is defined as $s = \rho_t^2 \simeq (r/a)^2 = y/a^2$, where a is the plasma minor radius. With the opportune changes we can finally obtain

$$\frac{\partial f_0}{\partial t} - \frac{\partial^2}{\partial s^2}\left[\frac{4sD_v}{a^2} f_0\right] + \frac{\partial}{\partial s}\left[\frac{4D_v}{a^2} f_0\right] = 0. \tag{4.45}$$

Similarly to what is observed for the Coulomb collision numerical scheme, this advection-diffusion equation can be solved with a stochastic term in the equations of motion. For a population of markers we apply, at each timestep, the radial displacement

$$s(t_i) = s(t_{i-1}) + \mathcal{R}\sqrt{2\left(\frac{4D_v s}{a^2}\right)\mathrm{d}t} + \left(\frac{4D_v}{a^2}\right)\mathrm{d}t, \tag{4.46}$$

for a time interval $\mathrm{d}t$, where $\mathcal{R} \in N(0,1)$.

The quantity D_v in equation (4.46) provides the link between the variables introduced in section 3.1, the GENE code and the VENUS code. The procedure for tracking the fast ion anomalous redistribution works as follows. The background turbulence for a fusion device is first simulated by the GENE code. The quantities defined in section 3.1 are then extracted from the GENE code diagnostics and the diffusion coefficient D_v is calculated. The anomalous diffusivity D_v is then read by the VENUS code to simulate the cumulative effect of fast ion anomalies and Coulomb collisions. An example of the particle diffusivity experienced by an energetic ion during its slowing down can be observed in figure 4.7. As the particle transfers its energy to the background plasma, its initial position in velocity space (indicated in the figure with a magenta "x") moves to the region where larger diffusivities are found. Clearly, transport can still be neoclassical (only collisional) if

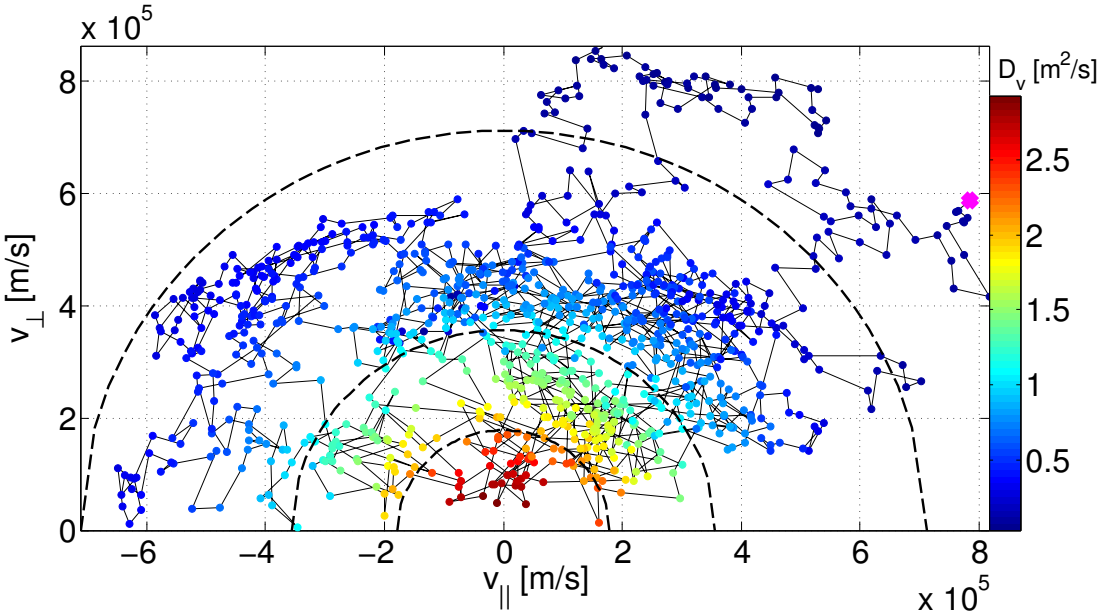

Figure 4.7: Slowing down of a neutral beam particle (birth position is indicated in magenta) in the TCV tokamak. The 25 keV deuterium particle transfer its energy until background thermal velocities are found (dashed lines represent 1, 2 and 4 $v_{th,i}$). The color code represents the corresponding anomalous diffusion coefficient experienced by the particle during the thermalization process, in $\mathrm{m}^2 \cdot \mathrm{s}^{-1}$.

a particle is thermalized before anomalous transport becomes important. Longer slowing down times, on the other hand, can result in larger anomalies as energetic ions interact with microturbulent fields for longer time scales. This is the case of the DEMO tokamak which will be presented in section 6. For the moment, the first application of the numerical platform for a present day machine, the TEXTOR tokamak, is presented in the next section.

4.5 VENUS simulations of the TEXTOR tokamak

Part of this thesis work was dedicated to the comparison between the theoretical results obtained with the VENUS code and experiments. In particular, the VENUS code was employed together with the ASCOT code for the validation of experimental data in the TEXTOR tokamak. A successful benchmark was undertaken which provided both a good agreement between the two codes and the Collective Thomson Scattering (CTS) diagnostic. The results presented shortly, also submitted for publication [110], will then confirm the solid physical background embedded in the VENUS code.

TEXTOR (Tokamak Experiment for Technology Oriented Research) is a circular, medium-sized device operated at the Forschungszentrum in Jülich, Germany. It serves as an important experiment in the field of plasma-wall interactions and it is equipped with a neutral beam heating system. Plasma temperatures in excess of the kiloelectronvolt can be achieved at relatively large plasma densities ($n_e > 3 \times 10^{19}$ m^{-3}). Several diagnostics are installed on the machine, among which a powerful CTS system. CTS diagnostics measure the features of an electromagnetic wave in the GHz range traveling through the plasma volume. The modifications of the incident wave, injected with an antenna outside the machine, is measured from an external receiver. Differences between the injected and the scattered radiation are a result of the wave-fast particle interactions in the plasma. As a consequence, CTS systems can be used to probe the energetic ion features. Furthermore, local measurements are also possible by choosing a convenient intersection between the injected radiation path and the receiver line of sight (see ref. [101] for an insightful description of the CTS diagnostic in TEXTOR).

A series of experiments were recently performed in TEXTOR to prove the potential of the CTS diagnostic as a fast ion probe [110], using the NBI system with 50 keV hydrogen beams in deuterium plasma. The particular configuration of the TEXTOR tokamak, with oppositely directed plasma current and magnetic field, means that the neutral beam system creates passing particles with dominantly negative pitch angle $\lambda = v_{\parallel}/v$. Several acquisitions at different radial and toroidal positions were performed with the CTS system. The VENUS code and the ASCOT code, both sharing similar equations of motion and collision operators, were the theoretical instruments chosen for the experimental data validation. As the codes do not include a sawtooth crash model, important for fast ion redistribution [50], experimental acquisitions were performed a few milliseconds before the crash event. The numerical simulations, performed on the basis of real plasma parameters, are first performed with no anomalous diffusion coefficient. The theoretical energetic ion distribution function $f(\lambda, E)$, obtained with VENUS and ASCOT can be observed in figure 4.8. This figure is obtained with the integration of the 4D distribution function $f(R, Z, \lambda, E)$ over the real space. The excellent agreement between the two codes further highlights the effort undertaken in the VENUS upgrade. The 4D distribution function was then inserted in a synthetic CTS diagnostic and compared with the experimental data. The results of figure 4.9 correspond to TEXTOR plasma discharges #111822 (left) and #111506 (right) and clearly show the good agreement between the experiments and the outcome of the numerical simulations. Some discrepancies are present in the bulk plasma velocity region, shown only partially in the figure to underline the fast ion region. The small disagreement is due to slightly different equilibrium reconstructions in the two codes and to the presence in the ASCOT code of Z_{eff} effects. In VENUS, slowing down and pitch angle scattering phenomena are reproduced by only considering a plasma where only one ion species is present. The effect of anomalous transport in these scenarios seemed small or negligible,

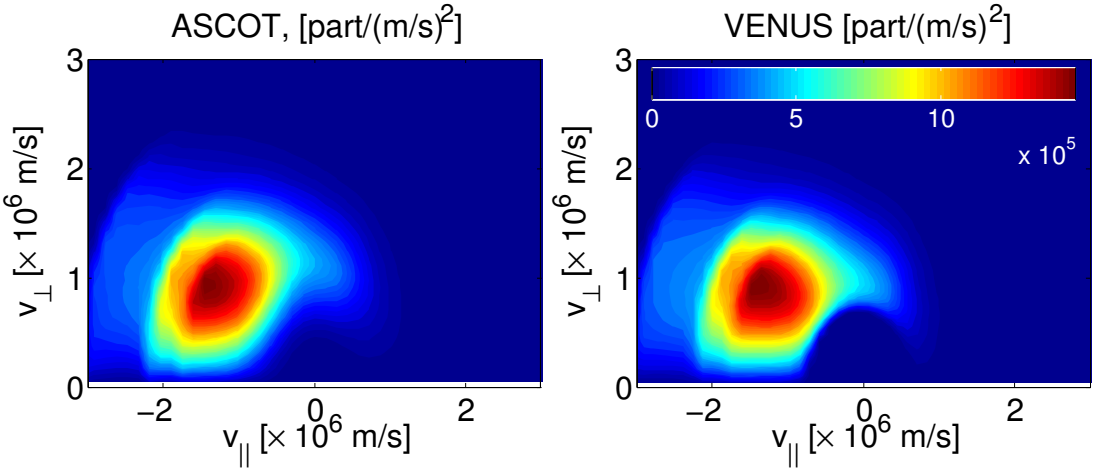

Figure 4.8: Comparison between the real space averaged fast ion distribution function calculated by the ASCOT code (left panel) and the VENUS code (right panel) for TEXTOR plasma discharge #111822.

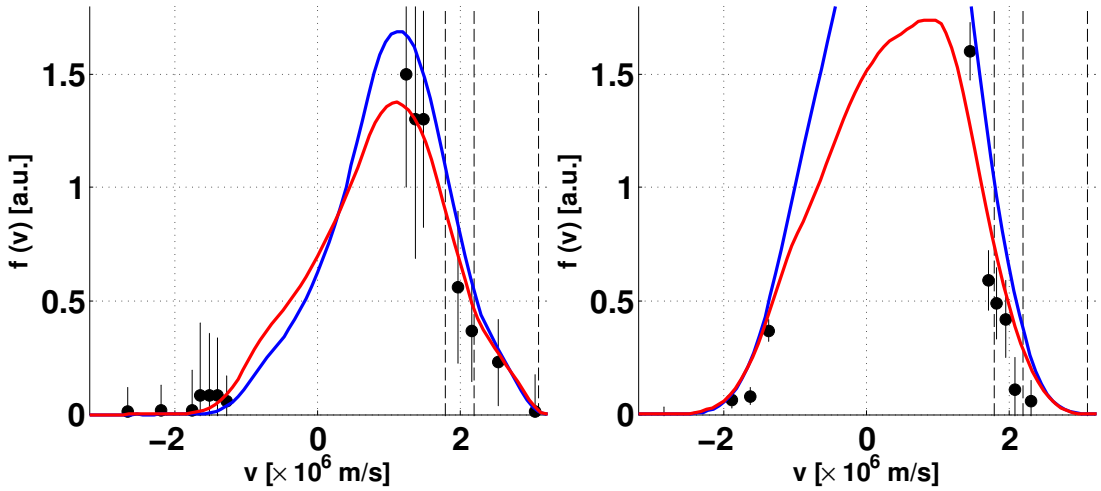

Figure 4.9: Fast ion distribution function in velocity space for TEXTOR plasma discharges #111822 (left panel) and for #111506 (right panel). The experimental observation of the CTS diagnostic (black dots) is compared to the ASCOT and VENUS code simulations (red and blue, respectively). A detailed discussion of the units in the figure can be found in ref. [110].

an assumption further validated by the small value of the Δ parameter introduced in the previous chapter. For these two discharges, where the diagnostic was probing the fast ion distribution in the plasma core, we obtain $\Delta < 10^{-1}$ and it is reasonable to expect negligible effects from microturbulence.

Further comparisons with experimental data were undertaken revealing discrepancies between the numerical forecast and CTS data. In the curves of fig-

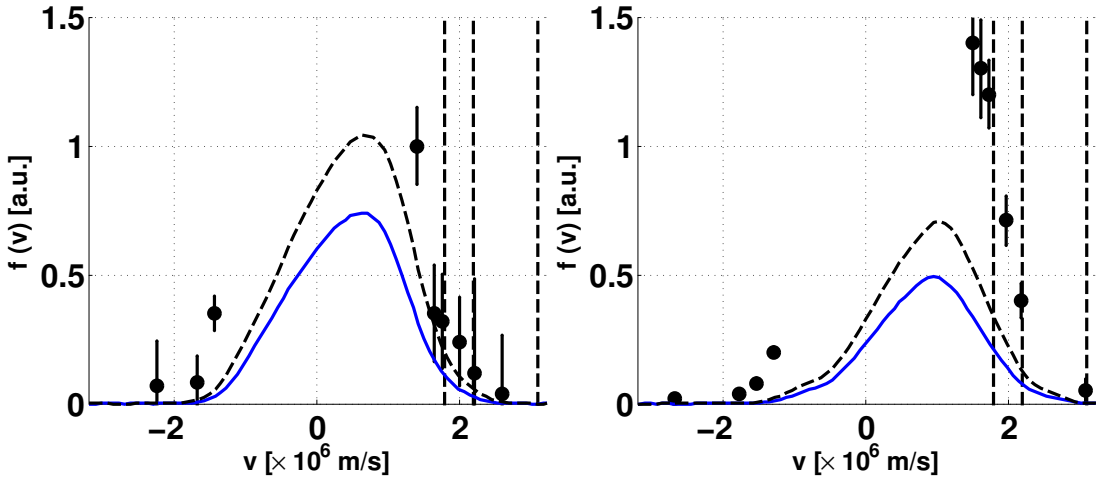

Figure 4.10: Velocity space distribution function of the beam ion population in the TEXTOR tokamak for plasma discharges #111512 (left panel) and for #111509 (right panel). A clear mismatch is observed between the experimental data (black dots) and the simulations with the VENUS codes (blue lines, respectively). Better results are obtained with the inclusion of anomalous transport in the VENUS code (dashed black line), although the discrepancy is still present (especially for plasma discharge #111509). The diffusion coefficient employed in the simulations assumes a background diffusivity of 0.5 $m^2 \cdot s^{-1}$and a shape of $D_{\text{anomalous}}$ similar to TCV, discussed in the next chapter.

ure 4.10 we can see the discrepancies between the VENUS code (blue line, respectively) with the experimental data (black dots). Experiments were carried out in conditions similar to plasma discharges #111822 and #111506, where good agreement was found. The greatest difference between the two scenarios was the plasma region observed by the CTS diagnostic, now close to mid-radius. Turbulent transport was conjectured as a potential source of particle redistribution from the core to the diagnosed position. For this reason, VENUS simulations were performed with the anomalous diffusion obtained for the TCV tokamak described in chapter 5. After the opportune renormalisation, a better match for the experimental data was obtained. Although improved, there is still significant discrepancy for plasma discharge #111509. The hypothesis that Alfvén eigenmodes were present in this particular case was put forward and further experiments are planned to verify this assumption.

4.6 Conclusions

This chapter was dedicated to the description of recent upgrades to the single particle code VENUS. Corrections to the collisional diffusion operator described in [108, 109] were made. In addition, Monte Carlo operators for phase space diffusion were added to the code to simulate the anomalous transport. The anomalous radial diffusion scheme is based on the set of variables described in the previous chapter and accepts input from the GENE code. To simulate the beam ion behavior, a source term representing NBI systems was also implemented. Benchmarks were performed with the ASCOT code and good agreement was found. Furthermore, the upgraded VENUS code was employed to interpret experimental data from the CTS diagnostic in the TEXTOR tokamak. The comparison between theory and experiments was promising. Some discrepancies with experimental data, however, were found. The inclusion of anomalous transport partially improved the the collisional results, but Alfvénic activity, not modeled by our code, is a possible candidate for the theory-experiment gap. In the next chapter, similar analyses will be performed to study the fast ion physics of the planned neutral beam upgrade of the Tokamak à Configuration Variable .

Chapter 5

Fast ion confinement properties of the TCV's planned neutral beam system

It is the aim of this chapter to investigate the physics of the fast ions created with the planned neutral beam system in the Tokamak à Configuration Variable (TCV). The TCV tokamak is introduced in section 5.1, where the main features of the plasma device and of the envisaged NBI system are also presented. The behavior of the injected deuterium ions, in the absence of microturbulent fields, is discussed in section 5.2. It is found that shine-through effects, resulting from the deposition of non-ionized neutrals over the vacuum vessel, is usually small. Only in low density plasmas heat losses of the order of MW/m^2 were found. First orbit losses, described in the same section, are even less threatening. Although beam power as large as 40% can be lost in counter-current configuration, it would be spread over a larger surface. Less than a few kW/m^2 would be deposited on the walls of the device and plasma operation would not be significantly reduced.

Anomalous transport is considered in section 5.3, where microturbulent fields in the TCV tokamak are characterized on the basis of gyrokinetic GENE simulations. The numerical particle diffusivity obtained with the theoretical framework presented in chapter 3 is then used in VENUS simulations. It is shown that in high temperature plasmas beam ions are generally redistributed. The fast ion core pressure, for example, drops by more than 50% in some discharges. On the other hand, intermediate to low temperature operation is less affected. Apart from some exceptional cases, efficient plasma heating with the planned neutral beam system is possible. It is also concluded that, given the adequate diagnosing capabilities, TCV would represent a unique machine where to investigate the fast ion transport.

5.1 The TCV tokamak and the planned neutral beam system

The Tokamak à Configuration Variable (TCV, [111]) is located at the École Polytechnique Fédérale de Lausanne (EPFL), in Switzerland. It is operational since the early 90s, with the main goal to investigate the importance of magnetic geometry over confinement, stability and transport. Plasma shaping is obtained with

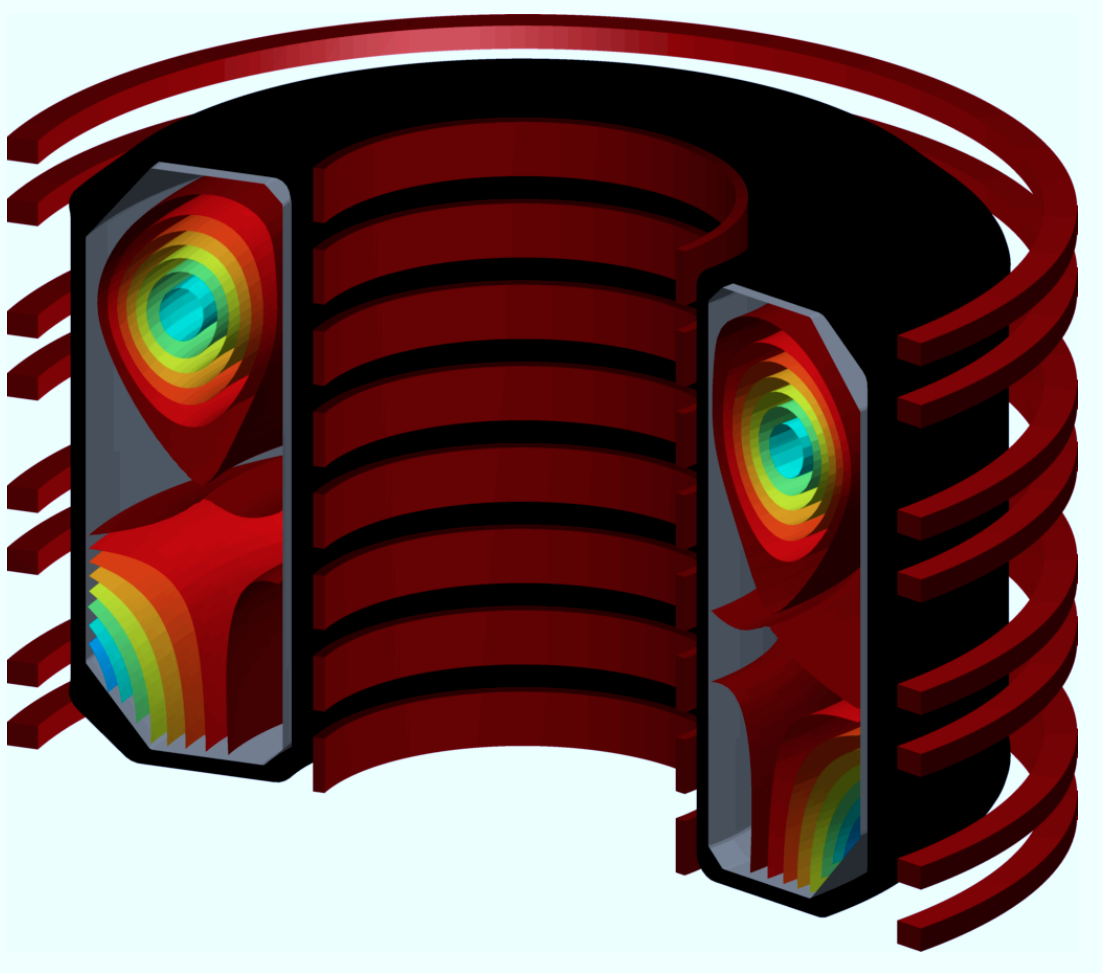

Figure 5.1: Simplified drawing of the Tokamak à Configuration Variable (TCV). The external vessel (black), the carbon tiles (grey) and the poloidal field coils (red) are shown. Also shown is a snowflake diverted equilibrium [112].

16 poloidal field (PF) coils (figure 5.1). Different plasma triangularities, including negative ones, can be produced. Furthermore, TCV holds the record for the largest tokamak plasma elongation.

Different diagnostics are installed in the TCV tokamak. For the studies reported here, the main features of the background plasma are studied with the far infrared interferometer (FIR), the Thomson scattering diagnostic and two soft X-ray systems (DMPX and XTOMO). Magnetic probes, mounted inside the vacuum vessel, are used to investigate the poloidal field structure. A low power neutral beam system (DNBI) is used to detect the background ion temperature and plasma rotation, together with a charge exchange recombination spectroscopy system (CXRS). Neutral particle analyzers (NPA and cNPA) reconstruct the energy spectrum of particles escaping the plasma. This provides information on the plasma temperature and, once coupled with the DNBI system, on fast ion losses.

A fast framing camera is used, together with Langmuir probes, for the analysis of plasma wall interaction. Visible radiation in the edge is measured by photodiodes (PD) and bolometers (BOLO). Plasma turbulence can be studied with a dedicated correlation ECE system.

The TCV tokamak represents an important experiment in the field of electron plasma heating, with nine gyrotrons installed for this purpose. Six of these generate microwaves at a frequency of 82.7 GHz, the second harmonic of the electron cyclotron resonance. A cluster of three gyrotrons provides electromagnetic waves at 118 Ghz, the third harmonic, which can be used in higher density plasmas. Up to 4.5 MW of electron cyclotron heating (ECH) can be injected in the machine with real-time steerable mirrors ("launchers"). With the appropriate alignment of these mirrors, non inductive current can be driven with the ECCD technique. The same system is also used for advanced control of plasma instabilities.

Many successful experiments have been carried out on TCV during the past 20 years (for example, see refs. [17, 112, 113, 114, 115, 116, 117, 118, 119, 120]). It has notably provided cutting-edge results for ITER-oriented studies thanks to the great flexibility of the PF coils, heating and diagnosing systems. The main limitation of such plasma device is the low ion temperatures achieved, with T_e/T_i routinely larger than one due to $\tau_{\text{thermal equilibrium}} \gg \tau_{\text{confinement}}$. For this reason, a neutral beam heating system was recently proposed to investigate the $T_e/T_i \simeq 1$ regime [121].

5.2 Beam deposition and the classical description of fast ion confinement in TCV

We dedicate this section to the study of beam deposition, unperturbed motion and classical effects in the neutral beam system planned for TCV. With "unperturbed" we define the particle motion with the only influence of the background magnetic equilibrium. The planned NBI system in the TCV tokamak would provide a heat source for the background ions, which could then reach and also surpass electron temperatures. This is achieved by injection particles at energies lower than the critical value $E_c \simeq 19\,T_e \simeq 100$ keV. Feasibility studies demonstrated the possibility of installing two NBI systems injecting deuterium at energies between 20 and 35 keV for a total power of 1 MW each (700 kW at the plasma boundary). For the purpose of this investigation, we choose the injection energy $E_b = 25$ keV, with power for each fractional energy $\left[P_E, P_{E/2}, P_{E/3}\right]/P_{tot} = [68, 24, 8]\,\%$. Quasi-tangential injection is planned for optimal beam deposition (figure 5.2). The balanced injection with two neutral beam systems would be useful for rotation studies. However, the counter-current beam might suffer from large particle losses. For this reason, a study of the beam shine-through and first orbit losses are required. We first survey the parameters of the simulated plasma discharges, chosen with different temperatures and densities to cover a sufficiently broad

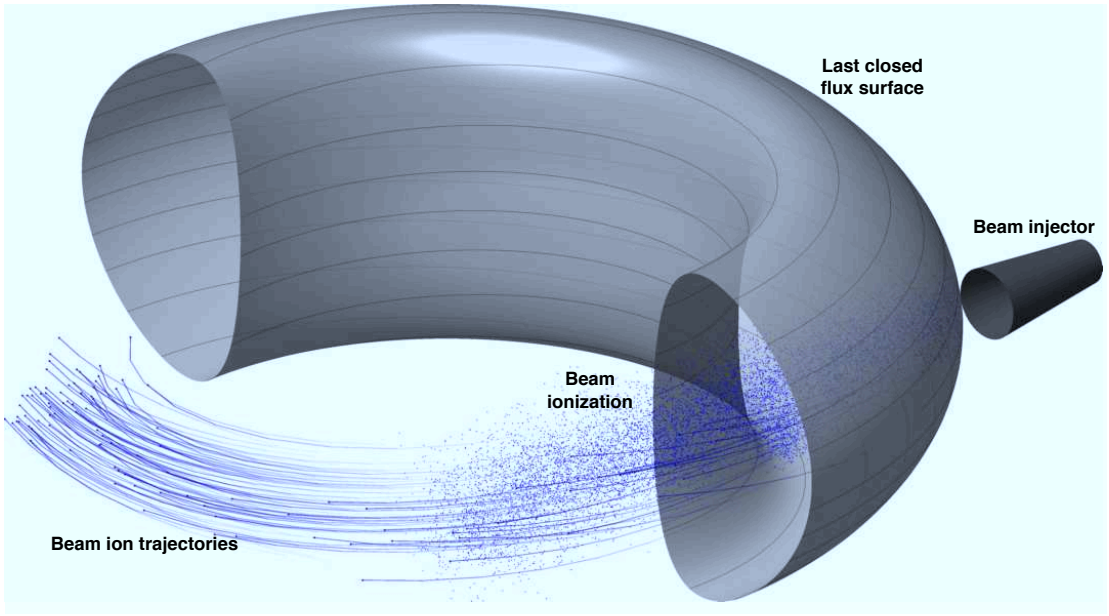

Figure 5.2: Illustrative drawing of the neutral beam injection in the TCV tokamak. A modeled beam source is represented, together with the consequent particle ionization in the plasma volume. The last closed flux surface of plasma discharge #31761 is represented in grey, together with magnetic field lines (dark grey). The characteristic orbits of sampled beam ions are illustrated, showing dominantly passing particles.

physical range. Different plasma currents, with the inclusion of a reverse shear discharge, are also examined.

5.2.1 Plasma discharge description

The main features of the TCV plasma discharges investigated in this chapter are illustrated in figure 5.3. Different plasma currents are surveyed, the lowest being the 86 kA of the reverse shear eITB plasma discharge #29866. More conventional discharges, with monotonic q profiles, are also studied. Temperatures range from 1 keV (#27489) to 12 keV (#25013). Anomalous transport is particularly sensitive to the ratio of the injection energy and the electron temperature (E_{nbi}/T_e), as discovered in chapter 3. The latter quantity is shown in figure 5.4 for each plasma discharges considered. In the same figure we observe the particle diffusivity expected at $(\rho_t, \theta) = (0.5, 0)$ for plasma discharge #29866, whose detailed description is given in section 5.3.1. Bulk densities are also important for anomalous transport, since lower values of $n_{e,i}$ reduce fast ion collisionality (see equation (4.20)). Longer thermalization times result in a larger fast ion-turbulence interaction. Plasma density also influences neutral beam ionization and, as a consequence, shine-through effects.

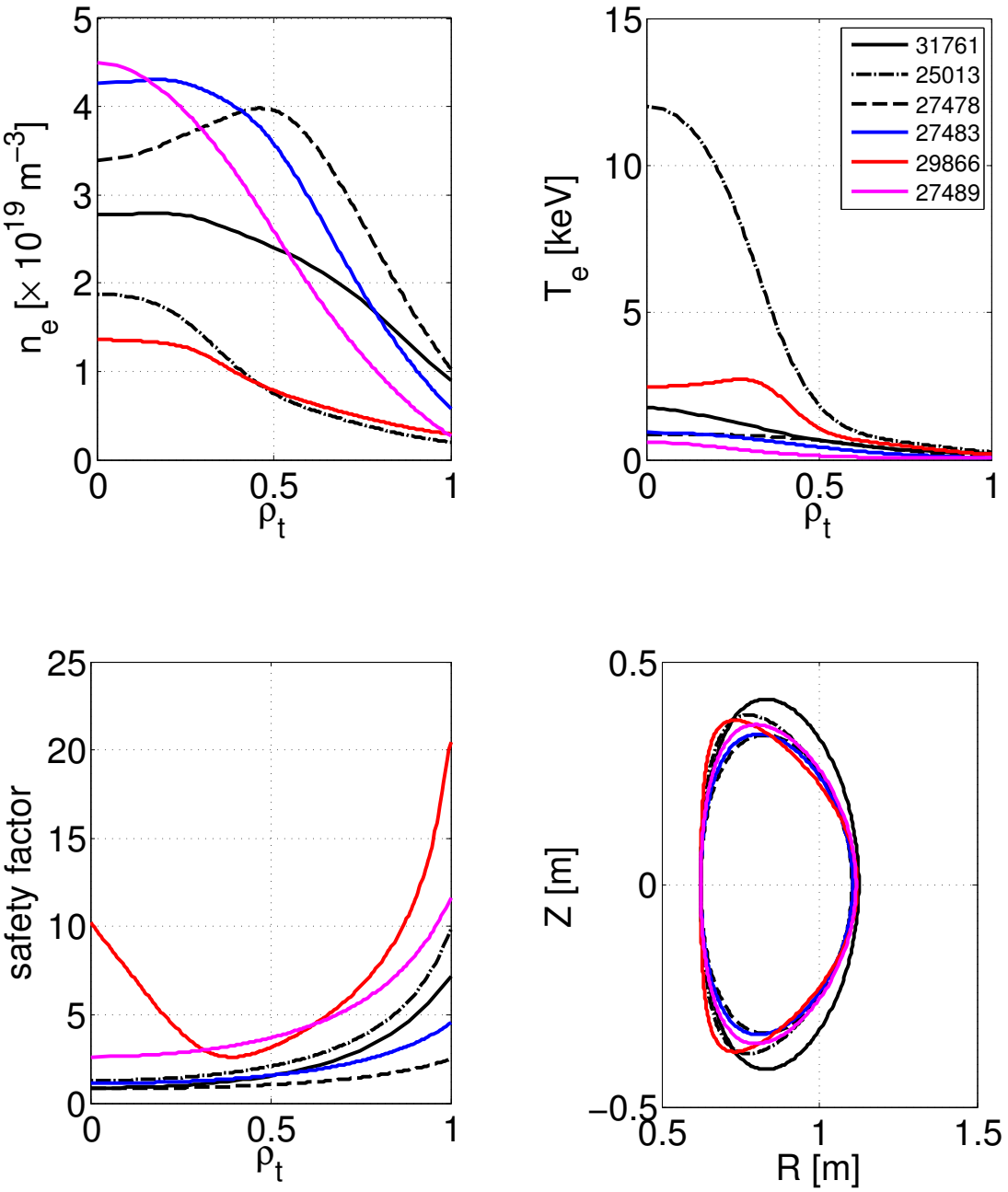

Figure 5.3: Plasma density (top left), temperature (top right), safety factor (bottom left) and last closed flux surface (bottom right) for different TCV plasma discharges.

5.2.2 Shine-through

The neutral beam particles that are not ionized after traveling through the plasma hit the plasma vessel. This effect, known as shine-through, can lead to excessive heating of plasma facing components and damage the wall. The equation describ-

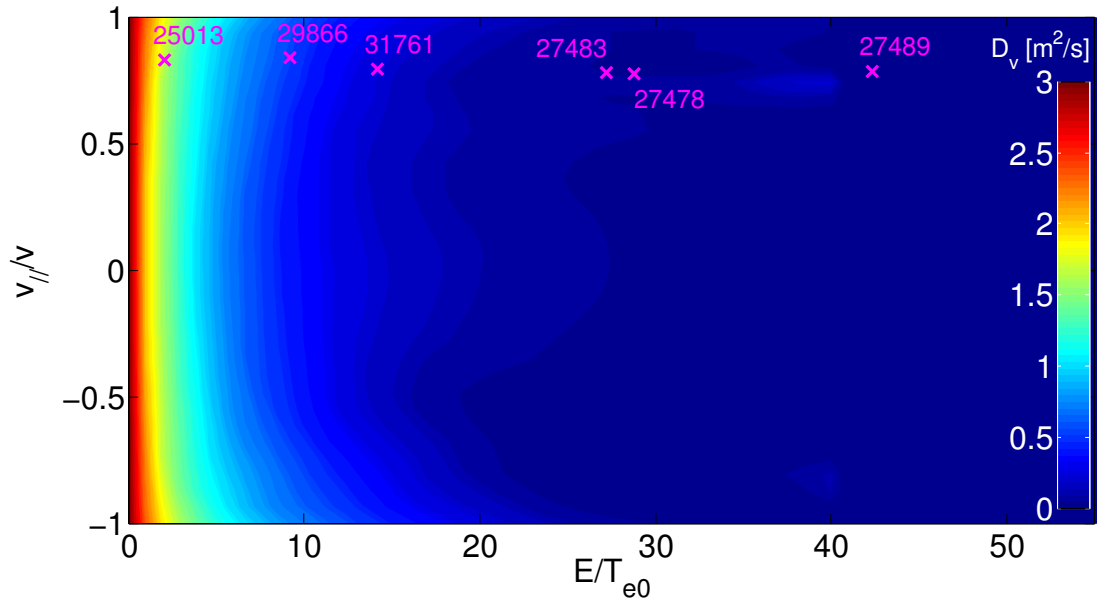

Figure 5.4: Injection energy, normalized to the plasma temperature, for the plasma discharges surveyed in this chapter. The particle diffusivity expected at mid-radius, $\theta = 0$, for plasma discharge #29866 is also represented.

ing the beam attenuation in a plasma is given by

$$\frac{N_b(\ell)}{N_{b,0}} = e^{-\int_0^\ell n_e(\ell')\sigma_{\text{eff}}(\ell')d\ell'}, \tag{5.1}$$

where ℓ is the position along the beam path, σ_{eff} the ionization cross section and n_e the plasma density. The non-ionized fraction of a neutral beam at the exit point L is then given by

$$N_b(L) = N_{b,0}e^{-\int_0^L n_e(\ell')\sigma_{\text{eff}}(\ell')d\ell'}. \tag{5.2}$$

We observe in figure 5.5 the beam attenuation for TCV plasma discharge #31761. This plasma scenario is characterized by a very efficient deposition with less than 1% particles losses. Scenarios at lower plasma densities than here, $n_e \simeq 3 \times 10^{19}\, m^{-3}$, can suffer from large shine-through. This is what we observe in figure 5.6. The beam deposition efficiency, defined as $P_{\text{deposited}}/P_{\text{injected}}$, is plotted for each plasma discharge described in section 5.2.1. A good ionization rate is expected for the densities considered. Only for plasma discharges #29866 and #25013, characterized by $n_{e,0} < 2 \times 10^{19}$ m^{-3}, losses larger than 10 % are observed. This would correspond to almost 100 kW entirely deposited over a small surface of the vessel tiles. For a beam spread of 2^o, $L = 2$ m and a squared beam source measuring 20 cm on the side, the impact area would be slightly larger than 0.2 m^2 , leading to $P_{\text{loss}} < 5$ MW/m^2 . TCV tiles in the low field side of the vessel can not be exposed to such heat deposition. To prevent damage to plasma facing

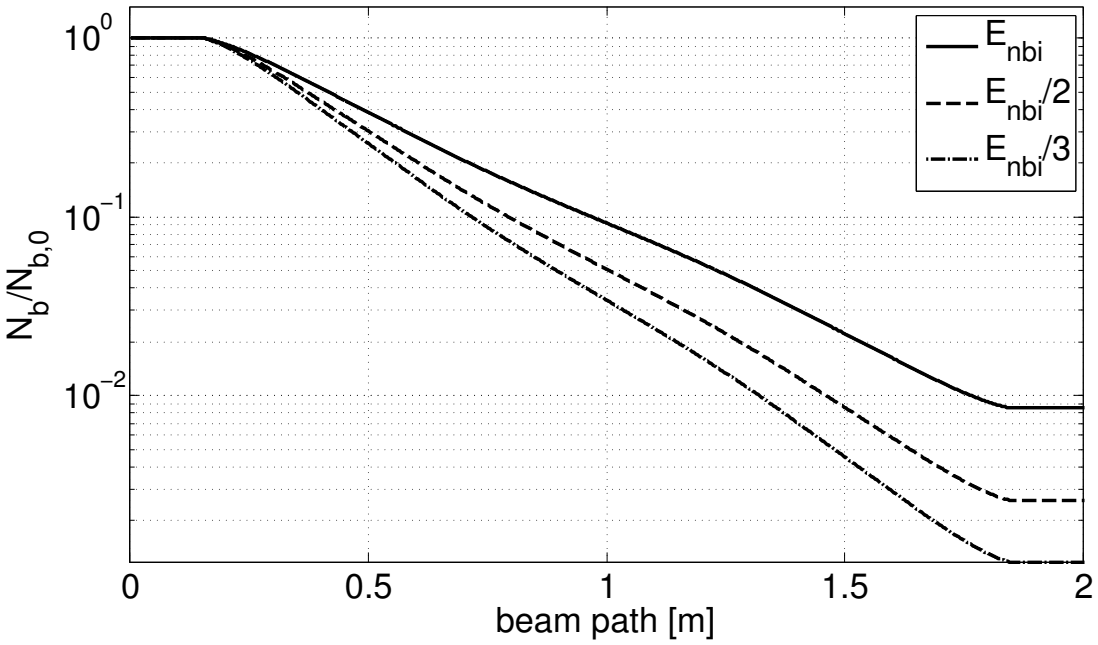

Figure 5.5: Beam attenuation for TCV plasma discharge #31761, for each energy fraction injected by the neutral beam system.

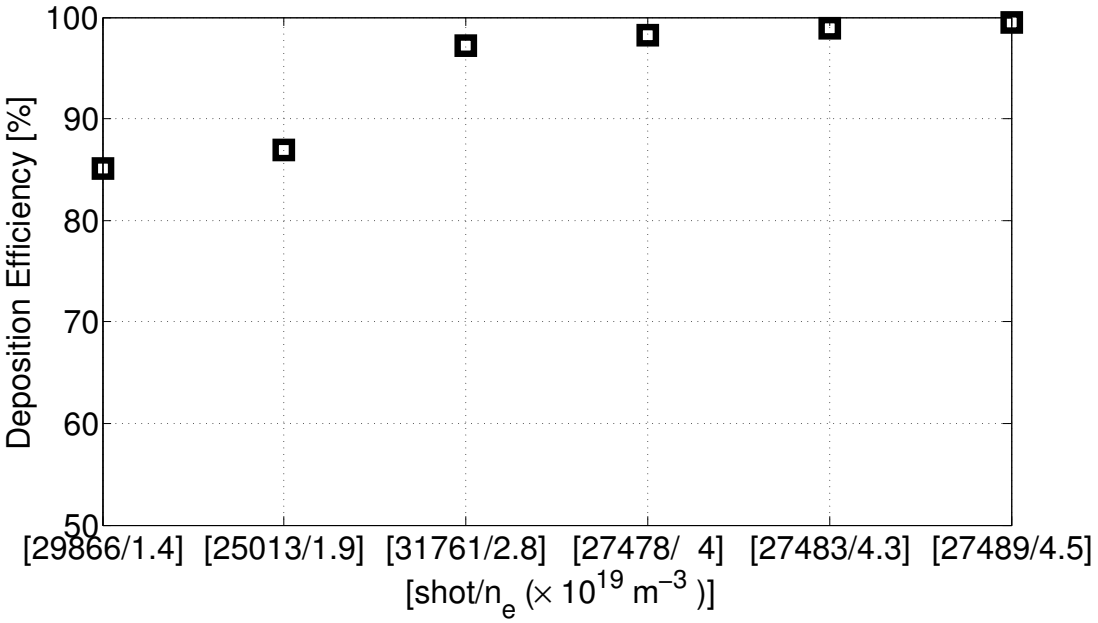

Figure 5.6: Beam deposition efficiency, defined as $P_{\text{deposited}}/P_{\text{injected}}$, for the TCV plasma discharges analyzed in this chapter. The electron density in the plasma core is also shown on the x-axis.

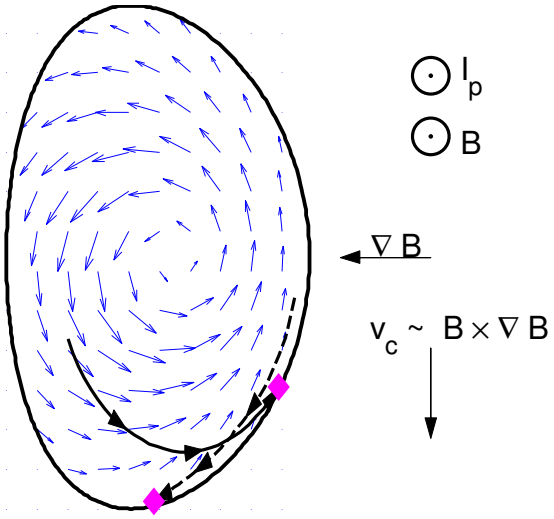

Figure 5.7: Illustration of the first orbit losses effect. The curvature drift pushes co-passing ions (black solid line) from the high field side of the tokamak to outside the plasma volume. The same phenomenon characterizes cr-passing ions generated in the low field side (black dashed line). The magenta marker indicates the loss position, the magnetic field is represented with blue arrows.

materials, shorter duration for NBI injection is envisaged for such low densities. Beam efficiency for the other plasma discharges does not represent a threat to the machine for routine operation.

5.2.3 First-orbit losses

Tangential neutral beam systems are an efficient source of predominantly passing ions, such as those observed in figure 5.2. We noted that the confinement of these particles depends on their birth position in the tokamak and the direction of the initial toroidal velocity with respect to the plasma current [122]. Particles follow the magnetic field lines and are subject to the curvature drift $\mathbf{v}_c \simeq \mathbf{B} \times \nabla \mathbf{B}$. If a particle streams in the same direction as the $\mathbf{v}_c$ drift at the ionization point it might be pushed outside the last closed flux surface (LCFS). This phenomenon is illustrated in figure 5.7 for a typical TCV equilibrium (I_p and B have the same direction). This figure shows the trajectory of a co-passing particle generated in the high field side (HFS) of the tokamak. The particle follows the magnetic field lines, the blue arrows pointing downwards. The strong curvature drift, also pointing downwards, pushes the particle outside the LCFS at the position indicated in magenta. Similarly, the trajectory of a counter-passing particle generated in the low field side (LFS) is represented (dashed black line). The particle now streams in the opposite direction of the current/magnetic field and is once again expelled from the plasma volume by the $\mathbf{v}_c$ drift.

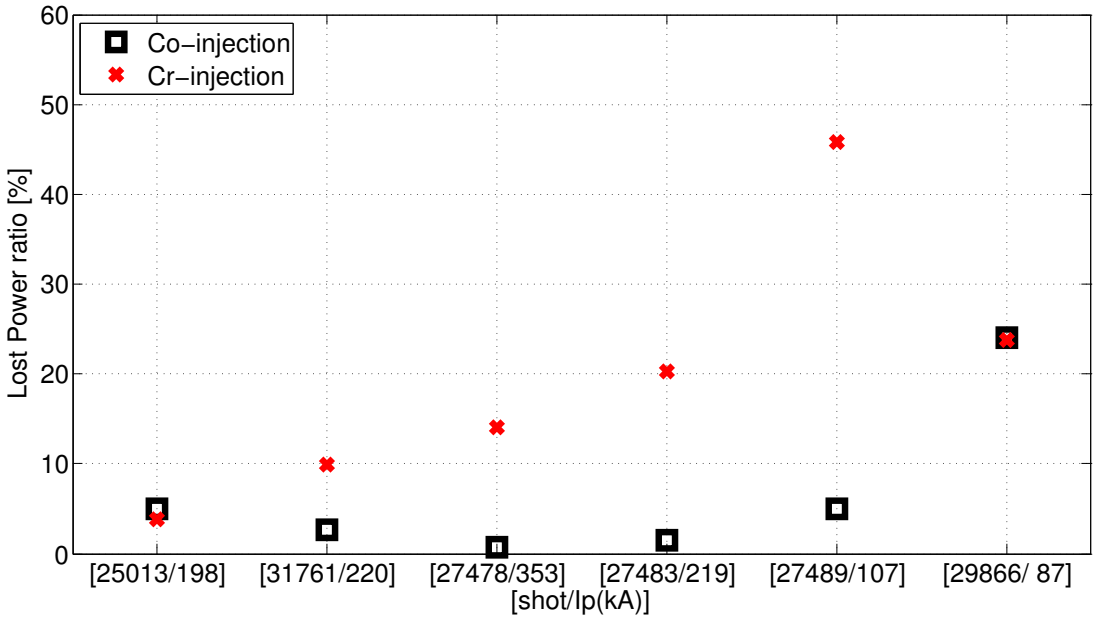

Figure 5.8: Beam fraction lost due to first orbit losses for the TCV plasma discharges analyzed in this chapter. Plasma current for each discharge is also indicated as well as the results for co- and counter-injection.

Two different choices can be made for tangential neutral beam injection.

Co-NBI. In this configuration, the neutral beam points in the same direction of the plasma current. Particles are mostly co-passing, generated in the low field side region and well confined in the plasma. Co-passing ions generated near the plasma edge of the HFS of the tokamak are lost but, usually, only a few are present. A small amount of trapped ions, confined in the LFS and generally lost in the HFS, are created with this configurations. No counter-passing particles are created with co-NBIs.

Counter-NBI. In the counter-NBI configuration, the NB system and the current are oriented in opposite directions. Most of the beam source produces counter-passing ions that are poorly confined in the LFS of the tokamak (where the beam is usually ionized). This is the reason why cntr-NBIs are not usually employed in experiments.

To study first orbit losses for the co- and cntr-NBIs proposed for TCV, we simulate the unperturbed motion of energetic ions for the plasma discharges of figure 5.3. We calculate the power lost due to particles exiting the plasma before completing a poloidal turn. The results are reported in figure 5.8. We see that the first orbit (or prompt) losses depend strongly on the plasma current as the radial size of particle orbits becomes larger with smaller I_p. As a consequence, losses are more important for low current (large q). The co-NBI, as expected, is

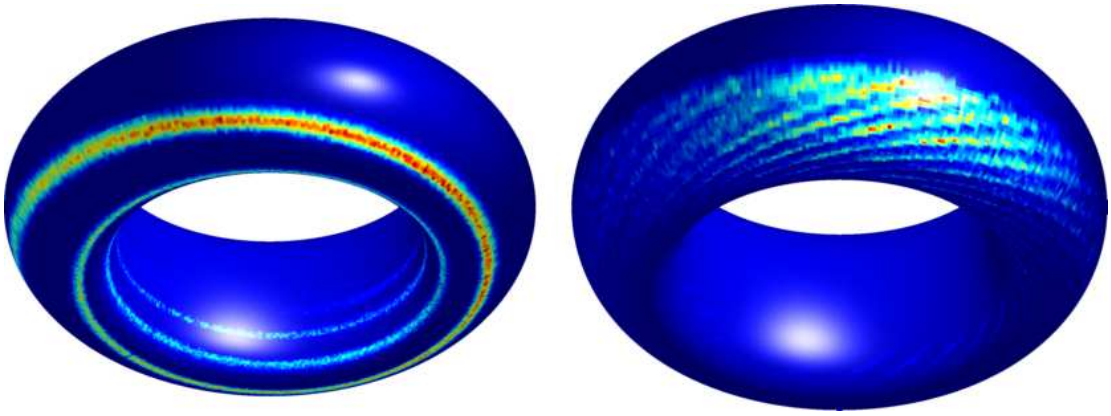

Figure 5.9: The locations of first orbit losses on the last closed flux surface for plasma discharges #27489 (counter-injection, left) and #31761 (co-injection, right). The color code is proportional to the loss power.

in general efficient. Only for the lowest-current plasma discharge #29866, can it result in important losses (about a quarter of the deposited energy). For routine operation, characterized by plasma currents above 100 kA, a consistent part of the injected particles are ionized and well confined in the plasma.

Results for the counter-NBI system are less optimistic. Losses well above 10% even at large plasma currents are obtained. For low plasma currents, $I_p < 200$ kA, half the beam power is lost. Plasma shape plays a role, too. For example, the counter-current losses of the large triangularity shot #29866 are much less than in other, more elongated plasmas (#27489, for instance). A similar case is plasma discharge #31761 which has more co-losses than the same-current, lower-elongation shot #27483.

Although large, the lost power due to first orbit losses would not represent a danger for the vacuum vessel. The heat accumulated by the tiles would be distributed over a wide region, in contrast to what was observed for the rather concentrated shine-through losses. This effect is shown in figure 5.9 with a sketch of the heat loss position on the last closed flux surface for two plasma discharges. Particles escape the plasma in the lower region of the tokamak over a large surface and acceptable values of $\mathrm{kW/m^2}$ are then predicted. We can conclude that first orbit losses do not pose a threat for the operation of the TCV tokamak using co-injection. However, the employment of two beams for rotation studies (balanced injection) would be functional only in a very limited range of plasma conditions. A summary of the results discussed so far is given in table 5.1.

5.2.4 Neutral beam slowing down

We now analyze plasma discharge #29866 in more detail. We employ the beam source term presented earlier and we perform a VENUS simulation with the inclusion of collisions. We evolve the phase space features of $\mathcal{N} = 3 \times 10^6$ numerical

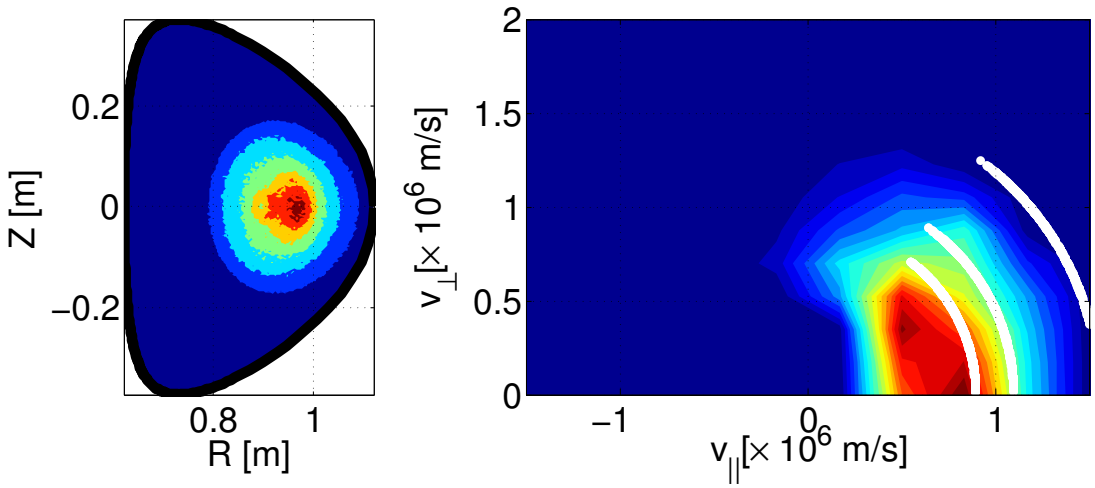

Figure 5.10: Neutral beam ion density as a function of minor radius (left panel) generated by the 1 MeV (700 kW in the plasma) neutral beam injector in plasma discharge #29866. On the right panel the real-space averaged velocity space distribution is illustrated. White lines represent the birth region of the injected particles.

markers for $t = 0.3$ s. The beam slowing down time is $\tau_{sd} \simeq 0.1$ s. The results in figure 5.10 describe the beam ion density profile obtained from the numerical simulations. We observed a rather peaked profile with the presence of an unusual central bump. This artifact is generated by truncation errors in the vicinity of the magnetic axis. The inclusion of collisions also enlarges the number of fast ions lost to the plasma boundary, with an increase of 5% with respect to the collisionless case.

The right panel of figure 5.10 represents the beam ion distribution function, averaged over real space. We observe the effect of particles slowing down from their birth region, represented with white in the figure, to thermal values. The strongly tangential injection is evident in the predominantly passing ion characteristics of the distribution. Therefore, a substantial neutral beam driven current

shot	$n_{e0}[\times 10^{19} m^{-3}]$	q_{min}	I_p [kA]	Shine-Through [%]	Prompt [%]	
					co-	cr-
29866	1.3	3	87	15	25	25
31761	2.8	1	220	3	3	10
25013	1.9	2	198	12	4	5
27478	3.5	1	353	2	1	14
27483	4.2	2	219	1	2	20
27489	4.5	2.5	107	< 1	5	46

Table 5.1: Plasma features of the TCV plasma discharges investigated in this chapter.

for this scenario is expected. The value of $I_{\rm nbi} \simeq 500$ kA is obtained from numerical simulations without electron screening [123]. This value represents a large overestimate and more detailed ASTRA simulations revealed that beam current between 150 kA and 80 kA can be driven [121]. Together with the large bootstrap fraction obtainable in the TCV tokamak [17], we envisage an additional source of non inductive current drive with the NBI system. The physics of advanced scenarios, strategically important for the development of steady-state tokamak reactors, could then be studied in more detailed.

5.3 Anomalous beam ion redistribution

The results presented so far shed light on the classical physics of beam ions in TCV. The limitations imposed by an excessive beam shine-through and first orbit losses were investigated. First simulations with the inclusion of Coulomb collisions were also performed. Along with classical effects, we now show that microturbulence is also important for NB transport in TCV.

5.3.1 GENE simulations

To perform VENUS simulations with the inclusion of anomalous effects, we first need to evaluate the particle diffusivity resulting from the presence of microturbulence. For this, the local flux-tube version of the GENE code is employed. This code provides an estimate for the particle diffusivity only in a narrow location

$$D_v(\rho_{\text{flux tube}}, \theta, \lambda = v_\parallel/v, E). \tag{5.3}$$

To cover the full radial domain of the TCV tokamak we employ two different techniques. At first, we assume particle diffusivity to be radially constant (superscript "c")

$$D_v^c(\rho, \theta, \lambda, E) = D_v(\rho = 0.5, \theta, \lambda, E). \tag{5.4}$$

The drawback of this choice is the inability to predict the different turbulent characteristics as we move to different radial regions. For example, the stabilization of trapped electron modes (TEMs) in the core, where trapping effects are negligible, can not be simulated. With a second method several flux tube simulations [124] at different radial (superscript "r") locations are performed to obtain

$$D_v^r(\rho, \theta, \lambda, E) = D_v(\rho_i, \theta, \lambda, E). \tag{5.5}$$

The index i represents the radial position of the flux tube simulation. Numerical interpolations could then be used to obtain the turbulent fields for regions radially located between different flux tube positions. This, as far as we know, has never been done before in any simulation.

Flux tube simulations can largely overestimate the particle transport and numerous linear runs, such as those presented in the next chapter for ITER, are required to assure that the turbulent background is reasonably described. To avoid performing an excessive number of gyrokinetic simulations we proceed as follows. We obtain a first estimate of the numerical diffusivity

$$D_v^j(\rho_t, \theta, \lambda, E), \tag{5.6}$$

where $j = [c, r]$ from equations (5.4) or (5.5). We can then scale the value of D_v to match a first guess of experimental values, usually obtained with transport codes for the Maxwellian background. Numerically, we impose the constrain

$$\left\langle D_v^j \right\rangle_{T_{bg}} = D_{\text{experimental}}, \tag{5.7}$$

where the brackets represent an average over a Maxwellian with a temperature T_{bg}, performed over the velocity space domain and the poloidal angle

$$\langle \chi \rangle_{T_{bg}} = \frac{\int \mathrm{d}\theta J(\theta) \int \mathrm{d}\mathbf{v} \left[\chi f_0(T_{bg})\right]}{\int \mathrm{d}\theta J(\theta) \int \mathrm{d}\mathbf{v} \left[f_0(T_{bg})\right]}. \tag{5.8}$$

The condition is matched at different radial locations to create a particle diffusivity consistent with experimental values.

To simulate the turbulent fields in the TCV tokamak we follow the analysis of Lapillonne and co-workers [125], who performed linear and nonlinear gyrokinetic simulations to characterize TCV turbulence. They focused in particular on the electron internal transport barrier (eITB) plasma discharge #29866, also analyzed with the VENUS code in the previous sections. We choose this plasma discharge since it was characterized by a rich spectrum of turbulent fields, created by the nonlinear evolution of trapped electron modes (TEMs) and ion temperature gradient (ITG) microinstabilities. These are the same fields that will characterize future burning plasma experiments.

Nonlinear GENE simulations are run in the local limit with the parameters of Ref. [125]. The box size is $(L_x, L_y) = (115, 78)$ in real space and $(L_{v_\parallel}, L_\mu) = (3\, v_{th_j}, 9\, T_j)$ in velocity space for the j-th species. The resolution is $N_{(x,k_y,z,v_\parallel,\mu)} = (128, 32, 16, 48, 16)$ for a total number of $1.50 \cdot 10^8$ grid points per species, which is a rather large number. The values of q_0 and magnetic shear are chosen from the magnetic reconstruction of the CHEASE code [88]. Plasma β_e is set to 10^{-4} as only electrostatic turbulence is expected. The electron population is characterized by density and temperature gradients $R_0/L_{n,e} = 3.73$ and $R_0/L_{T,e} = 14.79$. These parameters for the background deuterium are $R_0/L_{n,i} = 4.19$ and $R_0/L_{T,i} = 4.98$. A large electron temperature $T_e = 3.5\, T_i$, corresponding the the pre-NBI heating phase, is chosen. Beam ions are modelled with a strongly peaked distribution ($R_0/L_{T,nbi} = 0$, $R_0/L_{n,nbi} = 45$). This choice is consistent with the numerical framework described in chapter 3.

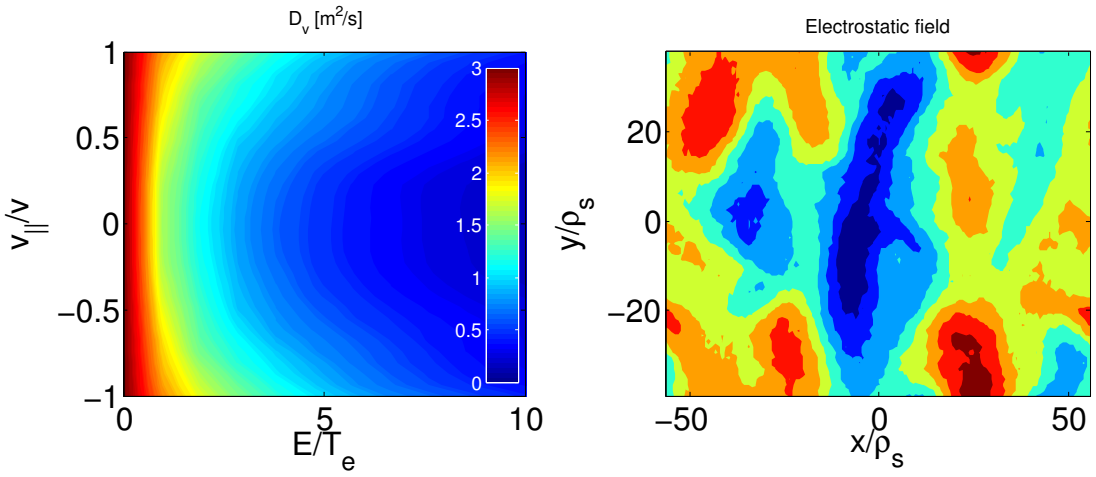

Figure 5.11: (Left panel) Beam ion diffusivity for plasma discharge #29866 as a function of the normalized particle energy and pitch angle. The results are shown at $\rho_t = 0.5$ and $\theta = 0$. (Right panel) Electrostatic turbulent field simulated by the GENE code at the same position.

The particle diffusivity obtained with the GENE code for this scenario is illustrated in figure 5.11, together with a snapshot of the turbulent fields. Results are consistent with what was observed in the previous chapter. Quite significant diffusivities are found for energies up to $5\,T_e$, above which orbit averaging effects become important, thus reducing the particle transport to "classical" levels. Small transport is found for low values of the parallel velocity, which corresponds to large Larmor radii suppressing the turbulent fields experienced by the particle. The low-$v_\parallel$ velocity space region, however, is not accessible to the vast majority of neutral beam ions.

The results shown in figure 5.11 correspond to the outcome of a single flux tube simulation. The findings are extended with 9 other flux tube simulations to cover the full radial extent of the TCV tokamak. The reconstructed particle diffusivity D_v^r in real space, for different energies, is represented in figure 5.12. Some important conclusions can be inferred from this figure, which depicts the diffusivity D_v^r experienced at different positions by a particle characterized by $\lambda \simeq 1$. Particle diffusivity clearly lowers as the energy of the particle is increased (the color code is the same in the three panels). Furthermore, turbulent fields develop in the low field side of the tokamak, where the combination of pressure gradients and curvature drift favors microinstabilites. We also observe that towards the magnetic axis only strongly localized modes at $\theta \simeq 0$ are present. A probable explanation is the suppression near the magnetic axis of trapped electron modes, a microinstability that usually exhibits long structures in the poloidal plane. This stabilization is not captured by the variable D_v^c of equation (5.4), not plotted here. Not much quantitative differences, however, will be found in the next section where

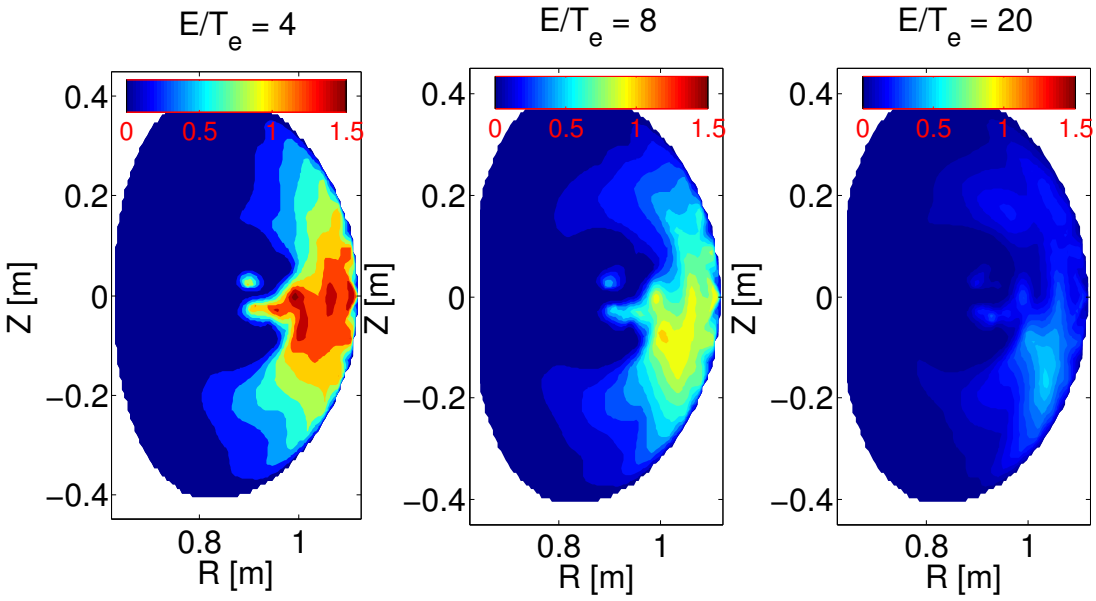

Figure 5.12: Particle diffusivity D_v^r of a strongly passing beam ion ($\lambda \simeq 1$) as a function of the particle position. The results, obtained with the GENE code, are shown for three different energies to appreciate the transport suppression.

the two methods will be directly compared.

5.3.2 Simulations of plasma discharge #29866

We now have all the ingredients needed to perform a full numerical investigation of plasma discharge #29866 using the VENUS code. Three simulations are carried out, one assuming no anomalous effects, and two with the inclusion of D_v^c and D_v^r (equations (5.4) and (5.5), respectively). A sufficiently large number of markers, 3×10^5 is chosen. Their time evolution is tracked for 0.3 seconds, about three times the particle slowing down time. The results of the simulations are shown in figure 5.13. Strong fast ion redistribution and losses are expected for this scenario. For example, we observe a sharp decrease of the fast ion density in the core and important beam power losses. In the same figure the large amount of particle losses is also shown. The reason for such a strong effect is the large electron temperature, leading to a small E_{nbi}/T_e ratio. In addition, small plasma collisionality leads to slow thermalization for fast ions, which can then experience diffusive phenomena for longer times.

The fast ion pressure profile is also studied and strong redistribution observed (figure 5.14). The presence of microturbulent fields has a similar detrimental effect on the stored fast ion stored energy. While in the collisional case we observe heat losses of 33%, this amount is doubled with anomalous effects (more than 60%). The efficiency of the NBI technique for plasma heating is then compromised in

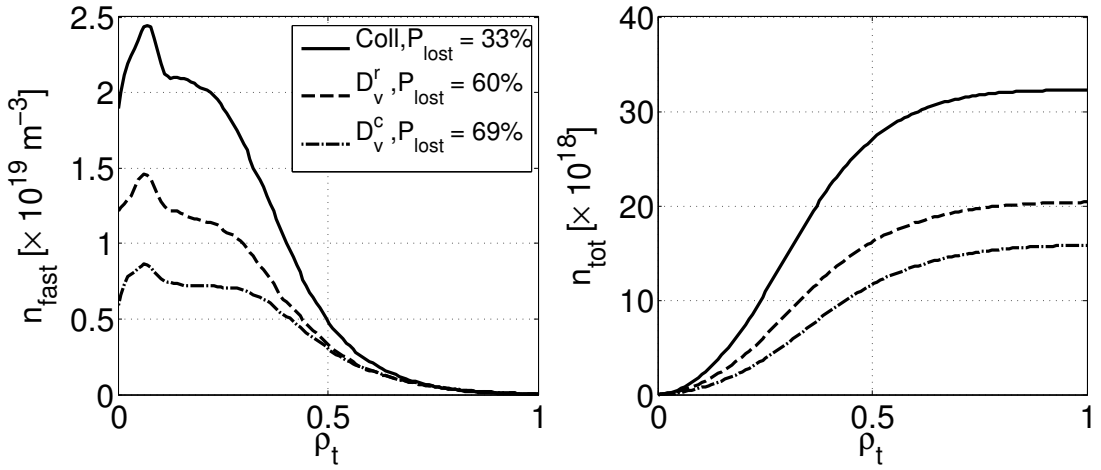

Figure 5.13: Beam ion redistribution for plasma discharge #29866. In the left panel the fast ion profile is illustrated when no anomalous transport is considered (solid line). The effect of two different anomalous diffusivities, D_v^r (equation (5.5)) and D_v^c (equation (5.4)), is shown (dashed and dashed-dotted line, respectively). The heat power lost is also indicated in the legend box. The total number of particles enclosed in the flux surface ρ_t is shown in the right panel.

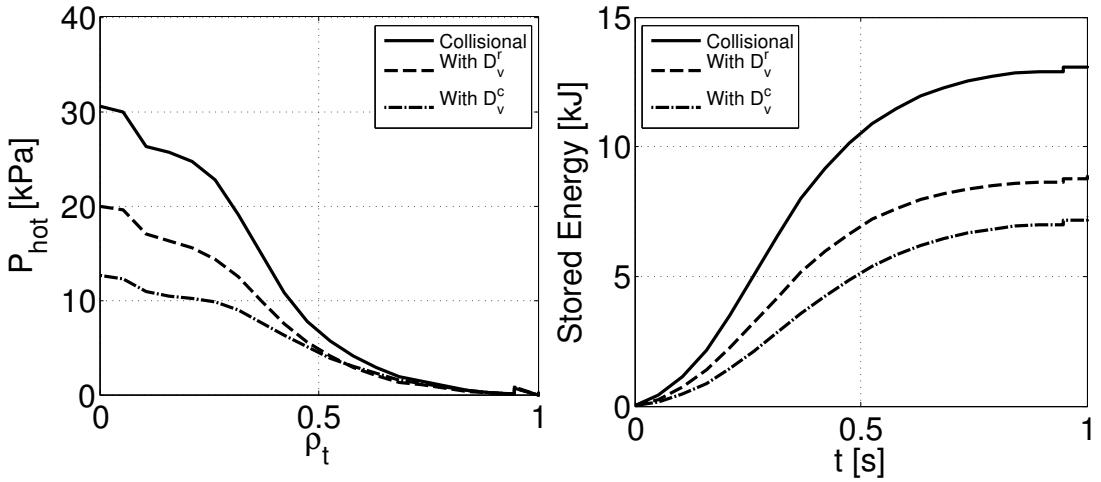

Figure 5.14: Fast ion pressure as a function of minor radius (left, plasma discharge #29866). Three simulated fast ion profiles are shown, one obtained in the absence of turbulence (solid line) and two with the employment of two different anomalous diffusivities, D_v^r and D_v^c, is shown (dashed and dashed-dotted line, respectively). The total fast ion energy as a function of minor radius is shown in the right panel.

such scenarios.

The simulations in figure 5.13 are performed with the inclusion of the two

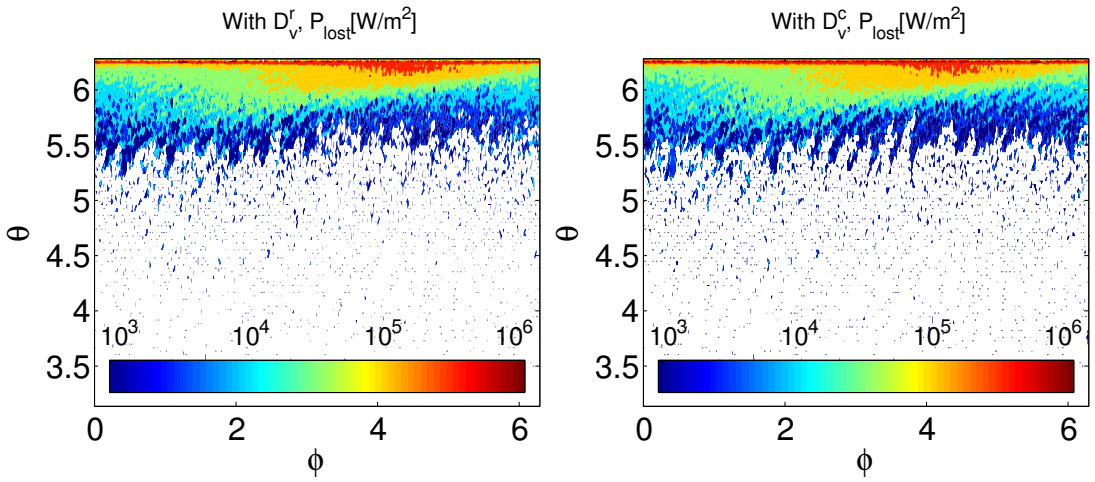

Figure 5.15: Heat power loss as a function of the position over a flux surface with the employment of the anomalous diffusivity D_v^r (left) and D_v^c (right). Results are shown for plasma discharge #29866.

anomalous diffusivities D_v^r and D_v^c. Despite the different reasoning leading to their definition, results are qualitatively similar. For example, both techniques predict a strong impact of turbulence on the transport of beam ions. Furthermore, LCFS particle losses are similar in magnitude and in their poloidal localization, as it is evident from figure 5.15. Here, heat losses are shown to be concentrated close to the outboard mid-plane. Here, the distance between passing ions and the last closed flux surface is the smallest. The observed peak power density of 7 MW/m^2 approaches the upper limit of the carbon tiles for the length of a pulse (a couple of seconds). Only with the modulation of the beam source, or with the strengthening of the low field side plasma facing elements of the vessel, could operation in such scenarios be performed with the NBI.

5.3.3 Simulations of high and low temperature TCV plasmas

The results presented in the previous section focused on a very specific plasma scenario. With only 87 kA of plasma current the reverse shear discharge was particularly affected by turbulent redistribution, given a long particle slowing down time and a low ratio $E_{nbi}/T_e < 8$. Large particle losses, however, were observed even in the absence of turbulent transport. We now focus on a wider range of discharges, spanning several values of plasma temperature and density.

Let us consider TCV plasma discharges #31761 and #25013. The former is an L-mode plasma discharge with low temperature ($T_e < 2$ keV), intermediate density ($n_e \simeq 3 \times 10^{19}$ m^{-3}) and large elongation. The latter represents an H-mode scenario with large temperature ($T_e > 10$ keV) and density ($n_e \simeq 4 \times 10^{19}$ m^{-3}).

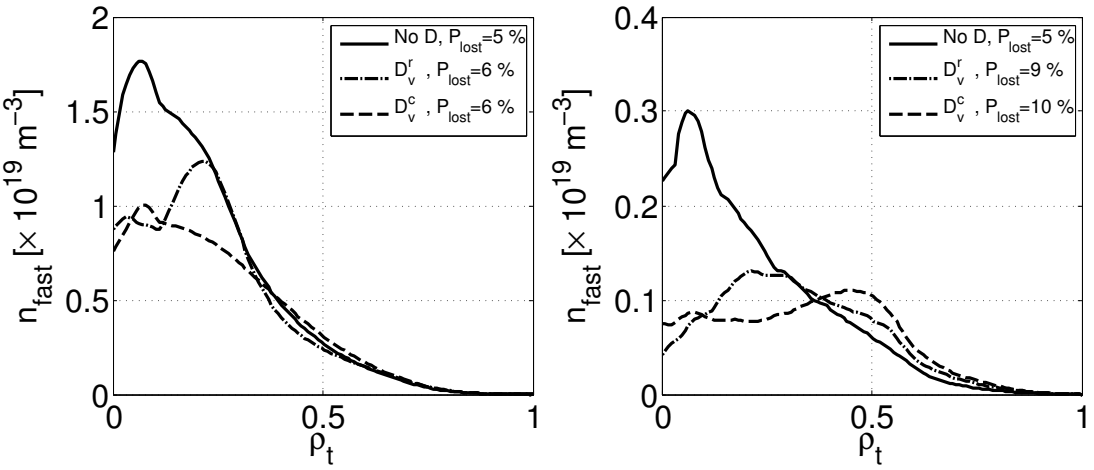

Figure 5.16: Fast ion density for plasma discharge #31761 (left panel) and #25013 (right panel). Results without the inclusion of anomalous transport are shown with a solid line. The profile obtained with the inclusion of the anomalous diffusion coefficients D_v^c and D_v^r are shown with dashed-dotted and dashed lines, respectively. The ratio between lost power and injected power is represented in the legend.

Both discharges are characterized by similar plasma currents, 220 kA and 190 kA, respectively. These scenarios are routinely created in TCV, which makes them particularly interesting cases for our study. We employ the same turbulent diffusivity simulated for plasma discharge #29866, which can be considered as a reference case, to ease the computation requirements. Although the ITG/TEM mixture is expected to change from case to case, the particle diffusivity exhibited the universal features described in chapter 3. Qualitative conclusions can be then drawn using the anomalous diffusivity D_v^j obtained in the previous section.

Three numerical simulation, for each plasma discharge, are performed with the VENUS code. Two simulations include anomalous effects in the form of the diffusion coefficients D_v^r and D_v^c. A third simulation is performed with only collisions. The results, illustrated in figure 5.16, highlight the different behaviour of the two discharges. In the left panel of the figure, the results for the L-mode plasma discharge #31761 clearly show a smaller redistribution than for the previously simulated shot #29866. The collisional losses for shot #31761, established at 4% of the injected power, are only slightly enhanced to 5-6%. The main reason for such a small increase is the rather large ratio $E_{\rm nbi}/T_e > 15$. Large anomalous effects, on the other hand, are found for plasma discharge #25013 (right panel of figure 5.16), characterized by $E_{\rm nbi}/T_e = 2$. Strong particle redistribution as well as non negligible heat losses are observed. The power lost without microturbulence, 5%, is almost doubled with anomalous transport. Notable effects are also found for the power deposition profile which, as we can see in figure 5.17, is strongly redistributed. Small consequences, on the other hand, are envisaged for plasma

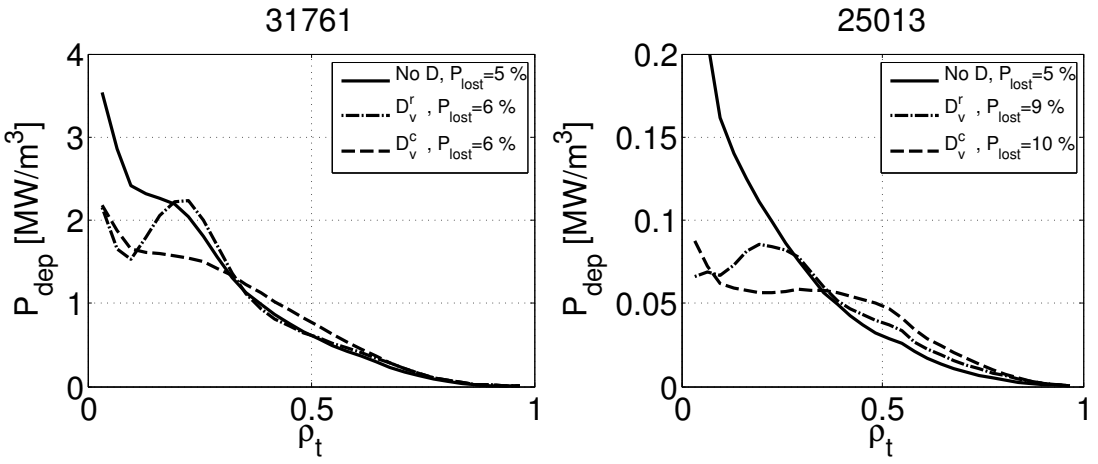

Figure 5.17: Power deposition for plasma discharge #31761 (left panel) and #25013 (right panel). Results without the inclusion of anomalous transport are shown with a solid line. The profile obtained with the inclusion of the anomalous diffusion coefficients D_v^c and D_v^r are shown with dashed-dotted and dashed lines, respectively. The ratio between lost power and injected power is represented in the legend.

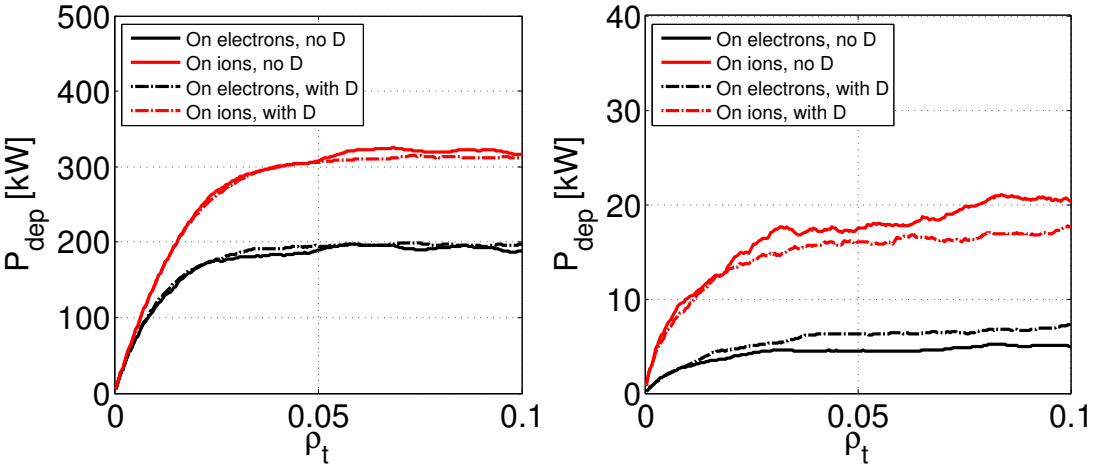

Figure 5.18: Beam power deposition for plasma discharges #31761 and #29866 (left and right panels, respectively). The simulations are performed with the VENUS code with and without the inclusion of anomalous diffusion (solid and dashed lines). The power given to ions and electrons is shown in red and black.

discharge #31761.

Power deposition as a function of time is shown in figure 5.18. Plasma heating is not modified in plasma discharge #31761 with the introduction of microturbulent fields. Electrons and ions would still receive the same amount of power from

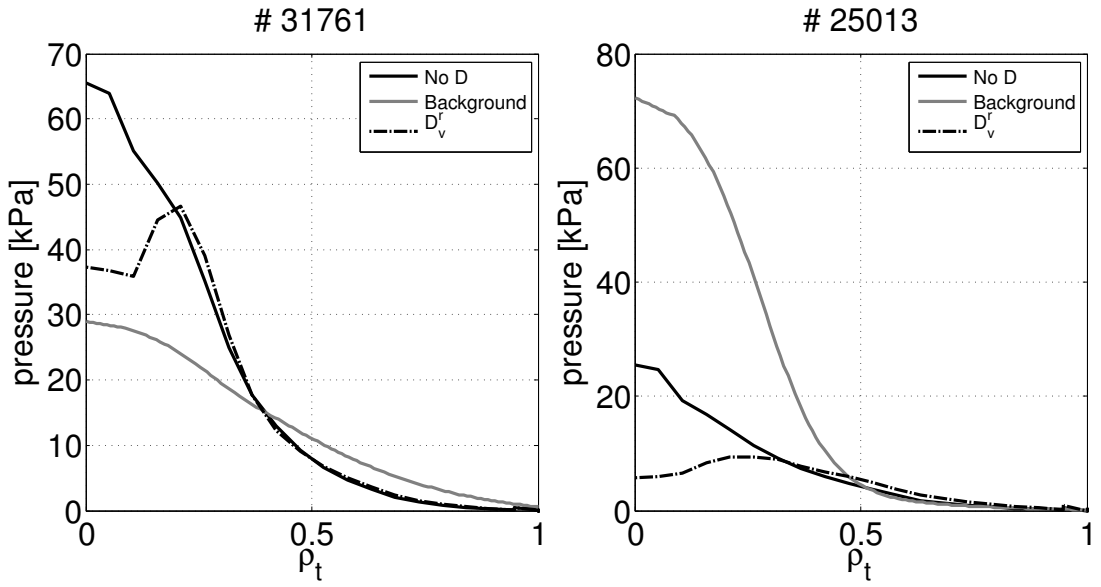

Figure 5.19: Fast ion pressure calculated by the VENUS code for plasma discharges #31761 (left panel) and #25013 (right panel). Results are shown with (dashed line) and without (solid line) the inclusion of anomalous transport. The background plasma pressure is shown in grey.

the neutral beam, consistently with what observed in figure 5.17. In a similar way, the overall power transferred to the bulk plasma would almost be unchanged by microturbulence for plasma discharge #25013. However, more energy is transferred to the electrons than to the ions. This is a consequence of moving energetic ions to colder plasma regions towards the edge. Here, they interact more with electrons since their critical energy lowers (the lower $E_c \propto T_e$, the larger is the energy given to electrons). A final remark can be made on the the total power given by the beam to the bulk plasma in the two discharges, which changes by an order of magnitude. This is a consequence of the the large electron temperature of plasma discharge #25013, which is close to the beam injection energy (E_{nbi}/T_e).

Fast ion pressure. The neutral beam system in TCV would create important fast ion pressures given the large power and the relatively small size of the tokamak. The redistribution of the pressure profile for plasma discharges #31761 and #25013 is shown in figure 5.19. More important modifications are again found for the latter discharge. The parallel to perpendicular fast ion pressure also changes from a collisional to a turbulent case (figure 5.20) given the different effect of turbulence on different classes of particles. Both the pressure content of the fast ion distribution and the corresponding $p_{\parallel}/p_{\perp}$ profiles contribute to the establishment of the background equilibrium [102]. The inclusion of these higher order corrections to the background equilibrium, neglected in this work, is envisaged and recent numerical platforms can be exploited for this purpose [126].

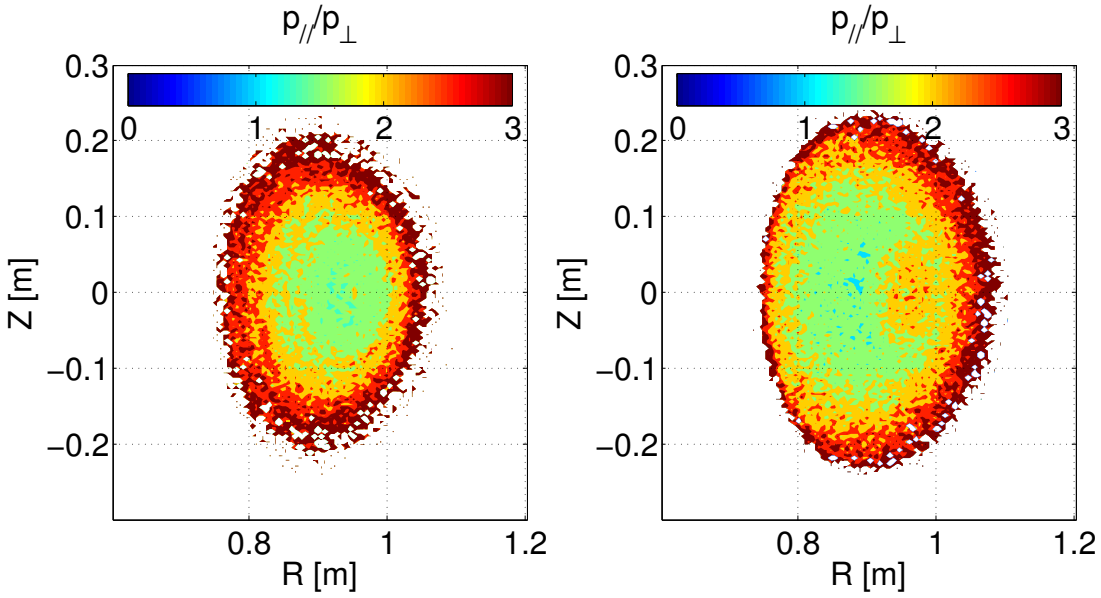

Figure 5.20: Ratio of parallel to perpendicular pressure for plasma discharge #25013 with only collisional effects and with the inclusion of anomalous transport (left and right panel, respectively).

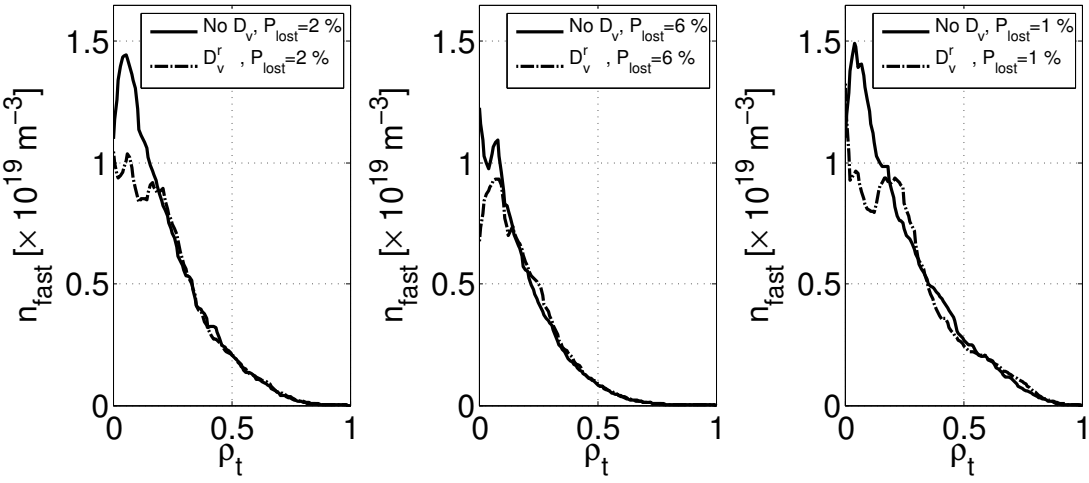

Figure 5.21: Fast ion density for plasma discharges (left to right) #27489, #27483 and #27478. Results are shown with and without the inclusion of anomalous transport (dashed-dotted and dashed line, respectively). The power loss at the LCFS, normalized to the injected power, is also shown in the legend.

5.3.4 Fast ion anomalous transport in low temperature discharges

The investigation can now be completed with three other plasma discharges from our database: #27489, #27483 and #27478, all characterized by intermediate to large plasma densities and low temperatures. We perform two different simulations with $3{\cdot}10^5$ numerical markers for each plasma discharge. The first simulation is performed without the presence of anomalous transport. A second simulation is then run with the anomalous diffusivity D_v^r defined in equation (5.5). The results of figure 5.21 show that small microturbulent transport is generated due the relatively small temperatures of these discharges, $T_e \simeq 1$ keV. Only in the plasma core some redistribution of the strongly peaked fast ion profile is observed.

To demonstrate that no consequences on the heat deposition are expected, we further investigate plasma discharge #27489 (figure 5.22). Negligible modifications to the power deposition profile are expected. Furthermore, the total power transferred from the beam ions to the background electrons and ions is preserved when anomalous transport is included. The results further validate the observation that the heating of TCV plasmas would be only slightly affected by microturbulence for electron temperatures in the order of the keV.

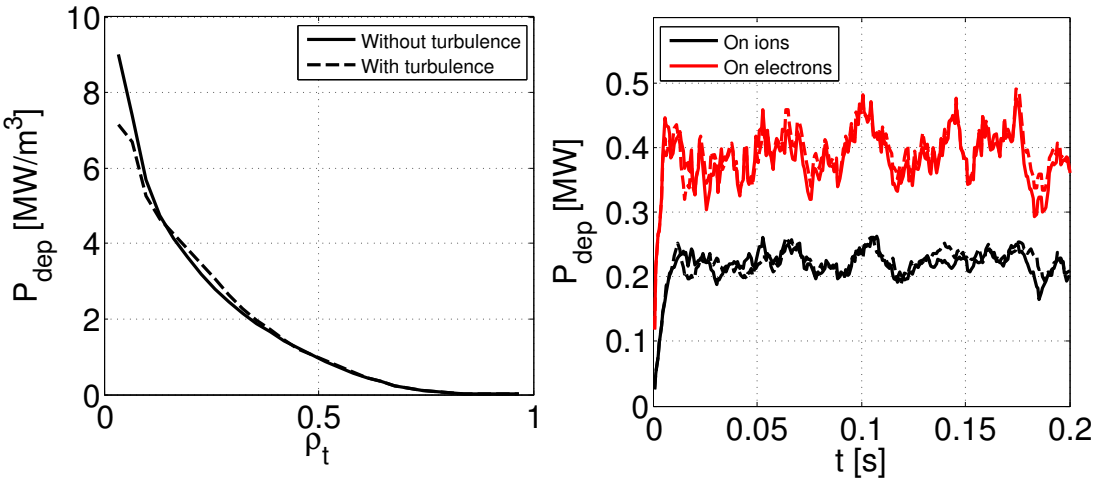

Figure 5.22: Fast ion heat deposition as a function of minor radius (left panel) and time (right panel) for plasma discharge #27489. Simulations are performed with and without the inclusion of microturbulent fields (dashed and sold line, respectively). In the right panel heat deposition on ions (red) and electrons (black) is shown separately .

shot	T_{e0} [keV]	P_{lost} [%]	Δ	n_{nbi} redistribution	P_{dep} red./losses
29866	2.5	30	0.5	strong	strong
25013	12	4	0.7	medium	medium
31761	2.0	1	0.3	small	small
27483	<1.0	0.1	<0.1	negligible	negligible
27478	<1.0	0.1	<0.1	negligible	negligible
27489	<1.0	0.1	<0.1	negligible	negligible

Table 5.2: Main features of the plasma discharges investigated in this chapter, together with the conclusion of the anomalous transport analysis. The power lost indicated in the table is only due to the presence of microturbulent fields (collisional losses are subtracted).

5.3.5 Comments on the neutral beam heating system in TCV

The results presented throughout this chapter can be interpreted in two different ways. We could conclude that anomalous beam ion redistribution affects the heating properties of the neutral beam upgrade. However, anomalous heat losses were in general below 10%. The $T_e/T_i = 1$ target, which is the original purpose of the NB system, is well within reach. Furthermore, such losses can also be handled by the plasma wall quite effectively. If needed, some tiles can be reinforced. Under such conditions, obtained in 5 discharges out of the 6 studied in this chapter, the installation of the co-NBI in TCV would be a success (see table 5.2). From

table 5.2 we can also observe how the parameter Δ can be used to evaluate the possibility of having fast ion redistribution.

Physics research in the anomalous energetic ion transport further motivates the installation of a neutral beam system in TCV. The experimental evidence of anomalous fast ion transport was demonstrated on two tokamaks: ASDEX in 2007 [61] and DIII-D in 2009 [79]. Further investigations in the simple magnetized toroidal device TORPEX are being performed [86, 127], with promising results. The absence of supportive analysis on other machines is mostly due to the difficulties in the fast ion measurements and diagnostics. For this reason, feasibility studies on the creation of a fast ion D_α diagnostic (FIDA [80]) in TCV are being performed. Together with the possibility of "tuning" the fast ion-turbulent interaction by changing the electron temperature (with the ECE heating), TCV represents an exceptional device where the turbulent fast ion transport can be studied.

5.4 Conclusions

In this chapter we presented the fast ion physics associated with the neutral beam system envisaged for the Tokamak à Configuration Variable (TCV). Studying the effect of plasma shaping on particle confinement, transport and stability in the $T_e = T_i$ regime motivates such an upgrade. We showed throughout this chapter that anomalous transport phenomena could be important depending on the background plasma temperature. The effect of turbulence can then be regulated with plasma heating and studied experimentally, which gives a further motivation for the NBI installation.

The main features of the plasma device were presented in section 5.2. The possibility of spanning several values of plasma density, temperature, current and shape was illustrated. The current design for a neutral beam system in the TCV tokamak proposes the installation of two 1 MW injectors. We first showed that excessive shine-through could affect some low density plasmas. Given reasonable plasma densities, however, very good beam deposition was observed. Strong first orbit losses, however, would affect the choice of a counter-current injector. More than 10% of the injected power would be routinely lost, even at large plasma current, for a counter-current neutral beam.

The impact of anomalous redistribution was studied in section 5.3. The background fields were first characterized with the GENE code. We considered a scenario where microturbulence is generated by the nonlinear saturation of ion temperature gradient and trapped electron modes. The variables defined in chapter 3 were then employed. The anomalous particle diffusivity, defined as a function of velocity, was found and employed in the VENUS code to assess anomalous redistribution. Depending on the slowing down time, plasma temperature and density, various responses to anomalous transport were found. For example, large beam ion redistribution was observed for the plasma discharge #25013 while only minor consequences, both in terms of density profile and power deposition, affected beam injection in shot #27489. Small energy losses were found, generally below 10%, apart from the case of plasma discharge #29866 where 60% losses were found. The electron temperature was found to be the key parameter influencing the fast ion-microturbulence interaction. The flexibility in varying T_e, with the TCV gyrotron heating system, would result in versatility for fast ion studies.

We can conclude that anomalous transport would not compromise TCV operation, except for some known cases where particular attention should be paid. In fact, the installation of the planned NBI in TCV would provide a tool for (anomalous) fast ion studies, of interest for future devices.

Chapter 6

Turbulent transport of fast ions in ITER and DEMO burning plasmas

The turbulent redistribution of energetic ions in ITER and DEMO is presented in this chapter. The efficient heating of the background plasma with fast ion thermalization is a fundamental requirement to achieve optimal fusion reactions in future devices. Furthermore, a substantial component of non inductive current must be driven by beam ions in next step fusion devices. Anomalous energetic ion transport could reduce the neutral beam driven current drive and therefore compromise the production of hybrid and advanced scenarios in ITER and DEMO.

The steady state scenario in ITER is illustrated in section 6.1. We highlight in particular the need for a significant amount of neutral beam driven current, with a profile tailored to achieve an optimal q profile for long pulse operation. Beam ion redistribution is studied in sections 6.2 and 6.3. The background turbulence is reproduced with the GENE code in the section 6.2 while in 6.3 the impact on the beam driven current is assessed with the VENUS code. The beam ion turbulent transport is found to be small in ITER, due to the large injection energy ($E_{\rm nbi}/T_e > 30$). Alpha particle transport is also negligible and no significant anomalous effects on steady state operation are therefore envisaged. The predictions for DEMO, the first demonstration nuclear power plant, are discussed in section 6.4. It is shown that anomalies can appear for such high temperature plasmas due to the longer fast ion slowing down time and the intermediate $E_{\rm nbi}/T_e$ ratio ($E_{\rm nbi}/T_e \simeq 20$).

6.1 ITER steady-state scenario

ITER is a large sized tokamak currently designed to prove the feasibility of nuclear fusion as a reliable source of energy. It is the first tokamak designed and constructed to produce more fusion energy than that required to initiate nuclear reactions. During the flat top of the standard scenario inductive operation a fusion gain $Q = 10$,

$$Q = \frac{\text{Fusion Power}}{\text{Injected Power}}, \tag{6.1}$$

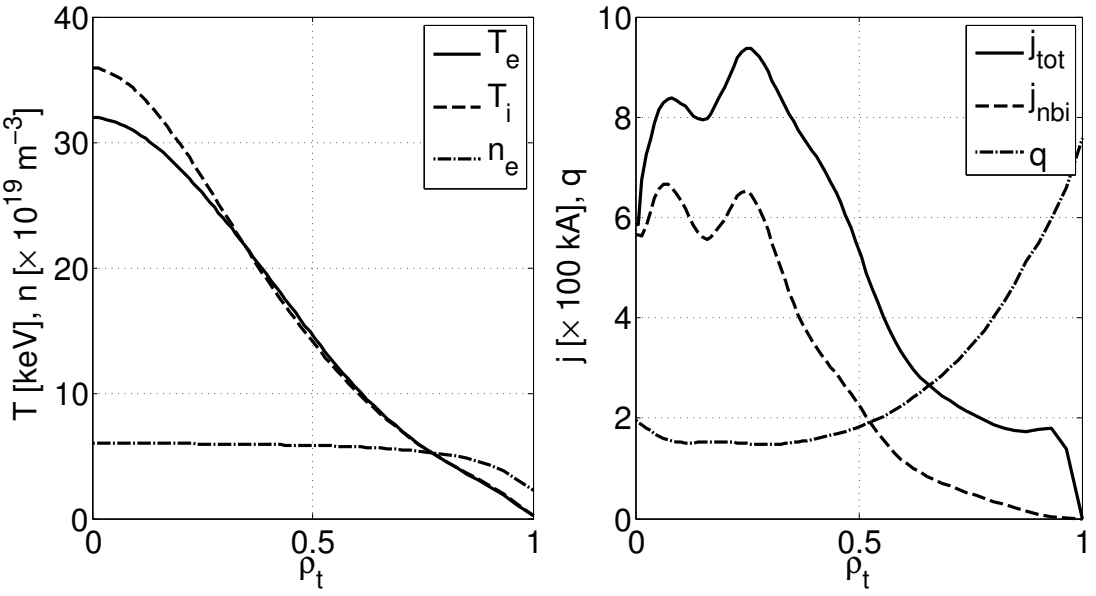

Figure 6.1: Density and temperature profiles of the background species of an ITER steady state scenario (left panel). Total current density profile and beam driven fraction as a function of the normalized toroidal flux (right panel). Also shown is the resulting safety factor profile as computed by the CHEASE code [88].

is envisaged. The duration of the ohmic phase, however, is limited by the transformer and such high Q can only be obtained with pulsed operation.

Steady state represents an important mode of operation of the ITER tokamak where longer pulses can be created by replacing the Ohmic fraction of the plasma current with non inductive methods. A fusion gain $Q = 5$ is potentially achievable with external heating and, only in part, with alpha particle thermalization. A fundamental requirement for steady state operation is the accurate control of the current profile to create MHD stable plasmas. The expected temperature and density profiles, as well as the safety factor and magnetic shear, are shown in figure 6.1 where we can see that a large fraction of the plasma current is provided by the neutral beam system. The NBI system, designed to inject > 30 MW of 1 MeV deuterium beams, is also a significant source of plasma heating.

The turbulent transport could affect ITER operation, as it was also found in section 5.3 for the NBI injected ions in the Tokamak à Configuration Variable. Small to medium turbulent fast ion transport is expected if we consider the parameter Δ defined in chapter 3. For ITER's parameters, we obtain $\Delta = 0.3$, a value which might indicate a small effect for the fast ion density. However, even small beam ion redistribution can be detrimental. For example, the flat safety factor profile (for $\rho_t < 0.5$) envisaged for stability considerations [26] can be modified by the loss of beam driven current. Modifications could lead to unwanted

MHD activity (sawteeth, NTMs, infernal modes) and possibly disruptions.

6.1.1 Preliminary GENE simulations

Preliminary GENE simulations are performed to investigate the fast ion diffusivity and to clarify the importance of detailed gyrokinetic simulations of the background fields. The nonlinear runs are carried out with a real space resolution of $(n_x, n_{k_y}, n_z) = (128, 22, 48)$ points, for a radial extension of $L_x = 150\rho_s$ and a maximum resolved wave number of $k_\perp \rho_s = \sqrt{g^{yy}} k_y \rho_s = 1.55$, where $c_s = \sqrt{T_e/m_i}$ and $\rho_s = c_s/(q_i B/m_i)$. The flux tube simulation parameters are calculated at $\rho_t = 0.5$ with parameters dictated by the profiles of figure 6.1. We assume electrons and ions to have similar temperatures and densities, i.e. $T_e = T_i$, $n_e = n_i$. The effect of the magnetic geometry is accounted for by the GENE-CHEASE interface described in ref. [128]. The local values of the safety factor and the magnetic shear are $q_0 = 1.55$ and $\hat{s} = (\rho/q)dq/d\rho = 0.4$, respectively. A pessimistic value of $\beta_e = 2\mu_0 p_{e_0}/B^2_{\text{axis}} = 0.6\%$ is employed to avoid the influence of kinetic ballooning modes (KBM) [91]. The logarithmic gradients for electrons and ions are $\Omega_{n_{i,e}} = 0.3$, $\Omega_{T_i} = 6.4$ and $\Omega_{T_e} = 0$, where

$$\Omega_\chi = \frac{R_0}{L_\chi} = \frac{R_0}{a}\frac{\mathrm{d}\ln\chi}{\mathrm{d}\rho_t}. \tag{6.2}$$

Here, R_0 and a are the major and the minor radii of the tokamak, respectively. The choice of a flat electron temperature profile restricts our analysis to ion temperature gradient (ITG) modes only.

The transport of two suprathermal populations, representative of beam ions and alpha particles, is studied. Given the low concentration of these energetic populations, of the order of 1% [29, 129], they are considered in the passive tracer limit. The formalism introduced in 3.1 is used, in particular to identify the kinetic diffusivity of equation (3.35). A strong density gradient is then chosen for both species: $R_0/L_n = 15$. Large temperatures $T = 30\,T_e$ are employed to investigate a sufficiently broad region of velocity space.

The analysis of the linear phase of the background microinstability reveals, as expected, a dominant ITG mode peaking at $k_\perp \rho_s = 0.35$, where $\gamma = 0.2 c_s/R_0$. During the saturated phase of the simulation, the maximum amplitude of the electrostatic field is found at $k_\perp \rho_s = 0.21$. A larger scale length, together with a lower intensity, characterizes $\delta A_\parallel$, which peaks at $k_\perp \rho_s \simeq 0.1$. The different length scales of the two perturbations can be observed in the illustration of figure 6.2.

The velocity space transport is quantified by the kinetic diffusivity D_v given in (3.22)

$$D_v = -\frac{\delta f_1}{\nabla f_0}\delta u. \tag{6.3}$$

Finite values of β_e, such as those studied here, generate non negligible magnetic perturbations. As a consequence, two components of the particle diffusivity can

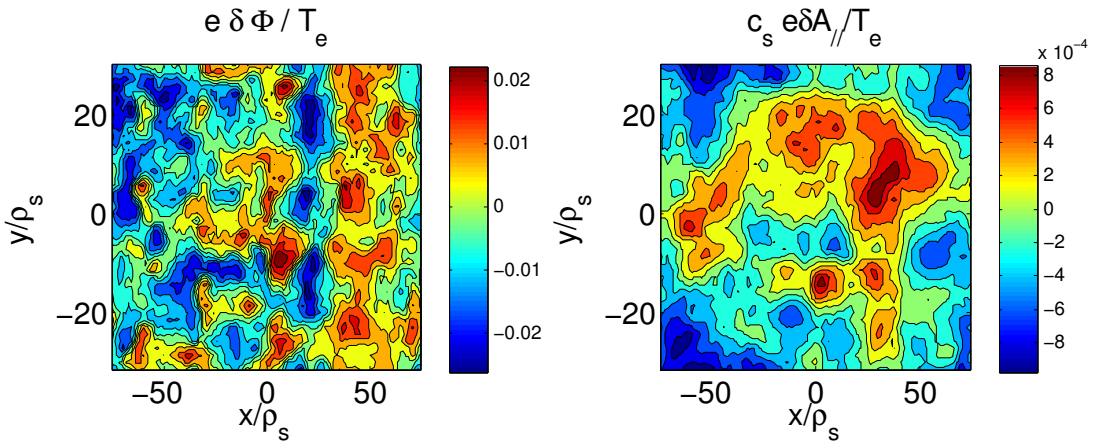

Figure 6.2: Snapshot of the perturbed electrostatic (left) and magnetic (right) potential in the ITER steady state scenario.

be identified. The first, already discussed and employed in the analysis of TCV in the previous chapter, is

$$D_v^{\mathrm{es}} = -\frac{\delta f_1}{\nabla f_0}\delta u_{E\times B}, \tag{6.4}$$

$$\delta u_{E\times B} = -\frac{\boldsymbol{\nabla}\delta\bar{\Phi}\times\mathbf{B}}{B^2}\cdot\mathbf{e}_r. \tag{6.5}$$

Gyroaveraged quantities are indicated with an overbar. Here, we make use of the $\mathbf{E}\times\mathbf{B}$ drift in equation (3.22) and for this reason we shall refer to this as the "electrostatic" component of the particle diffusivity. The second component is called "magnetic"

$$D_v^{\mathrm{m}} = -\frac{\delta f_1}{\nabla f_0}\delta u_{A_\parallel}, \tag{6.6}$$

$$\delta u_{A_\parallel} = -v_\parallel\frac{\boldsymbol{\nabla}\delta\bar{A}_\parallel\times\mathbf{B}}{B^2}\cdot\mathbf{e}_r. \tag{6.7}$$

For large plasma β_e, this component of the particle diffusivity can become important [73]. In the forthcoming discussion, the relative importance of the electrostatic and magnetic particle diffusivities is considered. Absolute units will be shown to allow for a comparison with collisional values, not expected to be larger than $D_{\mathrm{coll}} \simeq 0.1\ \mathrm{m}^2\cdot\mathrm{s}^{-1}$ in ITER [130].

6.1.2 Electrostatic fast ion transport

Using the nonlinear simulation performed in the previous section we can obtain the velocity space dependent diffusivity $D_v^{\mathrm{es}}(\mathbf{v})$. The results for deuterium ions are shown in figure 6.3. This figure is obtained by slicing the radial electrostatic diffu-

sivity $D_v^{\rm es}(v_\parallel, v_\perp)$ at different energies, while keeping the ratio $\mu B_{\rm axis}/E$ constant. We choose the value of $\mu B_{\rm axis}/E = 0.8$ for trapped particles and $\mu B_{\rm axis}/E = 0.4$ for passing particles. The trapped/passing boundary is found at $\mu B_{\rm axis}/E \simeq 0.75$. As we can see from the curves shown in the figure, the transport of energetic ions is strongly larger than neoclassical expectations. Good agreement with the theoretical scalings presented in the previous section is also found: $D_v^{\rm es} \simeq (E/T_e)^{-1}$ and $D_v^{\rm es} \simeq (E/T_e)^{-3/2}$ for passing and trapped ions, respectively. It is evident from the figure that the particles in the lower energy range interact significantly with the turbulent fields and that the energy decay appears only in the high energy limit. Both classes of particles therefore experience radial diffusivities larger than collisional estimates for energies up to 1 MeV. This result suggests that turbulent transport might lead to anomalous beam ion redistribution and further analyses are performed in the next section to verify the observations.

The results for alpha particles are similar to those obtained for deuterium ions. The curves in figure 6.4 clearly show that enhanced diffusivities can be found over a very large energy range (up to $E = 3$ MeV) for both passing and trapped particles. The shape in the diffusivity of alpha particles also resembles that of deuterium ions (figure 6.3), with a shift towards higher energies due to a heavier mass. As a consequence, the resonance described in section 3.2 also moves towards higher energies.

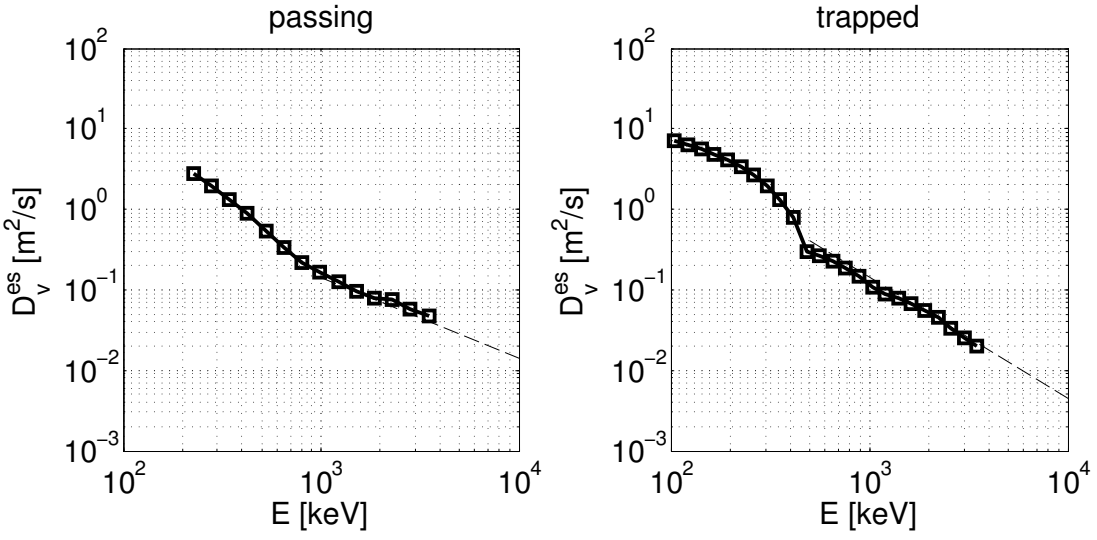

Figure 6.3: Neutral beam ion transport: electrostatic particle diffusivity of high energy deuterium in the simulated ITER steady state scenario, as a function on energy. The numerical results for passing ions ($\mu B_{\rm axis}/E = 0.4$, left panel) and trapped ions ($\mu B_{\rm axis}/E = 0.8$, right panel) are plotted together with the scalings predicted by [73] (dashed lines). These are, namely, $D_v^{\rm es} \simeq E^{-1}$ for passing particles and $D_v^{\rm es} \simeq E^{-3/2}$ for trapped particles.

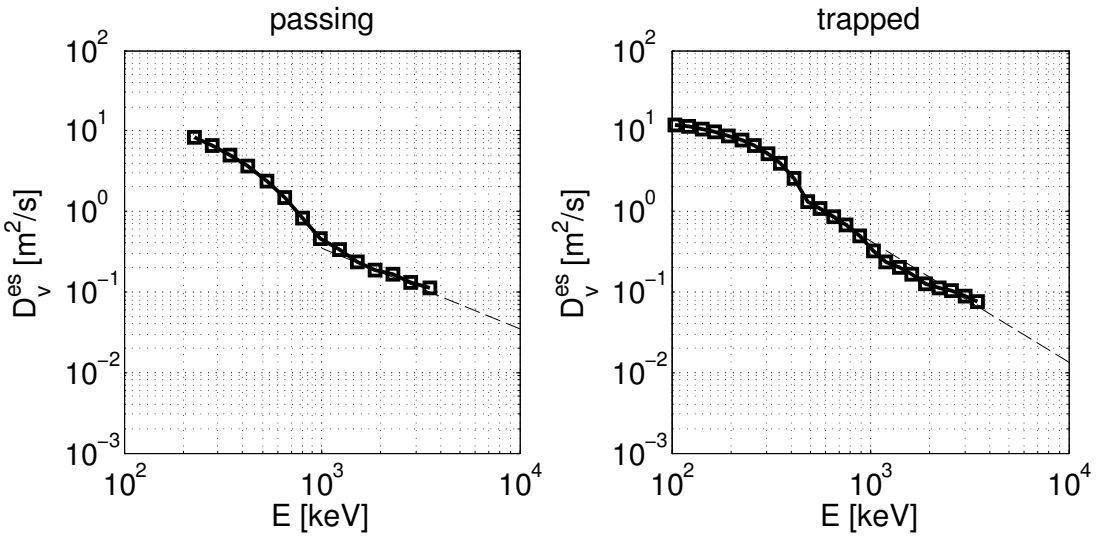

Figure 6.4: Alpha particle transport: electrostatic particle diffusivity $D_v^{\rm es}$, Eq. (3.22), of passing ($\mu B_{\rm axis}/E = 0.4$, left panel) and trapped ($\mu B_{\rm axis}/E = 0.8$, right panel) alpha particles as a function of energy. The theoretical scalings of Refs. [72, 73], $D_v^{\rm es} \simeq E^{-1}$ for passing particles and $D_v^{\rm es} \simeq E^{-3/2}$ for trapped particles, are also plotted (dashed lines).

6.1.3 Magnetic transport of energetic ions

We now study the magnetic turbulent transport of suprathermal particles. In equation (6.7) we note that the perturbed magnetic drift $\delta u_{A_\parallel}$ includes a $v_\parallel$ term which is not present in the electrostatic equivalent $\delta u_{E\times B}$. For this reason, it was suggested in [73] that the energetic ion transport in magnetic turbulence is large for finite-β plasmas. Furthermore, it was concluded that particles with a large parallel energy are transported by magnetic turbulence more effectively than by electrostatic fields. To further investigate this, we study the magnetic diffusivity $D_v^{\rm m}$ of passing particles ($\mu B_{\rm axis}/E = 0.1$) and trapped particles ($\mu B_{\rm axis}/E = 0.9$). The results for both alpha particles and deuterium are plotted in figure 6.5. It is observed that the magnetic transport of energetic ions is 0.2 $\mathrm{m}^2 \cdot \mathrm{s}^{-1}$for particles with large parallel energies. This result is valid even for the small perturbations considered here,

$$\frac{\delta B_\perp}{B} \simeq \frac{k_\perp \delta A_\parallel}{B_{\rm axis}} < 10^{-4}. \tag{6.8}$$

Despite the importance of magnetic transport, however, our results point to the conclusion that transport is mainly electrostatic. Stronger magnetic perturbations, not observed in this work, are required to enlarge $D_v^{\rm m}$ which is small also due to the long spatial scales (small gradients) of $\delta A_\parallel$ (figure 6.2). As a consequence, magnetic transport becomes larger than the electrostatic equivalent only at very large energies, not accessible to beam ions nor to alpha particles. The

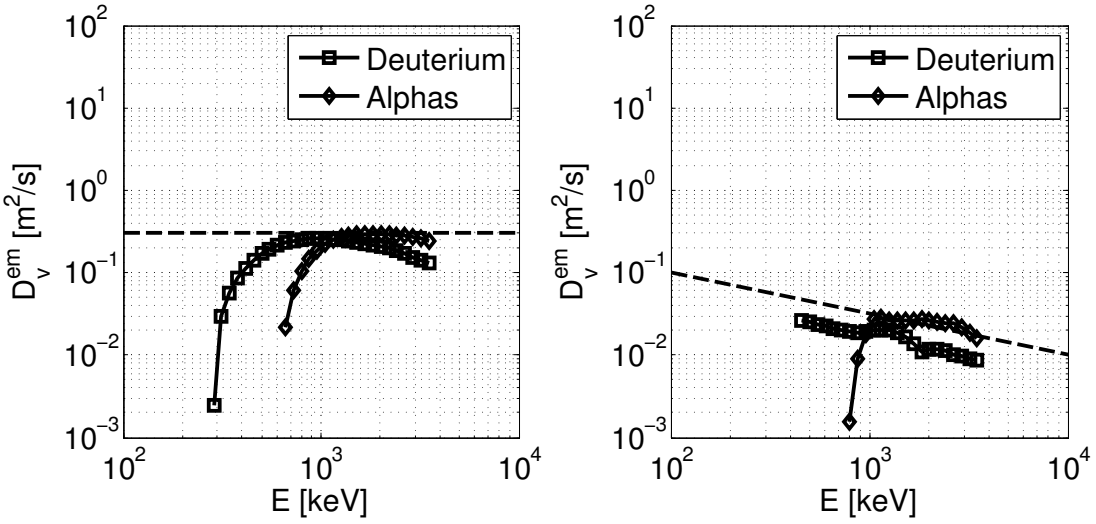

Figure 6.5: Magnetic particle diffusivity of alpha particles (diamonds) and high energy deuterium (squares) in the ITER steady state scenario, as a function of energy. The numerical results for passing particles ($\mu B_{\rm axis}/E = 0.1$, left panel) and trapped ions ($\mu B_{\rm axis}/E = 0.9$, right panel) are plotted together with the scalings predicted by [73] (dashed lines, constant diffusivity for passing particles and $D_v^{\rm m} \simeq E^{-1/2}$ for trapped particles).

same conclusions will also be drawn in section 6.2 and it seems plausible that magnetic transport is not as detrimental as pictured in [73].

6.1.4 Reduced instability drive

The results of the numerical simulations shown in the previous section predict fast ion diffusivities larger than the neoclassical estimates employed in predictive models for ITER. It is not excluded, however, that the gyrokinetic simulations overestimated the turbulent strength and, as a consequence, the particle transport. For example, it is conjectured in the literature that ITG modes are responsible for making it challenging, from an experimental point of view, to arbitrarily increase the ion temperature gradient (i.e. the microinstability drive) above the ITG threshold [131]. The same is observed in theoretical investigations. For fixed-gradient simulations, such as those discussed here, unrealistic transport levels are obtained if the parameters describe a scenario well above the onset of the ITG instability. This is the case in the simulations presented so far, with an observed background ion heat conductivity $\chi_i \simeq 15$ m$^2 \cdot$ s^{-1}, a large value if compared to the expected anomalous heat conductivity which is of the order of 1 m$^2 \cdot$ s^{-1}. By artificially reducing the ion temperature gradient from $\Omega_{T_i} = 6.4$ to $\Omega_{T_i} = 3$ we obtain more realistic fluxes, i.e. $\chi_i \simeq 2$ m$^2 \cdot$ s^{-1}.

The transport reduction is also found for the energetic ion diffusivity as we can observe, for alpha particles, in figure 6.6. Only alphas below 600-700 keV

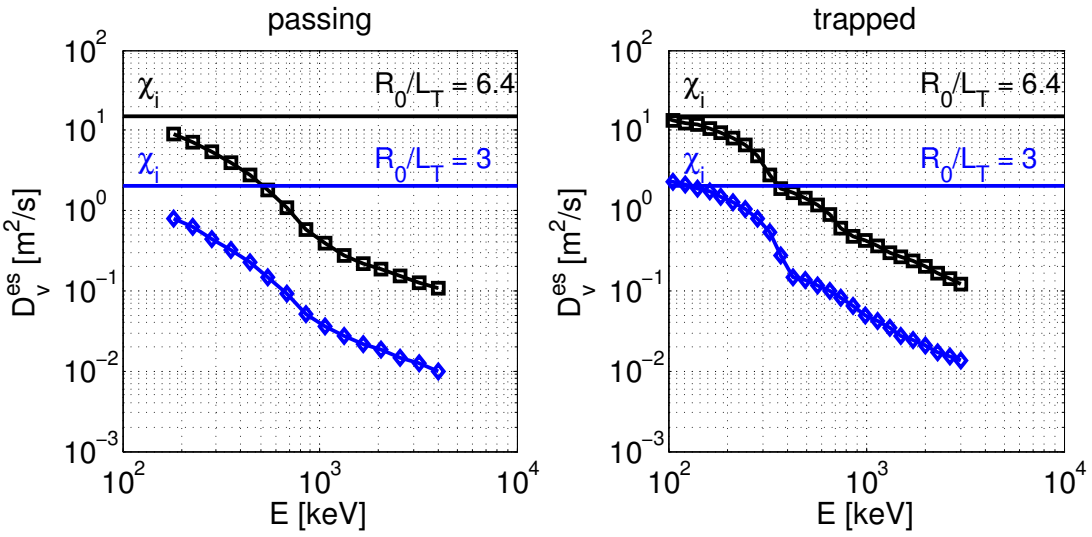

Figure 6.6: Electrostatic diffusivity comparison with contrasting instability drive: particle diffusivity $D_v^{\rm es}$ of alpha particles, as a function of energy, for passing ions ($\mu B_{\rm axis}/E = 0.4$, left panel) and trapped ions ($\mu B_{\rm axis}/E = 0.8$, right panel). The numerical results of the simulation with a reduced instability drive ($\Omega_{T_i} = 3$, blue) are plotted together with the results of the original ITER simulation ($\Omega_{T_i} = 6.4$, black). Solid horizontal lines represent the background heat conductivity for the corresponding logarithmic gradient.

experience larger-than-neoclassical transport and an efficient fusion product thermalization is then expected. A more detailed analysis is required before drawing similar conclusions for the NBI population.

6.2 Linear and nonlinear gyrokinetic simulations of the ITER steady state scenario

In this section we investigate the fast ion turbulent transport starting from the linear features of the background microinstabilities. In particular, we wish to identify the linear threshold of the most unstable mode which, as we shall see, is an ion temperature gradient mode. Nonlinear simulations will then be run close to the linear threshold. The analysis is not restrained to ITG turbulence and trapped electron modes will also be found. The interplay between linear drive and finite β effects will also be clarified.

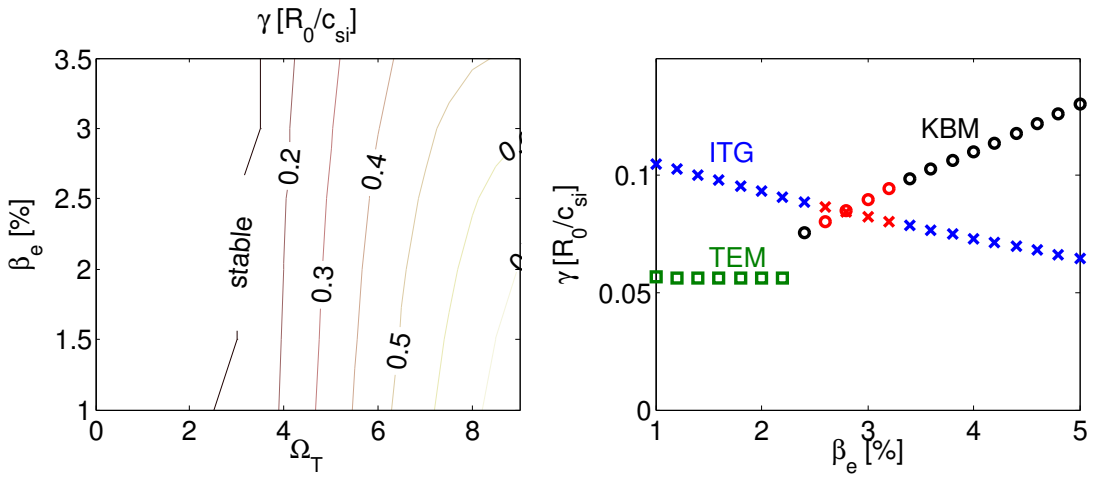

Figure 6.7: Linear growth rate of the the ion temperature gradient (ITG) mode as a function of Ω_T and β_e (left panel). The right panel shows the influence of β_e on the three most unstable modes at $\Omega_T = 3.5$. The eigensolver module requires a large number of iterations to converge when different modes are characterized by a similar growth rate. This is the case in the region at $2.4\% < \beta_e < 3.2\%$, where the computational demanding simulations are replaced by interpolated values (red markers).

6.2.1 Linear gyrokinetic simulations

The introductory linear analysis focuses on the influence of two parameters on the growth rate of small scale instabilities. The first parameter is the logarithmic temperature gradient of the background species Ω_T. Given the flat density profile characterizing this scenario, this is the main instability drive and determines the intensity of the background turbulence. The second parameter is β_e, which affects the structure of the microturbulent modes [91]. Furthermore, β_e determines the strength of magnetic fluctuations, which influences the fast ion motion [73].

We simulate a deuterium plasma at mid-radius $\rho_t = 0.5$, focusing on a single mode at $k_y\rho_s \simeq 0.8$. In this definition $\rho_s = c_{s_i}/(eB/m_i)$ is the Larmor radius of the ion species and $c_{s_j} = \sqrt{T_e/m_j}$ (j represents the species index). The two dimensional scan as a function of Ω_T and β_e is illustrated in fig. 6.7. We observe in the left panel of the figure that the linear growth rate of the ITG mode is governed by changes in Ω_T, as expected. The ITG branch becomes stable for values of Ω_T below 3. Also shown is the effect of β_e on the growth rate of the ITG instability for fixed $\Omega_T = 3.5$ (right panel). As previously observed in Refs. [91, 94], an increase in the electron pressure β_e has a small but stabilizing effect on the ITG turbulence. We can also conclude that the turbulence is not affected by the presence of kinetic ballooning modes which appear at $\beta_e > 2\%$. For the value of $\beta_e = 1.5\%$ expected for ITER, trapped electron modes are present.

We keep the nominal $\beta_e = 1.5\%$ for this scenario and further investigate the

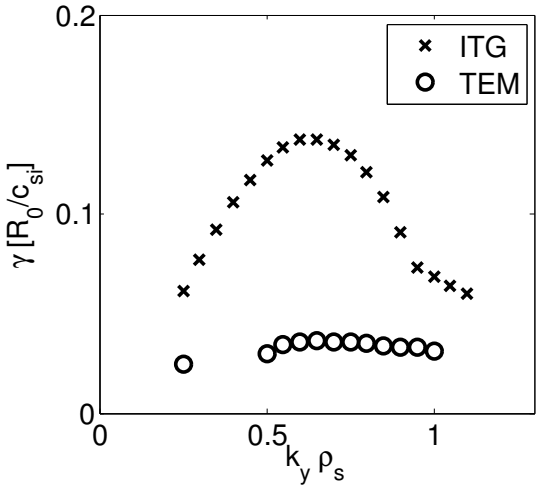

Figure 6.8: Linear growth rate, as a function of k_y, of the two most unstable modes. The largest γ is found for an ITG mode, with subdominant TEM at similar wavelengths.

presence of subdominant modes at $\Omega_T = 3.5$, close to marginal stability. The analysis is carried out focusing on different wavenumbers k_y. The results of fig. 6.8 reveal the existence of two instabilities. The first corresponds to the aforementioned ITG modes, while the second represents trapped electron modes. Further linear simulations have been performed to clarify the possible presence of electron temperature gradient (ETG) modes (figure 6.9). It is found that the largest growth rate of this instability, rescaled to electron units, is much lower than the ITG growth rate. Only a minor interaction between ETG and ITG modes is thus expected [132]. The two instabilities develop independently and we can focus on a narrower k_y range, neglecting ETG modes. This makes the analysis less demanding from a computational point of view.

6.2.2 Nonlinear GENE simulations and velocity space analysis

We now perform a set of nonlinear simulations to verify whether the linear features of the ITG/TEM modes are preserved. This introductory analysis is particularly useful to obtain realistic background transport levels. We simulate a deuterium plasma with a box size in real space $(L_x, L_y) = (125, 80)\rho_s$, and one poloidal turn in z. The extent of the velocity space domain is $(L_{v_\parallel}, L_\mu) = (3v_{th_e}, 9\,T_e)$. The real and velocity space grids are $(n_x, n_y, n_z) = (96, 32, 16)$ and $(n_{v_\parallel}, n_\mu) = (32, 8)$. We choose a realistic value of $\beta_e = 1.5\%$ and we perform three runs at $\Omega_T = \{3.5, 4, 4.5\}$. The results of fig. 6.10 demonstrate the well known similarities between linear and nonlinear features of the microturbulent transport. In

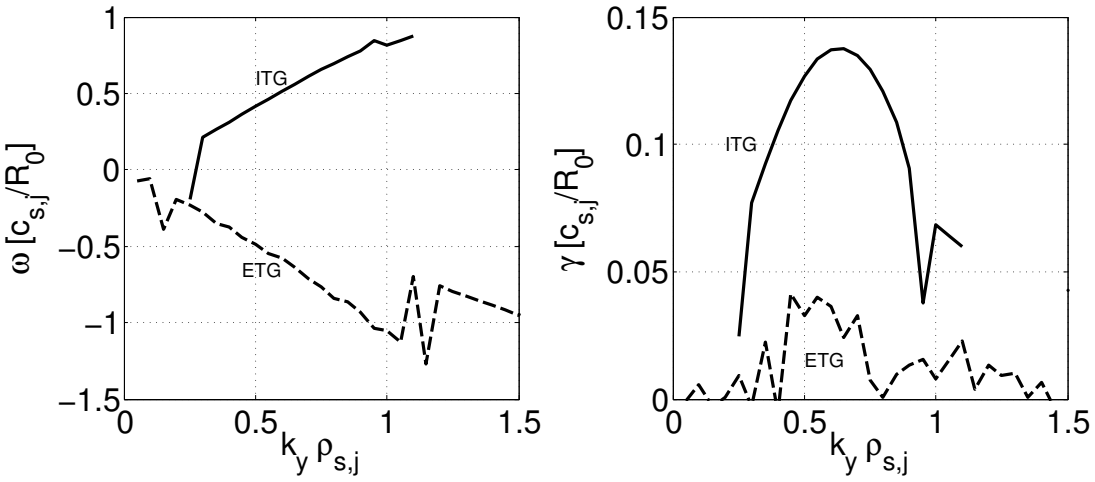

Figure 6.9: Linear frequency (left panel) and growth rate (right panel) of ITG and ETG modes (solid and dashed lines, respectively). Both ω and γ are normalized to the appropriate species units, i.e. $j = e$ for ETG and $j = i$ for ITG.

particular, a larger temperature gradient results in stronger turbulence. This set of nonlinear simulations can also help us towards the best choice of parameters for the remainder of our investigation. As ITER is expected to operate at values of χ_i close to 2 $\mathrm{m}^2 \cdot \mathrm{s}^{-1}$ [133], we choose $\Omega_T = 3.5$ for the execution of more detailed analysis.

A nonlinear simulation with improved velocity space resolution is now performed for the $\Omega_T = 3.5$ scenario. The chosen grid size is $(n_x, n_y, n_z) = (192, 64, 48)$ and $(n_{v_\parallel}, n_\mu) = (64, 32)$. The box size in real space is $(L_x, L_y) = (125, 80)\rho_s$, and one poloidal turn in z. The extent of the velocity space domain is $(L_{v_\parallel}, L_\mu) = (3v_{th_j}, 9\,T_j)$ for the j-th species. The background species are characterized by similar temperatures ($T_i = 0.8\,T_e$), flat density profiles and, as anticipated, $\Omega_T = 3.5$. This value is close to the marginal stability region of the dominant ITG modes. We keep the nominal value of $\beta_e = 1.5\%$. A distribution of deuterium ions, in the passive tracer limit, is also included in the simulation. The transport of this population, representative of NBI ions, is evaluated with the kinetic diffusivity of equation (3.22).

The results shown in fig. 6.11 demonstrate the significance of turbulent transport of fast ions. Neoclassical expectations (0.1 $\mathrm{m}^2 \cdot \mathrm{s}^{-1}$) are exceeded by passing particles at large $|\lambda| = |v_\parallel|/v$, which are characterized by fast circulating orbits around the poloidal plane, moderate radial drifts and most importantly small Larmor radii. Therefore, the beneficial gyroaveraging effects usually observed for energetic ions are weakened. This indicates that before the slowing down is concluded, NBI ion trajectories can be modified by microturbulence. On the other hand, the large Larmor radius of trapped particles effectively suppresses the

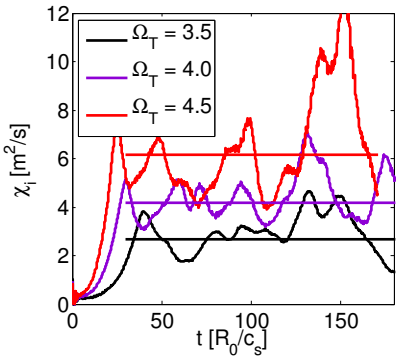

Figure 6.10: Nonlinear heat diffusivity χ_i, as a function of time, for three different values of Ω_T. The closest value to ITER expectations of the heat diffusivity is found for $\Omega_T = 3.5$.

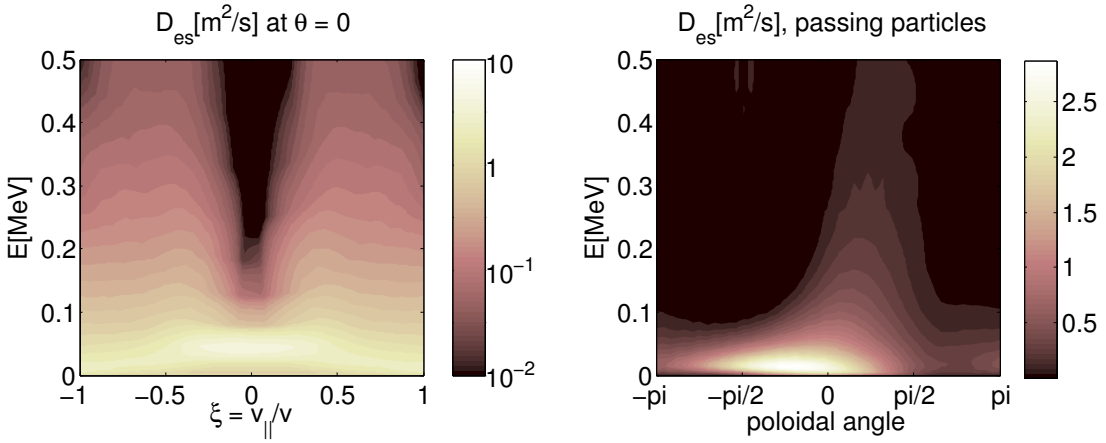

Figure 6.11: Electrostatic diffusivity, as a function of energy and pitch $\lambda = v_\parallel/v$, for particles on the outboard midplane (left panel). The particle diffusivity is also shown as a function of energy and poloidal angle for passing particles at $\lambda \simeq 1$ (right panel).

particle transport as we observe in the $\lambda \simeq 0$ region of the plot.

The particle energy and pitch λ are not the only parameters regulating the intensity of the radial transport. Indeed, the turbulent fields in tokamak geometry exhibit strong poloidal variations. In the outboard mid-plane the instability is the strongest, as expected from the adverse alignment of the curvature drift and the pressure gradient. The energetic ion transport reflects this poloidal asymmetry (fig. 6.11).

The transport of energetic ions due to magnetic fluctuations has also been investigated. It is found that magnetic transport plays only a minor role in this scenario. The magnetic turbulent transport never exceeds $D_v^{\mathrm{m}} < 10^{-2}\ \mathrm{m}^2 \cdot \mathrm{s}^{-1}$,

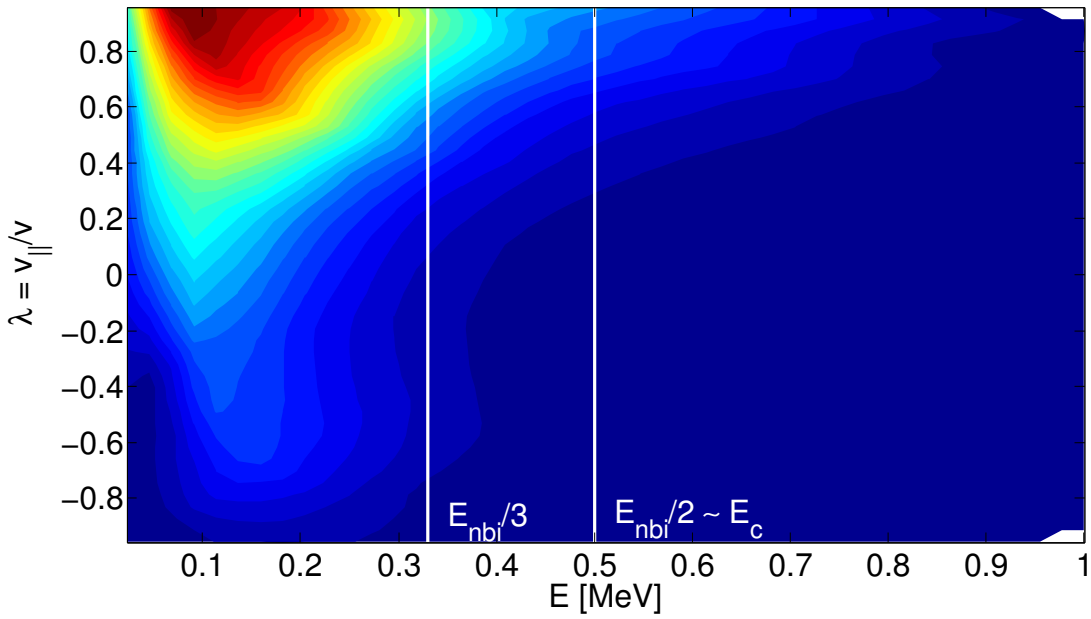

Figure 6.12: Slowing down distribution function of beam ions as a function of energy and pitch angle (left panel). The pitch angle scattering expected for lower energy ions is evident for $E < E_c$.

a small value that motivates our choice to ignore it for the subsequent analyses. Only the electrostatic transport is then considered for the single particle investigation presented in the next section.

6.3 VENUS simulations of the neutral beam injection in the ITER steady state scenario

The VENUS code is employed in this section to quantify the turbulent beam ion transport. We first perform a set of simulations in the "collisional" case (i.e. without turbulence) with the NB source term (1 MeV, 30 MW) calculated by the beam deposition model. The particle motion of $2.4 \cdot 10^5$ markers under the influence of Coulomb collisions is simulated. The resulting distribution function in velocity space is shown in fig. 6.12. Particles are injected in a narrow region of velocity space at high energies and $\lambda \simeq 1$. Close to the birth energy, energetic ions lose energy on the background electrons. This process reduces the energy of the beam particles without notably affecting their pitch angle λ. As these particles approach $E_c \simeq 500$ keV (in the central region in figure 6.12) they interact more importantly with the background ions. As a consequence, we observe a distinct broadening of the distribution in pitch angle. The resulting beam ion density and current profiles, both in the collisional case and in presence of microturbulence, are calculated in the next section.

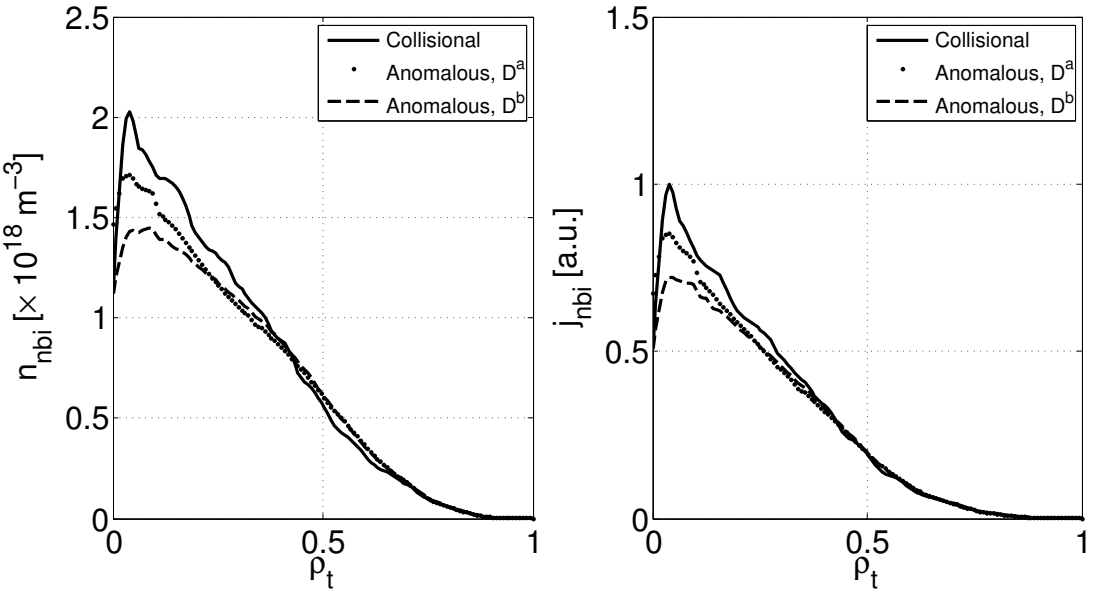

Figure 6.13: Neutral beam density (left panel) for the collisional case (solid black line) and the anomalous model with a Gaussian (dots) and a constant radial envelope (dashed line). The beam driven current is also represented in the right panel, with the same convention on the line style.

6.3.1 Anomalous redistribution of the NBCD profile

The impact of turbulent transport of the beam driven current is now evaluated. The kinetic diffusivity calculated in section 6.2.2 for $\rho_t = 0.5$ is used for this purpose. Our model is based on a local approximation and estimates the particle diffusivity in a particular radial position. Radial dependencies, such as those observed in ref. [70], are reproduced with the definition of a radial envelope

$$D_{\text{anomalous}}(\rho_t, \theta, \lambda, E) = D_{\text{envelope}}(\rho_t) \times \underbrace{D_v^{\text{es}}(\lambda, E, \theta)}_{\text{from GENE}}. \tag{6.9}$$

We consider two choices of D_{envelope}. The first one is a Gaussian function with variance $\sigma/a = 0.25$, chosen to reproduce the observations of [70]. We refer to the resulting anomalous diffusivity as D^a for sake of clarity. The second is a constant function $D_{\text{envelope}} = 1$, shown to be a good model for TCV in the last chapter. We call the resulting diffusivity D^b.

The results of the numerical simulation of the neutral beam redistribution are illustrated in fig. 6.13. The beam ion density is only slightly redistributed as we can observe from the curves in the left panel, due to the large injection energy. Somewhat larger beam ion density redistribution is observed when using the anomalous diffusivity D^b. Associated with this observation is a smaller NBCD profile redistribution. The current is mostly driven in the high energy region where lower diffusivities are observed, thus explaining the numerical result. These

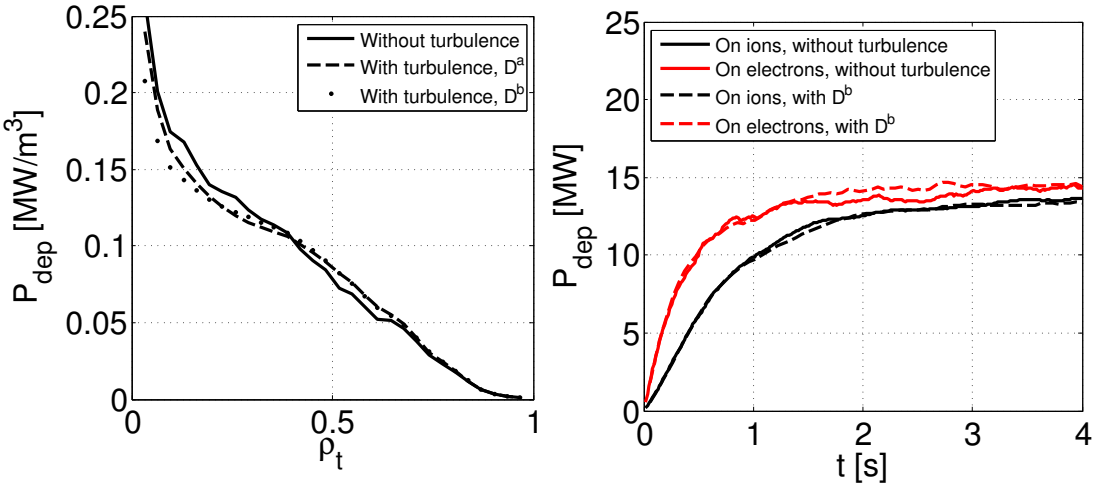

Figure 6.14: (Left panel) Power deposition profile simulated by the VENUS code with the inclusion of only collisions (solid black line) and the anomalous diffusivities D^a and D^b (dashed and dotted line, respectively). (Right panel) Time trace of the power given to the background plasma by beam ions during their thermalization. Solid lines describe the collisional case while dotted lines represent simulations performed with the inclusion of anomalous effects. The power given to electrons and to ions is also shown (red and black lines, respectively).

negligible modifications further justify not recomputing the equilibrium when $j_{\rm nbi}$ changes. Particle losses, already established at 1.2% for a collisional case, do not change once anomalous transport is added to the simulation.

In figure 6.14 we observe that the radial profile of the heating deposition on electrons and ions does not change significantly with the inclusion of microturbulence. Differences in the time trace of the heating deposition, calculated with VENUS and shown in the same figure, are also negligible. We conclude that microturbulence has a small effect on the fast ion physics in ITER steady state scenario.

6.4 DEMO

DEMO will be the first thermonuclear device to generate electrical power. Its construction will be based on the guidelines provided by ITER and is planned to be operational after the year 2035. Recent analysis highlighted the key features of the device [16]. It will be larger than ITER, with an expected major radius $R_0 = 8.5$ m and toroidal field $B_0 = 6$ T. Regarding plasma characteristics, background densities are constrained by the Greenwald limit and will therefore resemble those of ITER. We choose $n_{\rm plasma} = 8 \times 10^{19}$ m^{-3}. Larger temperatures are envisaged, which result in smaller values of $E_{\rm nbi}/T_e$ (for this theoretical exercise, we consider

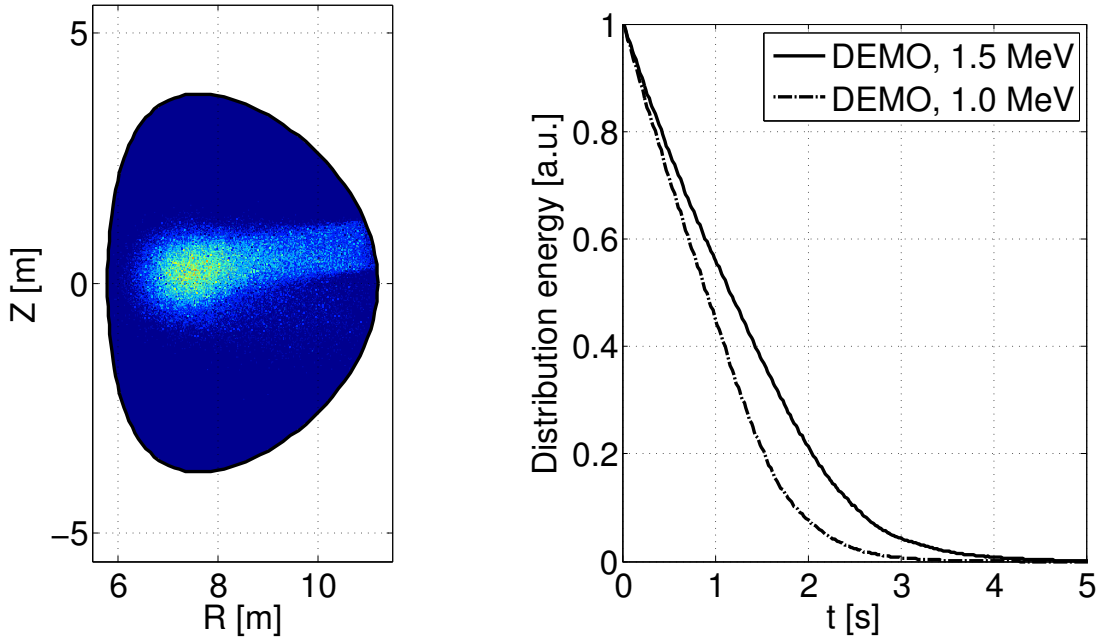

Figure 6.15: Beam footprint of the 1.5 MeV NBI in DEMO (left panel). The curves in the right panel illustrate the time required in DEMO to thermalize two mono-energetic distributions of beam particles , at 1 and 1.5 MeV.

a peak electron temperature of 50 keV). This could cause anomalous beam ion transport, which motivates our analysis.

6.4.1 The neutral beam system in DEMO

The neutral beam heating system in DEMO is expected to deliver deuterium beams at energies between 0.5 and 2 MeV. For the purpose of our study two possibilities are investigated: 1.5 and 1.0 MeV. The beam footprint is shown in figure 6.15. We choose a tangential geometry similar to ITER, although perpendicular injection is also contemplated to better access the plasma core of this large device. In the right panel of the same figure we illustrate the time required to thermalize the two energetic populations at mid-radius. As we shall see shortly, the longer thermalization time of the 1.5 MeV population offsets the reduced diffusivity (due to the larger $E_{\rm nbi}/T_e$ ratio) on particle redistribution. Indeed, we can predict the anomalous fast ion behaviour by evaluating the parameter $\Delta = \sqrt{\langle D \rangle \tau_{sd}}/a$. For the 1.5 MeV beam, characterized by a slowing down time of 3 seconds, we obtain $\Delta = 0.8$. A slightly smaller value of 0.75 is obtained for the 1.0 MeV beam, as the smaller $\tau_{sd} = 2$ s is compensated by the $\langle D \rangle$ which is almost 50% larger. Fast ion redistribution is therefore expected.

6.4.2 Anomalous beam ion transport in DEMO

Further gyrokinetic simulations are not required in this case as we choose to employ the particle diffusivity D^b obtained for the ITER steady state scenario. We consider the particle diffusivity obtained with the constant radial envelope described for ITER. The energy and pitch angle dependence of $D_v^{\rm es}$ are the same, with the choice of normalization

$$D_v^{\rm demo}(\rho_t, \theta, E/T_e, \lambda) = A \cdot D_v^{\rm iter}(\rho_t, \theta, E/T_e, \lambda). \tag{6.10}$$

The ratio between the gyro-Bohm diffusivity of the two scenarios provides the constant A

$$A = \frac{D_{gb}^{\rm demo}}{D_{gb}^{\rm iter}} = \left[\frac{T_{e,\rm demo}}{T_{e,\rm iter}}\right]^{3/2} \frac{B_{\rm iter}}{B_{\rm demo}} \simeq 2.5. \tag{6.11}$$

Two simulations for each injection energy are carried out. One ("collisional") simulation is performed with only the contribution of background magnetic fields and collisions to the particle motion. In a second ("anomalous") simulation, turbulent transport is also included. Both runs assume the same safety factor and background density profiles used for the ITER steady state scenario. The $\mathcal{N} = 1.2 \times 10^5$ markers introduced in VENUS simulations are followed for 4 seconds, a time reasonably close to the fast ion slowing down time.

Results for the 1 MeV neutral beam system. The results in figure 6.16 highlight possible beam ion redistribution of the 1 MeV neutral beam system in DEMO. In the left panel of the figure, for example, we recognize substantial differences in the fast ion profiles between the collisional and anomalous VENUS simulations. Redistribution is observed with the displacement of particles from the core to the central plasma region. This result is even more evident in the central and right panels of the figure where the poloidal cross section of the fast ion density in collisional and anomalous simulations is shown. The reason for the larger particle transport with respect to the ITER case is the different $E_{\rm nbi}/T_e$ ratio. In this case, $(E_{\rm nbi}/T_e)^{\rm demo} = 20$ is substantially lower than $(E_{\rm nbi}/T_e)^{\rm iter} > 30$. Furthermore, longer slowing down times are expected in DEMO and particles interact with turbulent fields over longer time scales. A positive result of the numerical analysis is the negligible amount of anomalous particle and heat losses.

Results for the 1.5 MeV neutral beam system. The redistribution of the 1.5 MeV NBI is very similar to that of the previously discussed lower energy system (figure 6.17). The analogy between the results is rather surprising if we consider the different $E_{\rm nbi}/T_e$ obtained with the two injectors. However, beam redistribution is roughly given by the product of the anomalous diffusivity (the strength of the interaction) and the slowing down time (the duration of the interaction). When enlarging the beam energy to 1.5 MeV, the longer slowing down

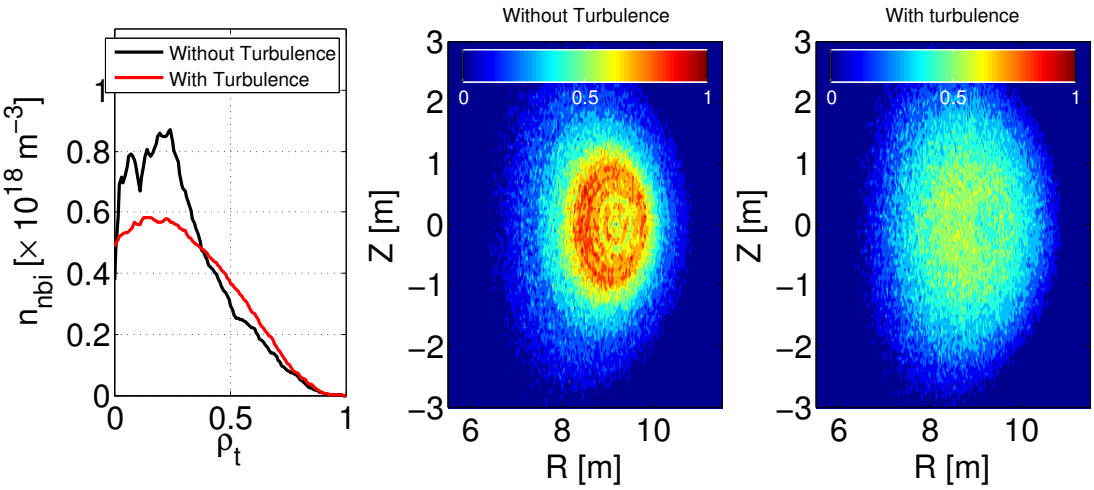

Figure 6.16: (Left panel) Fast ion density, as a function of minor radius, in a DEMO discharge heated with the 1 MeV neutral beam system. Results are illustrated for a purely collisional case (black) and with the addition of the anomalous transport (red). The poloidal cross section of the fast ion density is illustrated for collisional and anomalous simulations in the central and in the right panel, respectively.

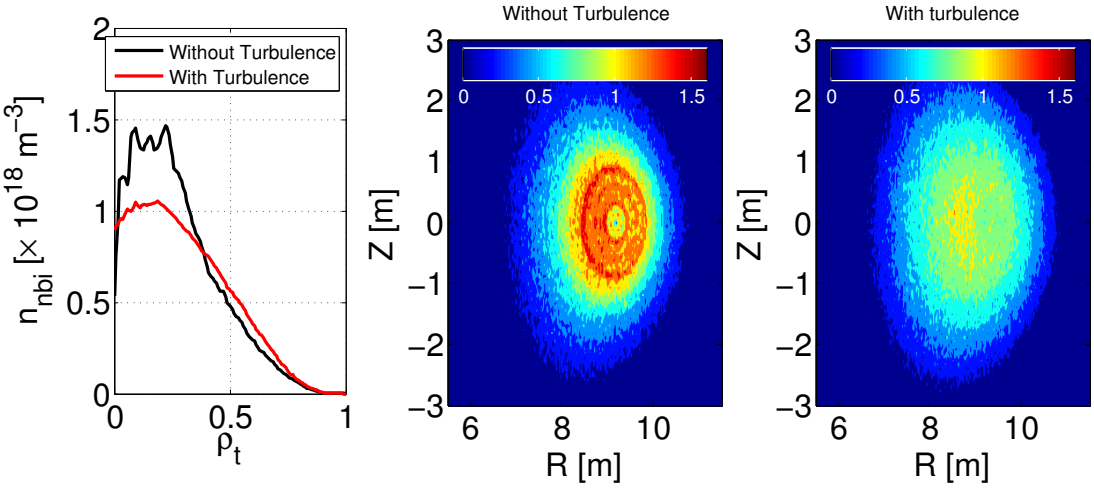

Figure 6.17: (Left panel) Fast ion density, simulated by the VENUS code, of the 1.5 MeV neutral beam system with collisions (black) and the inclusion of anomalous transport (red). The poloidal cross section of the fast ion density is also illustrated in the central and right panels for simulations without and with turbulent diffusivity (central and right panels, respectively)

.

time (figure 6.15) compensates the reduced particle diffusivity deriving from the larger $E_{\rm nbi}/T_e$ ratio (here we assume the same background temperature).

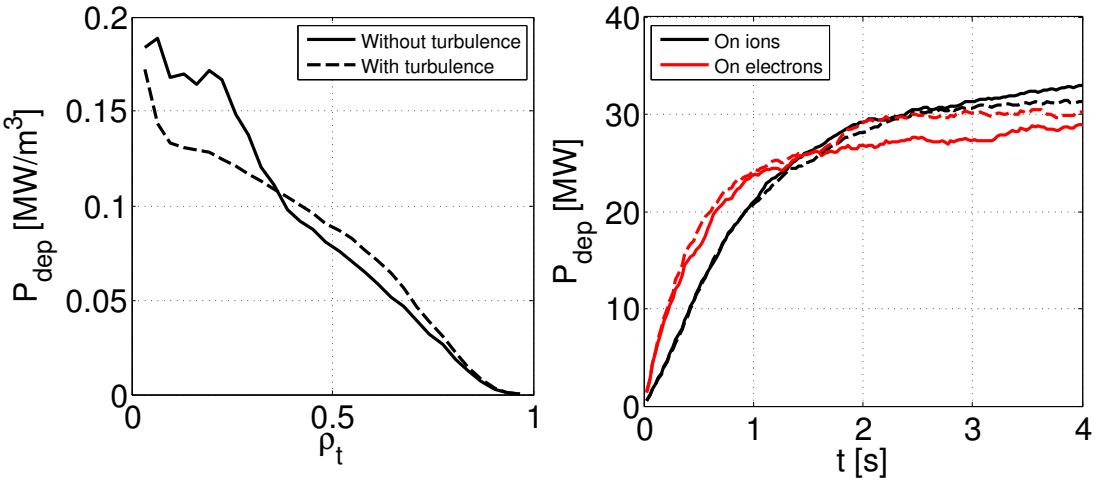

Figure 6.18: (Left panel) Power deposition profile from VENUS simulations with and without turbulent fields (dashed and solid line, respectively). (Right panel) Power deposition, as a function of time, on ions and electrons (black and red lines, respectively). Dashed lines represent simulations with the inclusion of anomalous transport.

The heating deposition profile of the 1.5 MeV system is also redistributed by small scale turbulence. In figure 6.18 we observe the displacement of the deposition layer towards the edge of the plasma when turbulence is taken into account. This has important consequences on electron and ion heating, too. Without turbulence, more energy is given to ions than electrons (solid lines of figure 6.18, right panel). Since turbulence moves energetic ions towards colder plasma regions, their critical energy lowers ($E_c \propto T_e$). The consequence is that fast ion energy is equally transferred to the background electrons and ions (dashed lines of figure 6.18, right panel), a great difference with respect to collisional estimates. This effect must be considered when evaluating DEMO performance.

Results for a smaller density scenario To further convince the reader of the importance not only of the $E_{\rm nbi}/T_e$ ratio, but also of the fast ion slowing down time, we perform a last simulation of the DEMO tokamak. We reproduce a scenario with the same parameter of the one we just analyzed and we only modify the plasma density $n_{\rm plasma} = 6 \times 10^{19}$ m^{-3}. Given the lower density we obtain a longer slowing down time $\tau_{sd} = 4$ s and consequently a larger $\Delta = 0.9$. A set of simulations with the VENUS code confirms that stronger redistribution of the fast ion density is observed in such scenario (figure 6.19). For this reason, high density scenarios must be privileged, where possible, to minimize influence of turbulent fields. Collisional effects, however, alter the response of microinstabilities [134] and should be taken into account in more detailed models.

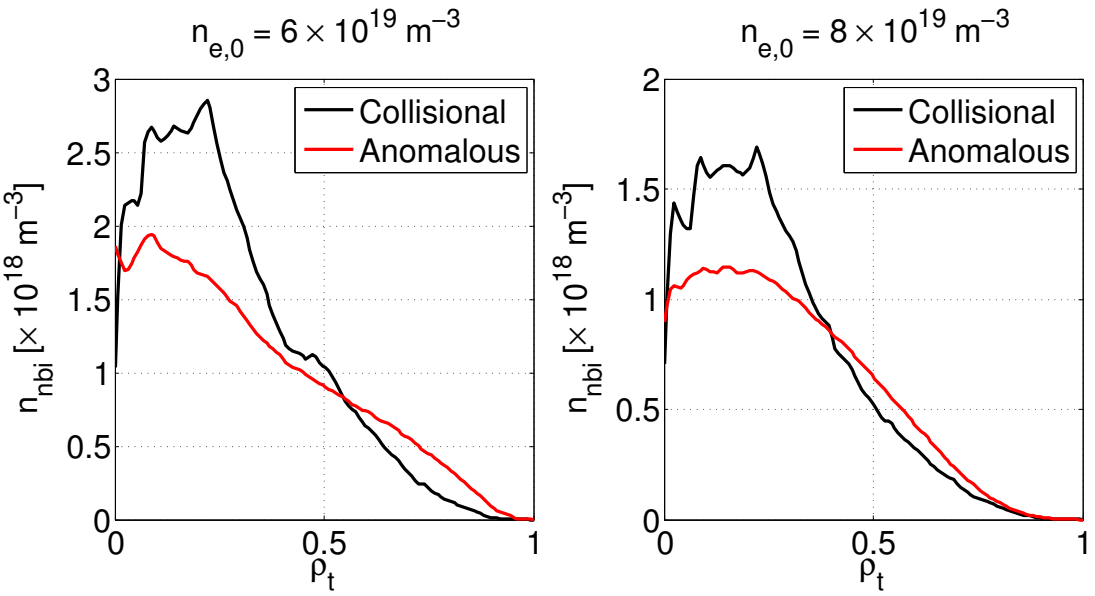

Figure 6.19: (Left panel) Beam ion density profile in DEMO, for a low (left) and high (right) density plasma. Results obtained with only collisional effects are shown in black. The outcome of simulations where also anomalous transport is considered is shown in red.

6.5 Conclusions

Numerical simulations of beam ion redistribution in ITER were presented in this chapter. The investigations were carried out with the GENE code, simulating the background microturbulence, and the VENUS code, reproducing the fast ion motion with the influence of the simulated fields. Linear and nonlinear simulations were performed with the GENE code to identify the set of parameters describing ITER turbulence, a mix of ion temperature gradient and trapped electron modes. Finite beta effects were also retained, although we concluded that fast ion transport is mostly electrostatic, i.e. driven by the $\mathbf{E} \times \mathbf{B}$ drift, and that magnetic perturbations are too small to have an effect. We first observed very small turbulent diffusivities, concluding that alpha particles are essentially unaffected by turbulence. To draw conclusions on the NBI ions, the kinetic diffusivity obtained with GENE simulations was used in the VENUS code. It was concluded that the neutral beam in ITER is only slightly redistributed due to the large injection energy ($E_b/T_e = 1$ MeV/30 keV > 30).

An outlook for DEMO was presented in section 6.4. Anomalous redistribution for two different beams in DEMO, injecting deuterium at 1 MeV and 1.5 MeV, was evaluated. Depending on the purpose of neutral beam injection in DEMO, different conclusions can be drawn. A slight reduction in the overall beam ion efficiency is predicted if the NBI in DEMO only serves the purpose of plasma heating. However, the NBI could be used to drive non inductive current, in which

case redistribution would be highly detrimental as it modifies the safety factor profile, usually tailored to maximize the MHD-accessible region [26]. DEMO is still being designed and neither the NBI power, nor the injection energy or geometry, are definitive. Our study suggests that anomalous transport must be considered when establishing the optimal injection energy.

Chapter 7
Conclusions

Finding a clean solution to the ever growing energy demand problem represents a great challenge for modern society. A possible solution to the problem is nuclear fusion. Among the most promising fusion experiments are *tokamaks*, an example of magnetic confinement devices first developed in Russia in 1968. Ever since, our understanding of tokamak physics has been improving, paving the way for higher performance devices, such as ITER, and for the first demonstration power plant, DEMO. Despite great advances, however, the scientific community is still trying to address some physics issues that influence fusion performance. For example, small scale turbulent fields are responsible for the *anomalous* transport of background heat and particles and extensive studies are carried out to mitigate their influence. It is shown in this work that *microturbulence* also affects the motion of energetic ions, which are important both for self-heating (by fusion reaction by-products) and for the external heating of burning plasmas.

7.1 Summary

In this thesis, first estimates of the transport of Maxwellian distributed energetic ions are established in the presence of microturbulent fields. Large cross field transport is observed even at temperatures much larger than the plasma background. This result is in apparent contradiction with gyroaveraging considerations. As the numerical tools employed in this analysis are initially limited to a collective transport description, the development of more accurate transport quantities is developed. In the theoretical framework employed in this thesis, diffusion and convection are redefined according to the phase space characteristics of the particles considered. These *kinetic* transport quantities, whose consistency is demonstrated with numerical simulations, are suitable for investigating the transport of ions with different energies and, consequently, the effects of gyroaveraging. Numerical diagnostics are also embedded in the GENE code to directly evaluate the kinetic transport of fast ions from nonlinear gyrokinetic simulations. The first study carried out with this method focused on fast ion transport in a circular tokamak plasma. Comparisons are made with the collisional diffusion expected for suprathermal ions, $D_{\text{coll}} = 0.1\ \text{m}^2 \cdot \text{s}^{-1}$. It is noted that energetic ion transport is significantly larger than D_{coll}, especially for intermediate energies, $1 < E_{\text{fast}}/T_e < 15$. Gyroaveraging effects are accounted for and are found to be non-negligible only at larger energies. To directly quantify the impact on tokamak

operation, the single particle code VENUS has been upgraded to simulate the fast ion motion with collisions and turbulence.

The fast ion physics associated with the planned installation of a neutral beam system on Tokamak à Configuration Variable is studied with dedicated VENUS and GENE simulations. It is demonstrated that the turbulent transport of beam ions strongly depends on the scenario and that it could even cause the loss of one third of the beam power. Anomalies are nevertheless modest at plasma temperatures of the order of 1 keV, suggesting that other heating systems in TCV can be employed to regulate anomalous fast ion transport for experimental studies.

The analysis then focuses on the next step tokamak device ITER. The background turbulence is characterized on the basis of linear GENE simulations. It is revealed that a mixture of ITG, TEM and ETG modes would contribute to the generation of the turbulent background in ITER. The ETG mode activity is particularly weak and can be neglected. Our nonlinear simulations demonstrates that magnetic turbulence, depicted as particularly detrimental in a recent work [73], has little effect on the fast particle transport for the cases considered in this work. Furthermore, it is shown that the transport of fusion born products driven by electrostatic fluctuations is much smaller than the transport driven by collisions, due to the large birth energy of alpha particles. Similar conclusions hold for beam particles. Hence, fast ion confinement in ITER should not be affected significantly by small scale turbulence.

Less optimistic results were obtained for DEMO, the first demonstration power plant. Due to the large plasma temperature and the consequently small values of E_{nbi}/T_e, it was shown that electrostatic turbulence can cause significant beam ion redistribution. Potentially large effects are observed for the beam driven current and the heat deposition in the plasma. In particular, a fraction of the beam energy would be given to the the background electrons instead of the bulk ions, reducing the fusion yield and changing the current drive properties.

7.2 Outlook

There are some limitations in the numerical tools employed in this thesis. In particular, plasma turbulence has been simulated with a flux tube code in the local approximation, which can fail to capture non local effects. Global simulations, although demanding from the computational side, could be an improvement. For such studies, recent upgrades to the GENE code [135] could be employed. Furthermore, the effect of magnetic turbulence on fast ions has only been studied in this thesis and in the recent work of Hauff [73]. Similar investigations with different gyrokinetic codes must clarify the importance of this transport phenomenon for future high-β plasmas.

Experimental verification is greatly needed, too. The turbulent transport of fast ions has only recently been observed in a limited number of experiments [61, 79, 85, 86]. This subtle phenomenon is rather difficult to measure and it is often

concealed by MHD activity. The impact on future machines, however, must be accurately predicted and the collaborative effort of the community is already growing. In the framework of this thesis and of the International Tokamak Physics Activity (ITPA) group, new experiments are being run, or planned, on DIII-D [136], ASDEX-U [62] and ALCATOR C-Mod [137]. The analysis of previous D-T plasma discharges in the JET and TFTR devices, where alpha particle anomalies were found, is currently under way. The Tokamak à Configuration Variable would also offer very interesting conditions for studying the interaction of energetic ions and turbulence. Given the flexibility of the machine and the powerful ECRH system, it would be possible to "tune" the interaction. Further experiments are contemplated on basic plasma experiments, such as TORPEX and LAPD, to elucidate fundamental aspects of the fast ion interaction with turbulence. In conclusion, additional effort of the scientific community, both from theory and experiments, is required to shed more light on this important area of plasma physics, which is, as of today, only partially understood.

Appendix A

Flux tube field mapping to real coordinates

The turbulent fields simulated by GENE are restricted to a small radial domain in the local approximation employed in this thesis. In the flux tube framework, the analysis is further restricted to a small domain in the toroidal direction. A reconstruction of the turbulent fields in a full real space domain is not possible given the assumptions of a limited radial domain. On the other hand, fields can be mapped on an entire toroidal (and poloidal) domain for dedicated global studies, such as the investigations with the HMGC code.

Let us start by describing the two simulation domains we want to interface. The simulation domain in GENE is described by the (ν, z) variables

$$\nu = q\theta - \phi, \tag{A.1}$$

$$z = \theta, \tag{A.2}$$

where ν is a renormalization of the binormal variable y and q is the local value of the safety factor. The analogous inverse mapping is also given

$$\theta = z, \tag{A.3}$$

$$\phi = qz - \nu. \tag{A.4}$$

Once a simulation output is read in GENE variables, one can simply map an arbitrary quantity Φ to real space as

$$\Phi(\theta, \phi) = \Phi(\theta(z), \phi(\nu, z)). \tag{A.5}$$

This assumption holds for electromagnetic fields and simple interpolation routines can be used to obtain the quantity of interest over a regular grid, as usually required by numerical codes. A problem arises, however. The mapping is quite simple to implement, but a flux surface will not be entirely covered by a typical simulation. Only a tight ribbon will be obtained, as from Fig. 2.5.

A.1 Extending the domain

The full toroidal mapping can be obtained, as said, by replicating the turbulent ribbon of figure 2.5 a finite number of times. To do so, we exploit tokamak periodicities and GENE boundary conditions. One of the natural boundary conditions

inside the code is given for the ν coordinate

$$\Phi(\nu + L_\nu, z) = \Phi(\nu, z). \tag{A.6}$$

Comparing this condition to the toroidal continuity

$$\Phi(\nu + 2\pi, z) = \Phi(\nu, z). \tag{A.7}$$

reflects the fact that the ν variable spans an entire fraction of the toroidal domain, or

$$L_\nu = \frac{2\pi}{N}. \tag{A.8}$$

The value N can be obtained by considering that the box size in units of length in the GENE code is given by

$$L_\phi/N = L_y = \frac{2\pi}{k_y^{\min}} = \frac{2\pi\rho_s}{\hat{k}_y^{\min}}, \tag{A.9}$$

where $\rho_s = \sqrt{T_e m_i}/(eB)$ and a hat indicates a quantity normalized according to GENE conventions. In particular, the $\hat{k}_y^{\min}$ quantity is an input parameter to the code. The toroidal length of a tokamak with major radius R_0, on the other hand, is given by

$$L_\phi = 2\pi R_0, \tag{A.10}$$

so we obtain

$$N = \left[\frac{R_0}{\rho_s}\right] \hat{k}_y^{\min} \tag{A.11}$$

At this point, we just have to replicate the ribbon as many times as needed to fill the domain of our interest. There is a further condition to satisfy.

Throughout the discussion of the field mapping we considered a single flux surface at a radial location r where $q(r) = q$. The radial dependence of q can be obtained once the the radial periodicity, so far ignored, is taken into account. The Fourier decomposition along the radial direction implies the continuity periodicity along the x direction

$$f(x_i, \nu, z) = f(x_f, \nu, z). \tag{A.12}$$

Furthermore, fusion devices have a poloidal continuity which can be written, in GENE coordinates, as

$$f(x_f, \nu, z) = f(x_f, \nu - 2\pi q_f, z). \tag{A.13}$$

Equations A.12 and A.13 thus give

$$f(x_f, \nu - 2\pi q_f, z) = f(x_1, \nu - 2\pi q_i, z) \tag{A.14}$$

and therefore

$$\Delta q = N' \frac{L_\nu}{2\pi} = \text{from above} = \frac{N'}{N}. \tag{A.15}$$

Δq is the total safety factor variation along the radial variable. The value N' can be retrieved from the codes parameters as the variable `nexc`. Given a simple example with $\hat{k}_y^{min} = 0.02$, `nexc` $= 5$ and $R_0/\rho_s = 10^3$

$$N = 20 \tag{A.16}$$

$$\Delta q = 0.2. \tag{A.17}$$

The result of such a mapping can be seen in Fig A.1. In ITER the number N is much larger than 10^2.

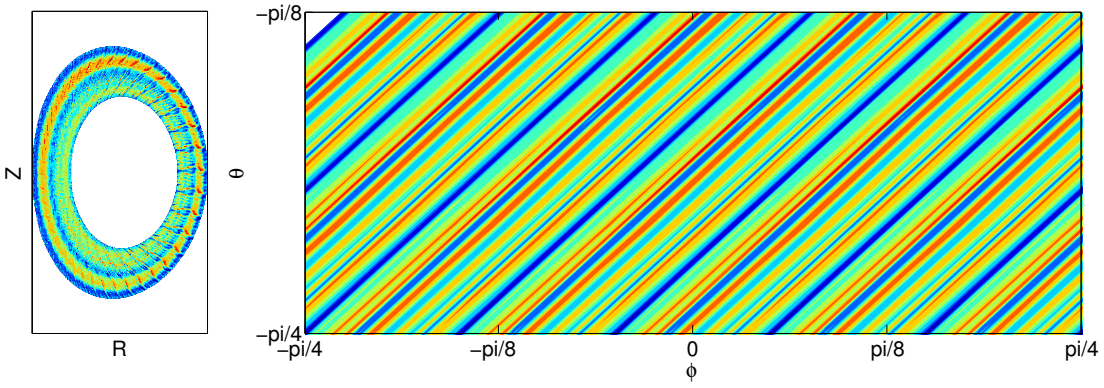

Figure A.1: Numerical representation of the turbulent field mapping from GENE to real space coordinates. (Left panel) Snapshot of the electrostatic turbulent field calculated by the GENE code in real space coordinates. (Right panel) Detail of the field reconstruction on a flux surface, for a particular radial position.

Appendix B

Analytical scaling of the energetic particle transport

In chapter 3.1 it was shown that the transport of Maxwellians was characterized by the $D_\alpha \simeq (T_\alpha/T_e)^{-1}$ scaling at large temperatures. This scaling can also be obtained by analytically solving Eq. 3.26, which can be written in this case as

$$D(T_\alpha) = \frac{\int dE\sqrt{E}D(E)e^{-E/T_\alpha}}{\int dE\sqrt{E}e^{-E/T_\alpha}}. \tag{B.1}$$

To ease the calculation, we shall employ $n = 1$ in the definition of $D(E)$ as from Eq. (3.44). Defining $\lambda_\alpha = T_\alpha/T_e$, we obtain

$$\begin{aligned} D(\lambda_\alpha) = &-\sqrt{L/\lambda_\alpha}e^{-L\lambda_\alpha} + \Gamma\left(\sqrt{L/\lambda_\alpha}\right) \times \\ &\times \left(\frac{1}{2}\sqrt{\pi} - L\sqrt{\pi}/\lambda_\alpha\right) + L\sqrt{\pi}/\lambda_\alpha, \end{aligned} \tag{B.2}$$

where Γ is the error function. The first order Taylor expansion of the previous expression for $\lambda_\alpha \to \infty$ gives the expected $D \simeq \lambda_\alpha^{-1}$ dominant term. In Ref. [60], an asymptotic analysis revealed the existence of the slightly faster scaling $D \simeq \lambda_\alpha^{-3/2}$. The different theoretical prediction of Ref. [60] could be justified either by the particular approximations introduced in the latter work (large shear, no parallel dynamics), or by the simple model defined in Eq. (3.44). Also, the linear model could be inaccurately describing the long energy tails in the diffusivity, which is a nonlinear phenomenon. The difference between linear and nonlinear theories, however, are probably insignificant when describing distributions characterized by fast energy tails (i.e. thermal populations), as already pointed out in Refs. [60, 66].

Appendix C

A synthetic diagnostic for the gamma-ray camera at JET

The D-T fusion production rate in a tokamak with Beryllium impurities can be measured from the 4.4 MeV γ-rays produced by the nuclear reaction

$$^{9}\mathrm{Be}(^{4}\mathrm{He}, \mathrm{n}\gamma)^{12}\mathrm{C}. \tag{C.1}$$

This reaction has a threshold energy of $\simeq$ 1.7 MeV, which is mainly carried by the Helium nuclei as Beryllium is not characterized by energies larger than the background plasma temperature. The detection of γ-rays at 4.4 MeV at JET is therefore a signature of the presence of high energy α particles in the plasma. The velocity space characteristics of the reactants can be unveiled by studying the shape of the energy spectrum of the γ-rays. This is a technique usually applied to neutrons and it can be used to obtain the plasma temperature or to benchmark transport models [138, 139, 140]. The same procedure applies to γ-rays, whose otherwise monochromatic energy spectrum is broadened by Doppler effects caused by the velocity of the emitting Carbon in the laboratory frame. The kinematics of the nuclear reaction creating the Carbon nuclei (Fig. C.1) needs to be taken into account.

The Doppler shift of a γ-ray produced by a non-relativistic emitter observed in the laboratory frame is given by

$$\Delta E_\gamma = E_0 \left(\frac{\left|\mathbf{v}_{em}^{lab}\right|}{c} \cos\beta \right). \tag{C.2}$$

Here, E_0 corresponds to the rest energy of the γ-ray (4.4 MeV in our case), β is the angle between the velocity of the emitter $\mathbf{v}_{em}^{lab}$ in the laboratory frame and the observer. The velocity of the emitter is provided by the following relation

$$\mathbf{v}_{em}^{lab} = \mathbf{v}_{em}^{cm} + \mathbf{v}_{cm}. \tag{C.3}$$

The "lab" and "cm" superscripts identify quantities calculated in the laboratory frame or in the center of mass frame, respectively. In our model we consider an isotropic velocity $\mathbf{v}_{em}^{cm}$, namely

$$\frac{\mathbf{v}_{em}^{cm}}{|\mathbf{v}_{em}^{cm}|} = [\cos\varphi \sin\psi]\,\hat{R} + [\sin\varphi \sin\psi]\,\hat{Z} + [\cos\psi]\,\hat{\phi}, \tag{C.4}$$

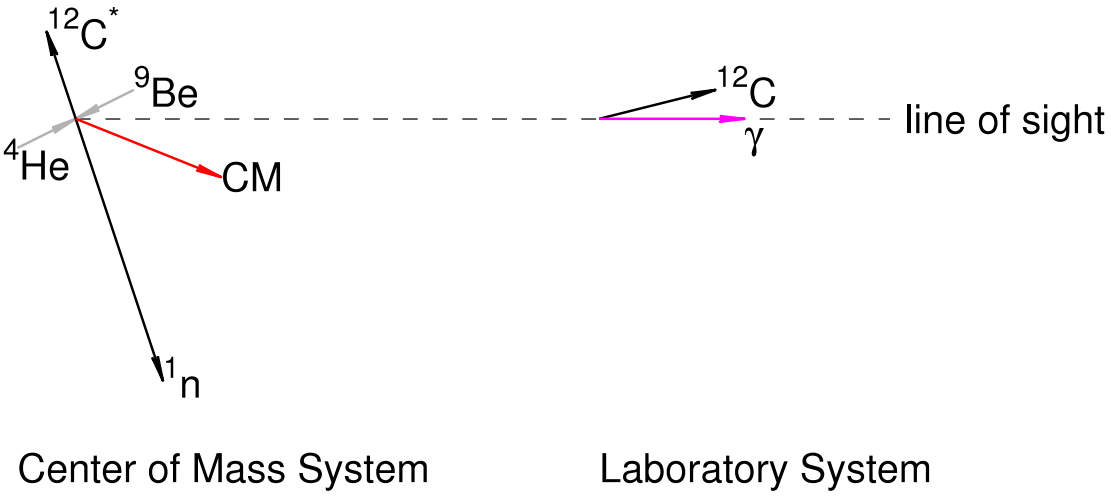

Figure C.1: Kinematic of the $^{9}\mathrm{Be}(^{4}\mathrm{He}, \mathrm{n}\gamma)^{12}\mathrm{C}$ reaction. The ^{12}C creation is isotropic in the center of mass frame. The energy of the emitted γ-ray in the laboratory frame is Doppler shifted with respect to the rest energy E_0, as of Eq.(C.2).

where (φ, ψ) are uniformly distributed (and uncorrelated) variables. The velocity of the emitting nucleus in the center of mass frame can be obtained from simple momentum and energy balance

$$v_{em}^{cm} = \sqrt{\frac{2\left(Q + K - E_0\right) m_3}{m_4^2 + m_3 m_4}} \equiv \sqrt{\frac{E_s}{\mu_{34}}}. \tag{C.5}$$

Here, Q is the energy released in the reaction (5.70 MeV for the reaction of interest here) and K is the kinetic energy of the reactants in the center of mass frame. The labels $(3, 4)$ identify the nuclear reaction products, where 4 is the nucleus emitting the γ-ray (^{12}C for our analysis). Monte Carlo methods and the equations above have been implemented in a numerical platform for estimating the energy spectrum and the spatially resolved emissivity of the γ-rays produced by the nuclear reaction.

C.1 The Numerical Platform

The numerical procedure and the Monte Carlo algorithm are built as follows. Two reactants are randomly extracted from their respective distributions $f_1(\mathbf{x}, v_\parallel, v_\perp)$ and $f_2(\mathbf{x}, v_\parallel, v_\perp)$. The particle velocity is given by

$$\mathbf{v} = v_\parallel \mathbf{e}_\parallel + v_\perp \mathbf{e}_\perp, \tag{C.6}$$

where $\mathbf{e}_\parallel = \mathbf{B}/\left|\mathbf{B}\right|$. The perpendicular unit vector $\mathbf{e}_\perp$ contains the gyromotion of the charged particles, namely

$$\mathbf{e}_\perp = \mathbf{e}_1 \cos\alpha + \mathbf{e}_2 \sin\alpha. \tag{C.7}$$

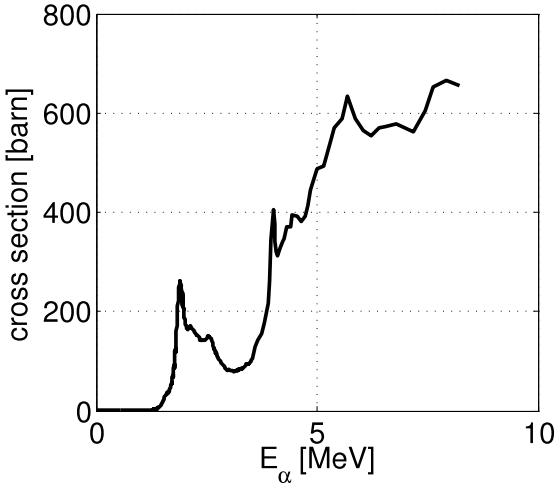

Figure C.2: Cross section of the $^{9}\mathrm{Be}(^{4}\mathrm{He}, \mathrm{n}\gamma)^{12}\mathrm{C}$ reaction, as experimentally observed and tabulated in the EXFOR database [141]. The increase in the cross section above 4 MeV accounts for the possibility of exciting the second energy level at 7.65 MeV.

As the gyromotion of a particle is usually neglected in numerical codes providing the input files to the synthetic diagnostic, it needs to be reintroduced in the calculation. For this, we choose α as a randomly distributed variable in the range $[0, 2\pi]$. This Monte Carlo angle is extracted for the reactants while for the emitter. The stochastic couple (φ, ψ) of Eq. C.4 is also generated for the reaction product. The magnetic unit vectors are expressed as a function of (R, Z) in order to simplify the calculation of the scalar product

$$\cos\beta = \frac{\mathbf{v}_{em} \cdot \hat{l}}{|\mathbf{v}_{em}|}, \tag{C.8}$$

where $\hat{l}$ is the line of sight vector expressed in real space coordinates. The orthonormal set $(\mathbf{e}_1, \mathbf{e}_2, \mathbf{e}_\parallel)$ is expressed as

$$\begin{aligned} \mathbf{e}_1(R,Z) &= \frac{\boldsymbol{\nabla}\psi(R,Z)}{|\boldsymbol{\nabla}\psi(R,Z)|} \\ \mathbf{e}_2(R,Z) &= \mathbf{e}_\parallel(R,Z) \times \mathbf{e}_1(R,Z), \end{aligned} \tag{C.9}$$

where the equilibrium functions are retrieved from the output of a CHEASE run. The energy of the emitted γ-ray is calculated from (C.2) and (C.3). The spectral line enters the energy spectrum with a weight

$$w = f_1(\mathbf{x}, \mathbf{v}_1)\mathrm{d}\mathbf{x}\mathrm{d}\mathbf{v}_1 \times f_2(\mathbf{x}, \mathbf{v}_2)\mathrm{d}\mathbf{x}\mathrm{d}\mathbf{v}_2 \times \sigma(\mathbf{v}_1 - \mathbf{v}_2). \tag{C.10}$$

This relation can be interpreted as the product between the phase space density of the reactants and the probability that their interaction give rise to the emission

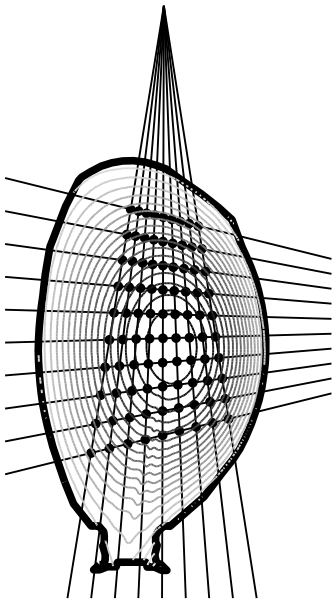

Figure C.3: Modelled geometry of the gamma camera system installed at JET. The detector accounts for 9 vertical and 10 horizontal lines of sight. The system is capable of reconstructing the spatial emissivity of γ-rays in the plasma employing tomographic techniques [142].

of a γ-ray. The latter is given by the interaction cross section, obtained from the EXFOR database [141] quantified and reported on Fig. C.2. The energy spectrum $f(\mathbf{x}, E)$ generated by the nuclear reaction between these two species is then integrated in the energy variable to obtain the spatially resolved γ-ray emissivity $I(\mathbf{x})$

$$I(\mathbf{x}) = \int dE f(E, \mathbf{x}) \simeq \sum_{i=1}^{\mathrm{N_{bins}}} dE_i f_i(\mathbf{x}). \tag{C.11}$$

The spatial points $\mathbf{x} = (R, Z)$ are considered as the intersection between the 9 vertical and 10 horizontal lines of sight of the γ-ray camera installed at JET, modelled as in Fig. C.3.

In our general model, the reacting Beryllium and Helium nuclei can be extracted from several distribution functions. In velocity space, one can provide a temperature profile, an effective temperature or a single-energy distribution. In real space, the density of particles can be assumed as spatially uniform, flux surface-dependent or as a two dimensional map. The platform has been built in order to accept experimental data for the impurity profiles and numerical predictions for the fast ion distribution. However, both distribution functions f_{He} and f_{Be} are externally loaded from data files and the synthetic diagnostic allows for a more flexible usage and a large variety of analyses.

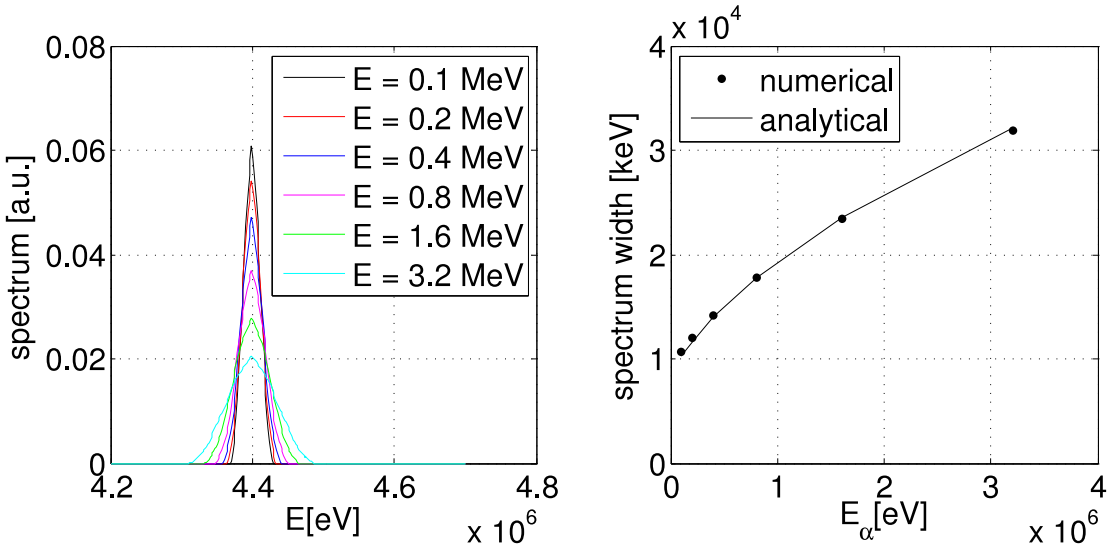

Figure C.4: Doppler broadening of the 4.44 MeV γ-ray generated by the nuclear reaction $^{9}\mathrm{Be}(^{4}\mathrm{He}, \mathrm{n}\gamma)^{12}\mathrm{C}$. The Beryllium is assumed as being static while a monochromatic and isotropic distribution of α-particles has been considered. The analytical prediction of Eq.(C.19) (solid curve) has been fit to the numerical simulation results (black dots). Each energy scan required $8 \cdot 10^6$ Monte Carlo particles.

C.2 Comparison with analytical scalings of the spectrum width

The Doppler broadening of the γ-ray spectrum can be analytically estimated for benchmarking purposes. Let us consider an isotropic and monochromatic distribution of ^{4}He particles interacting with a static background of ^{9}Be impurities. We can calculate the expectation values of some characteristic quantities and compare them with the outcome of numerical simulations. The expectation value of an arbitrary function G is defined as

$$\langle G(\xi) \rangle_{\xi} = \frac{\int d\xi f(\xi) G(\xi)}{\int d\xi f(\xi)} \tag{C.12}$$

The expectation value of E_γ represents the peak of the distribution of the γ-rays emitted from the particular reaction considered. For our case, the peak in the emission is not expected to shift ($\langle \Delta E_\gamma \rangle = 0$) as long as no particular directionality in the velocity of the ^{12}C is present. The broadening of the spectrum is quantified by $\langle \Delta E_\gamma^2 \rangle$, and can be analytically estimated as

$$\frac{\langle \Delta E_\gamma^2 \rangle}{E_0^2} = \left\langle \frac{|\mathbf{v}_{cm} + \mathbf{v}_4^{cm}|^2}{c^2} \cos^2 \beta \right\rangle \tag{C.13}$$

where the average is performed over all velocity space variables. If we consider cold impurities, the velocity of the center of mass becomes

$$\mathbf{v}_{cm} = \frac{m_\alpha \mathbf{v}_\alpha}{m_\alpha + m_{Be}}. \tag{C.14}$$

Let us calculate the first term in the expectation value of Eq. (C.2), and keep the second one as a parameter to fit, as

$$\left\langle \Delta E_\gamma^2 \right\rangle = \frac{A^2}{c^2} \left\langle |\mathbf{v}_{cm} + \mathbf{v}_4^{cm}|^2 \right\rangle. \tag{C.15}$$

We can develop the square in the previous equation as

$$\left\langle |\mathbf{v}_{cm} + \mathbf{v}_4^{cm}|^2 \right\rangle = \left\langle |\mathbf{v}_{cm}|^2 \right\rangle + \left\langle |\mathbf{v}_4^{cm}|^2 \right\rangle + \underbrace{\langle 2\mathbf{v}_4^{cm} \cdot \mathbf{v}_{cm} \rangle}_{=0}, \tag{C.16}$$

so that

$$\left\langle |\mathbf{v}_{cm}|^2 \right\rangle = \left\langle \left| \frac{m_\alpha \mathbf{v}_\alpha}{m_\alpha + m_{Be}} \right|^2 \right\rangle = \frac{2 m_\alpha E_\alpha}{(m_\alpha + m_{Be})^2} = \frac{8 \not{m}_n E_\alpha}{169 \cdot \not{m}_n^2}. \tag{C.17}$$

At the same time, the following identity holds

$$\begin{aligned} \left\langle |\mathbf{v}_4^{cm}|^2 \right\rangle = \left\langle \frac{E_s}{\mu_{34}} \right\rangle = 2\left(Q + \langle K \rangle - E_0\right) \times \left[\frac{m_n}{m_C^2 + m_n m_C} \right] = \\ = \frac{Q - E_0 + 9/13 E_\alpha}{78 m_n}. \end{aligned} \tag{C.18}$$

Finally, Eq.C.15 becomes

$$\sqrt{\left\langle \Delta E_\gamma^2 \right\rangle} = A \sqrt{\left[\frac{Q - E_0 + 9/13 E_\alpha}{78\, E_n^0} + \frac{8 E_\alpha}{169 E_n^0} \right]}. \tag{C.19}$$

where $E_n^0 = m_n c^2$. This relation, and the energy scaling in particular, are found to be very accurate when considering the results reported in Fig. C.4. A similar scan has been performed while modelling the Helium species as a Maxwellian distribution with a characteristic effective temperature T_{eff}. The expected Doppler broadening is completely analogous to the one found in Eq.(C.19), employing the correct expectation value of v_α^2 over a Maxwellian. The analytical expression thus becomes

$$\sqrt{\left\langle \Delta E_\gamma^2 \right\rangle} = A \sqrt{\left[\frac{Q - E_0 + 27\, T_{\text{eff}}/26}{78\, E_n^0} + \frac{12\, T_{\text{eff}}}{169 E_n^0} \right]}, \tag{C.20}$$

which again is in good agreement with the outcome of a numerical simulation, as of Fig. C.5.

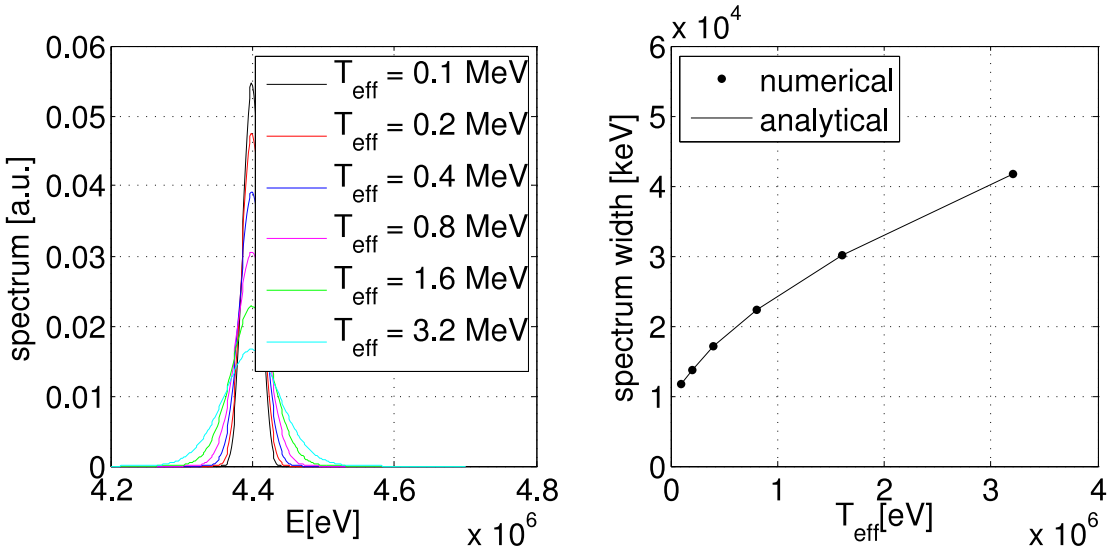

Figure C.5: Doppler broadening in the emission of the 4.44 MeV γ-ray line generated by the interaction of static Beryllium nuclei and thermal Helium. The analytical predictions of Eq.(C.20), represented as a solid curve, have been fit to the numerical result, represented as black dots. For each simulation, 10^8 Monte Carlo particles have been employed.

C.3 Spatial Emissivity

This section is dedicated to the spatial reconstruction of the radiation emissivity $I(R, Z)$ as calculated by the synthetic diagnostic. In order to allow for comparisons between theoretical models and tomographic reconstructions of spatial emissivity, the synthetic diagnostic returns the point-by-point γ-ray production rate once the energy spectrum is integrated as in Eq.(C.11). For our analysis, we have chosen the equilibrium from the JET plasma discharge #61341. The α-particle density has been simulated with the TRANSP code assuming classical and neoclassical effects. The Beryllium density and temperature profiles have been analytically approximated as

$$\begin{aligned} n &= n_0 \left[1 - (r/a)^2\right]^{\alpha_n}, \\ T &= T_0 \left[1 - (r/a)^2\right]^{\alpha_T}. \end{aligned} \tag{C.21}$$

For this analysis, a peak temperature of 8 keV has been chosen (Fig. C.6). The shaping parameters α_n and α_T have been set to 1/10 and 6, respectively. These parameters are representative of an impurity in thermal equilibrium with the background plasma and a quite uniform density across flux surfaces. The peak density n_0 is kept as a free parameter and can be provided by comparisons with experimental measurements. Therefore, the synthetic diagnostic can also be employed as a useful tool for probing the actual Beryllium density in a JET plasma. The simulated spatial emissivity of γ-rays can be observed in Fig. C.7. We can

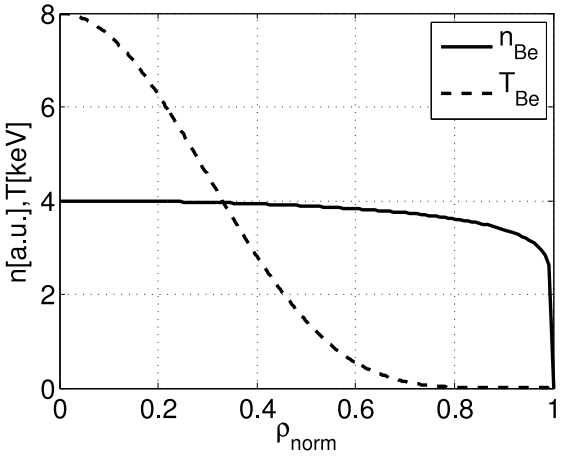

Figure C.6: Modeled density and temperature profiles of Beryllium nuclei for a JET plasma discharge, as defined in Eq.(C.21)

see how the spatial γ-ray emissivity closely resembles the alpha particle density. This is due to the choice of a flat density profile for the impurity species, as the γ-ray emissivity is roughly proportional (without considering the interaction cross section) to

$$I \simeq n_{He} n_{Be}. \tag{C.22}$$

The assumption of a uniform radial density profile for the Beryllium justifies the assumptions of Ref. [142] where single particle orbits have been considered as representative of the alpha particle density and γ-ray spatial emissivity. Given a more peaked impurity profile, often occurring in presence of turbulent pinches [143], the situation changes profoundly (Fig. C.8). This time, the difference between the α-particle density map and the light emission is evident. Single particle motion, in this configuration, can no longer be used for interpreting experimental data, as a more complex interaction between distribution functions is responsible for the γ-ray emission.

The synthetic diagnostic is particularly suitable for the analysis of the fast ion behavior in the presence of electromagnetic waves and plasma instabilities, e.g. to study the interaction between Alfvén modes and fusion products. The theory of sawtooth-driven redistribution of fast ions [49] can be extensively verified by using a sufficient number of time frames. In the end, comparisons between the synthetic diagnostic predictions and JET measurements can provide a deeper insight on the slowing down and the spatial transport of fusion products.

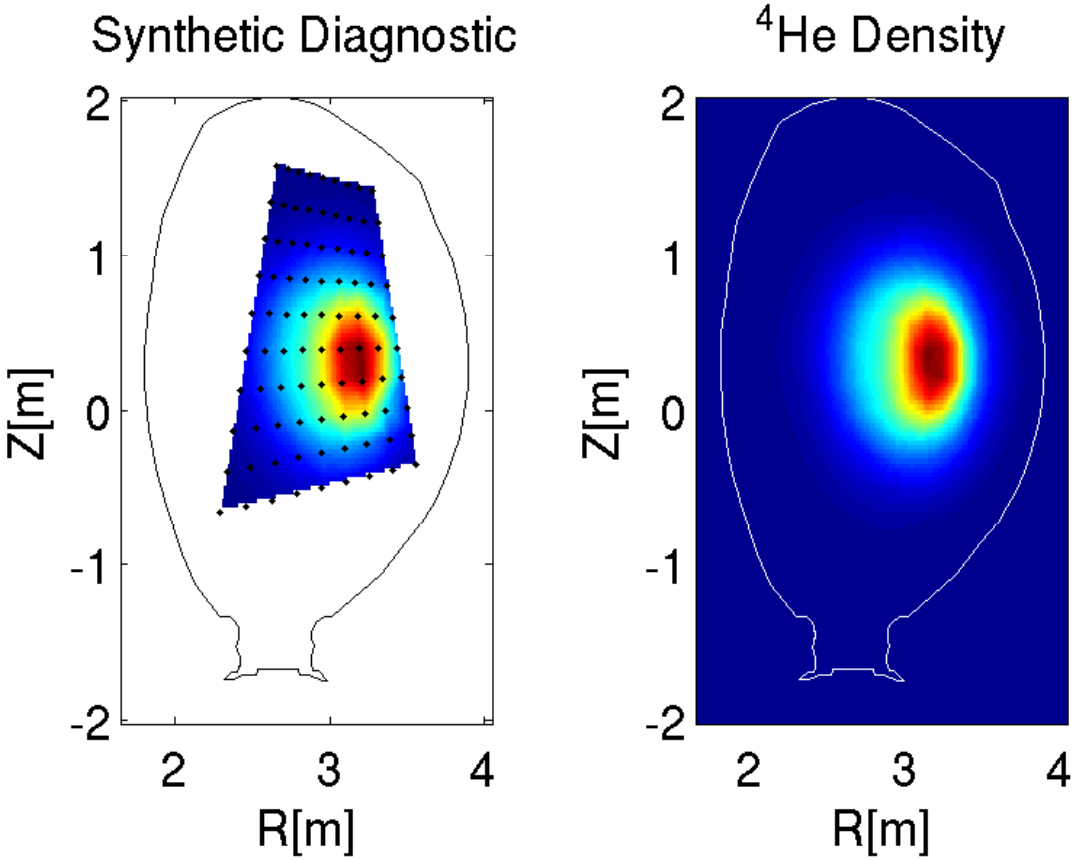

Figure C.7: Spatial distribution of the γ-ray emission in a JET tokamak plasma (left), modeled by considering simple analytical temperature and density profiles for the background Beryllium impurity. The Helium nuclei have been considered as a monochromatic distribution of 3.5 MeV α-particles (right). The output of the synthetic diagnostic is potentially comparable to the tomographic reconstructions described in Ref. [142]. This simulation has been performed with $4.3 \cdot 10^7$ particles.

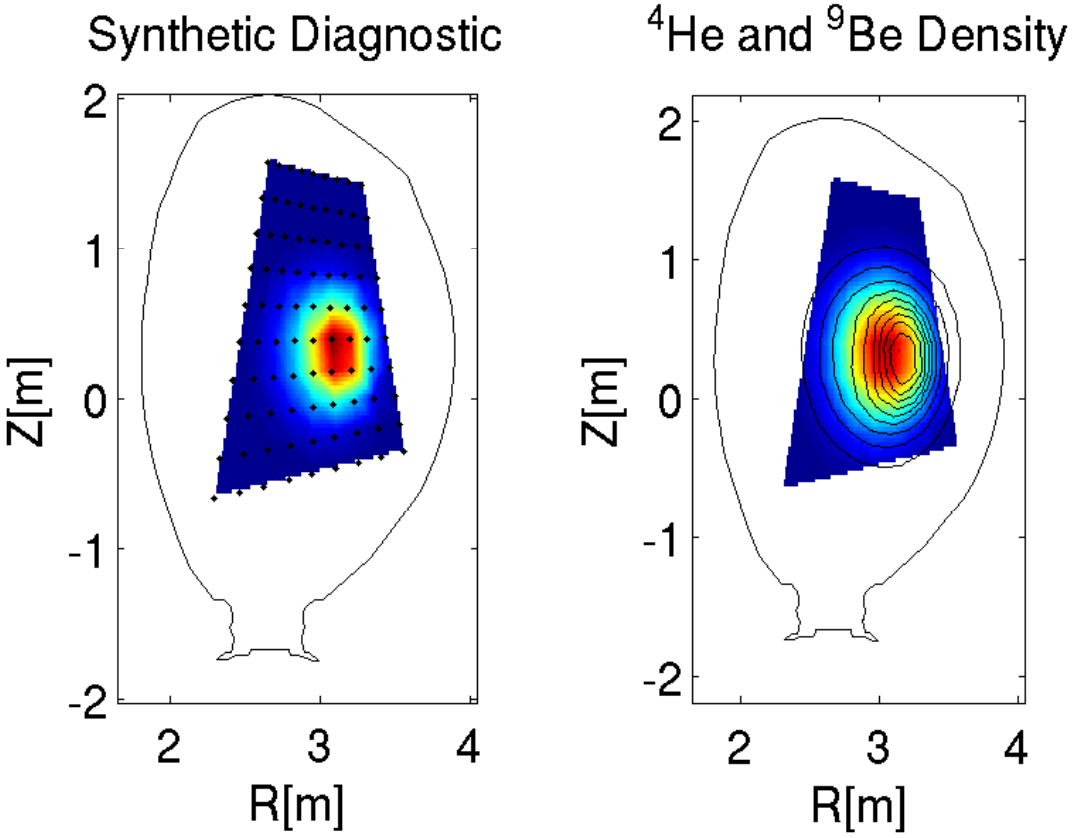

Figure C.8: Spatial distribution of the γ-ray emission in a JET tokamak plasma (left), modeled by considering a peaked Beryllium density profile. On the right, the spatial distribution of Beryllium (color) and α-particles (black isolines) are represented. The result shows how a non uniformly distributed impurity in a plasma can strongly affect the spatial γ-ray emissivity. This simulation has been performed by using $1.8 \cdot 10^8$ particles.

Bibliography

[1] Scientific American. "The Future of Nuclear Power." (2009).

[2] R. J. Goldston *et al.* "Proliferation Risks of Fusion Energy: Clandestine Production, Covert Production, and Breakout." In 9^{th} *IAEA Technical Meeting on Fusion Power Plant Safety* (2009).

[3] J. D. Lawson. "Some Criteria for a Power Producing Thermonuclear Reactor." *Proceedings of the Physical Society B*, **70**, 6 (1957).

[4] J. Wesson. *Tokamaks*. Oxford Science Publication (2004).

[5] H. Alfvén. "Existence of Electromagnetic-Hydrodynamic Waves." *Nature*, **150**, 405 (1942).

[6] L. Chen, R. B. White, and M. N. Rosenbluth. "Excitation of Internal Kink Modes by Trapped Energetic Beam Ions." *Physical Review Letters*, **52**, 1122 (1984).

[7] W. W. Heidbrink, R. Hay, and J. D. Strachan. "Confinement of Fusion Reaction Products during the Fishbone Instability." *Physical Review Letters*, **53**, 1905 (1984).

[8] B. Coppi and F. Porcelli. "Theoretical model of fishbone oscillations in magnetically confined plasmas." *Physical Review Letters*, **57**, 2272 (1986).

[9] S. von Goeler, W. Stodiek, and N. Sauthoff. "Studies of Internal Disruptions and m=1 Oscillations in Tokamak Discharges with Soft-X-Ray Tecniques." *Physical Review Letters*, **33**, 1201 (1974).

[10] F. Porcelli, D. Boucher, and M. N. Rosenbluth. "Model for the sawtooth period and amplitude." *Plasma Physics and Controlled Fusion*, **38**, 2163 (1996).

[11] Z. Chang, *et al.* "Observation of Nonlinear Neoclassical Pressure-Gradient-Driven Tearing Modes in TFTR." *Physical Review Letters*, **74**, 4663 (1995).

[12] X. Garbet, Y. Idomura, L. Villard, and T. H. Watanabe. "TOPICAL REVIEW: Gyrokinetic simulations of turbulent transport." *Nuclear Fusion*, **50**(4), 043002 (2010).

[13] J. P. Graves, *et al.* "Sawtooth-Control Mechanism using Toroidally Propagating Ion-Cyclotron-Resonance Waves in Tokamaks." *Physical Review Letters*, **102**(6), 065005 (2009).

[14] J. I. Paley, *et al.* "From profile to sawtooth control: developing feedback control using ECRH/ECCD systems on the TCV tokamak." *Plasma Physics and Controlled Fusion*, **51**(12), 124041 (2009).

[15] R. Aymar, *et al.* "Overview of ITER-FEAT - The future international burning plasma experiment." *Nuclear Fusion*, **41**, 1301 (2001).

[16] D. J. Ward. "The physics of DEMO." *Plasma Physics and Controlled Fusion*, **52**(12), 124033 (2010).

[17] S. Coda, O. Sauter, M. Henderson, and T. Goodman. "Full bootstrap discharge sustainment in steady state in the TCV tokamak." In *22nd IAEA Fusion Energy Cconference* (2008).

[18] S. Bernabei, *et al.* "Lower-Hybrid Current Drive in the PLT Tokamak." *Physical Review Letters*, **49**, 1255 (1982).

[19] Y. Peysson. "Transport of fast electrons during LHCD in TS, JET, and ASDEX." *Plasma Physics and Controlled Fusion*, **35**, B253 (1993).

[20] A. Ando, *et al.* "Plasma current generation and sustainment by electron cyclotron waves, in the WT-2 tokamak." *Physical Review Letters*, **56**, 2180 (1986).

[21] S. Coda, *et al.* "High-power ECH and fully non-inductive operation with ECCD in the TCV tokamak." *Plasma Physics and Controlled Fusion*, **42**, 311 (2000).

[22] M. R. Wade and the DIII-D Team. "Development in the DIII-D tokamak of advanced operating scenarios and associated control techniques for ITER." *Nuclear Fusion*, **47**, 543 (2007).

[23] N. Oyama and the JT-60 Team. "Overview of JT-60U results towards the establishment of advanced tokamak operation." *Nuclear Fusion*, **49**(10), 104007 (2009).

[24] F. Romanelli, JET-EFDA Contributors, and R. Kamendje. "Overview of JET results." *Nuclear Fusion*, **49**(10), 104006 (2009).

[25] H. Meyer, *et al.* "Overview of physics results from MAST." *Nuclear Fusion*, **49**(10), 104017 (2009).

[26] C. Gormezano, *et al.* "Chapter 6: Steady state operation." *Nuclear Fusion*, **47**, 285 (2007).

[27] W. W. Heidbrink and G. J. Sadler. "REVIEW PAPER: The behaviour of fast ions in tokamak experiments." *Nuclear Fusion*, **34**, 535 (1994).

[28] F. Porcelli, L.-G. Eriksson, and I. Furno. "Topological transitions of fast ion orbits in magnetically confined plasmas." *Physics Letters A*, **216**, 289 (1996).

[29] A. Fasoli, *et al.* "Progress in the ITER Physics Basis Chapter 5: Physics of energetic ions." *Nuclear Fusion*, **47**(6), S264 (2007).

[30] K. Tobita, T. Nakayama, S. V. Konovalov, and M. Sato. "Reduction of energetic particle loss by ferritic steel inserts in ITER." *Plasma Physics and Controlled Fusion*, **45**, 133 (2003).

[31] K. L. Wong, *et al.* "Excitation of toroidal Alfvén eigenmodes in TFTR." *Physical Review Letters*, **66**, 1874 (1991).

[32] W. Heidbrink, *et al.* "An investigation of beam driven Alfvén instabilities in the DIII-D tokamak." *Nuclear Fusion*, **31**(9), 1635 (1991).

[33] A. Fasoli, *et al.* "Overview of Alfven eigenmode experiments in JET." *Nuclear Fusion*, **35**(12), 1485 (1995).

[34] A. Fasoli, *et al.* "Active excitation and damping rate measurement of intermediate-n toroidal Alfvén eigenmodes in JET, C-Mod and MAST plasmas." *Plasma Physics and Controlled Fusion*, **52**(7), 075015 (2010).

[35] M. A. van Zeeland, *et al.* "Measurements and modeling of Alfvén eigenmode induced fast ion transport and loss in DIII-D and ASDEX Upgrade." *Physics of Plasmas*, **18**(5), 056114 (2011).

[36] W. W. Heidbrink, *et al.* "Anomalous Flattening of the Fast-Ion Profile during Alfvén-Eigenmode Activity." *Physical Review Letters*, **99**(24), 245002 (2007).

[37] M. García-Muñoz, *et al.* "Convective and Diffusive Energetic Particle Losses Induced by Shear Alfvén Waves in the ASDEX Upgrade Tokamak." *Physical Review Letters*, **104**(18), 185002 (2010).

[38] M. Podestà, *et al.* "Non-linear dynamics of toroidicity-induced Alfvén eigenmodes on the National Spherical Torus Experiment." *Nuclear Fusion*, **51**(6), 063035 (2011).

[39] M. P. Gryaznevich, *et al.* "Recent experiments on Alfvén eigenmodes in MAST." *Nuclear Fusion*, **48**(8), 084003 (2008).

[40] S. Briguglio, F. Zonca, and G. Vlad. "Hybrid magnetohydrodynamic-particle simulation of linear and nonlinear evolution of Alfvén modes in tokamaks." *Physics of Plasmas*, **5**, 3287 (1998).

[41] G. Vlad, *et al.* "Particle simulation of energetic particle driven Alfvén modes in NBI heated DIII-D experiments." *Nuclear Fusion*, **49**(7), 075024 (2009).

[42] P. Lauber, S. Günter, A. Könies, and S. D. Pinches. "LIGKA: A linear gyrokinetic code for the description of background kinetic and fast particle effects on the MHD stability in tokamaks." *Journal of Computational Physics*, **226**, 447 (2007).

[43] F. Zonca, *et al.* "Kinetic structures of shear Alfvén and acoustic wave spectra in burning plasmas." *Journal of Physics Conference Series*, **260**(1), 012022 (2010).

[44] W. W. Heidbrink. "Basic physics of Alfvén instabilities driven by energetic particles in toroidally confined plasmas." *Physics of Plasmas*, **15**(5), 055501 (2008).

[45] L. Chen and F. Zonca. "Theory of Alfvén waves and energetic particle physics in burning plasmas." *Nuclear Fusion*, **47**, 727 (2007).

[46] K. McGuire, *et al.* "Study of High-Beta Magnetohydrodynamic Modes and Fast-Ion Losses in PDX." *Physical Review Letters*, **50**, 891 (1983).

[47] F. Nabais, *et al.* "Impact of strongly driven fishbones and Alfvén Eigenmodes on fast ion losses." *Nuclear Fusion*, **50**(11), 115006 (2010).

[48] J. P. Graves, *et al.* "Sawtooth control in fusion plasmas." *Plasma Physics and Controlled Fusion*, **47**, B121 (2005).

[49] Y. I. Kolesnichenko and Y. V. Yakovenko. "Theory of fast ion transport during sawtooth crashes in tokamaks." *Nuclear Fusion*, **36**, 159 (1996).

[50] D. C. Pace, *et al.* "Transport of energetic ions due to sawteeth, Alfvén eigenmodes and microturbulence." *Nuclear Fusion*, **51**(4), 043012 (2011).

[51] M. García-Muñoz, *et al.* "LETTER: NTM induced fast ion losses in ASDEX Upgrade." *Nuclear Fusion*, **47**, 10 (2007).

[52] H. Naitou, T. Kamimura, and J. M. Dawson. "Kinetic effects on the convective plasma diffusion and the heat transport." *Journal of the Physical Society of Japan*, **46**, 258 (1979).

[53] R. B. White and H. E. Mynick. "Alpha particle confinement in tokamaks." *Physics of Fluids B*, **1**, 980 (1989).

[54] J. R. Myra, P. J. Catto, H. E. Mynick, and R. E. Duvall. "Quasilinear diffusion in stochastic magnetic fields: Reconciliation of drift-orbit modification calculations." *Physics of Fluids B*, **5**, 1160 (1993).

[55] G. Manfredi and R. O. Dendy. "Test-Particle Transport in Strong Electrostatic Drift Turbulence with Finite Larmor Radius Effects." *Physical Review Letters*, **76**, 4360 (1996).

[56] R.J. Hawryluk and the TFTR team. *Phys. Plasmas*, **5**, 1577 (1998).

[57] W. W. Heidbrink, *et al.* "The diffusion of fast ions in Ohmic TFTR discharges." *Physics of Fluids B*, **3**, 3167 (1991).

[58] E. Ruskov, W. W. Heidbrink, and R. V. Budny. "Radial Diffusion-Coefficient for Counter-Passing MeV Ions in the TFTR Tokamak." *Nuclear Fusion*, **12**, 2219 (1991).

[59] E. Ruskov, W. W. Heidbrink, and R. V. Budny. "Diffusion of beam ions at the Tokamak Fusion Test Reactor." *Nuclear Fusion*, **35**, 1099 (1995).

[60] C. Estrada-Mila, J. Candy, and R. E. Waltz. "Turbulent transport of alpha particles in reactor plasmas." *Phys. Plasmas*, **13**(11), 112303 (2006).

[61] S. Günter, *et al.* "Interaction of energetic particles with large and small scale instabilities." *Nuclear Fusion*, **47**, 920 (2007).

[62] A. Herrmann and O. Gruber. "Overview of ASDEX Upgrade Results." *Fusion Science and Technology*, **44**, 569 (2003).

[63] T. Hauff and F. Jenko. "Turbulent E×B advection of charged test particles with large gyroradii." *Phys. Plasmas*, **13**(10), 102309 (2006).

[64] T. Hauff and F. Jenko. "E×B advection of trace ions in tokamak microturbulence." *Phys. Plasmas*, **14**(9), 092301 (2007).

[65] C. Angioni and A. G. Peeters. "Gyrokinetic calculations of diffusive and convective transport of α particles with a slowing-down distribution function." *Phys. Plasmas*, **15**(5), 052307 (2008).

[66] C. Angioni, *et al.* "Gyrokinetic simulations of impurity, He ash and α particle transport and consequences on ITER transport modelling." *Nuclear Fusion*, **49**(5), 055013 (2009).

[67] F. Jenko, W. Dorland, M. Kotschenreuther, and B. N. Rogers. "Electron temperature gradient driven turbulence." *Phys. Plasmas*, **7**, 1904 (2000).

[68] T. Dannert and F. Jenko. "Gyrokinetic simulation of collisionless trapped-electron mode turbulence." *Phys. Plasmas*, **12**(7), 072309 (2005).

[69] T. Dannert, *et al.* "Turbulent transport of beam ions." *Phys. Plasmas*, **15**(6), 062508 (2008).

[70] W. Zhang, Z. Lin, and L. Chen. "Transport of Energetic Particles by Microturbulence in Magnetized Plasmas." *Physical Review Letters*, **101**(9), 095001 (2008).

[71] W. Zhang, *et al.* "Scalings of energetic particle transport by ion temperature gradient microturbulence." *Physics of Plasmas*, **17**(5), 055902 (2010).

[72] T. Hauff and F. Jenko. "Mechanisms and scalings of energetic ion transport via tokamak microturbulence." *Phys. Plasmas*, **15**(11), 112307 (2008).

[73] T. Hauff, M. J. Pueschel, T. Dannert, and F. Jenko. "Electrostatic and magnetic transport of energetic ions in turbulent plasmas." *Physical Review Letters*, **102**(7), 075004 (2009).

[74] M. Albergante, *et al.* "Anomalous transport of energetic particles in ITER relevant scenarios." *Phys. Plasmas*, **16**(11), 112301 (2009).

[75] M. Albergante, J. Graves, A. Fasoli, and X. Lapillonne. "Microturbulence driven transport of energetic ions in the ITER steady-state scenario." *Nuclear Fusion*, **50**(8), 084013 (2010).

[76] M. Albergante, *et al.* "Numerical modelling of electromagnetic turbulent transport of energetic ions in burning plasmas." *Plasma Physics and Controlled Fusion*, **53**(5), 054002 (2011).

[77] J. L. Luxon. "A design retrospective of the DIII-D tokamak." *Nuclear Fusion*, **42**, 614 (2002).

[78] M. Murakami, *et al.* "Off-axis neutral beam current drive for advanced scenario development in DIII-D." *Nuclear Fusion*, **49**(6), 065031 (2009).

[79] W. Heidbrink, *et al.* "Evidence for Fast-Ion Transport by Microturbulence." *Physical Review Letters*, **103**, 175001 (2009).

[80] W. W. Heidbrink. "Fast-ion Dα measurements of the fast-ion distribution (invited)." *Review of Scientific Instruments*, **81**(10), 100000 (2010).

[81] M. Keilhacker, A. Gibson, C. Gormezano, and P. H. Rebut. "REVIEW: The scientific success of JET." *Nuclear Fusion*, **41**, 1925 (2001).

[82] Y. F. Baranov, *et al.* "Anomalous and classical neutral beam fast ion diffusion on JET." *Plasma Phys. and Controlled Fusion*, **51**(4), 44004 (2009).

[83] A. Sykes, *et al.* "First results from MAST." *Nuclear Fusion*, **41**, 1423 (2001).

[84] M. Turnyanskiy, *et al.* "Study of the fast ion confinement and current profile control on MAST." *Nuclear Fusion*, **49**(6), 065002 (2009).

[85] S. Zhou, *et al.* "Turbulent transport of fast ions in the Large Plasma Device." *Physics of Plasmas*, **17**(9), 092103 (2010).

[86] A. Fasoli, *et al.* "Electrostatic instabilities, turbulence and fast ion interactions in the TORPEX device." *Plasma Physics and Controlled Fusion*, **52**(12), 124020 (2010).

[87] X. Lapillonne. *Local and Global Eulerian Gyrokinetic Simulations of Microturbulence in Realistic Geometry with Applications to the TCV Tokamak*. Ph.D. thesis, Ecole Polytechnique Fédérale de Lausanne (2010).

[88] H. Lütjens, A. Bondeson, and O. Sauter. "The CHEASE code for toroidal MHD equilibria." *Computer Physics Communications*, **97**, 219 (1996).

[89] E. Fable, C. Angioni, and O. Sauter. "The role of ion and electron electrostatic turbulence in characterizing stationary particle transport in the core of tokamak plasmas." *Plasma Physics and Controlled Fusion*, **52**(1), 015007 (2010).

[90] C. Zucca (2007). Private communication.

[91] M. J. Pueschel, M. Kammerer, and F. Jenko. "Gyrokinetic turbulence simulations at high plasma beta." *Phys. Plasmas*, **15**(10), 102310 (2008).

[92] J. D. Gaffey, Jr. "Energetic ion distribution resulting from neutral beam injection in tokamaks." *Journal of Plasma Physics*, **16**, 149 (1976).

[93] F. Jenko and W. Dorland. "Nonlinear electromagnetic gyrokinetic simulations of tokamak plasmas." *Plasma Phys. and Controlled Fusion*, **43**(26), A141 (2001).

[94] J. Candy. "Beta scaling of transport in microturbulence simulations." *Phys. Plasmas*, **12**(7), 072307 (2005).

[95] Y. Chen, *et al.* "Simulations of turbulent transport with kinetic electrons and electromagnetic effects." *Nuclear Fusion*, **43**, 1121 (2003).

[96] M. Kotschenreuther, G. Rewoldt, and W. M. Tang. "Comparison of initial value and eigenvalue codes for kinetic toroidal plasma instabilities." *Computer Physics Communications*, **88**, 128 (1995).

[97] D. Testa and M. Albergante. "A Phenomenological Explanation for the Anomalous Ion Heating Observed in the JET Alpha Heating Experiment of 1997." (2011). To be submitted to *Nature*.

[98] W. Heidbrink (2011). Private communication.

[99] O. Fischer, W. A. Cooper, M. Y. Isaev, and L. Villard. "Neoclassical transport and α particle confinement in novel 3-D reactor systems." *Nuclear Fusion*, **42**, 817 (2002).

[100] T. Kurki-Suonio, *et al.* "ASCOT simulations of fast ion power loads to the plasma-facing components in ITER." *Nuclear Fusion*, **49**(9), 095001 (2009).

[101] S. Michelsen, *et al.* "Fast ion millimeter wave collective Thomson scattering diagnostics on TEXTOR and ASDEX upgrades." *Review of Scientific Instruments*, **75**, 3634 (2004).

[102] G. A. Cooper, *et al.* "Exact canonical drift Hamiltonian formalism with pressure anisotropy and finite perturbed fields." *Physics of Plasmas*, **14**(10), 102506 (2007).

[103] S. P. Hirshman and J. C. Whitson. "Steepest-descent moment method for three-dimensional magnetohydrodynamic equilibria." *Physics of Fluids*, **26**, 3553 (1983).

[104] S. Brunner, T. M. Tran, and J. Hittinger. "Review of the Landau Collision Operator and Approximate Linearized Forms for Numerical Implementation." (2011). To be submitted for publication.

[105] S. Brunner (2011). Private communication.

[106] T. Kuosela (2011). Private communication.

[107] J. Daniel (2011). Private communication.

[108] M. Jucker, *et al.* "Integrated modeling for ion cyclotron resonant heating in toroidal systems." *Computer Physics Communications*, **182**, 912 (2011).

[109] M. Jucker. *Self-Consistent ICRH Distribution Functions and Equilibria in Magnetically Confined Plasmas*. Ph.D. thesis, Ecole Polytechnique Fédérale de Lausanne (2010).

[110] D. Moseev, *et al.* "Comparison of measured and simulated fast ion velocity distributions in the TEXTOR tokamak." *Plasma Physics and Controlled Fusion*, **53**(10), 105004 (2011).

[111] A. Fasoli and TCV Team. "Overview of physics research on the TCV tokamak." *Nuclear Fusion*, **49**(10), 104005 (2009).

[112] F. Piras, *et al.* ""Snowflake" H Mode in a Tokamak Plasma." *Physical Review Letters*, **105**(15), 155003 (2010).

[113] F. Hofmann, *et al.* "On the possibility of creating doublet-shaped plasmas in TCV." In *Proc. 23rd EPS Conference on Controlled Fusion and Plasma Physics* (1996). Proc. 23rd EPS Conference on Controlled Fusion and Plasma Physics, Kiev, Ukraine, June 1996.

[114] T. P. Goodman, F. Felici, O. Sauter, and J. P. Graves. "Sawtooth Pacing by Real-Time Auxiliary Power Control in a Tokamak Plasma." *Phys. Rev. Lett.*, **106**(24), 245002 (2011).

[115] J. I. Paley, *et al.* "Real time control of the sawtooth period using EC launchers." *Plasma Physics and Controlled Fusion*, **51**(5), 055010 (2009).

[116] R. A. Pitts, *et al.* "Parallel SOL flow on TCV." *Journal of Nuclear Materials*, **363**, 505 (2007).

[117] F. Piras, *et al.* "Snowflake divertor plasmas on TCV." *Plasma Physics and Controlled Fusion*, **51**(5), 055009 (2009).

[118] A. Bortolon, B. P. Duval, A. Pochelon, and A. Scarabosio. "Observation of Spontaneous Toroidal Rotation Inversion in Ohmically Heated Tokamak Plasmas." *Physical Review Letters*, **97**(23), 235003 (2006).

[119] Y. Camenen, *et al.* "Experimental demonstration of an up-down asymmetry effect on intrinsic rotation in the TCV tokamak." *Plasma Physics and Controlled Fusion*, **52**(12), 124037 (2010).

[120] A. Marinoni, *et al.* "The effect of plasma triangularity on turbulent transport: modeling TCV experiments by linear and non-linear gyrokinetic simulations." *Plasma Physics and Controlled Fusion*, **51**(5), 055016 (2009).

[121] A. N. Karpushov, *et al.* "A scoping study of the application of neutral beam heating on the TCV tokamak." *Fusion Engineering and Design*, **In Press, Corrected Proof**, (2011).

[122] W. W. Heidbrink, *et al.* "Beam-ion confinement for different injection geometries." *Plasma Physics and Controlled Fusion*, **51**(12), 125001 (2009).

[123] J. P. Graves, *et al.* "LETTER: Experimental verification of sawtooth control by energetic particles in ion cyclotron resonance heated JET tokamak plasmas." *Nuclear Fusion*, **50**(5), 052002 (2010).

[124] F. Jenko (2010). Private communication.

[125] X. Lapillonne, *et al.* "Non-linear gyrokinetic simulations of microturbulence in TCV electron internal transport barriers." *Plasma Physics and Controlled Fusion*, **53**(5), 054011 (2011).

[126] M. Jucker, J. P. Graves, W. A. Cooper, and T. Johnson. "Ion cyclotron resonance heating with consistent finite orbit widths and anisotropic equilibria." *Plasma Physics and Controlled Fusion*, **53**(5), 054010 (2011).

[127] K. Gustafson and A. Fasoli. "Fast ion transport in a simple magnetized plasma." (2011). To be submitted for journal publication.

[128] X. Lapillonne, *et al.* "Clarifications to the limitations of the s-α equilibrium model for gyrokinetic computations of turbulence." *Phys. Plasmas*, **16**(3), 032308 (2009).

[129] ITER Physics Expert Group on Confinement and Transport. "Chapter 2: Plasma confinement and transport." *Nuclear Fusion*, **39**(12), 2175 (1999).

[130] ITER Physics Expert Group on Energetic Particles, Heating and Current Drive. "Chapter 5: Physics of energetic ions." *Nuclear Fusion*, **39**, 2471 (1999).

[131] P. Mantica, *et al.* "Experimental Study of the Ion Critical-Gradient Length and Stiffness Level and the Impact of Rotation in the JET Tokamak." *Phys. Rev. Lett.*, **102**(17), 175002 (2009).

[132] T. Görler and F. Jenko. "Scale Separation between Electron and Ion Thermal Transport." *Physical Review Letters*, **100**(18), 185002 (2008).

[133] E. J. Doyle, *et al.* "Chapter 2: Plasma confinement and transport." *Nuclear Fusion*, **47**, 18 (2007).

[134] Z. Lin, *et al.* "Effects of Collisional Zonal Flow Damping on Turbulent Transport." *Physical Review Letters*, **83**, 3645 (1999).

[135] X. Lapillonne, *et al.* "Nonlinear quasisteady state benchmark of global gyrokinetic codes." *Physics of Plasmas*, **17**(11), 112321 (2010).

[136] E. Doyle, *et al.* "Demonstration of ITER operational scenarios on DIII-D." *Nuclear Fusion*, **50**(7), 075005 (2010).

[137] L. Lin, *et al.* "Studies of turbulence and transport in Alcator C-Mod H-mode plasmas with phase contrast imaging and comparisons with GYRO." *Physics of Plasmas*, **16**(1), 012502 (2009).

[138] L. Ballabio, J. Källne, and G. Gorini. "Relativistic calculation of fusion product spectra for thermonuclear plasmas." *Nuclear Fusion*, **38**, 1723 (1998).

[139] F. Ognissanto, *et al.* "Line integration effects on ion temperatures in tokamak plasmas measured with neutron emission spectroscopy." *Review of Scientific Instruments*, **79**(10), 100000 (2008).

[140] M. Albergante. *Fast ions dynamics effects on neutron emission spectroscopy at JET*. Master's thesis, Universitá di Milano - Bicocca (2006).

[141] `http://www.nndc.bnl.gov/exfor/exfor00.htm`.

[142] V. G. Kiptily, *et al.* "LETTER: Gamma-ray imaging of D and ^{4}He ions accelerated by ion-cyclotron-resonance heating in JET plasmas." *Nuclear Fusion*, **45**, L21 (2005).

[143] C. Angioni and A. G. Peeters. "Direction of Impurity Pinch and Auxiliary Heating in Tokamak Plasmas." *Physical Review Letters*, **96**(9), 095003 (2006).

Acknowledgements

The four years of doctoral studies at the EPFL constituted a wonderful experience. The continuous interaction with many valuable colleagues and friends shaped the person I have become. Although it is impossible to list them all, I will give it a try (if you find your name more than once, this is done on purpose).

I would first like to thank Ambrogio and Jonathan for their outstanding supervision. Their presence and foresight made me realize what I could achieve and, most importantly, what was simply out of reach. Some paths are just too impervious and learning to recognize them is probably the most valuable lesson they ever taught me.

Technical assistance on the codes employed in this thesis was essential to avoid restless nights in front of the screen. Tilman Dannert and Frank Jenko taught me the fundamentals of the GENE code, which is the backbone of this project. The great scientific help from Fulvio Zonca, Sergio Briguglio, Gregorio Vlad and Giuliana Fogaccia (in Frascati) has been as important when dealing with the HMGC code (and fast particle physics in general). I would also like to acknowledge Martin Jucker's help, both with the VENUS code and with everyday challenges (i.e. by reminding me when it was the right moment for a *PAUSE!*).

The continuous interaction with CRPP colleagues provided the inspirational environment needed during a research project. First of all, it would have been impossible to survive a Ph.D. thesis without my office mates: Martin, David, Nicolas and Wubie. Among those who provided valuable scientific help to my thesis I would love to acknowledge Stephan Brunner, Tony Cooper, Duccio Testa, Xavier Lapillonne and Federico Felici. Their suggestions and criticism have been vital and for this I am extremely grateful. Sharing time, experiences, scientific discussions and (sadly) exams with Ph.D students at CRPP has been a great experience. Furthermore, I realized how many great minds are concentrated in this lab. Among these, let us not forget the precious secretaries. Without Celine, Edith, Heidi, Nadia, Séverine and Veronique I would have been completely lost!

It would have been impossible to accomplish my doctoral studies without the encouragement I desperately needed at the beginning of my journey in Switzerland. My parents and my brothers are the reason why I am here and why I haven't given up when facing apparently unsurpassable trials. I am equally grateful to Giorgia for this. Our paths may have parted, but I will never forget the wonderful time together and the strength you gave me when I most needed it.

GP, Fede and Ale, you're probably the unluckiest guys in the world. You were there when I first arrived in Switzerland and although you had to cope with my relentless verbosity for four years, you still talk (listen?) to me. Thanks for this, for the great holidays in Mykonos and Ibiza and for the hospitality in Winterthur, Punta Ala and San Diego. GP, I really hope we will once be able to laugh at South Park episodes together as we did in the past.

GP, Luigi, Claudia, Marzia, Fede, Ludo, Livia, David and Evy: grazie mille (ovvia citazione degli 883). Whenever life got boring in Lausanne (and it seldom happened), you restored the party-oriented equilibrium I wished for. I really hope the 2moreraw production will keep on existing.

Being Lausanne such a wonderful city, it inevitably attracts great people. In these four years, I had the luck to meet many of them and for this I will never be grateful enough. Just to name a few, how can I not mention Annamaria, Chris(topher Luke), Fra, Osi, Sanja and Vero?

Un grazie particolare va agli amici della piazza di Gallarate sui quali so di poter contare per impareggiabili momenti di delirio ad ogni rientro in Italia ed ad ogni visita a Losanna. Siete leggendari, non cambiate mai!

L'ultimo ringraziamento è particolarmente sentito. È rivolto alla persona con la quale sto condividendo un lungo viaggio di ritorno dalla California (del quale approfitto per scrivere queste righe). Non posso che dirti una cosa dopo i fantastici momenti passati insieme: iE!

Mattia Albergante

Italian nationality, born 29/11/1982
Place de la Palud, 1
1003 Lausanne (VD)
Switzerland
+41(0) 76 212 0471
mattia.albergante@epfl.ch

Profile

Highly enthusiastic and greatly interested in new challenges, I have developed solid problem solving skills and modelling techniques in heterogenous fields of research (from physics to econometrics).
During my studies I have been continuously working with statistical models and software development in an extensive variety of programming languages and platforms.

Education

PH.D. IN PHYSICS, ÉCOLE POLYTECHNIQUE FÉDÉRALE DE LAUSANNE, 2007 - OCTOBER 2011

Thesis on the numerical modelling of the anomalous fast ion behavior in nuclear fusion devices.
The thesis focused on the creation of a numerical platform capable of simulating the interaction between microturbulent fields and energetic ions. The numerical code has been created by interfacing and upgrading previously existing codes as well as developing a synthetic diagnostic. Successful benchmarks have been performed.
During the period spent at the EPFL I was also responsible of the joint experiments on the interaction between energetic particles and turbulence in the framework of the ITPA project.

M.SC. IN PHYSICS, UNIVERSITY OF MILAN-BICOCCA, 2004 - 2006, MAGNA CUM LAUDE

Thesis on the numerical and experimental analysis of the neutron emission spectroscopy from plasmas. The work was mostly carried out at the JET laboratories in Oxford (UK) and concentrated on the interpretation of experimental data from the MPRu and TOFOR spectrometers with a set of numerical codes.

BACHELOR IN PHYSICS, UNIVERSITY OF MILAN-BICOCCA, 2001 - 2004

Thesis on algorithm development for stock market cross-correlation generation in the ARCH model.
A series of C++ routines have been created to implement a novel algorithm describing the behaviour of the S&P500 stock market and the cross-correlations therein.

Software Development and IT expertise

Strong computational skills developed over a decade of code development, both for work and personal interest.

Solid knowledge of C, C++, Matlab, Fortran and Python on Linux/Mac OSX platforms. I've been also studying and writing codes/scripts for iOS.

A great knowledge of the Office suite and LaTeX document writing has also been obtained during my studies. I have created and put online a small number of websites written in HTML with SQL database access and PHP scripting.

Profound knowledge of the following operative systems: Mac OSX (10.5 and 10.6), Linux (Ubuntu in particular). Good knowledge of Windows platforms (XP and Vista).

Languages

ITALIAN

Mother tongue

ENGLISH

Fluent speaking and writing, learnt during years of working experience in international environments.

FRENCH

Very good speaking and writing, following the doctoral studies in French speaking Switzerland.

GERMAN

Basic knowledge after a six-month study, undertaken for personal interest, at the EPFL.

List of publications

FIRST AUTHOR

M. Albergante, *et al.*, "Anomalous transport of energetic particles in ITER relevant scenarios", Physics of Plasmas, **16**, 112301 (2009)

M. Albergante, *et al.*, "Microturbulence driven transport of energetic ions in the ITER steady-state scenario", Nuclear Fusion, **50**, 084013, (2010)

M. Albergante, *et al.*, "Numerical modelling of electromagnetic turbulent transport of energetic ions in burning plasmas", Plasma Physics and Controlled Fusion, **53**, 054002 (2011)

CO-AUTHOR

D. Testa and M. Albergante, "Evidence for a new path to the self-sustainment of the thermonuclear fusion in magnetically confined burning plasma experiments", Nature (to be submitted, 2011)

E. H. Roman, M. Albergante, *et al.*, "Modeling cross correlations within a many-assets market", Physical Review E, **73**, 036129 (2006)

C. Hellesen, M. Albergante, *et al.*, "Neutron spectroscopy measurements and modeling of neutral beam heating fast ion dynamics", Plasma Physics and Controlled Fusion, **52**, 085013 (2010)

F. Ognissanto, *et al.,*"Line integration effects on ion temperatures in tokamak plasmas measured with neutron emission spectroscopy" Rev. Sci. Instrum. **79**, 10E511 (2008)

J. P. Graves, *et al.*,"Control of Magnetohydrodynamic Stability by Phase Space Engineering of Energetic Ions in Tokamak Plasmas", Nature Physics (submitted, 2011)

D. Moseev, *et al.*, "Comparison of measured and simulated fast ion velocity distributions in the TEXTOR tokamak", submitted to Plasma Physics and Controlled Fusion (2011)

W. A. Cooper, *et al.*, "Helical core tokamak MHD equilibrium states", Plasma Physics and Controlled Fusion (submitted, 2011)

CONFERENCE PROCEEDINGS

M. Albergante, *et al.,* "Numerical modelling of electromagnetic turbulent transport of energetic ions in burning plasmas", Invited talk at the Theory of Fusion Plasmas conference, Varenna (Italy, 2010).

M. Albergante, *et al.*, "Influence of fine scale turbulence on the transport of high energy populations in burning plasmas", 37th EPS conference on Plasma Physics, Dublin (Ireland, 2010). Winner of the IOP Poster Prize.

M. Albergante, *et al.*, "Microturbulence driven transport of energetic ions in the ITER steady-state scenario", Invited talk at the IAEA Technical Meeting on Energetic Particles, Kiev (Ukraine, 2009).

M. Albergante, *et al.*, "Interaction between fast particles and turbulence", Contributed poster at the Theory of Fusion Plasmas conference, Varenna (Italy, 2008).